CZECH TECHNICAL UNIVERSITY IN PRAGUE
FACULTY OF ELECTRICAL ENGINEERING
DEPARTMENT OF ELECTROMAGNETIC FIELD

Design and implementation of optical camera-based communication systems for Internet-of-things applications

DOCTORAL THESIS BY SHIVANI RAJENDRA TELI

2021

Declaration of Originality

I, the undersigned, hereby declare that this doctoral thesis is the result of my research in our research team and my contribution corresponds to that specified at the beginning of each research chapter. The thesis was written under the professional supervision of Prof. Stanislav Zvánovec, using the literature and resources listed in the Bibliography and References.

In Prague, 2021

....
Ing. Shivani Rajendra Teli

Acknowledgement

Firstly, I would like to express my thanks to my supervisor Prof. Stanislav Zvanovec, who supported and guided me during my studies and gave me the opportunity to be a part of a great team of people. Many thanks also belong to our optical team, it was my pleasure to collaborate with them on optic topics.

I would like to acknowledge Prof. Zabih Ghassemlooy for the opportunity to setup a virtual secondment campaign at Northumbria University under his guidance and his opinions and advice, which have significant impact on the results presented in this thesis. I would like to thank Prof. Rafael Perez-Jimenez for the opportunity to spend 3 months at Universidad de Las Palmas de Gran Canaria and for his support and inputs to my research activities. I would like to thank Dr. Petr Chvojka and Dr. Stanislav Vitek for their support and advice.

Finally, special thanks go to my family and friends for their never ending support and patience.

Abstract

Optical wireless communications (OWC) systems offering advantages such as higher bandwidth, an unregulated spectrum, resistance to electromagnetic interference and a high order of reusability, have emerged as a complementary technology to radio frequency. Within OWC, the optical camera communication (OCC) technology utilizing camera-based receiver (Rx) represents an extension of photodetector Rx based visible light communications (VLC) with the advantage of no extended hardware cost of the Rx. The availability of cameras in smart devices such as smartphones, traffic networks, security surveillance, vehicles, etc., can be effectively exploited as an optical Rx, thus enabling the implementation of VLC-OCC links. Therefore, the thesis focuses on the design and implementation of VLC-OCC based technologies and their applications within indoor and outdoor Internet of Things (IoT).

Low data rates IoT-based applications including device-to-device communications, mobile attocells, vehicle-to-everything, infrastructure-to-vehicle or vehicle-to-infrastructure, vehicle-to-vehicle, smart environments (homes, offices, hospitals), etc. need to be considered. However, the major challenge in implementing such systems is the requirement for flicker-free transmission at lower data rates (i.e., most cases in IoT applications). Therefore, in this thesis, a low data rate rolling-shutter (RS)-based multi-channel multiple-input multiple-output OCC scheme and a novel wireless communications link using an illuminating optical fiber as a transmitter for indoor OCC based IoT environments, which is flicker-free is proposed and analyzed. Moreover, a novel technique to extend the RS-based OCC system for long range outdoor IoT-based applications by reducing the spatial bandwidth of the camera in the out-of-focus regions is experimentally derived. On the other hand, in order to support user based high data rates for applications such as internet surfing, downloading big data, etc., along with above mentioned low data rate IoT-based links within smart environments, a hybrid optical IoT based VLC-OCC system is proposed and analyzed.

Key Words

Optical wireless communication, visible light communication, optical camera communications, Internet of things, CMOS image sensor

Abstrakt

Systémy optické bezdrátové komunikace (OWC) nabízejí řadu výhod, jako je větší šířka pásma, neregulované spektrum, odolnost proti elektromagnetickému rušení a vysokou opakovatelnost použití, a mohou být vhodnou doplňující technologií k systémům v radiofrekvenčních pásmech. V rámci OWC pak technologie komunikace optickými kamerami (OCC) využívající přijímač (Rx) založený na kameře představuje rozšíření komunikace ve viditelném světle (VLC) založené na klasickém fotodetektoru. Zde navíc u většiny chytrých zařízení nedochází ke zvýšeným nákladům na hardware Rx. Širokou dostupnost kamer v chytrých zařízeních, jako jsou smartphony, dopravní sítě, bezpečnostní dohled, vozidla atd., lze efektivně využít jako optický Rx, což umožňuje jednoduchou implementaci VLC-OCC spoje. Proto se tato disertační práce zaměřuje na návrh a implementaci technologií založených na VLC-OCC a jejich aplikace v rámci vnitřního a venkovního Internetu věcí (IoT).

Aplikace založené na IoT s nízkou datovou rychlostí zahrnují komunikace mezi zařízeními, mobilní attocelly, spoje typu vehicle-to-everything, infrastructure-to-vehicle or vehicle-to-infrastructure, vehicle-to-vehicle, inteligentní prostředí (domácnosti, kanceláře, nemocnice) atd. Hlavní výzvou při implementaci těchto systémů je však požadavek na přenos bez blikání vysílače při nižších rychlostech dat (tj. ve většině případů v aplikacích IoT). Proto v této práci bylo navrženo vícekanálové multiple-input multiple-output OCC schéma na bázi rolovací závěrky (RS) využívající osvětlovací optické vlákno jako vysílač pro vnitřní OCC. Kromě toho byla navržena a experimentálně odvozena nová technika k rozšíření systému OCC pro venkovní IoT aplikace založená na RS se snížením prostorové šířky pásma kamery v oblastech mimo zaostření. Pro podporu paralelního přenosu vysoké datové rychlosti pro aplikace, jako je surfování na internetu, stahování velkých dat atd., a zároveň stálou podporu nízkých datových rychlostí OCC byl navržen a analyzován nový hybridní optický VLC-OCC systém.

Klíčová Slova

Optické bezvláknové komunikace, komunikace ve viditelném světle, komunikace optické kamery, Internet věcí, Obrazový snímač CMOS

Contents

Abbreviations

1D	One Dimension
2D	Two Dimension
3D	Three Dimension
4G	Fourth Generation
5G	Fifth Generation
ADC	Analog-to-Digital Converter
BER	Bit Error Rate
CCD	Charge-Coupled Device
CIM	Color Intensity Modulation
CMOS	Complementary Metal-Oxide-Semiconductor
CoC	Circle of Confusion
D2D	Device-to-Device
DCO-OFDM	DC-biased Optical Orthogonal Frequency Division Multiplexing
FOV	Field of View
fps	frames per second
FSO	Free Space Optics
GS	Global Shutter
HS-PSK	Hybrid-Spatial Phase Shift Keying
IM	Intensity Modulation
IoT	Internet of Things
IR	Infrared
IS	Image Sensor
ISK	Intensity Shift Keying
LCD	Liquid Crystal Display
LED	Light Emitting Diode
LOS	Line-of-Sight
MD	Motion Detection
MIMO	Multiple-Input Multiple-Output
MMW	Millimeter Wave
MSE	Mean Squared Error
NLOS	Non-Line-of-Sight

NN	Neural Network
NRZ	Non-Return to Zero
NSM	Nyquist Sampling Modulation
OCC	Optical Camera Communication
OFDM	Orthogonal Frequency Division Multiplexing
OFDMA	OFDM Access
OIoT	Optical IoT
OLED	Organic Light Emitting Diode
OOK	On-Off Keying
OWC	Optical Wireless Communication
PD	Photodetector
PHY	Physical Layer
PPI	Pixel Per Inch
PSNR	Peak-Signal-to-Noise Ratio
RF	Radio Frequency
RGB	Red, Green and Blue
ROI	Region-of-Interest
RS	Rolling Shutter
Rx	Receiver
S2-PSK	Spatial 2-PSK
SIMO	Single-Input Multiple-Output
SNR	Signal-to-Noise Ratio
SS	Shutter Speed
SSK	Space Shift Keying
Tx	Transmitter
UPSOOK	Undersampled Phase Shift On-Off Keying
UV	Ultraviolet
V2V	Vehicle-to-Vehicle
V2X	Vehicle-to-Everything
VL	Visible Light
VLC	Visible Light Communication
VPPM	Variable Pulse-Position Modulation
WDM	Wavelength Division Multiplexing

List of Symbols

Symbol	Description
a	pixel length
A_{lens}	camera's external lens
d_c	distance between center of lens and image
d_{img}	diameter of Tx image
d_{IS}	distance between center of lens and IS
d_L	distance of object from camera lens
D_{lens}	diameter of lens aperture
d_{Tx}	diameter of Tx
E_n	energy captured by n^{th} row
F	focal ratio
f	focal length of lens
f_R	camera frame rate
f_{stop}	aperture
g	gap between two pixels
G_i	focused image intensity
G_o	defocused image intensity
G_v	camera gain
H	height of IS in pixels
$h_{\text{ch, u, v}}$	channel impulse response of (u,v)-th pixel
$h(t)$	combined impulse response of channel and camera
I_{peak}	peak intensity
I_{Rx}	intensity of received image frames
I_{Tx}	intensity of transmitted image frames
k	magnification factor of lens
k_o	magnification factor of camera at reference link span
L	transmission distance
l_{IS}	size of IS
l_{LED}	size of LED
L_o	reference link span
m	Lambertian order

$M_{[v,u]}$	mask of pixels
N_{columns}	number of columns
N_{row}	number of rows
$n(t)$	additive white Gaussian noise
$P_{\text{Rx}(t)}$	received power at camera
$P_{\text{Tx}(t)}$	transmitted power
R_b	data rate
$s(t)$	generated signal
t_{exp}	exposure time
$t_{\text{row-exp}}$	row exposure time
$t_{\text{read-out}}$	read out time
$t_{\text{row-shift}}$	row shift time
U	number of row of IS
U(.)	Heaviside step function
V	number of columns of IS
V_{ADC}	voltage sampled by ADC
V_{pixels}	voltage obtained from pixel integration of light
W	width of IS in pixels
x_G	gray scale
$x(t)$	intensity modulated light
$y(t)$	received signal
$\otimes$	time domain convolution
$\otimes \otimes$	2D convolution operator
η	quantum efficiency of IS
θ_e	emission angle
Ψ	incident angle
(ξ_x, ξ_y)	coordinates of the centre of the image
σ	standard deviation
$\sigma_{b,x}$	standard deviation in x direction on image plane
$\sigma_{b,y}$	standard deviation in y direction on image plane
σ'_i	parameter of model

CHAPTER 1 | Introduction

The fifth generation (5G) wireless network is being developed as a new platform for mobile networks, rather than just extending the capacity and reliability of the existing fourth generation (4G) [1, 2]. As such, the focus in the 5G standard is on capacity enhancement, massive connectivity, and ultra-high reliability (low latency) [1]. They stem largely from an increasing number of users and smart devices connecting to a cellular network in the Internet of things (IoT) domain as part of smart cities. Given the rise of IoT, 5G is well positioned to be the standard framework for global communication platforms, which support real-time interactions with wireless sensor networks and devices at a large scale [3]. While 5G is still yet to be finalized, some of the candidate technologies have emerged: *A*) Millimeter wave (MMW) ranging from 30 - 300 GHz and higher frequency bands such as infrared (IR) and visible light (VL) ranging from 300 GHz to 400 THz and 400 THz - 800 THz, respectively which are intended to dramatically increase the spectrum efficiency, especially base stations, by utilizing a carrier frequency [4]. *B*) Massive multiple-input multiple-output (MIMO), which could provide hundreds of ports for both uplink and downlink utilizing dozens of antennas to extend the capacity by a factor of 22 or more. *C*) Small cells based base stations, which offer the relay-based capability for signal transmission between base stations and mobile users. The requirements in communication systems design to support IoT are as follows (*i*) less complexity and cost-effectiveness; (*ii*) resource availability; (*iii*) quality of service and reliability; (*iv*) transmission range; (*v*) safety; and (*vi*) low power consumption.

IoT represents the network of physical devices, sensors within the smart environments, and their inter-connectivity enables objects to communicate and exchange data between themselves. As the IoT paradigm opens the doors to innovations, which contribute to interactions between objects and humans, it enables the realization of smart cities, infrastructures, and services for enhancing the quality of life and improving better utilization of resources [5]. The radio frequency (RF) and Android-based IoT have been implemented for home automation systems as part of smart home environments [6]. A Raspberry Pi camera based body detection using passive infrared sensors and computer vision for security application was proposed in [7]. A survey on IoT applications for outdoor environments such as traffic surveillance and accident detection systems, which provides a smart way to handle traffic and solve concerned problems, was presented in [8].

Over the last decade, an increasing number of multimedia-capable and Internet-connected mobile devices have demanded highly reliable and high-speed connectivity for both indoor and outdoor applications [1]. With the introduction of IoT, these demands are becoming even higher. So far, conventional RF-based communications have been the dominant technology for meeting these demands by employing complex coding and multilevel modulation schemes as well as spatial diversity. However, the RF spectrum has largely reached its saturation level with slow-down in the achievable spectrum efficiency [9]. As a potential alternative to congested RF-based communication systems, optical wireless communication (OWC) is envisioned as a next-generation communications system, which could deliver very high-speed and reliable data transmission in a specific application in both indoor and outdoor environments [10, 11].

The extensive deployment of smart devices within smart environments (i.e., homes, offices, industrial halls and device-to-device (D2D) communications) as of the emerging IoT represents a major challenge for communication networks service providers in order to provide cost-effective and high quality of service wireless connectivity [12]. In parallel to the developments in the RF domain, there is the potential to adopt a complementary wireless technology of OWC in certain areas where connectivity can readily be established [10]. Figure 1.1 shows the electromagnetic spectrum including the optical regions, i.e., the three main bands of ultraviolet (UV), IR, and VL utilized within OWC. OWC operates at the mentioned optical regions for communication which spectrum is abundant to provide much higher bandwidth than RF based systems [13–16]. Both radio waves and microwaves have a total bandwidth of approximately 300 GHz. On the other hand, the IR, VL, and UV light offer a theoretical bandwidth of 20 THz, 320 THz, and 75 PHz, respectively [13–16]. OWC technology covers various transmission media for both indoor and outdoor environments, i.e. IR communication, free space optics (FSO) using laser beam transmitter (Tx), visible light communication (VLC) using light emitting diode (LED), optical camera communication (OCC) using a camera receiver (Rx), and UV communication using UV light as its medium. Figure 1.1 also illustrates these exemplary OWC systems. Within the latter two bands, VLC, FSO, and OCC, see Figure 1.1, can be potentially considered as part of the 5G networks for the realization of IoT [12].

VLC is an emerging technology, which has been proposed for the 5G networks. It utilizes LED-based lighting fixtures and photodetectors (PD) to simultaneously provide data communications and illumination in indoor environments with possible extension to outdoor areas as well [17]. Note that, the visible wavelength band of 370-780 nm provides a massive bandwidth of 400 THz, which is 10,000 times larger than the RF bandwidth [18], see Figure 1.1. In addition, the VLC technology offers inherent security at the physical layer (PHY), immunity to RF electromagnetic interference, and free licensing [11]. The LEDs offer several benefits over existing lighting infrastructures, such as lower power consumption, longer life expectancy, higher energy efficiency, reduced
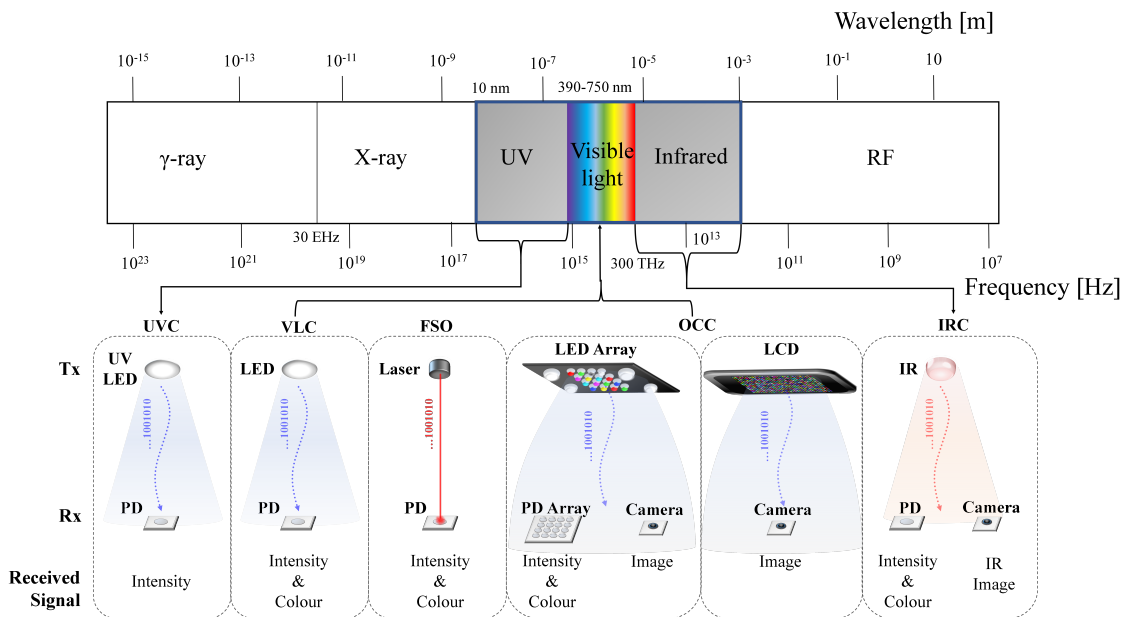
Figure 1.1: Electromagnetic spectrum along with exemplary schemes of OWC.

maintenance, lower heat generation characteristics and fast switching speed (orders of magnitude higher) [19, 20]. Therefore, it can be said, *"the VLC technology utilizing smart LEDs could join the dots of IoT"*. The VLC can enable true IoT as most consumer smart devices come with LEDs and cameras, which can be used for data communications and indoor localization [21].

On the other hand, over the past few years, we have seen smart devices with built-in high-resolution complementary metal-oxide-semiconductor (CMOS) cameras [22]. These CMOS cameras are capable of capturing high-resolution videos with a resolution of at least 1280 × 720 pixels and a capture rate of 30 frames per second (fps) [23, 24], which are more than adequate for low-speed applications. Due to the large scale and increasing availability of mobile phones, smartphone VLC can be attractive, as nearly all mobile users effectively carry and regularly use camera-based optical Rxs. Not only smartphones but also the majority of new generation smart devices have built-in CMOS cameras, providing the ability to capture photos and videos as well as being used for data communications (low-speed), indoor localization and range findings [23, 25]. The smartphone or camera-based VLC has been studied within the framework of OWC [26] and considered as a candidate for IEEE 802.15.7rl standard and is referred to as OCC [27]. OCC represents an extension of VLC with the advantage of no additional hardware to establish D2D communications at low R_b and indoor positioning [28]. Unlike conventional VLCs, which employ PDs as the Rx, in OCC a mobile phone CMOS camera is used as the Rx [25]. That is, OCC captures two dimension (2D) data in the form of image sequences, thus is able to transmit more information compared to PD-based VLCs. The OCC technology is making remarkable progress in the key application as part of the fourth industrial revolution i.e., IoT, smart vehicles, etc. [29].

As the IoT paradigm opens the doors to innovations that contribute to a novel type of interactions among things and humans, it enables the realization of smart cities, infrastructures, and services for enhancing the quality of life and utilization of resources. VLC with a huge frequency spectrum integrated with IoT can open up a wide range of indoor as well as outdoor applications using optical transmission links [30]. It can therefore be termed as optical IoT (OIoT). Figure 1.2 illustrates various solutions that can be provided by the OIoT from connecting devices to human value as:
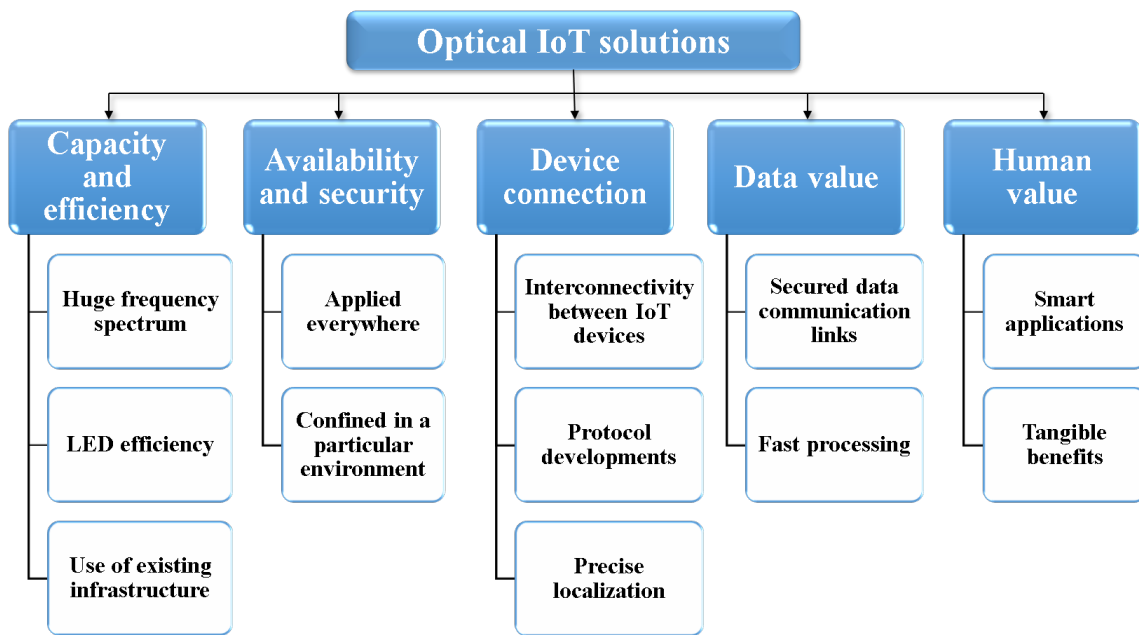

Figure 1.2: OIoT advances

- **Capacity and efficiency**
  Due to the increasing demand for high-speed wireless services, the RF spectrum (3 kHz – 300 GHz, see Figure 1.1) is being congested, thus resulting in the bandwidth bottleneck. The visible light spectrum (see Figure 1.1) offers bandwidth orders of magnitude higher than RF, which can be effectively utilized in IoT networks [31]. In addition, small and compact VLC modules for OIoT can be easily implemented into the existing lighting infrastructure. LEDs represent green-lighting devices, which are being widely used at a global level because of the high power efficiency of 80% compared to traditional lights [32]. A recent report from the U.S. Department of Energy states, by the year of 2025, it is possible to save energy by up to 217 terawatt-hours by using LED-based lighting technology [33].

- **Availability and security**
  The OIoT system based on VL can be designed by re-using the ubiquitous lighting

4

infrastructure with only a few additional modules (modulation unit, digital-to-analog converter, and driving circuit), which can be included in the LED lighting systems. Due to the rapid growth of the LED industry, it is expected that the cost of VLC transceivers will be reduced.

Security is an important issue in RF communications since RF signals can penetrate walls and other objects, thus compromising on the link security at the physical level. In contrast to RF, light signals can be confined within a specific well-defined area both indoor and outdoor, thus making eavesdropping almost impossible unless the Rx is within the field of view (FOV) of the Tx. In addition, lights generated by LEDs are safe for the environment, provided the illumination level is below the recommended standard.

- **Device connection**
  The inter-connectivity between various OIoT devices can be maintained by means of adopting the most suitable handover algorithm to ensure seamless communications while mobile devices are moving around within a certain transmission range of course [34]. For longer range, relayed based OIoT could be adopted. Moreover, protocol developments for the PHY, Media Access Control and upper layer design to optimize link reliability are studied under IEEE 802.15.7 [35].

  On the other hand, a combination of VLC and OCC systems can also be leveraged for indoor localization with very high positioning accuracy. Indoor positioning and localization are achieved by using the LED lights similar to the global positioning system. The experiment results in [36] demonstrate a mean positioning error of less than 1.7 cm using an indoor VLC based positioning system based on orthogonal frequency division multiplexing access (OFDMA).

- **Data value**
  Secured data communication links can be formed using VL as the carrier signal in OIoT. The new, fast and efficient adaptation techniques for VLC have been studied in [37] to improve the Rx signal-to-noise ratio (SNR) ratio and to reduce the required time to estimate the position of the VLC Rx.

- **Human value**
  Developing cost-effective, environmentally friendly and efficient OIoT within smart environments (i.e., homes, hospitals, industries, cities, etc.) would be possible, which offers higher speed and safer communications.

In the first part of the doctoral thesis, state-of-the-art OCC is presented in chapter 2, describing the principles of OCC technology, channel characterization and modulation schemes. The objectives of the thesis are given in chapter 3. Then, the thesis core is demonstrated in chapter 4 by a collection of journal papers presenting a description of

their contributions and relevance to the thesis topic. In the end, the achieved results, conclusions and future research topics are summarized in chapter 5.

CHAPTER 2

State-of-the-Art

M otivated by the advancements and availability of OCC-Rxs, i.e., cameras, OCC technology has been considered as a promising alternative within OWC, especially for low-rate IoT-based environments. In this chapter, the basic principles of OCC, MIMO-OCC Tx and Rx characteristics and channel characterization along with camera Rx-based capturing techniques are presented. Finally, an overview of recent advancements in OCC modulation schemes is also presented.

The following subsections describe the state-of-the-art as it relates to the goals of this thesis.

2.1 Optical camera communication technology

As VLC technology utilizes an existing illumination infrastructure, OCC extends the idea further by utilizing existing Rx, i.e., digital cameras in daily used smart and mobile devices. In OCC, single or multiple digital image sensor (IS) cameras in-built within smart devices and LEDs or display screens are employed as the OCC Rx and Tx, respectively. These digital cameras with IS containing a large number of micro-scale PDs are used for photography, vision, surveillance, motion detection, augmented reality [38], virtual reality [39], localization and positioning [21, 40], and data communications [41]. Note, localization and positioning using OCC is beyond the thesis topic and will not be discussed here. This development has led to the emergence of OCC, which has gained interests within the researchers and is being considered as an option in IEEE 802.15.7m (TG7m) visible light communication task group [27].

Unlike VLC that can only capture intensity (one dimension (1D) data) with a single PD Rx, the major advantage of OCC lies in parallel capturing of 2D image data with colors (i.e., spectral resolution). Image processing on the Rx side also provides OCC with advantages to classify shapes and estimate the distance-based depth perception from the vision of cameras. However, in OCC, R_b is limited by the frame-rate f_R of the ISs, i.e., camera. R_b can be increased by using higher frame rate cameras, which are very costly and the camera capture speed, which is defined as the physical parameter of the sensor (electronics) and the graphics processor speed in the hardware domain. The f_R of the camera is generally confined to either 30 fps or 60 fps, except for some slow-motion capable

cameras with f_R of 120-240 fps. Some specialized high-speed cameras are available with f_R ranging from 1000 to 21000 fps [42]. However, these cameras are not suitable for the use in mobile devices and are less likely implemented for OCC applications. Therefore, OCC is further extended to offer massive MIMO capabilities in order to increase R_b using LEDs and PD arrays in the form of multiple pixels in ISs for IoT applications in both indoor and outdoor environments [43].

Figure 2.1 shows a general overview of MIMO-OCC scheme. Recent studies in this area have outlined the use of liquid crystal display (LCD)s with multiple embedded neopixels, LCD or organic light emitting diode (OLED)-based mobile phone screen [22] and LED arrays [24] together with commercial LEDs installed as the MIMO Tx units in indoor as well as outdoor infrastructures. The Tx units in MIMO can be modulated using the simple on-off keying (OOK) [16] data format or complex modulation schemes such as color intensity modulation (CIM) MIMO [44] and undersampled phase shift on-off keying (UPSOOK) [45] to improve the data throughput. The modulated signals can be captured on the Rx side via the line-of-sight (LOS) [16] or non-line-of-sight (NLOS) based on diffuse reflections [46]. In [16, 22, 46], a range of CMOS technology-based cameras used in the mobile phone (front/rear camera), digital single-lens reflex cameras with higher capture speeds (ranging from 50 to 1000 fps) and surveillance cameras were reported. These CMOS cameras can capture images or record videos in global shutter (GS) and rolling shutter (RS)-based capturing modes at different shutter speed (SS) and resolutions.
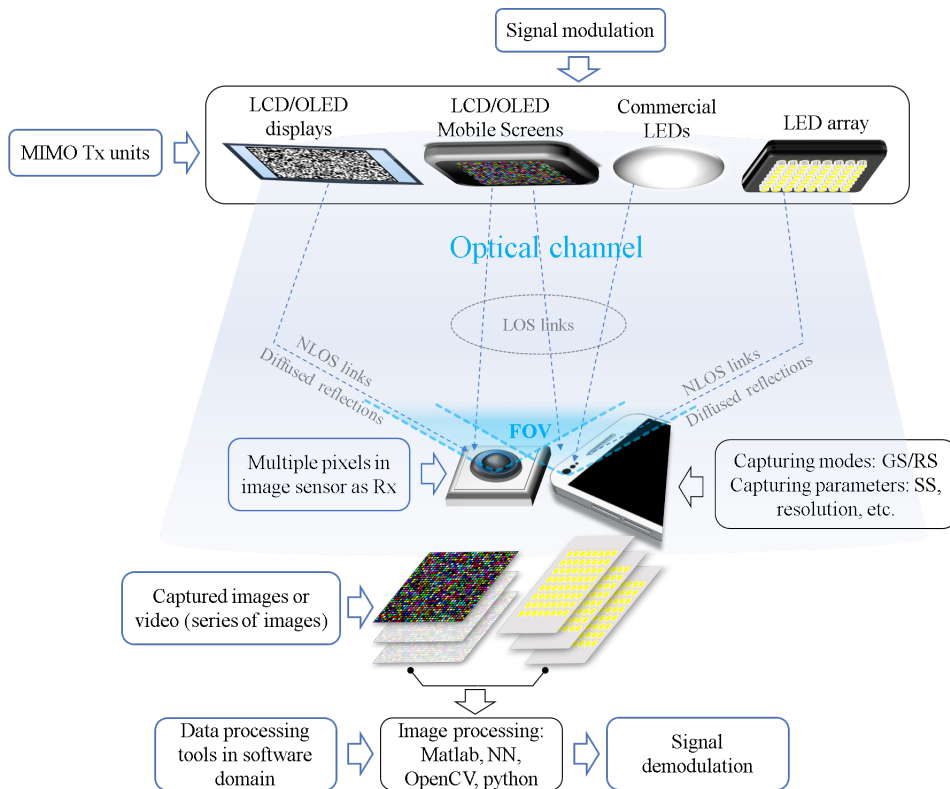

Figure 2.1: Overview of MIMO-OCC

As previously mentioned, the IS captures the intensity modulated Tx in the form of a video recording or image frames at particular fps. Therefore, to perform an OCC reception and data evaluation, image processing tools in the software domain (i.e., MATLAB, OpenCV and Python) [47, 48] should be employed on the Rx side. Image processing is of paramount importance in OCC for demodulation of the received data in the form of captured image frames. Therefore, it is necessary to have robust and reliable image processing algorithms and schemes. In recent years, Neural network (NN) has attracted much attention to solving complex problems related to image recognition using an intelligent machine-learning technique. NN can be adopted for identifying objects' shape in images, transcribe speech into text, match classified items, and select relevant results of a search [49]. Along with image processing, an artificial NN equalizer, when used in VLC, can achieve high R_b by reducing the influence of intersymbol interference [50, 51]. NN in the form of *trained neurons* also plays an important role in motion detection (MD) over the existing indoor OCC links as was demonstrated in one of our works [52].

In this thesis, a camera Rx within MIMO-OCC system is used to connect the dots of indoor and outdoor OWC links. Therefore, in the following, the OCC Tx and Rx characteristics, and GS and RS mechanism are described.

■ **OCC transmitter**

The thesis particularly focuses on the transmission links and the camera Rx capturing techniques rather than OCC Tx modules. Therefore, in this section we provide a brief overview of the OCC Txs. As previously mentioned, a range of commercially available single or multiple LEDs in the form of array and LCD or OLED-based displays and mobile phone screens can be deployed as the OCC Tx [11]. In particular, the LED Txs are primarily used as the source of illumination within most IoT environments. The LED-based Txs are composed of a lamp, a driver, and an enclosure. The commercial lamps have a driver circuit for controlling the current flow that helps to control the brightness. For OCC implementations, this circuit needs modifications for introducing the modulated signal into the LED without compromising the LED's illumination performance [11]. In a traditional OCC system, a random data stream generated in the software domain, e.g., MATLAB, is applied to the modulator, LED driver and then to the LED Tx.

In general, for transmitting the data, the light source's intensity is controlled through the driving current of the LEDs. At first, the data is converted into an optical message, and then the corresponding sequence is used to switch the driver's circuit. The switching frequency depends on the selected modulation scheme. Furthermore, some OCC systems utilize a LED/LCD/OLED-based screen as Tx. In this particular case, the display is controlled through software using one or more drivers depending on the specific necessity of the application and the possibility of image

generation. High-throughput links such as visual MIMO systems for screen-camera communications link were studied and proposed in [53].

Depending on the selected application of the OCC system, a white light Tx can be deployed using additive color method which employs three LEDs: red, green and blue (RGB). The output of those LEDs is combined to obtain the white light. This solution gives control over the light's exact color, incorporates three channels to the communication systems so the signal can be multiplexed, and provide faster modulation ratios. Various modulation formats developed for the OCC data transmission will be described later in the subsection: modulation schemes.

Over the past few years, multiple neopixel boards have been used in electronic devices such as screen displays in home automation, advertising, televisions, human interfaces, etc. [54]. These devices can be used as part of the Tx to provide IoT based MIMO-OCC links in smart environments. Furthermore, a combination of LED-array Txs and OCC with a PD array can be used as massive MIMO to deliver parallel transmission and therefore higher data rates R_b in a range of applications, including the massive IoT which is one of the major goals of this thesis.

■ **OCC receiver**

The camera Rx consists of an imaging lens, an image sensor along with Bayer filter and an internal image processor which is a 2D array of nanoscopic PDs that detects information in the form of an image see (Figure 2.2). A lens is a device that converges or diverges light beams. The light is projected passing through the focal point of the lens on the sensor surface. In imaging, convex lenses are used to create a real image on the image plane of the camera, which is located at the image sensor plane. However, for the purpose of variable magnification and image correction, usually a complex set of convex and concave lenses are used in a lens system. The magnification factor of the lens can be expressed as:

$$k = \frac{f}{f - d_L},$$
(2.1)

where d_L is the distance of the object from the lens and f is the focal length of the lens.

Bayer filter is attached over the sensor in order to make each pixel sensitive to either of the primary colors (RGB). Note, the sensor only captures monochromatic images without a Bayer filter [55]. The internal image processor performs image processing by demosaicing method to form a colored output image which is the data image for OCC post-processing [56].
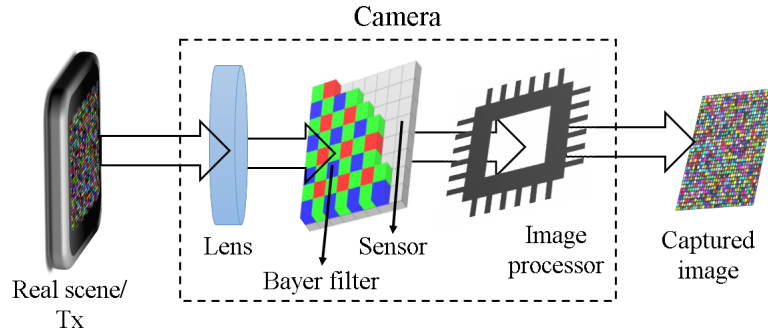
Figure 2.2: Schematic of a digital camera

The maximum achievable R_b in OCC can be obtained as [57]:

$$R_b = \frac{1}{8}WH(\log_2 x_G)f_R, \tag{2.2}$$

where, $W \times H$ is the size of IS in terms of pixels, x_G is the gray scale signal obtained from each pixel and f_R is the camera capture speed in fps. Note, 1/8 is a rate reduction factor for three dimension (3D) formats. For example, considering a 1000 fps QVGA (320×240 pixels) 256 gray scale IS, the maximum achievable R_b is 76.8 Mbps [57]. However, this is impractical R_b as each of pixels in the IS should represent a unique data transmission which is not practical due to long and varying transmission distance (L) between the camera and the Tx.

Moreover, IS resolution (IS_{Res}) with respect to dimensions (either horizontal or vertical) can be calculated as twice the size of FOV over the size of the smallest feature of the camera IS_{Res}. To make accurate measurement of captured image, a minimum of two pixels per smallest feature is considered. Considering numerical calculation, if the FOV covers 200 mm and the smallest feature needed capturing is 2 mm, the required IS_{Res} is 200 pixels. Therefore, a camera with a resolution of 640×480 pixels would be effective because 200 pixels is less than the smallest dimension, which is 480 pixels. For smartphone cameras, the pixel density, usually referred to as pixel per inch (PPI), is given as:

$$PPI = \frac{\sqrt{W^2 + H^2}}{\text{Diagonal screen size}}. \tag{2.3}$$

The higher the PPI, the more details can be found within the image.

The exposure time sets the amount of light that reaches the IS, which determines how light or dark an image will appear. Note, too much light captured will overexpose (too bright/no details) images, thus resulting in the blooming effect, while less light results in underexposed (dark/grainy/less details) images. The blooming effect means that the number of photons reaching the detector exceeds its maximum capacity, and

the excess photons will either spill and merge to adjacent pixels or are not counted, thus leading to non-precise intensities [58]. The camera's exposure is based mainly on three camera settings: aperture, ISO and SS as shown in Figure 2.3 [59].
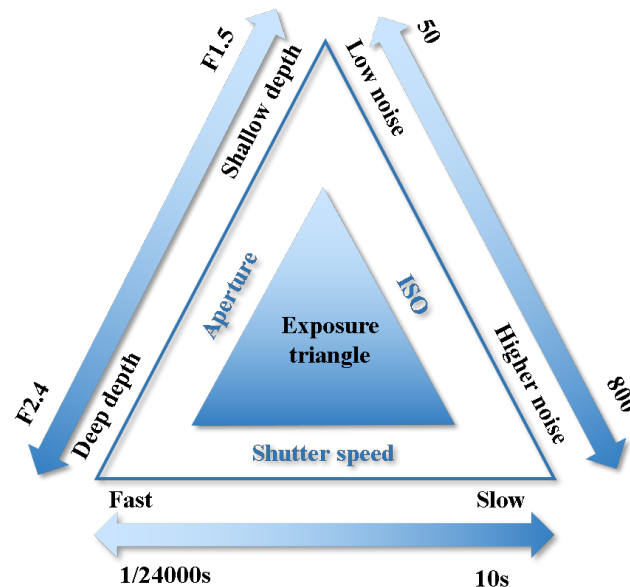
Figure 2.3: Camera exposure triangle.

A camera's SS is typically measured in fractions of a second. Slow SSs allow more light incident and are used for low-light and night photography, while fast SSs help to freeze motion [59].

Aperture, or also called as f_{stop}, controls the amount of light being captured through the lens as well as controls the depth of field, which is the portion of a scene that appears to be sharp. For a very small aperture, the depth of field is large, while for a large aperture, the depth of field is small. In photography, the aperture is expressed by F number (focal ratio) that represents the ratio of the diameter of the lens aperture to the length of the lens [59]. Higher ISO (i.e., the sensitivity of camera) means faster light absorbed by the sensor, but at the cost of increased noise level [59].

■ **Global and rolling-shutter mechanisms**

There are two types of camera sensors, i.e., a charge-coupled device (CCD) and a CMOS sensor. CMOS technology is a mature technology used in a wide range of devices such as solid-state memories, CPUs, and ISs. In the CMOS technology, metal-oxide semiconductor field effect transistors (MOSFET) are used for switching. The applications of CMOS cameras range from professional photographing cameras, low-cost cameras, and surveillance to industrial high-speed machine vision. CCD is not installed within mobile devices (smartphones) due to its larger analog-to-digital converter (ADC) as compared to CMOS. The advantages of using CMOS over CCD

cameras include low power consumption, faster readout, more programmability, and low cost. Therefore, CMOS is widely implemented in smartphones due to its compact ADC design. The major difference between CCD and CMOS sensors is in the capturing modes, i.e., the shutter mode. CCD sensors use GS while most CMOS sensors use RS capturing modes, as illustrated in Figure 2.4(a) and (b). As in [60], CMOS sensors can be used in both RS and GS capturing modes based on the system requirements. Accordingly, CMOS is preferred for communication applications in the literature [61–63].
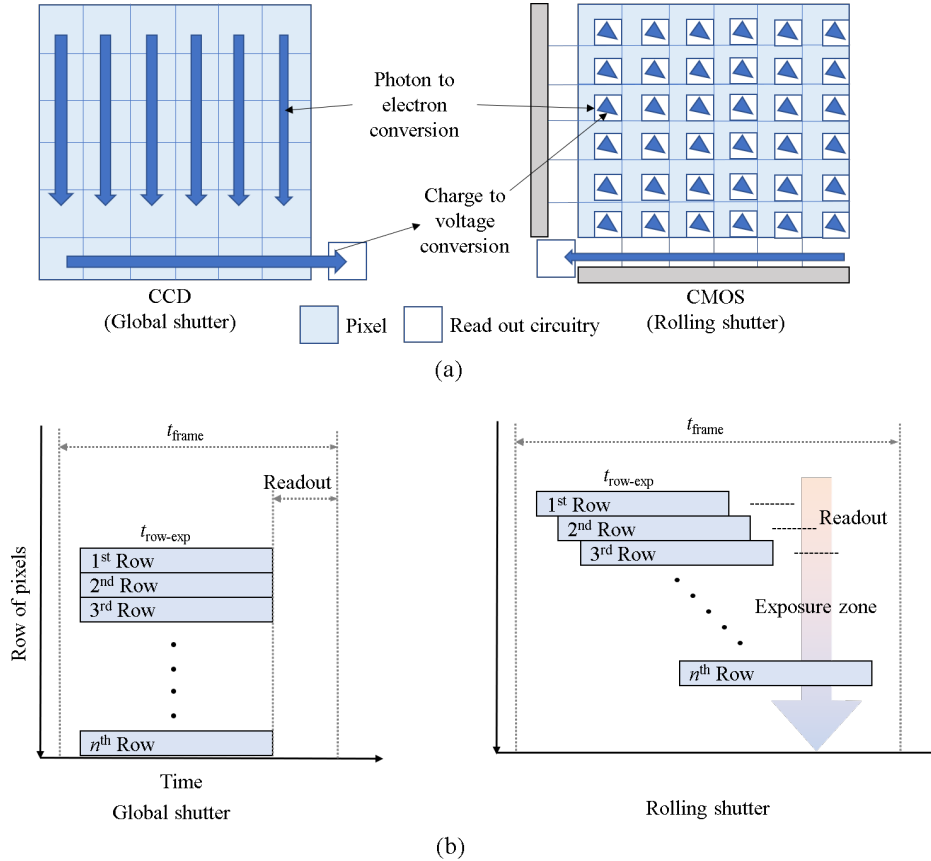

Figure 2.4: (a) CCD and CMOS ISs, and (b) GS and RS mechanisms

A GS camera allows its sensor to be exposed to light once, i.e., it can hold either the ON or OFF state of an LED in a single frame [24], see Figure 2.4(b). The CMOS-RS camera sequentially integrates light on all pixels and then it operates similarly as a scanning function. Unlike a GS camera, in RS capturing mode, the sensor scans row-by-row of pixels (line wise) the entire image which therefore introduces a sequential readout technique. This scan process is tied to the system clock and limited by the sampling rate of the ADC. The pixel sensors within the camera continuously integrate the light that falls on their surface and then each row of pixels is exposed simultaneously at the exposure time $t_{\text{row-exp}}$. In RS cameras, the readout time $t_{\text{read-out}}$ ensures that there is no overlapping of the rows of pixels and allows multiple exposures in a single captured image. The latter enables multiple

LED states to be achieved at the same time in a single frame as each row is exposed once to the light. Therefore, the captured image of the switched LED is composed of a set of black and white stripes.

On the other hand, due to single large ADC, GS in CCD takes longer capturing and processing time for the whole frame, which is reduced in CMOS sensors due to smaller ADC. Due to compact ADC, faster processing, and advancements of electronic fabrication, CMOS sensors are preferably installed and utilized. Therefore, CMOS is employed for high-speed cameras with a capture rate beyond 1000 fps, which cannot be accomplished using the CCD sensor due to its slower ADC.

Using the RS effect of a CMOS IS for VLC can be promising to provide flicker-free OCC links as well as to increase the R_b [64]. This enables multiple LED states (ON/OFF) to be captured at the same time. Therefore, for an LED that flickers ON and OFF according to the modulated binary bit stream, the captured image contains a bunch of black and white stripes. The stripes widths depend on the modulation frequencies, and the number of strips depends on the distance between the camera and LED [64].

Note that, in the RS capturing mode, each row starts with a certain delay, which results in the row shift, $t_{\text{row-shift}}$. The frame time is given as:

$$t_{\text{frame}} \leq N_{\text{row}} \times t_{\text{row-shift}} + t_{\text{row-exp}}, \tag{2.4}$$

where N_{row} is the pixel rows, which is based on the camera resolution. Note, $t_{\text{row-exp}}$ is the exposure time of the last row per frame (very small value).

2.2   Optical camera communication channel specifics

This subsection describes various OCC transmission links and CMOS IS noise characterization.

■ **Transmission links**
  In OCC, the transmitted light signal will arrive at the Rx (i.e., IS) via both the LOS and NLOS paths. However, the LOS becomes the dominant path when using Txs and Rxs with very narrow FOV. The channel specific features and variations of RS-based MIMO-OCC transmission links are outlined below:

• **LOS MIMO-OCC links**
  Traditional indoor VLC or OCC LOS links with high R_b over a range of transmission spans have been adopted in many applications including *(i)* short-range RS-based indoor MIMO-OCC LOS (1-5 m) flicker-free links using multilevel intensity modulation (IM) with R_b of 10 kbps [65]; *(ii)* a beacon jointed packet reconstruction scheme

with R_b of 5.76 kbps [66]; *(iii)*, screen modulation techniques followed by the 2M-ary quadrature-amplitude modulation format [67]; *(iv)* and raptor code with linear time encoding and decoding (R_b of 1 kbps) [68]. Note, in LOS-based systems, it is possible some NLOS may be detected at the Rx, which will result in time delay spread.

- **NLOS MIMO-OCC links**
  In some scenarios, such as D2D communications, it is possible that there might not be a LOS path between the Txs and the Rxs. Therefore, the communications will be via the NLOS paths, which offer mobility and flexibility but at the cost of lower R_b [46, 69]. NLOS-MIMO links based on space and time division multiple access technique with R_b of 1 kbps and flicker-free transmission over a 10 m link span were reported in [46]. A 152 bits NLOS link (1.5 m) with a low level of error correction code using image processing techniques such as background compensation blooming mitigation, extinction-ratio enhancement and Bradley adaptive thresholding for RS demodulation was investigated in [70].

- **Tx and Rx orientations**
  In MIMO-OCC links we need to as well consider both the Tx and Rx orientation angles. Some practical solutions considering different orientations and placements of the Tx and the Rx to support mobility scenarios in an indoor environment needs to be investigated. In [44], the angular rotation θ from 0° to 70° along with parallel movement of a RGB-based LED array (16×16 LEDs) Tx and a 330-fps camera-based Rx operating in the GS capturing mode over a link span of 60 cm was reported. Note, in [44], the refresh rate for the LED array was set to 82 Hz, which is less than the maximum allowed flickering time period standard rate of 200 Hz [71], thus providing flickering transmission and rotation support over a link span of 60 cm [44]. On the other hand, 60-LED-based array was used to provide both data transmission and frame synchronization. In [72], a practical orientation independent RS-based NLOS OCC link performing wide Rx's orientation for indoor applications with R_b of 7 kbps over a transmission link span of 50 cm was presented. However, the Tx should be designed in such a way to ensure that there are sufficient reflections from many directions to ensure link availability.

- **Focused and defocused links**
  In OCC links, the captured Tx's focused image size decreases with the increasing link span as given by the relationship as:

$$d_{\text{img}} = \frac{d_{\text{Tx}} f}{d_L}, \tag{2.5}$$

where d_{Tx} and d_{img} are the diameter of the Tx and the diameter of the projected Tx's image on the IS at the focal length f of the lens in use, respectively. This

therefore constitutes a limitation for RS-based OCC links, as the received signal area on the IS of the camera, which determines the N_{rows} (i.e., the ON and OFF states of the Tx) obtainable, decreases with the increasing transmission distance. Consequently, this limitation can be reduced by operating the camera in its out-of-focus (i.e., defocused) mode. Figure 2.5 shows a lens, IS, and object configuration. The IS could be moved from position 1 to 2, where varying sizes of the projected object's image are obtainable. Importantly, we can use the defocusing feature of the camera, i.e., by altering the distance between the lens and the IS, to allow the Tx's image to converge beyond the focal point, whereby a larger footprint of the Tx is obtained.
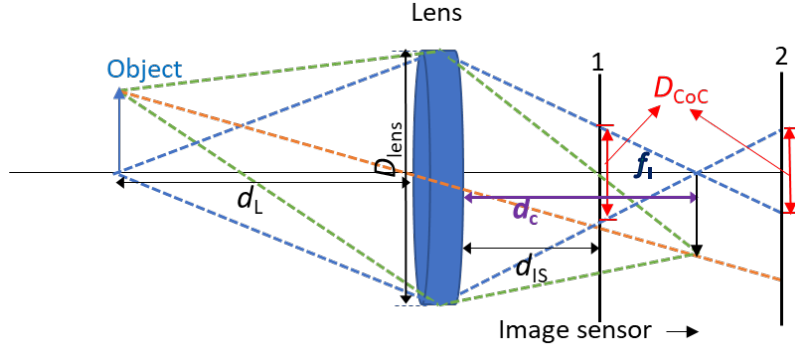

Figure 2.5: Example of lens, IS, and object configuration.

Consequently, more N_{rows} are visible (detectable by the Rx (camera)), as illustrated in Figure 2.6 for the defocused modes. Note that defocusing of the camera results in a disc-shaped pattern known as a circle of confusion (CoC), which is convoluted with the image as given by [73]:

$$G_o(x,y) = G_i(x,y) \otimes \otimes G_{CoC}(x,y), \tag{2.6}$$

where G_o(x, y) and G_i(x, y) are the defocused and focused image intensity functions, respectively, $\otimes \otimes$ is the 2D convolution operator, and G_{CoC}(x, y) is the CoC disc function, which is the same shape as the camera's lens aperture. For a circular aperture, we have [73]

$$G_{CoC}(x,y) = U(\sqrt{x^2 + y^2}) - U(\sqrt{x^2 + y^2} - 0.5 D_{\text{CoC}}), \tag{2.7}$$

where the diameter of CoC, D_{CoC}, is the same as the width of the defocused image of a point source and is given as [73]:

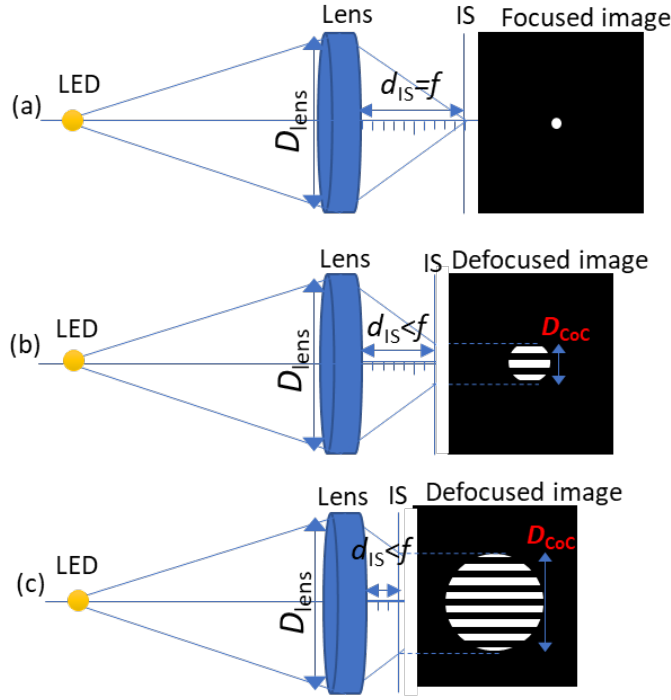$$D_{\text{CoC}} = \frac{D_{\text{lens}}}{2d_c} |d_C - d_{\text{IS}}|, \tag{2.8}$$

Figure 2.6: Examples of width of captured Tx images on IS based on varying lens and IS configurations.

U(.) is the Heaviside step function, $D_{\text{lens}} = f/f_{\text{stop}}$ is the diameter of the lens aperture, f_{stop} is the focal stop number of the lens aperture, d_{IS} is the distance between the center of the lens to the IS, and d_c represents the distance between the center of the lens and the image, which can be obtained as [73]:

$$d_c = \frac{d_L f}{d_L - f}.$$
(2.9)

Note that the size of CoC depends on the aperture diameter D_{lens} for collecting the light rays of d_{IS} and d_c. Consequently, to increase defocusing (i.e., D_{CoC}) in order to have the best signal area, $|d_C - d_{\text{IS}}|$ must be maximized, and lower values of f_{stop} should be used to obtain larger D_{lens}. However, the amount of achievable defocusing is limited to the camera's optics design configuration.

- **Region-of-interest (ROI)-based signaling**

  As part of image processing techniques, a concept of ROI is often employed to extract an interested region or the information from the captured (source) image. The ROI is defined as a portion of an image extracted for some other operations, such as various intelligence, surveillance, and reconnaissance applications, to detect potential targets or ROIs in digital imagery.

  In OCC, the transmission distance L between the LED and the camera needs considering, since as this distance increases, the size of ROI in the picture reduces,

thus reducing the number of received messages per frame. ROI is defined as [48]:

$$\text{ROI} = \min(1, \frac{l_{\text{LED}} \cdot f}{L \cdot l_{\text{IS}}}), \qquad (2.10)$$

where l_{LED} and l_{IS} are the sizes of the LED and IS, respectively. By performing the ROI the coordinates of the captured LED in the image frames obtained are, top-left: (x_1, y_1) and bottom-right: (x_2, y_2).

■ **CMOS IS noise characterization**

 The schematic block diagram of the proposed MIMO-OCC system with multiple Txs $(\text{Tx}_1–\text{Tx}_n)$ and IS Rx is shown in Figure 2.7. At the Tx, the data is generated in the form of OOK non-return to zero (NRZ) (OCC-NRZ) data $s(t)$ and is mapped using an LED driver to the Txs for IM. At the Rx, using an optical lens, the IS captures multiple light Txs as different point sources on different sections of the IS. It is therefore straightforward to spatially separate the multiple captured point sources and apply image processing for data detection. Therefore, for further analysis we consider the projection of one light source Tx on the camera Rx that can as well be applied to multiple captured point sources.
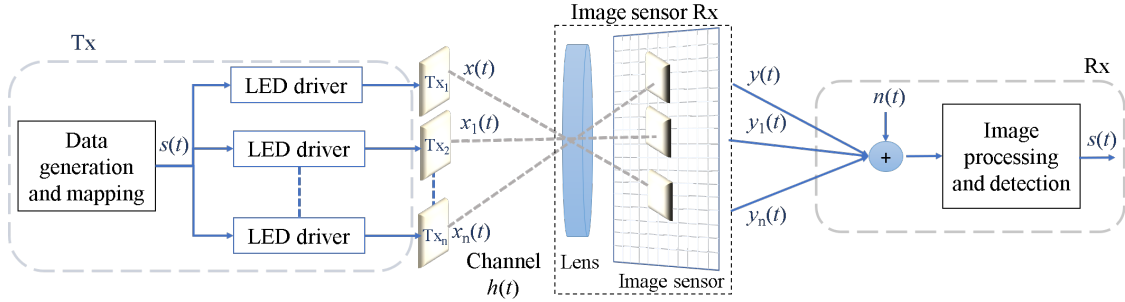

Figure 2.7: Schematic block diagram of MIMO-OCC link

The intensity-modulated light $x(t)$ is transmitted over a free space channel and is captured at the Rx using a CMOS RS camera. For the LOS link, the received signal $y(t)$ is given by [74]:

$$y(t) = \eta G_v x(t) \otimes h(t) + n(t), \qquad (2.11)$$

where $h(t)$ is the combined impulse response of the channel and camera, η is the quantum efficiency of the IS, $\otimes$ is the time domain convolution, and $n(t)$ is the additive white Gaussian noise including the ambient light induced shot noise and the noise in the camera (i.e., fixed pattern, thermal, photo-current shot (optical excess and electronics) and flicker noise sources) [75] and G_v presents the software defined global gain of the IS and the column amplifier block. Apart from exposure settings, G_v plays an important role to enhance the signal amplification while

passing through the camera ADC prior to being focused on the IS [76]. This is due to the fact that G_v presents the software-defined global gain of both the IS and the column amplifier block, which is given as:

$$G_v(\text{dB}) = 20\log_{10}(\frac{V_{\text{ADC}}}{V_{\text{pixels}}}), \tag{2.12}$$

where V_{ADC} is the voltage value, which is sampled by the ADC, and V_{pixels} is the voltage obtained from the pixel integration of light during the exposure time. Therefore, higher G_v mitigates the influence of ambient light on the integrity of data reception; and reducing t_{exp}.

The channel impulse response for the LOS link can be represented in matrix form as [77]:

$$h(t) = h_{(ch,u,v)(U \times V)}, \tag{2.13}$$

where U and V are the number of rows and columns of the image sensor and $h_{(ch,u,v)}$ is the channel impulse response of the (u,v)-th pixel. Using a single LED and a Gaussian mixture model, $h_{(ch,u,v)}$ is estimated as [77]:

$$h_{(ch,u,v)} = A \sum_{k=1}^{v} \frac{k^2 c_k}{2\pi\sigma_{x,k}\sigma_{y,k}k_o^2} \times \int_{a_x-\frac{a}{2}}^{a_x+\frac{a}{2}} \int_{a_y-\frac{a}{2}}^{a_y+\frac{a}{2}} \exp(-\frac{x^2}{2\sigma_{x,k}^2} - \frac{y^2}{2\sigma_{y,k}^2})dydx, \tag{2.14}$$

where $A = \frac{1}{a^2}$, a is the pixel length, k_0 and k are the magnification factor of the camera at a reference link span L_0 and at a distance of L, respectively, $\sigma_{(x,k)}^2 = (\frac{k}{k_o})^2\sigma_i'^2 + \sigma_{(b,x)}^2$, and $\sigma_{(y,k)}^2 = (\frac{k}{k_o})^2\sigma_i'^2 + \sigma_{(b,y)}^2$ with σ_i' denoting the parameter of the model and $\sigma_{b,x}$ and $\sigma_{b,y}$ is the standard deviations in the x and y directions on the image plane, respectively. In Equation 2.14, $a_x = (u-i)(a+g) - \xi_x$ and $a_y = (v-j)(a+g) - \xi_y$, where (ξ_x, ξ_y) and (i,j) are the coordinates of the centre of the image and the nearest pixel to this centre, respectively and g is the gap between two pixels.

The received power $P_{\text{Rx}}(t)$ at a camera coming from a Lambertian light source of order m and transmitted power $P_{\text{Tx}}(t)$ can be expressed as [11]:

$$P_{\text{Rx}}(t) = P_{\text{Tx}}(t) \cdot \frac{m+1}{2\pi} \cdot \cos^m\theta_e \frac{A_{\text{lens}}\cos\Psi}{L^2}, \tag{2.15}$$

where θ_e and Ψ are the emission and incident angles, respectively, and A_{lens} is the area of the camera's external lens. Based on the RS mechanism shown in Figure 2.4(b), we can express the energy E_n captured by the nth row as:

$$E_n = \int_{i \cdot t_{\text{rs}}}^{i \cdot t_{\text{rs}} + t_{\text{exp}}} \frac{P_{\text{Rx}}(t)}{\sum_j^u \sum_k^v M_{j,k}} dt, \tag{2.16}$$

19

where $M_{[v \times u]}$ is the mask of pixels where the source shape is projected. From the integral limits, it can be derived that the bandwidth of the Rx system decreases with the augment of the $t_{\exp}$. In other words, the longer is $t_{\exp}$, the more lines are simultaneously exposed, and the received signal is integrated in longer and less diverse time windows. For this reason, frames in OCC have to be acquired within short periods.

The SNR is defined as [78]:

$$\text{SNR(dB)} = 10 log_{10}(\frac{P_{\text{Rx}}(t)}{P_{\text{noise}}}). \tag{2.17}$$

If we consider noise corrupted signal as Equation 2.11 then the SNR is computed as:

$$\text{SNR(dB)} = 10 log_{10}(\frac{P_{\text{Rx}}(t)}{|y(t) - x(t)|^2}), \tag{2.18}$$

where $|y(t) - x(t)|^2$ is the squared error between original and corrupted signals. In the context of a signal estimation algorithm, the signal refers to the estimated signal and the noise to the difference (error) between the estimated and the original signal.

Note, if the definition of power is scaled by the number of points in the signal, this gives the mean squared error (MSE). This notion can be extended within OCC for actual transmitted and received images by summing twice of rows and columns of image vector or stretching the entire image into a single vector of pixels and applying the 1D definition. Therefore, SNR when concerned with signal images in OCC can be given as:

$$\text{SNR(dB)} = 10 log_{10} \frac{\sum\limits_{m=1}^{U} \sum\limits_{n=1}^{V} I_{\text{Tx}}(m,n)^2}{\sum\limits_{m=1}^{U} \sum\limits_{n=1}^{V} [I_{\text{Tx}}(m,n) - I_{\text{Rx}}(m,n)]^2}, \tag{2.19}$$

where $I_{\text{Tx}}(m,n)$ and $I_{\text{Rx}}(m,n)$ denote the intensity of the pixel of the transmitted and received image frames, respectively, at location (m, n). High values of SNR show that the error of the estimation is small and, therefore, among various image fusion methods the ones that exhibit higher SNR's can be considered of better performance.

The peak-signal-to-noise ratio (PSNR) and the MSE are measures similar to the SNR and can be defined as [78]:

$$\text{PSNR(dB)} = 10 log_{10} \frac{I^2_{\text{peak}}}{\text{MSE}}, \tag{2.20}$$

$$\text{MSE} = \frac{\sum\limits_{m=1}^{U} \sum\limits_{n=1}^{V} [I_{\text{Tx}}(m,n) - I_{\text{Rx}}(m,n)]^2}{N_{\text{column}} \times N_{\text{row}}}, \tag{2.21}$$

where I_{peak}^2 denotes the squared peak intensity of the measured frame and N_{column} and N_{row} are the number of columns and rows of the images, respectively. It can be seen that PSNR $\geq$ SNR and can be equal only when the original clean signal is constant and with maximum amplitude. In the case of PSNR, the major focus is on I_{peak} of the measured frame in order to measure the bandwidth of the signal or number of bits needed to represent it. Therefore, the major concern is how well high-intensity regions of the image come through the noise. This is much more content-specific than pure SNR and can find many reasonable applications such as image compression.

2.3 Modulation schemes

As OCC captures data in the form of images, the modulated bits can be carried by either color, intensity and spatial coordinate. Unlike PD-based VLC that captures only light intensity, OCC captures multiple colors simultaneously due to the employment of Bayer filters along with the spatial separation of multiple Txs due to its 2D coordinates in the image. Furthermore, an image also contains another interesting feature that is a shape which can be interpreted differently. Therefore, based on the carrier for the modulated bits, the OCC data can be modulated through the entities of color, intensity, spatial coordinate, and shape [79].

The study in [16] has described the OCC modulation schemes into five different categories such as Nyquist sampling modulation (NSM), high-f_R NSM, RS-based OCC, ROI signaling, and hybrid camera-PD modulation. These categories mainly depend on the tight relation between the parameters of Txs and the limitations on the camera Rx (limited fps). Table 2.1 gives an overview of recent advancements in OCC modulation schemes.

The f_R of the camera is generally limited to 30 or 60 fps; therefore, the flickering rate of the Tx is also limited to <60 Hz according to Nyquist sampling theorem [16]. Table 2.1 shows the recent modulation schemes such as OOK, DC-biased optical orthogonal frequency division multiplexing (DCO-OFDM), CIM and cell modulation used in NSM-based OCC schemes. These schemes use a GS Rx and have flickering transmission links due to lower fps and hence the modulation frequency. However, R_b and L in these schemes are increased using multiple LEDs in an array format as the Tx [44, 80].

Using a high-speed camera Rx, NSM can be further implemented for high-f_R based OCC schemes. Using high-f_R NSM, the modulation frequency can be > 200 Hz (maximum flickering time period standard for flickering requirements) [71]. Space shift keying (SSK) and hierarchical rate adaptation techniques using Rx with up to 1000 fps was proposed in [81, 82] for long range communications, see Table 2.1. However, high-speed cameras are expensive and not commonly used in smart devices. Therefore, in order to implement

flicker-free communication links, OCC takes advantage of the high sampling rate of the RS mechanism, which sequentially exposes lines of pixels to the incoming light [16].

Table 2.1: Overview of recent advancements in OCC modulation schemes

	Modulation schemes	**Camera capturing modes**	**Flicker-free illumination**	R_b **(kbps)**	L**(m)**
NSM	OOK [24, 83]	GS	No	0.2-1.2	0.3-2
	DCO-OFDM for vehicle-to-everything (V2X) [80]	GS	Yes	55×10^3	60
	CIM [44, 84]	GS	No	11.5-317.3	0.2-1.4
	Cell modulation [22, 85]	GS	No	0.4-112	0.1-1.2
High-f_R **NSM**	SSK [81]	GS	Yes	1	30
	Hierarchical rate adaptation [82]	GS	Yes	42.7	65
RS-based OCC	OOK for NLOS – MIMO space and time division multiple access [46]	RS	Yes	1	10
	Rolling OOK [86, 87]	RS	Yes	0.8-2.8	0.1-0.2
	Multilevel IM [65]	RS	Yes	>10	2
	Rolling UPSOOK [88]	RS	Yes	0.15	60
	Combination of UPSOOK-wavelength division multiplexing (WDM) and MIMO scheme [45]	RS	Yes	0.15	60
ROI signaling	Spatial 2-PSK (S2-PSK) [89]	GS	No	0.01	1.5
	Hybrid-spatial-phase shift keying (HS-PSK) and variable pulse-position modulation (VPPM) [90]	GS	Yes	0.03	100
	Selective capturing [91]	GS	No	6.9	1.75
Camera-PD	Manchester coded OCI [92]	GS	Yes	10×10^3	7.7
	Optical-orthogonal frequency division multiplexing (OFDM) OCI [93]	GS	Yes	55×10^3	1.5
Hybrid VLC/OCC	Hybrid multilevel OOK - intensity shift keying (ISK) [94]	RS	Yes	4.2 (OCC), 2.75×10^3 (VLC)	3
	Hybrid Manchester coding and VPPM [95]	RS	Yes	1.67 (OCC), 100 (VLC)	5.8

Table 2.1 includes the modulation schemes for RS-based OCC, i.e., the RS-based demodulation. The scheme focuses on the demodulation part that utilizes the aforementioned RS properties of CMOS sensors. Note, RS-based OCC offers flicker-free links in both LOS [86, 87] and NLOS [46] transmission scenarios. Moreover, MIMO schemes using a combination of UPSOOK and WDM, and multilevel IM have been investigated for long range and high-speed, respectively within the RS-based OCC system [45, 65].

In order to reduce the overall processing time on the Rx side, a smaller portion of the image containing only the Tx, called as ROI needs to be determined. Since the processing is carried out for a much smaller portion of the image, the processing time is considerably shortened and the efficiency of the image processing can be increased. This technique is useful to detect the exact Tx image captured in the outdoor scenarios that contains many other noise sources. A S2-PSK was developed considering the spatial separation capacity of the camera to fully decode a bit within a randomly sampled image [89]. For the high-rate data stream, single-carrier modulation or multiple-carrier modulation, such as HS-PSK or VPPM, can serve as viable solutions [90]. An alternate form of the ROI sampling modulation, termed as selective capture, was also proposed for pre-processing to shorten the frame capture period in a study and to produce the overall higher efficiency [91].

To propose a hybrid camera-PD modulation, a IS that consists of both pixels for image capture and PD cells specifically for communication was developed in [92, 93]. This study could provide a huge bandwidth of up to 10 MHz due to the use of PD cells. On the other hand, a VLC and OCC links using PD and a camera Rx, respectively to receive light signals from the same Tx simultaneously were proposed as hybrid VLC-OCC [94, 95]. Hybrid modulation formats such as multilevel OOK ISK and Manchester coding over VPPM were used to simultaneously transmit OCC and VLC signals. These schemes provide low rate OCC transmission ranging from 1-4 kbps and high rate VLC transmission from 100 kbps to 2.75 Mbps over a range of transmission spans (see Table 2.1).

CHAPTER 3 | Objectives of the Thesis

Due to the large scale and increasing availability of in-built cameras in smart devices and mobile phones as well as the pre-existing camera-based infrastructures such as traffic lights, security and surveillance, and vehicles, camera Rx-based VLC or OCC can provide several attractive applications for further communication and sensor networks. However, in OCC, the data rate is limited by the frame rate of the ISs. OCC can be further extended to offer massive MIMO capabilities in order to increase the data rate using LED and PD arrays in the form of multiple pixels in ISs for IoT applications in both indoor and outdoor environments. On the other hand, as listed in the survey in [96], for indoor OCC based IoT applications, low data rates ranging from few bps to kbps for transmitting short messages in D2D communications over shorter transmission spans can be more than sufficient. The major challenge in implementing such systems is the requirement for flicker-free transmission at lower data rates (i.e., most cases in IoT applications) for short and long range indoor and outdoor OCC systems for IoT applications, respectively. Therefore, the dissertation thesis has the following main goals:

- **G1:** To propose, develop and experimentally verify the new technologies based on MIMO and radiating fiber Tx's for OCC based IoT links

- **G2:** To propose the methodology of design and analysis of OCC based applications for indoor and outdoor IoT environments

- **G3:** To develop and validate a hybrid optical IoT-based VLC-OCC system to support user based high- and low-speed communications.

In order to attain G1, the following specific milestones have been set:

- To propose, design and characterize a simplified multi-channel Tx design

- To experimentally verify the performance of proposed Tx design within RS-based MIMO-OCC links with focus on the spatial frequency based angular orientation

- To propose and validate a novel technology of utilizing existing fiber optic lighting based infrastructures for OCC-based IoT links.

In order to attain G2, the following specific milestones have been set:

- To propose an enhanced functionality of NN assisted motion detection to address optical shadowing and control of smart devices within indoor OCC based IoT

- To enhance transmission link spans for outdoor OCC links by reducing spatial bandwidth of the camera in the out-of-focus and in-focus regions and to experimentally derive the link feasibility under turbulence and fog conditions.

In order to attain G3, the following specific milestones have been set:

- To develop an experimental test-bed for measurement and evaluation of the hybrid high-rate PD-VLC and low-rate indoor OCC-based IoT scheme.

4 | Achieved Results

CHAPTER

The core of the thesis is based on published research articles, including eight published in peer-reviewed journals with impact factor [J1-J8]. The full and original papers with bibliographic citations and individual paper contributions to the thesis are provided in the following sections.

Section 4.1 proposes an RS acquisition-based camera capturing in MIMO-OCC employing a small multi-channel designed LED array based Tx module. Experimental investigation of the indoor OCC system by employing a Raspberry Pi camera as the Rx with RS capturing mode for a range of camera shutter speed from 200 to 800 μs is carried out. Despite the small area of the display, flicker-free transmission is established using multiple channels within a single Tx unit with perfect inter-LED synchronization and a RS-based camera for use in short-range and low R_b IoT applications (display-based communication links or display-to-camera communications).

Section 4.2 provides the experimental analysis of various angular orientations of multiple Tx units using the Tx design proposed in Section 4.1. The transmission setups are defined considering the indoor dynamic, mobility, and multicasting scenarios in places such as shopping malls, hospitals, and offices, where the number of Txs can be placed at different locations with different angles depending on the interior design and the illumination requirements. The proposed scheme offers a valid solution irrespective of the availability of LOS and NLOS paths. A CMOS image sensor noise characterization is carried out in terms of the SNR and PSNR. The image and the respective communication link quality metrics are measured in terms of the PSNR and the rate of successfully received bits with respect to spatial frequency for different camera shutter speeds.

Section 4.3 presents a novel wireless communications link using an illuminating optical fiber as a Tx in OCC for IoT. This unique solution was motivated by a new and emerging fiber-optic lighting technology as an alternative to discrete illumination fixtures and semi-discrete LED stripes. A proof-of-concept system using an illuminating plastic optical fiber coupled with a light-emitting diode and a commercial camera as the Tx and the Rx, respectively is illustrated. I experimentally demonstrated flicker-free wireless transmission within the off-axis camera rotation angle range of 0-45° and the modulation frequencies of 300 and 500 Hz. This transmission setup resembles the IoT-based indoor dynamic, mobility, and multicasting scenarios for transmission of lower R_b.

Section 4.4 proposes the NN assisted MD system to track and detect the user motion over the mobile phone camera Rx-based OCC link that can be used to perform a relatively basic control of present or future smart devices in IoT environments such as OCC based smart homes where the device control via MD can aptly be facilitated. The proposed study is based on the performance evaluation of various NN training algorithms, which provides efficient and reliable MD functionality along with vision, illumination, data communications, and sensing in indoor OCC based IoT. Moreover, it is seen that the proposed NN assisted MD in the OCC system provides better results in terms of higher MD accuracy, less processing time and long transmission spans as compared to already existing MD schemes.

Section 4.5 focuses on the OCC system for IoT-based on OLED for long-range indoor and outdoor IoT-based applications. The recent inclusion of OLEDs in smart devices such as TV's (large displays in shopping malls and streets) and smartphones with the in-built cameras provides the opportunity to establish OCC systems based on OLED emitters for IoT. OLED Tx based VLC links with high R_b of up to a few Mbps at short link spans up to 1 m are already proposed in [97–99]. However, OLED based VLC links can be extended to offer longer link spans using camera based Rx in both indoor as well as outdoor environments. Therefore, the proposed OLED based OCC is implemented to allow longer link spans of up to 120 m for systems that require relatively low data transmission rates (up to 1 kbps) for both indoor and outdoor cases. To provide blooming mitigation, the system is tested for different exposure times.

The successful implementation of a 120 m long transmission link in Section 4.5 motivates to implement long-distance OCC (beyond 120 m) using RS based capturing. Section 4.6 presents a novel technique, to the best of our knowledge, to increase the link span of an RS-based OCC system by reducing the spatial bandwidth of the camera in the out-of-focus regions. Regardless of the Tx size and surface area, this technique helps to have a larger footprint of the light source on the IS without reducing the FOV. Using the proposed scheme, a 400 m LOS RS-based OCC link is demonstrated, which is to date the longest outdoor communication link reported in these systems. We developed a detection method to extract the information out of the video frames.

Following my previous research based on long-range RS-based OCC links for outdoor IoT, Section 4.7 focuses on the effect of turbulence and fog conditions on OCC links. In this work, we study the experimental OCC system under environmental phenomena emulated in a laboratory chamber. The experiment results demonstrate that heat-induced turbulence does not affect our system significantly, however, the attenuation caused by fog does decrease the signal quality. For this reason, a novel strategy of using the camera's built-in amplifier to overcome the optical power loss and to reduce the quantization noise induced by the ADC of the camera is proposed.

Section 4.8 presents the integration of both VLC-PD and OCC (IS-based VLC) links

simultaneously to provide a versatile optical IoT environment, where users can have a choice based on the Rx device and application to switch between high- and low-speed VLC with PDs- and ISs-based Rx. A single-input multiple-output (SIMO) hybrid VLC system utilizing a single LED-based Tx, and PD- and IS-based Rxs for simultaneous transmission of high- and low-speed data, respectively is experimentally demonstrated. It is envisaged that, the proposed scheme can provide versatile indoor services that allow users to receive data regardless of the devices used. For this reason, I proposed a novel hybrid modulation format that can be used for both high- and low-speed VLC links and have then developed an experimental test-bed for verification.

4.1 Optical camera communications for IoT - rolling-shutter based MIMO scheme with grouped LED array transmitter

This chapter is a version of the published manuscript:

S. R. Teli, V. Matus, S. Zvanovec, R. Perez-Jimenez, S. Vitek, Z. Ghassemlooy, "Optical camera communications for IoT - rolling-shutter based MIMO scheme with grouped LED array transmitter," *Sensors*, vol. 20, pp. 3361, 2020.

Connection to my Ph.D. thesis:

Short-range and low R_b IoT links in indoor environments such as D2D communications with short messages, indoor positioning, navigation, small identification information and communications through advertisements need to be considered. However, the major challenge in implementing such systems is the requirement for flicker-free transmission at lower R_b (i.e., most cases in IoT applications). Therefore, in this paper we propose a low R_b RS-based multi-channel MIMO-OCC scheme for indoor IoT environments, which is flicker-free. For this reason, we present a simplified design of MIMO-OCC grouped LED array-based Tx, using an 8×8 RGB LED array as the Tx and a commercial, low-cost Raspberry Pi camera (RaspiCam) as the Rx. Despite the small area of the display, flicker-free communication links with reception success of 100 % for 200 and 400 μs shutter speed values within the range of 20-100 cm are established. A method to extend link spans up to 1.8 m and the data throughput to 13.44 kbps using different configurations of the multi-channel Tx is provided.

Article

Optical Camera Communications for IoT–Rolling-Shutter Based MIMO Scheme with Grouped LED Array Transmitter

Shivani Rajendra Teli [1,*] , **Vicente Matus [2]** , **Stanislav Zvanovec [1]** , **Rafael Perez-Jimenez [2]** , **Stanislav Vitek [1]** and **Zabih Ghassemlooy [3]**

[1] Faculty of Electrical Engineering, Czech Technical University in Prague, Technicka, 16627 Prague, Czech Republic; xzvanove@fel.cvut.cz (S.Z.); viteks@fel.cvut.cz (S.V.)

[2] Institute for Technological Development and Innovation in Communications, Universidad de Las Palmas de Gran Canaria, 35001 Las Palmas, Spain; vicente.matus@ulpgc.es (V.M.); rperez@idetic.eu (R.P.-J.)

[3] Optical Communications Research Group, Northumbria University, Newcastle-upon-Tyne NE1 7RU, UK; z.ghassemlooy@northumbria.ac.uk

* Correspondence: telishiv@fel.cvut.cz

Abstract: In optical camera communications (OCC), the provision of both flicker-free illumination and high data rates are challenging issues, which can be addressed by utilizing the rolling-shutter (RS) property of the image sensors as the receiver (Rx). In this paper, we propose an RS-based multiple-input multiple-output OCC scheme for the Internet of things (IoT) application. A simplified design of multi-channel transmitter (Tx) using a 7.2×7.2 cm^2 small 8×8 distributed light emitting diode (LED) array, based on grouping of LEDs, is proposed for flicker-free transmission. We carry out an experimental investigation of the indoor OCC system by employing a Raspberry Pi camera as the Rx, with RS capturing mode. Despite the small area of the display, flicker-free communication links within the range of 20–100 cm are established with data throughput of 960 to 120 bps sufficient for IoT. A method to extend link spans up to 1.8 m and the data throughput to 13.44 kbps using different configurations of multi-channel Tx is provided. The peak signal-to-noise ratio of ~14 and 16 dB and the rate of successfully received bits of 99.4 and 81% are measured for the shutter speeds of 200 and 800 μs for a link span of 1 m, respectively.

Keywords: optical camera communications; rolling-shutter camera; Internet of things; multiple-input multiple-output; light-emitting diodes

1. Introduction

The fifth-generation (5G) telecommunication standards have set the new platform for mobile wireless networks, rather than just extending the transmission capacity and reliability of the 4G network [1]. With the three main focuses on capacity enhancement, massive connectivity, and ultra-high reliability (i.e., low latency), 5G development stems largely from the increasing number of users and smart devices within the context of Internet of things (IoT)-based smart environments being connected to the cellular networks [2]. In future smart environments, such as homes, offices, cities, etc., there will be a growing need for the communications networks that can facilitate connectivities between a large number of devices or sensors and the end-users [3]. This will mean access to substantial transmission resources (i.e., bandwidth), and thus a paradigm shift in the way the wireless transmission resources are utilized effectively.

To address this paradigm, a number of technologies have been proposed, including millimeter-wave [4], massive multiple-input multiple-output (MIMO) [5], small cell [6],

and optical wireless communications (OWC) [7,8], in order to meet the requirements of 5G-IoT. The popularity of the latter is due mainly to its inherent advantages of safety, security, low cost, and large transmission bandwidth, which are essential in IoT applications, particularly in indoor environments [8]. In indoor environments, the OWC technologies of visible light communications (VLC) and optical camera communications (OCC) have been widely considered and investigated [8,9]. While VLC can support major features of 5G in terms of the data rates, OCC can offer a promising solution. The VLC technology, which uses light-emitting diode (LED)-based lights as the transmitter (Tx), has a lower initial deployment cost. The cameras in smartphones (six billion front and rear cameras), and pre-existing camera-based infrastructures, such as traffic lights, security, surveillance, and vehicles can be adopted as the OCC receiver (Rx) effectively [10]. Reflecting on the OCC potential and its availability, the IEEE 802.15.7r1 task group has been established to develop a standard for OCC within OWCs [9]. Various OCC issues and considerations, such as image sensor architecture, synchronization, data rate, perspective distortion, flickering and dimming, MIMO, and diversity are studied in [11]. The use of high-rate Tx's, such as LEDs, and low-rate Tx's, such as liquid crystal displays and digital signage, in OCC schemes is also provided in [11]. Although OCC does not support high capacity link connectivities, due to the speed limit of cameras, it can be employed in numerous low data rate applications, such as indoor positioning, mobile robot navigation, vehicular communications, small identification information, and advertisements [8–11]. Despite lower data rates, OCC is simple to implement, with low path loss, additional imaging functionality, and spatial modulation capability, as compared with high rate VLC links [12].

However, in OCC, the data rate is limited by the frame-rate of the image sensors (ISs). The data rate can be increased by using higher frame rate cameras, which are very costly, and increasing the camera capture speed, which is defined as the physical parameter of the sensor (electronics) and the graphics processor speed in the hardware domain. Therefore, OCC is further extended to offer massive MIMO capabilities in order to increase the data rate, using LED and photodetector (PD) arrays in the form of multiple pixels in ISs for IoT applications, in both indoor and outdoor environments [13]. In addition, hybrid modulations schemes based on the intensity, color, spatial, phase, and frequency are also suggested in [12] as a solution to improve the transmission data rates in OCC.

The IEEE 802.15.7-2018 standard [14] defines new clauses for the physical layer (PHY) types V and VI for OCC links. These PHY layers are mainly intended for use in systems with diffused light sources and video displays with kbps data rates, as well as using complex modulation schemes of spatial two-phase shift keying (S2-PSK), dimmable spatial eight-PSK, undersampled frequency shift on-off keying (UPSOOK), variable transparent amplitude-shape-color, etc. However, the standard clauses on the PHYs V and VI are mainly on the demodulation schemes, and their real applications are still being revised.

In [13], a data rate of 126.72 kbps was achieved, using 192 data-carrying LEDs modulated using color intensity modulation (CIM) and a 330 frames per second (fps) global-shutter (GS) camera-based Rx, which is expensive and not commonly used, over a link span of 1.4 m. However, the Tx was set to the refresh rate (i.e., transmission frequency) of 82.5 Hz, which is still lower than the maximum allowed flickering time period of 5 ms (200 Hz) [14]. A red, green, and blue (RGB) LED-based rolling-shutter (RS) OCC (RS-OCC) utilizing a combination of UPSOOK, wavelength-division multiplexing, and MIMO offering improved space efficiency of 3 bits/Hz/LED was reported in [15]. In [16], a multilevel intensity modulation (IM) RS-based camera detection link with a data throughput of 10 kbps over a transmission range of 2 m was reported in [15,16]. Whereas, a beacon jointed packet reconstruction scheme for mobile-phone-based VLC with commercial white phosphor LEDs and a 60 fps RS camera achieved the net data rate of 10.3 kbps (172 bits/frame observed over a large LED surface) over a transmission distance of 20 cm [17]. In [18], COTS LEDs with raptor code (with linear time encoding and decoding, thus reduced computational complexity and decoding overhead) have been investigated in RS-OCC. Non-line-of-sight MIMO links using Luxeon LEDs based on diffused reflections and space and time division multiple access, as well as the equal gain combining technique, was reported in [19],

which achieved flicker-free transmission up to a 10 m link span. However, as listed in the survey in [20], for indoor OCC based IoT applications, low data rates ranging from 15 to 896 bps for transmitting short messages in device-to-device communications over transmission spans of 25 cm to 1 m is more than sufficient.

Over the past few years, multiple neopixel boards have been used in electronic devices such as screen displays in home automation, advertising, televisions, human interfaces, etc. [21]. These devices can be used as part of the Tx to provide IoT based MIMO-OCC links in smart environments. High-throughput links such as visual MIMO systems for screen-camera communications link were proposed in [22], where the impact of non-linear channel equalization, non-binary channel coding, probabilistic shaping, and non-linear precoding for high-order modulation schemes and respective applications such as inter/intra vehicle communications, near field communication, and augmented reality were investigated. In [22], it was shown that the reliability and throughput of the optical communication links can be improved using various channel coding techniques based on nonbinary low-density parity-check codes [23], polar and turbo codes [24], and advanced modulation schemes, such as chaos and LoRa [25]. As previously mentioned, short-range and low data rates IoT links in indoor environments such as device-to-device communications with short messages, indoor positioning, navigation, small identification information, and communications through advertisements need to be considered [26]. However, the major challenge in implementing such systems is the requirement for flicker-free transmission at lower data rates (i.e., most cases in IoT applications). Therefore, in this paper, we propose a low data rate RS-based MIMO-OCC scheme with grouped LED Tx for indoor IoT environments, which is flicker-free. For this reason, we present a simplified design of MIMO-OCC grouped LED array-based Tx, which uses 64-neopixel LEDs distributed in an 8×8 array and a commercial, low-cost Raspberry Pi camera (RaspiCam) as the Rx. The Tx unit is divided into eight different groups, with eight LEDs per group in order to increase the data rate and achieve flicker-free transmission. At the Rx, RaspiCam, with a resolution of 1920×1080 pixels and a capture speed of 30 fps, captures the LED array in RS-mode at different shutter speeds (SS) and transmission links L. The novelty of this work is on the design of a simplified Tx for multiple channels transmission-based LED grouping with perfect synchronization, and the use of an RS camera for flicker-free transmission in short-range and low data rates IoT applications. The paper gives a detailed analysis on the quality matrix of the captured image in terms of the peak signal-to-noise ratio, and the success rate of received bit sequences with respect to the transmission span and the camera's SS.

The remainder of the paper is organized as follows: Section 2 describes the proposed RS-based MIMO-OCC scheme using the grouped LED array, while Section 3 shows the experiment setup, followed by the discussion of results. Conclusions are drawn in Section 4.

2. Proposed RS-Based MIMO-OCC Scheme with Grouped LED Tx

2.1. MIMO-OCC Tx Characterization

A new, simple design of MIMO Tx unit is proposed in this paper, as illustrated in Figure 1. It is composed of a 64-neopixel array with an 8×8 small chip-LED, and a 1 cm-thick LED grouping grid, (see Figure 1a,b), which is attached over the Tx LED array. This LED grid is designed to divide a 64-neopixel chip-LED into eight different column-wise groups that are individual transmission channels with eight chip-LEDs per group to allow eight different data transmissions, using a single neopixel LED array. In addition, the LED grid (Figure 1c) is very effective in combating interference due to adjacent LEDs within the groups. The effect of interference with supporting analysis without using the grouping grid to capture the LED array with a GS-based camera Rx was initially reported by the authors in [27]. A 2 mm-thick opaline methacrylate LED diffuser, commonly used, is placed over the Tx [28]. The size of the LED array is 7.2×7.2 cm^2. Since the size of each chip-LED (i.e., 5×5 mm^2) is much smaller than the distance between the adjacent chip-LED (i.e., 9 mm), light from each LED is captured as a discrete image using an IS.
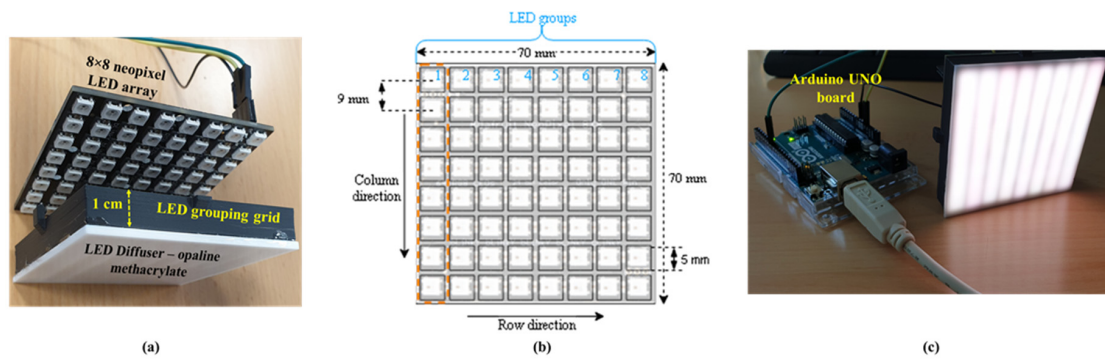
Figure 1. The transmitter (Tx) unit: (**a**) assembled unit with the grid and a diffuser, (**b**) an LED array configuration and (**c**) an Arduino Uno controller board and the LED panel.

Since both optical and electrical characterization of neopixel RGB LEDs are yet to be investigated, we first provide a characterization of the proposed MIMO Tx in terms of its optical radiation pattern and output optical power–current–voltage (L_{lux}-*I-V*) curves. The optical radiation pattern of the neopixel LEDs was measured to obtain its spatial intensity distribution for use in analyzing the coverage and signal distribution in VLC and OCC links [8]. The light intensity of LEDs defined in terms of the angle of irradiance θ is given by [8]:

$$I(\theta) = \frac{m+1}{2\pi} I(0) \cos^m(\theta), \ \theta = [-\frac{\pi}{2}, \frac{\pi}{2}], \tag{1}$$

where $I(0)$ is the center luminous intensity of an LED and *m* is Lambertian order given as [8]:

$$m = -\frac{\ln(2)}{\ln[\cos(\theta_{1/2})]}. \tag{2}$$

A lux meter was used to measure the angular dependence of the luminance of the LED (i.e., single and 8×8 horizontal and vertical array). As expected, the profiles for (i) a single LED represent a complete hemisphere close to Lambertian emitter with *m* of 1 (see Figure 2a); (ii) the LED array with no diffuser is broader with *m* of 0.74, due to the 9 mm spacing between the adjacent LED chips; and (iii) the LED array with the diffuser has *m* of 0.75 (see Figure 2b). Note that the measured radiation patterns can be further used to study the proposed MIMO-OCC links with mobility, and in a multi-user scenario. For example, rotation compensation schemes based on different Tx configurations [29] and wide receiver orientations [30] can be employed to ensure the operability of the proposed MIMO-OCC system in IoT environments.
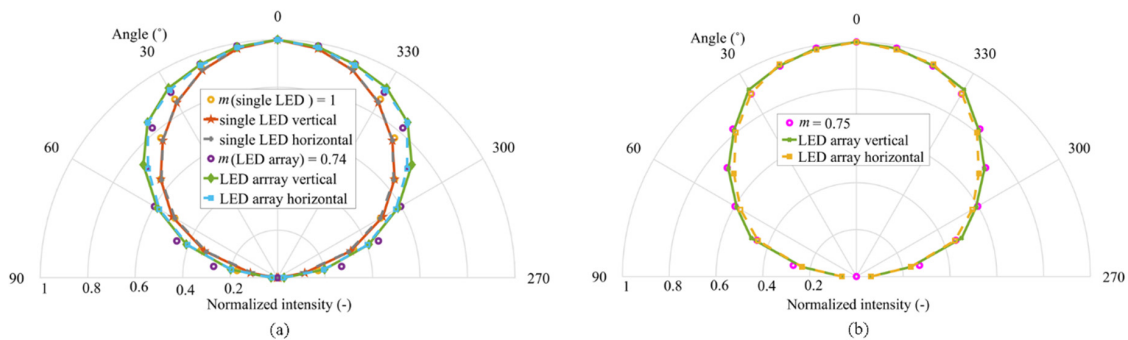

Figure 2. Measured Tx radiation patterns of: (**a**) a single LED in an array and for full LED array; and (**b**) a full LED array with the grid and the diffuser.

The illuminance levels of the LEDs were measured using a Testo 545 lux meter. Each neopixel in the array draws up to 60 mA of current *I* to turn ON at the maximum brightness. In realistic

environments, when the LED panel is to be used as a lamp, luminance can be efficiently controlled by varying switching power supply output current at the LED drive circuit. Therefore, the implementation of dimming techniques can be included as a part of the further extension of the proposed scheme [31,32]. However, increasing the power would induce crosstalk due to illumination from adjacent LEDs in the MIMO Tx [33].

In practical use, it is rare for all pixels to be turned ON at its maximum drawing current, due to the risk of overheating and damaging the LED panel. Therefore, it is recommended to drive each LED with $I_{LED} = 0.33I = 20$ mA [21]. Thus, the drive current for the LED array is estimated using the rule of thumb, as given by [21]:

$$I_{LED\text{-array}} = \frac{N_{pixels} \times I_{LED}}{1000},$$ (3)

where $N_{pixels} = 64$ is the total number of neopixel LEDs. In this work, $I_{LED\text{-array}}$ is set to 1.28 A for measuring the L_{lux}-*I-V* curves, which are depicted in Figure 3a,b for the MIMO-OCC Tx unit with, and without, the diffuser, respectively. Note: (i) the illumination levels are largely reduced, due to the use of the LED grid and the diffuser; (ii) linear L_{lux}-*I* plots, which are highly desirable in IM VLC systems; and (iii) the neopixels used either as a single LED chip or in an array depict similar optical characteristics to those of commonly used RGB LEDs.
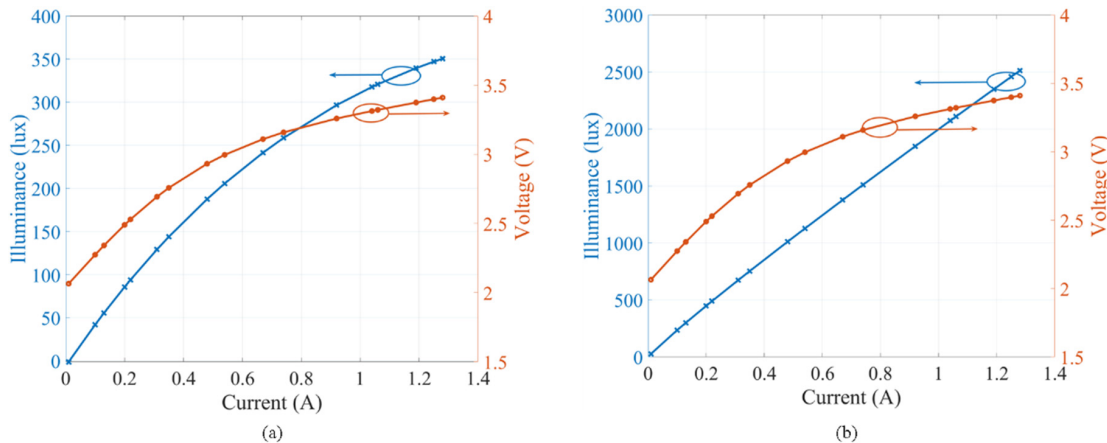
Figure 3. The L_{lux}-*I-V* curves of the multiple-input multiple-output-optical camera communications (MIMO-OCC) Tx unit: (**a**) with the diffuser attached; and (**b**) without the diffuser.

2.2. Rolling-Shutter Based MIMO Rx in OCC

The CMOS IS, along with the imaging lens, is composed of a large number of pixels, with each pixel acting as an independent PD. Unlike a conventional PD-based Rx, which cannot be used to separate the mixed signals, CMOS-based IS can capture lights coming from different directions, and project them onto different sections of the IS [13]. Therefore, spatial separation of incoming light signals and their intensities can be measured by obtaining the pixel value for each light source image in the received frame. Image processing can be applied to the received image frames to extract the data from pixelated images [13]. Therefore, CMOS IS can be used as the MIMO-OCC Rx without the need for extended hardware. In [34], the analysis of the MIMO-OCC Rx using Bayer-pattern filters, which can differentiate the incoming signals being transmitted from the MIMO Tx, was reported.

In an OCC-VLC system, the RS effect of a CMOS IS can be used to achieve flicker-free transmission and increased data rate [16–19]. In this mode, the camera sequentially integrates light on all pixels at the exposure time $t_{row\text{-exp}}$, similar to the scanning function, as illustrated in Figure 4a. In RS, the sensor scans the entire image row-by-row (line-wise) and generates a sequential readout. This scan process is governed by the system clock and is limited by the sampling rate of the analog to digital converter module. In GS-based IS, all pixels are exposed to the light simultaneously, i.e., ON or OFF states of the LED in a single frame [35], as illustrated in Figure 4b; while in RS, each row of pixels is exposed to

light at a given exposure time $t_{row\text{-}exp}$, sequentially similar to the scanning function. In RS cameras, the readout time $t_{read\text{-}out}$ ensures that there is no overlapping of the rows of pixels, and allows multiple exposures in a single captured image. The latter enables multiple LED states to be achieved at the same time in a single frame, as each row is exposed once to the light. Therefore, the captured image of the switched LED is composed of a set of black and white stripes. The proposed MIMO-OCC scheme differs from the RS-based OCC links (see Figure 4c), as in [16–19]. In traditional RS-based OCC, only a single bit is captured within one exposure time $t_{row\text{-}exp}$ (see Figure 4a), in contrast to the proposed work, where 8-bit (1-bit per channel) are captured in a single row with time $t_{row\text{-}exp}$, as depicted in Figure 4c. In addition, the proposed scheme can be used for flicker-free and high data rates transmission by allocating multiple bits per $t_{row\text{-}exp}$. The widths and the number of strips depend on the data rate (i.e., modulation frequencies) and the camera-LED distance, respectively [16,18].
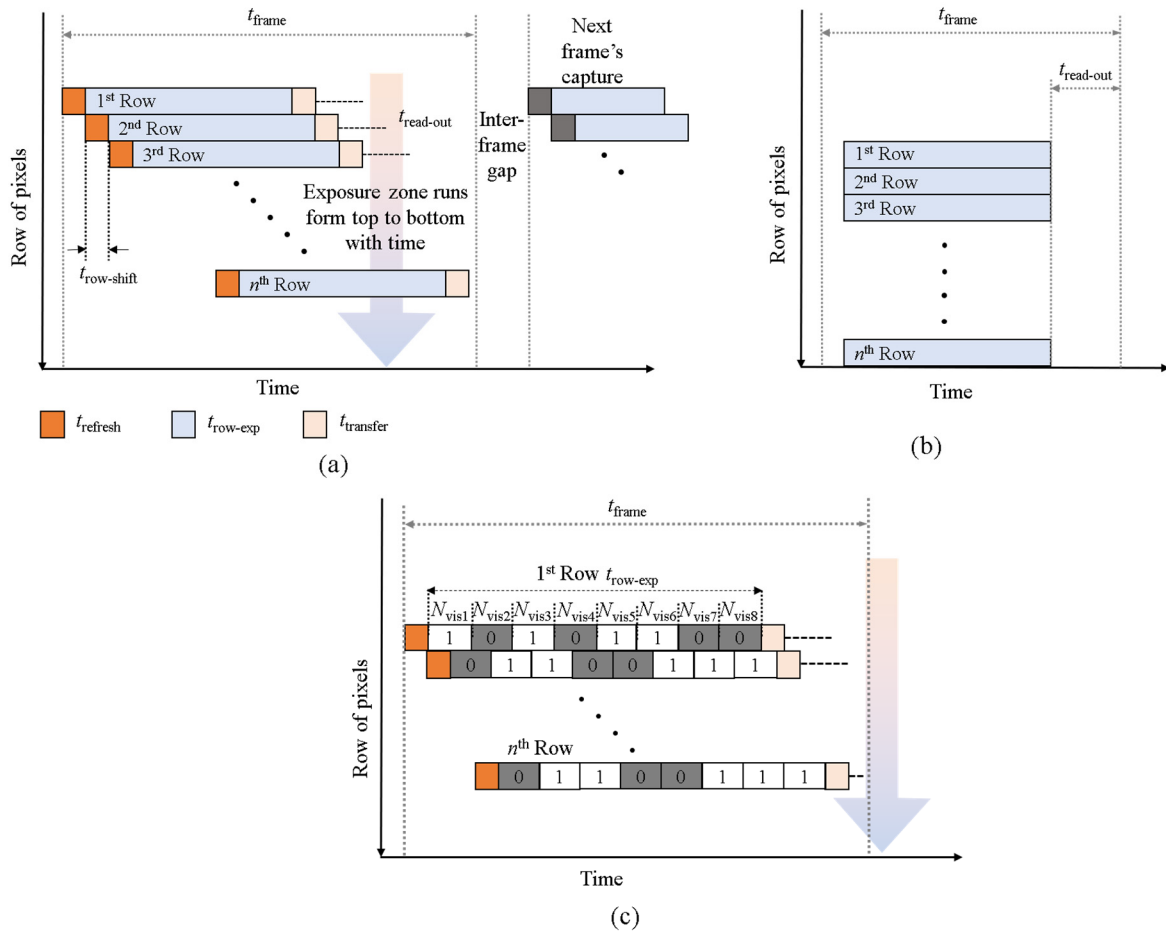
Figure 4. The camera capturing modes in OCC: (**a**) traditional rolling-shutter (RS) mechanism, (**b**) global-shutter (GS); and (**c**) RS-based capturing of the proposed multi-channel Tx.

Note that, in the RS capturing mode, each row starts with a certain delay, which results in the row shift, $t_{row\text{-}shift}$. The frame time is given as:

$$t_{frame} \leq N_{row} \times t_{row\text{-}shift} + t_{row\text{-}exp}, \tag{4}$$

where N_{row} is the pixel rows, which are based on the camera resolution. Note, $t_{row\text{-}exp}$ is the exposure time of the last row per frame (very small value).

2.3. System Overview of MIMO-OCC Using Proposed Multi-Channel Tx Design

Figure 5 illustrates the flow diagram for the proposed MIMO-OCC, using the 64-neopixel Tx unit and a RS-based RaspiCam as the Rx. The proposed scheme is an initial study to investigate the upper bounds of the system using the proposed Tx unit, therefore, we assume perfect synchronization and line-of-sight transmission. Neopixels are controlled in the Arduino software domain. First, N_{pixels} are assigned to N_{chips} of neopixels, which are then grouped column-wise into eight N_{groups} to form eight different transmission channels within one Tx unit. For data transmission, we have adopted a non-return-to-zero (NRZ) on-off keying (OOK) data format for IM of tri-color (band *i, j, k*) RGB channels (P_i, P_j and P_k) as $P_i + P_j + P_k = 1$ and $P_i + P_j + P_k = 0$, which is most commonly used in OCC. The data is generated in the Arduino unit and mapped to the LED addresses with the frequency, f_s, given as:

$$f_s = (t_{\text{chip}})^{-1},$$ (5)

where t_{chip} is the 1-bit time per neopixel chip, and its minimum value is 2.5 ms, due to Arduino hardware limitation to ensure flicker-free transmission at f_s of 400 Hz. The maximum number of visible bits per group in a single frame is given as:

$$N_{\text{visible}} = \left\lfloor \frac{t_{\text{frame}}}{t_{\text{chip}}} \right\rfloor.$$ (6)
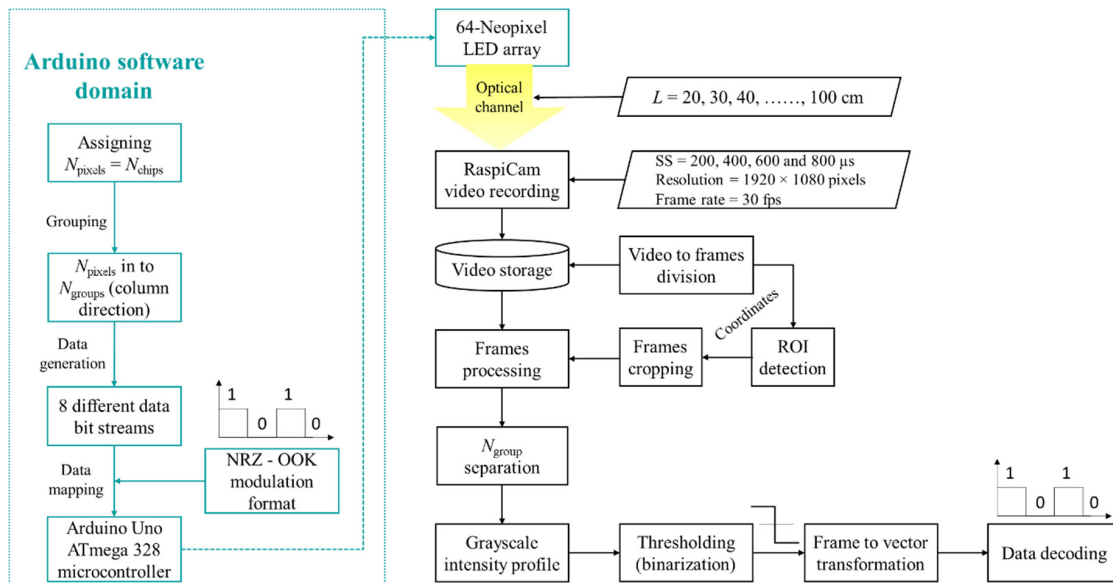
Figure 5. MIMO-OCC data processing flow diagram.

Note that N_{visible} will change with respect to the distance between the source and the camera, as well as camera resolution. Based on N_{visible}, the data transmission rate is given as:

$$R_d = N_{\text{groups}}\left(\frac{1}{t_{\text{chip}}}\right),$$ (7)

where N_{groups} is the number of data transmission channels in the Tx unit (see Figure 1b).

Table 1 shows the resolutions, frame rate and N_{visible} of RaspiCam. For further analysis, we selected a 1920 × 1080 pixel resolution, which is the most commonly used in cameras.

Table 1. RaspiCam resolutions.

Resolution (pixels)	Frame Rate (fps)	N_{visible} (bits)
1920×1080	30	8
3280×2464	15	22
1640×1232	40	10
1640×922	40	8
1280×720	90	6
640×480	200	4

To determine the upper bound of the system, we have selected NRZ-OOK data bit streams for IM of LED groups for transmission over the free space channel. Note that the same data is transmitted by all 8-LEDs per group, as shown in Figure 6.
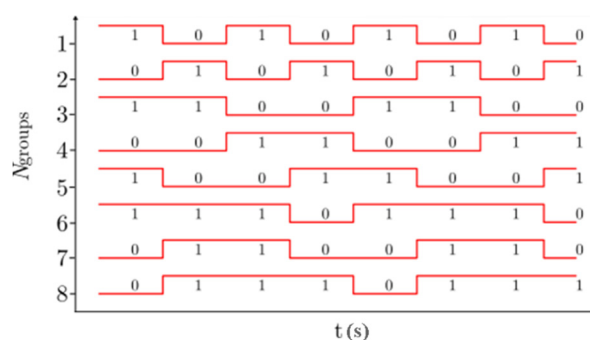
Figure 6. Data bit streams for intensity modulation (IM) of LED groups.

At the Rx, a RaspiCam for a given SS, resolution, and frame rate is used for capturing the images (i.e., recording a video stream for 3 s) of the IM light sources over an *L* ranging from 20 to 100 cm for post-processing. Note that a smaller image containing the emitter's signal information is transmitted, in order to speed up the processing time at the Rx. Therefore, the first step represents the detection of the region of interest (ROI) [36]. The obtained coordinates, which define boundaries of the ROI, are used for image cropping. Then, image processing is performed on the cropped images, which are then converted to the grayscale in order to retrieve the intensity profile. The threshold level is set based on the average of the received image intensity profile within the ROI. Following thresholding, binarization of the data frames is performed to convert the frame into vector transformation. This process is performed and applied to the remaining frames for decoding the transmitted data bit streams.

3. Experiment Results and Analysis

The experimental setup for investigating the proposed MIMO-OCC scheme is shown in Figure 7. The Tx unit is controlled using an Arduino Uno board, which is an open-source microcontroller board based on the ATmega328 [37]. The 64-bit long data stream (i.e., 8-bit per group, see Figure 6) is generated in the Arduino software domain and mapped to each LED address using the Arduino Uno board.

The key experimental parameters are listed in Table 2.

The camera used for capturing is the Raspberry Pi official camera (PiCamera V2), which is based on the Sony IMX219 sensor [38]. The RaspiCam is attached to the Raspberry touchscreen display to provide the easy interface and control over the camera capturing modes and settings. For the demonstration of the proposed study, experiments were performed for nine transmission distances and four different values of SS (see Table 2). The NRZ-OOK modulated signal was recorded in the form of a 3 s video stream (90 frames in total).

Figure 7. Experiment setup of the MIMO-OCC scheme.

Table 2. Key parameters of the experiment setup.

Parameter	Value
RaspiCam chip size	5.09 mm (H) × 4.930 mm (W) Diagonal: 4.60 mm
RaspiCam resolution	1920 × 1080 pixels
Raspberry display size	7 ″ (diagonally)
Raspberry display resolution	800 × 400 pixels
t_{chip}	2.5 ms
f_s	400 Hz
RaspiCam frame rate	30 fps
N_{row}	1080 pixels
N_{groups}	8 LED groups with 8LED/group
t_{frame}	0.216 ms
SS	200, 400, 600 and 800 μs
R_d	3.2 kbps
L	20–100 cm

The current proof-of-concept experiments were performed under the ambient light, where we measured the light intensity using a Testo 545 lux meter. The measured light intensity of the Tx with a diffuser was 300 lux at a distance of 50 cm. We also measured reflected lights from walls to be approximately 3.5 lux (±0.5 lux), which is very small compared with the Tx's illuminance; therefore, the ambient light influence on the integrity of data transmission is insignificant. The experiments were first conducted without a grid and a diffuser. To validate the scheme, a binary bit sequence of 1 and 0 was transmitted via all LEDs in the array. Figure 8 shows the original captured image frames with GS and RS modes, along with respective single row grayscale intensity profiles. Figure 8a shows the captured LED array using GS mode, along with its intensity profile at a maximum *L* of 20 cm. It can be seen that interference from the adjacent LEDs results in the blooming effect and, therefore, causes inter-cluster-interference. It can be seen that LED array captured using RS mode (see Figure 8b) at a minimum *L* of 5 cm, $N_{visible}$ is 4 at the surface of each LED. Moving farther away from the Tx, $N_{visible}$ is reduced to 3 at *L* of 7 cm (see Figure 8c). This is due to the reduced LED's surface area of 5 × 5 mm². Moreover, the RS rows also become saturated, which leads to inter-cluster-interference. Therefore, setting threshold levels become problematic, and hence lead to increased bit error rates (see Figure 8b,c). Therefore, further analysis was performed using the proposed LED array configuration shown in Figure 1.
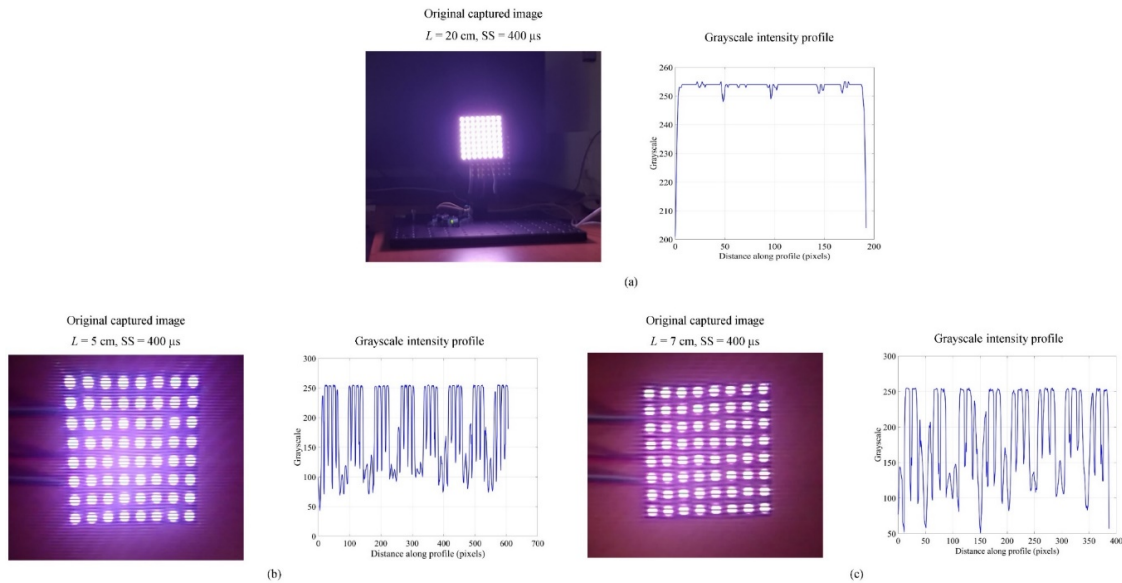
Figure 8. MIMO-OCC performance analysis without grouping grid and diffuser: captured images for data detection and their grayscale intensity profiles for: (**a**) GS captured image for *L* = 20 cm; (**b**) RS captured images for *L* = 5 cm; and (**c**) RS captured images for *L* = 7.

Figure 9 shows the original captured image frames with grouping grid and diffuser, quantized intensity of the detected data, and the top view of intensity profiles for *L* of 20, 60, and 100 cm, and SS of 200, 600, and 800 µs. The received intensity distribution within the image frame is shown in the form of quantized intensity profiles of the captured original images. These intensity profiles play an important role in determining the higher and lower intensities representing 1 and 0 bits in the received image frames for further thresholding and demodulation [39]. The dotted yellow box in the original image frames is the ROI, which fills only the captured Tx within the full image frame. The clear and sharp distinction between data lines of the adjacent N_{groups} can be seen at SS of 200 µs (see Figure 9a), while the lines get saturated for higher values of SS (see Figure 9b,c), which affects data demodulation (i.e., a higher number of bit error). Note that the camera's SS can be used to combat the effect of ambient lights, where lower and higher SS results in lower and higher levels of light to pass through the camera lens, as seen in the captured images in Figure 9.

Based on the received bits in the image frames, the data throughput is given as:

$$\text{Data throughput} = N_{\text{groups}} \times N_{\text{visible}} \left(\frac{\text{fps}}{2} \right), \tag{8}$$

Figure 10 illustrates the data throughput and N_{visible} with respect to *L*. Note that N_{visible} is the number of visible bits in each group. The maximum data throughput of 960 bps is observed at the minimum distance of 20 cm, where 8 full bits are visible in each group. The Tx illumination surface reduces with the increased *L*, thus resulting in reduced N_{visible} and the data throughput. For *L* of 100 cm, only one full bit is visible, therefore the data throughput is reduced to 120 bps.
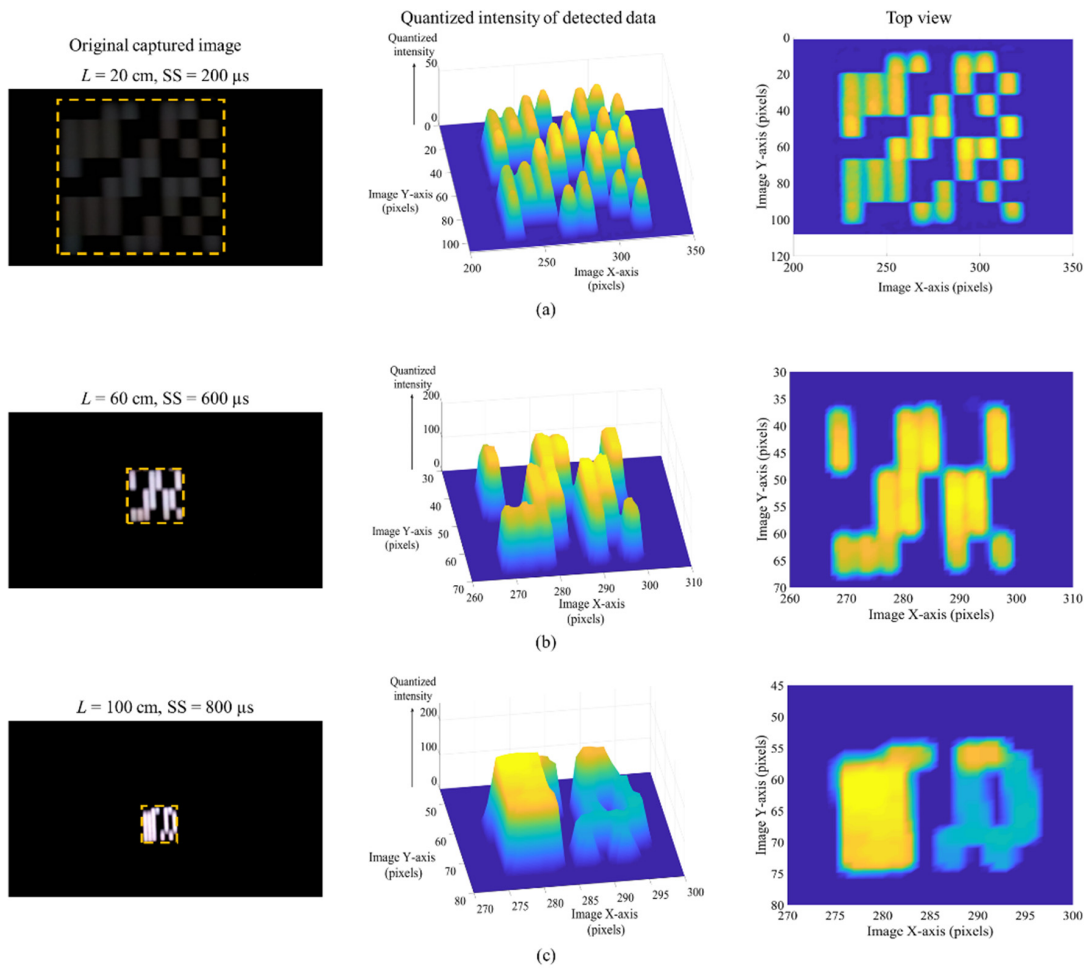
Figure 9. MIMO-OCC performance analysis with grouping grid and diffuser: the quantized intensity profiles of originally captured images for data detection at: (**a**) L = 20 cm and SS = 200 μs; (**b**) L = 60 cm and SS = 600 μs; and (**c**) L = 100 cm and SS = 800 μs.
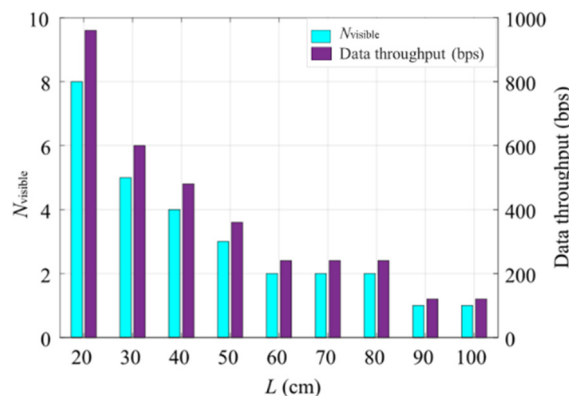

Figure 10. MIMO-OCC performance analysis: the data throughput with respect to $N_{visible}$ bits.

Table 3 shows the predicted data throughput based on the approximation of different Tx configurations, L, N_{groups}, and $N_{visible}$. It can be seen that increasing the number of LEDs leads to a larger surface area of the Tx, thus limiting higher values of $N_{visible}$. For example, for a Tx using a 24×24 LED array, 24 N_{groups} can be formed, which will increase the data throughput by up to 7.92 and 0.360 kbps for L of 60 and 160 cm, respectively; while for a Tx with a 32×32 LED array, 32 N_{groups} can be formed, which will increase the data throughput by up to 13.44 and 0.480 kbps for L of 80 and 180 cm, respectively.

Table 3. Theoretical (approximation) data throughput based on different Tx configurations.

Number of Neopixels	N_{groups}	L (cm)	N_{visible}	Data Throughput (kbps)
16×16	16	40–140	14 (max)–1 (min)	3.36 (max)–0.240 (min)
24×24	24	60–160	22–1	7.92–0.360
32×32	32	80–180	28–1	13.44–0.480

Since in OCC the data is captured in the form of a two-dimensional image, a conventional signal-to-noise ratio (SNR) measurement cannot fully reflect the quality of the link. Therefore, we have adopted peak signal-to-noise ratio (PSNR), which is widely used as a quality metric in image processing systems. To compute the PSNR, the mean squared error between the transmitted and received images is given by [39,40]:

$$\text{MSE} = \frac{\sum\limits_{m=1}^{H} \sum\limits_{n=1}^{W} [I_{Tx}(m,n) - I_{Rx}(m,n)]^2}{N_{\text{column}} \times N_{\text{row}}}, \tag{9}$$

where $I_{\text{Tx}}(m, n)$ and $I_{\text{Rx}}(m, n)$ are the intensity levels within the ROI of transmitted and received images of size height (H) × width (W), and N_{column} and N_{row} are the number of columns and rows of the images, respectively. The PSNR is then given as:

$$\text{PSNR} = 10 \log_{10}\left(\frac{R^2}{\text{MSE}}\right), \tag{10}$$

where R is the maximum span of input data (e.g., in the current scheme, the input image has an 8-bit unsigned integer data type; therefore, $R = 255$).

Figure 11a shows the performance of the OCC link in terms of PSNR with respect to L for different values of SS. As shown, PSNR increases with SS and decreases with the link span. This is due to the fact that the images of captured Tx at higher SS are more saturated, compared with those captured at lower SS (see Figure 9). The PSNR values of ~14 and ~16 dB are measured for SS values of 200 and 800 μs, respectively, for L of 100 cm, increasing by 4 and 3 dB for L of 20 cm for the same SS values, respectively.
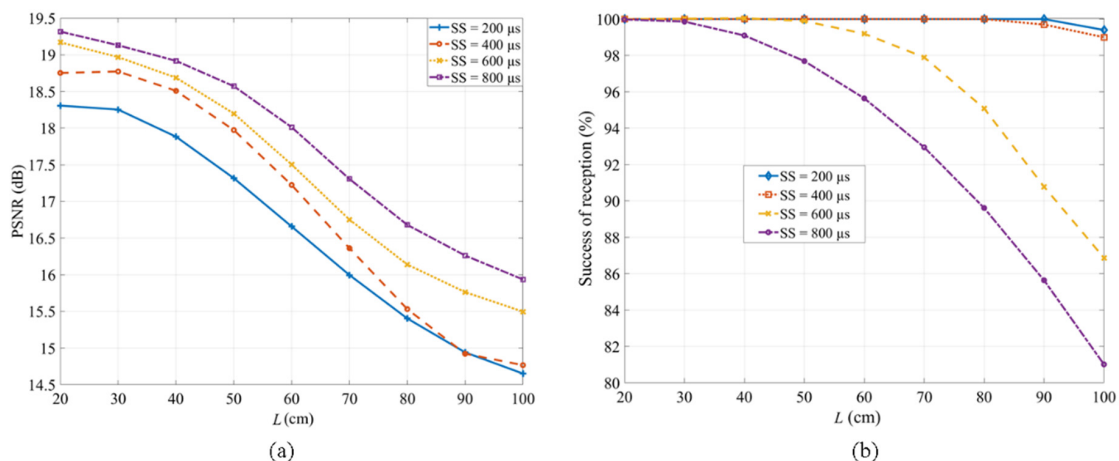

Figure 11. MIMO-OCC performance analysis: (**a**) the peak signal-to-noise ratio (PSNR); and (**b**) the percentage success of received bits with respect to L.

4. Conclusions

This paper demonstrated the experimental implementation of an RS acquisition-based camera capturing in MIMO-OCC, employing an LED array in an indoor static environment. The neopixel's light source could be used either as a single LED chip or an array display with similar optical characteristics to those of commonly used RGB LEDs. We showed the transmission spans of 7 cm and 1 m using

the Tx without, and with, the LED grid and a diffuser, respectively. The proposed system with the multi-channel LED array-based Tx offered the same performance at the SS of 200 and 400 μs over an *L* of 80 cm. However, at higher SS, the captured images were saturated, which resulted in increased PSNR and reduced percentage success of received bits. The maximum PSNR values of ~18 and ~19 dB and a 100% success rate of received bits were measured for the SS of 200 and 800 μs at the link span of 20 cm. A theoretical approximation (see Table 3) to further extend the *L* up to 1.8 m and the data throughput up to 13.44 kbps within the proposed MIMO-OCC using a grouped LED array by employing a Tx with a larger illuminating surface (large size) for practical indoor environments was provided. We conclude that the proposed Tx design can provide flicker-free transmission by employing multiple channels Tx with perfect inter-LED synchronization and an RS-based camera for use in short-range and low data rates indoor IoT applications, such as display-to-camera communications. The complexity of the proposed RS-based MIMO-OCC scheme will be further investigated for its implementation in practical scenarios, such as mobility, rotational support, and multiuser, based on ROI detection and bit or image pattern recognition within neural network algorithms.

Author Contributions: The contributions of the authors in this paper are the following: conceptualization: S.R.T. and V.M.; investigation: S.R.T. and V.M.; methodology: S.R.T.; project administration: S.Z., R.P.-J., and Z.G.; software: S.R.T.; validation: S.Z., R.P.-J., S.V., and Z.G. All authors have read and agreed to the published version of the manuscript.

Conflicts of Interest: The authors declare no conflicts of interest. The funders had no role in the design of the study; in the collection, analyses, or interpretation of data; in the writing of the manuscript; or in the decision to publish the results.

References

1. Boccardi, F.; Heath, R.W.; Lozano, A.; Marzetta, T.L.; Popovski, P. Five disruptive technology directions for 5G. *IEEE Commun. Mag.* **2014**, *52*, 74–80. [CrossRef]

2. Al-Fuqaha, A.; Guizani, M.; Mohammadi, M.; Aledhari, M.; Ayyash, M. Internet of Things: A Survey on Enabling Technologies, Protocols, and Applications. *IEEE Commun. Surv. Tutor.* **2015**, *17*, 2347–2376. [CrossRef]

3. Aksu, H.; Babun, L.; Conti, M.; Tolomei, G.; Uluagac, A.S. Advertising in the IoT Era: Vision and Challenges. *IEEE Commun. Mag.* **2018**, *56*, 138–144. [CrossRef]

4. Tercero, M.; von Wrycza, P.; Amah, A.; Widmer, J.; Fresia, M.; Frascolla, V.; Vijay, A. 5G Sstems: The mmMAGIC Project Perspective on Use Cases and Challenges between 6–100 GHz. In Proceedings of the IEEE Wireless Communications and Networking Conference Workshops (WCNCW), Doha, Qatar, 29 August 2016; pp. 200–205.

5. Kashima, T.; Qiu, J.; Shen, H.; Tang, C.; Tian, T.; Wang, X.; Kishiyama, Y. Large-scale massive MIMO field trial for 5G mobile communications system. In Proceedings of the 2016 International Symposium on Antennas and Propagation (ISAP), Okinawa, Japan, 24–28 September 2016; pp. 602–603.

6. Ayyash, M.; Elgala, H.; Khreishah, A.; Jungnickel, V.; Little, T.; Shao, S.; Rahaim, M.; Schulz, D.; Hilt, J.; Freund, R. Coexistence of WiFi and LiFi toward 5G: Concepts, opportunities, and challenges. *IEEE Commun. Mag.* **2016**, *54*, 64–71. [CrossRef]

7. Ghassemlooy, Z.; Popoola, W.; Rajbhandari, S. Visible Light Communications. In *Optical Wireless Communications*; Informa UK Limited: Colchester, UK, 2019; pp. 397–468.

8. Ghassemlooy, Z.; Popoola, W.; Rajbhandari, S. *Optical Wireless Communications*; Informa UK Limited: Colchester, UK, 2019.

9. Jang, M.J. IEEE 802.15 WPAN 15.7 Amendment-Optical Camera Communications Study Group (SG 7a). Available online: http://www.ieee802.org/15/pub/IEEE%20802_15%20WPAN%2015_7%20Revision1%20Task%20GroupOLD.htm (accessed on 18 November 2019).

10. Nguyen, T.; Islam, A.; Hossan, T.; Chowdhury, M.Z. Current Status and Performance Analysis of Optical Camera Communication Technologies for 5G Networks. *IEEE Access.* **2017**, *5*, 4574–4594. [CrossRef]

11. Le, N.T.; Hossain, M.A.; Jang, Y.M. A survey of design and implementation for optical camera communication. *Signal Process. Image Commun.* **2017**, *53*, 95–109. [CrossRef]

12. Liu, W.; Xu, Z. Some practical constraints and solutions for optical camera communication. *Philos. Trans. R. Soc. A Math. Phys. Eng. Sci.* **2020**, *378*, 20190191. [CrossRef]

13. Huang, W.; Tian, P.; Xu, Z. Design, and implementation of a real-time CIM-MIMO optical camera communication system. *Opt. Express* **2016**, *24*, 24567. [CrossRef]

14. IEEE Approved Draft Standard for Local and Metropolitan Area Networks—Part 15.7: Short-Range Optical Wireless Communications. In IEEE P802.15.7/D3a, pp. 1–428, 4 December 2018. Available online: https://standards.ieee.org/standard/802_15_7-2018.html (accessed on 23 April 2019).

15. Luo, P.; Zhang, M.; Ghassemlooy, Z.; Le Le Minh, H.; Tsai, H.-M.; Tang, X.; Png, L.C.; Han, D. Experimental Demonstration of RGB LED-Based Optical Camera Communications. *IEEE Photon. J.* **2015**, *7*, 1–12. [CrossRef]

16. Rachim, V.P.; Chung, W.-Y. Multilevel Intensity-Modulation for Rolling Shutter-Based Optical Camera Communication. *IEEE Photon-Technol. Lett.* **2018**, *30*, 903–906. [CrossRef]

17. Wang, W.-C.; Chow, C.-W.; Chen, C.-W.; Hsieh, H.-C.; Chen, Y.-T. Beacon Jointed Packet Reconstruction Scheme for Mobile-Phone Based Visible Light Communications Using Rolling Shutter. *IEEE Photon. J.* **2017**, *9*, 1–6. [CrossRef]

18. Yang, Y.; Hao, J.; Luo, J. CeilingTalk: Lightweight Indoor Broadcast Through LED-Camera Communication. *IEEE Trans. Mob. Comput.* **2017**, *16*, 3308–3319. [CrossRef]

19. Hassan, N.B.; Ghassemlooy, Z.; Zvanovec, S.; Biagi, M.; Vegni, A.M.; Zhang, M.; Luo, P. Non-Line-of-Sight MIMO Space-Time Division Multiplexing Visible Light Optical Camera Communications. *J. Light Technol.* **2019**, *37*, 2409–2417. [CrossRef]

20. Hasan, M.K.; Chowdhury, M.Z.; Shahjalal; Nguyen, V.T.; Jang, Y.M. Performance Analysis, and Improvement of Optical Camera Communication. *Appl. Sci.* **2018**, *8*, 2527. [CrossRef]

21. Burgess, P. Adafruit Neopixel Uberguide, WS2812B Datasheet; Philips, The Netherlands, 2019. Available online: https://cdn-learn.adafruit.com/downloads/pdf/adafruit-neopixel-uberguide.pdf (accessed on 13 June 2020).

22. Fujihashi, T.; Koike-Akino, T.; Orlik, P.; Watanabe, T. High-Throughput Visual MIMO Systems for Screen-Camera Communications. *IEEE Trans. Mob. Comput.* **2020**, 1. [CrossRef]

23. Jerkovits, T.; Liva, G.; I Amat, A.G. Improving the Decoding Threshold of Tailbiting Spatially Coupled LDPC Codes by Energy Shaping. *IEEE Commun. Lett.* **2018**, *22*, 660–663. [CrossRef]

24. Fang, Y.; Chen, P.; Cai, G.; Lau, F.C.M.; Liew, S.-C.; Han, G. Outage-Limit-Approaching Channel Coding for Future Wireless Communications: Root-Protograph Low-Density Parity-Check Codes. *IEEE Veh. Technol. Mag.* **2019**, *14*, 85–93. [CrossRef]

25. Elshabrawy, T.; Robert, J. Interleaved Chirp Spreading LoRa-Based Modulation. *IEEE Internet Things J.* **2019**, *6*, 3855–3863. [CrossRef]

26. Shahjalal; Hasan, M.K.; Chowdhury, M.Z.; Jang, Y.M. Smartphone Camera-Based Optical Wireless Communication System: Requirements and Implementation Challenges. *Electronics* **2019**, *8*, 913. [CrossRef]

27. Teli, S.R.; Zvanovec, S.; Ghassemlooy, Z. The first tests of smartphone camera exposure effect on optical camera communication links. In *Proceedings of the 2019 15th International Conference on Telecommunications (ConTEL), Graz, Austria, 3–5 July 2019*; Institute of Electrical and Electronics Engineers (IEEE): Piscataway, NJ, USA, 2019; pp. 1–6.

28. Chua, J.B.Y. System and Method for Enhancing Light Emissions from Light Packages by Adjusting the index of Refraction at the Surface of the Encapsulation Material. U.S. Patent 8,089,083, 3 January 2012.

29. Cahyadi, W.A.; Kim, Y.H.; Chung, Y.H.; Ahn, C.-J. Mobile Phone Camera-Based Indoor Visible Light Communications with Rotation Compensation. *IEEE Photon. J.* **2016**, *8*, 1–8. [CrossRef]

30. Cahyadi, W.A.; Chung, Y.H. Wide receiver orientation using diffuse reflection in camera-based indoor visible light communication. *Opt. Commun.* **2019**, *431*, 19–28. [CrossRef]

31. Gancarz, J.; Elgala, H.; Little, T.D. Impact of lighting requirements on VLC systems. *IEEE Commun. Mag.* **2013**, *51*, 34–41. [CrossRef]

32. Zafar, F.; Karunatilaka, D.; Parthiban, R. Dimming schemes for visible light communication: The state of research. *IEEE Wirel. Commun.* **2015**, *22*, 29–35. [CrossRef]

33. Pergoloni, S.; Biagi, M.; Cusani, R.; Scarano, G. Space-time multichannel adaptive filtering scheme for VLC color crosstalk equalization. *Opt. Express* **2018**, *26*, 19750–19761. [CrossRef] [PubMed]

34. Ghassemlooy, Z.; Uysal, M.; Khalighi, M.A.; Ribeiro, V.; Moll, F.; Zvanovec, S.; Belmonte, A. *An Overview of Optical Wireless Communications*; Springer Science and Business Media LLC: Berlin/Heidelberg, Germany, 2016; pp. 1–23.

35. Le, T.; Le, N.T.; Jang, Y.M.; Thithanhnhan, L.; Nam-Tuan, L.; Min, J.Y. Performance of rolling shutter and global shutter camera in optical camera communications. In *Proceedings of the 2015 International Conference on Information and Communication Technology Convergence (ICTC), Jeju, Korea, 28–30 October 2015*; Institute of Electrical and Electronics Engineers (IEEE): Piscataway, NJ, USA, 2015; pp. 124–128.

36. Thieu, M.D.; Pham, L.; Nguyen, T.; Chowdhury, M.Z. Optical-RoI-Signaling for Vehicular Communications. *IEEE Access* **2019**, *7*, 69873–69891. [CrossRef]

37. Atmel Corporation. *8-bit Microcontroller with 4/8/16/32K Bytes in System Programmable Flash*; Atmel Datasheet; Atmel Corporation: San Jose, CA, USA, 2009.

38. Sony Corporation. IMX219PQHS-C Datasheet; 2014. Available online: https://datasheetspdf.com/pdf/1404029/Sony/IMX219PQH5-C/1 (accessed on 13 June 2020).

39. Teli, S.R.; Zvanovec, S.; Ghassemlooy, Z. Performance evaluation of neural network assisted motion detection schemes implemented within indoor optical camera-based communications. *Opt. Express* **2019**, *27*, 24082–24092. [CrossRef]

40. Huynh-Thu, Q.; Ghanbari, M. Scope of validity of PSNR in image/video quality assessment. *Electron. Lett.* **2008**, *44*, 800. [CrossRef]

4.2 Spatial frequency-based angular behaviour of a short-range flicker-free MIMO-OCC link

This chapter is a version of the published manuscript:

S. R. Teli, S. Zvanovec, R. Perez-Jimenez, Z. Ghassemlooy, "Spatial frequency-based angular behaviour of a short-range flicker-free MIMO-OCC link," *Applied Optics*, vol. 59, pp. 10357-10368, 2020.

Connection to my Ph.D. thesis:

Unlike the previous study in Section 4.1, which focused on LOS links, in MIMO-OCC we need to consider both NLOS and Tx and Rx orientation based reception. In mobility scenarios, it is not the usual case to always have a surface providing ideally diffused reflections to receive the data via NLOS links. Therefore, in order to provide practical solutions considering different orientations and placements of the Tx and the Rx to support mobility scenarios in an indoor IoT environment, we study the angular rotation influence of multi-channel MIMO-OCC Tx units when placed *i*) at the same distance but different heights and *ii*) different distances from each other. The lab-scale experiments were performed in two different transmission setups where the static optimum angular orientation, θ, of two Tx units placed at different heights and distances from each other and the camera Rx was determined. The results depict that the proposed study provides a reception success of 100% at the optimum θ of 50° at lower captured values of spatial frequency of signal, which is projected onto the image sensor in the form of pixels for both the transmission setups.

appliedoptics

Spatial frequency-based angular behavior of a short-range flicker-free MIMO–OCC link

Shivani Rajendra Teli,[1,*] Stanislav Zvanovec,[1] Rafael Perez-Jimenez,[2] and Zabih Ghassemlooy[3]

[1]*Department of Electromagnetic Field, Faculty of Electrical Engineering, Czech Technical University in Prague, Technicka, Prague 16627, Czech Republic*
[2]*IDeTIC, Universidad de Las Palmas de Gran Canaria, Las Palmas 35001, Spain*
[3]*Optical Communications Research Group, Faculty of Engineering and Environment, Northumbria University, Newcastle NE1 7RU, UK*
Corresponding author: telishiv@fel.cvut.cz

In this paper, we provide a solution based on spatial frequency f_{sf} to study the angular behavior of a flicker-free, short-range indoor multiple–input multiple–output (MIMO) optical camera communications (OCC) link. We focus on the experimental investigation of OCC's performance for the transmitters (Txs) [i.e., light-emitting diode (LED) based arrays] located at the same and different distances from the receiver (Rx) with the off-axis rotation angle θ. We have used two 8×8 distributed LED arrays and a commercial low-cost complementary metal-oxide-semiconductor (CMOS) Raspberry Pi camera with the rolling-shutter capturing mode as the Tx and Rx, respectively. The image and the respective communications link quality metrics are measured in terms of the peak signal-to-noise ratio (PSNR) and the rate of successfully received bits with respect to f_{sf} for different camera shutter speeds (SS). A CMOS image sensor noise characterization is carried in terms of the signal-to-noise ratio (SNR) and PSNR. The proposed study provides a 100% success rate in data reception at the optimum θ of 50° at lower captured values of f_{sf}, which is projected onto the image sensor in the form of pixels. Moreover, the effect of channel saturation over f_{sf} is studied with respect to θ and SS and we show that, for θ exceeding the optimum value along transmission range, the f_{sf} area of the Txs reduces to less than ~50% of the captured Tx units at θ of 0°, where no data can be fully recovered.   © 2020 Optical Society of America

https://doi.org/10.1364/AO.404378

1. INTRODUCTION

The rapid advances made in development of a range of complementary metal–oxide–semiconductor-based (CMOS-based) camera [image sensors (IS)], which are used in mobile phones (front/rear camera), digital single-lens reflex cameras with higher capture speeds [ranging from 30 to 1000 frames per second (fps)], and surveillance cameras, have recently motivated research and development in camera-based visible light communications (VLC), which is also known as optical camera communications (OCC) in the IEEE 802.15.7r1 Task Group [1,2]. The CMOS cameras can capture images or record videos in capturing modes based on global shutter (GS) and rolling shutter (RS) at different shutter speeds (SS) and resolutions.

In VLC links with transmitters (Txs) based on light-emitting diodes (LEDs), a wide range of dimming levels with no flickering can be adopted to ensure both illumination and data communications [3]. The IEEE 802.15.7 VLC standard outlines the maximum allowed flickering time period (MFTP) of 5 ms (i.e., 200 Hz) [4]. However, consumer-grade cameras

have a limited capture rate of approximately 60 fps. As a result, signals in OCC links can be captured at a very low sampling rate compared to the data transmission rate, thus resulting in the loss of unsampled data and a lower probability of signal detection. Moreover, OCC synchronization should be considered carefully by means of signaling, which reduces the data throughput [5]. Furthermore, a combination of LED-array Txs and OCC with a photodetector (PD) array can be used as massive multiple-input multiple-output (MIMO) to deliver parallel transmission and therefore higher data rates R_b in a range of applications, including the massive internet of things (IoT) [6,7]. Unlike the conventional PD-based Rx used in VLC, where the separation of mixed signals is not possible, the CMOS-based IS can capture lights coming from different directions and project them onto different sections of the IS (i.e., illuminating different PDs) [7]. Therefore, in these scenarios spatial separation of incoming light signals and their intensities can be determined by measuring the pixel value per light source images on the received frame. The data from the pixelated images can then be recovered from the

captured image frames using an image processing algorithm implemented in MATLAB, OpenCV, and Python [7]. In this approach, the CMOS IS can be used as the MIMO–OCC Rx without a need for extended hardware. For commercial use, a number of applications have been developed, including OCC for the automotive industry by Intel (USA) [8] and for an online-to-offline marketing service by Panasonic (Japan) [9].

Although OCC does not support high-capacity transmission links, which is due to the speed limit of cameras, it can be employed in numerous low R_b and short-range indoor and outdoor IoT applications, including device-to-device communications, indoor positioning, localization, navigation, intelligent transportation systems, financial transactions, motion-based device control, small identification information, and communications through advertisements [3,10,11]. Note that in IoT-based smart environments links with R_b of a few kb/s are sufficient for information transmission and therefore there is no need for medium-speed transmission capabilities. However, the major challenge in implementing systems with a low R_b is the requirement for flicker-free transmission. Authors established flicker-free communications links using the grouped LED array concept in [12] using RS-based capturing Rx with a R_b of ~1 kb/s. The RS acquisition mechanism that sequentially integrates light on rows of pixels is the major advantage of CMOS IS used as the Rx in OCC [13].

In OCC, the transmitted light signal will arrive at the Rx (i.e., IS) via both the line-of-sight (LOS) and non-LOS (NLOS) paths. However, the LOS becomes the dominant path when using Txs and Rxs with very narrow fields of view. The RS-based MIMO-OCC transmission links are:

a. *LOS MIMO–OCC links.* Traditional indoor VLC or LOS OCC links with a high R_b over a range of transmission spans have been adopted in many applications, including: (i) short-range RS-based indoor MIMO–OCC LOS (1–5 m) flicker-free links using multilevel intensity modulation (IM) with a R_b of 10 kb/s [14]; (ii) a beacon jointed packet reconstruction scheme with a R_b of 5.76 kb/s [15]; (iii) screen modulation techniques followed by the $2M$-ary quadrature amplitude modulation format [16]; (iv) a CMOS RS effect-based scheme using the grayscale value distribution and machine learning algorithm to enhance R_b [17]; and (v) the raptor code with linear time encoding and decoding with a R_b of 1 kb/s [18]. Note that in LOS-based systems it is possible that some NLOS may be detected at the Rx, which will result in a time delay spread.

b. *NLOS MIMO–OCC links.* In scenarios such as device-to-device communications, it is possible that there might not be a LOS path between the Txs and the Rxs. Therefore, the communications will be via the NLOS paths, which offer mobility and flexibility but at the cost of a lower R_b [19,20]. NLOS–MIMO links based on space and the time division multiple access technique with a R_b of ~1 kb/s and flicker-free transmission over a 10 m link span was reported in [19]. A 152 bits NLOS link (1.5 m) with a low level of error correction code using image processing techniques such as background compensation blooming mitigation, extinction-ratio enhancement, and Bradley adaptive thresholding for RS demodulation was investigated in [21].

c. *Tx and Rx orientations.* Unlike previous studies, which focused on either a LOS or NLOS link, in MIMO–OCC links we need to considered both the Tx and Rx orientation angles. Some practical solutions considering different orientations and placements of the Tx and the Rx to support mobility scenarios in an indoor environment must be focused. In [6], the angular rotation θ from 0° to 70° along with parallel movement of a red, green, and blue based (RGB-based) LED array (16×16 LEDs) Tx and a 330 fps camera-based Rx operating in the GS capturing mode over a link span of 60 cm was reported. Note that in [6], the refresh rate for the LED array was set to 82 Hz, which is less than the MFTP standard rate of 200 Hz [4], thus providing flickering transmission and rotation support over a link span of 60 cm [6]. On the other hand, a 60-LED-based array is used to provide both data transmission and frame synchronization. In [22], a practical orientation independent RS-based NOLS–OCC link performing wide Rx's orientation for indoor applications with a R_b of ~ 7 kb/s over a transmission link span of 50 cm was presented. However, the Tx should be designed in such a way to ensure that there are sufficient reflections from many directions to ensure link availability. In [23], a CMOS RS pattern decoding scheme using the grayscale redistribution and differential grayscale packet selection was proposed and investigated to improve the decoding performance of the links under translational or rotational motions. The authors showed no significant signal degradation over a transmission range of up to 150 cm. Note, in applications with mobility, to ensure link availability, it is necessary to investigate various transmission scenarios considering different Txs angular orientations heights and distances from each other as well as from the Rx.

In this paper, we study multichannel MIMO–OCC considering the angular rotation of the Txs located at the same distance but different heights and distances from each other. These transmission setups are defined considering the indoor dynamic, mobility, and multicasting scenarios in places such as shopping malls, hospitals, and offices, where the number of Txs can be placed at different locations with different angles depending on the interior design and the illumination requirements. The proposed scheme offers a valid solution irrespective of the availability of LOS and NLOS paths. It is based on the optimum angular orientation of multiple Tx units for practical indoor IoT-based scenarios such as mobility and multi-Tx/Rx (multiuser). The proposed scheme employs two MIMO–OCC Tx units with a simplified design and a commercial low-cost Raspberry Pi camera (RaspiCam) as the Rx. The lab-scale experiments are carried out for two different transmission setups, where the effect of the optimum angular orientation θ of two Tx units located at different heights and distances from each other, as well as the camera-based Rx, is analyzed. For this reason, the spatial frequency f_{sf}, which represents the projection of a target, i.e., the Tx LED array over a captured image in terms of pixels, is used. The quality matrices of the captured image in terms of the peak signal-to-noise (PSNR) and the success rate of received bit sequences for a range of θ with respect to the f_{sf}, L, and SS are also analyzed.

This paper has five sections. Section 2 describes the proposed MIMO–OCC system, Section 3 shows the measurement setup followed by the experiment results and analysis in Section 4. Conclusions are then drawn in Section 5.

2. PROPOSED MIMO–OCC SYSTEM

A. CMOS IS Noise Characterization Within MIMO–OCC

The block diagram of the proposed MIMO–OCC system with multiple Txs ($Tx_1 - Tx_n$) and IS Rx is shown in Fig. 1(a). At the Tx, the data is generated in the form of on-off keying nonreturn to zero (OOK–NRZ) format $s(t)$ and is used for the IM of the LED via the LED driver. At the Rx, using an optical lens the IS captures multiple light Txs as different point sources on different sections of the IS. It is therefore straightforward to separate the multiple captured point sources and apply image processing for data detection. In this work, for further analysis we consider the projection of one Tx on to the Rx (i.e., camera), which can also be applied to multiple captured point sources. The intensity-modulated light signal $x(t)$ is transmitted over a free space channel and is captured at the Rx using a CMOS RS-based camera. For the LOS link, the received signal is given by [24]

$$y(t) = \eta x(t) \otimes h(t) + n(t), \tag{1}$$

where $h(t)$ is the combined impulse response of the channel and camera, η is the quantum efficiency of the IS, $\otimes$ is the time domain convolution, and $n(t)$ is the additive white Gaussian noise including the ambient light induced shot noise and the noise in the camera (i.e., fixed pattern, thermal (FPN)), photocurrent shot (optical excess and electronics), and flicker noise sources), as shown in Fig. 1(b) [25]. If the definition of power is scaled by the number of points in the signal, it will give the mean squared error (MSE). This notion can be extended in OCC for actual transmitted and received images by summing up twice the rows and columns of image vectors or stretching the entire image into a single vector of pixels and applying the one-dimensional (1D) definition. Therefore, in OCC signal images the SNR can be given as

$$\text{SNR (dB)} = 10 \log_{10} \frac{\sum_{m=1}^{W} \sum_{n=1}^{H} I_{Tx}(m, n)^2}{\sum_{m=1}^{W} \sum_{n=1}^{H} [I_{Tx}(m, n) - I_{Rx}(m, n)]^2}, \tag{2}$$

where $I_{Tx}(m, n)$ and $I_{Rx}(m, n)$ denote the intensity of the pixel of the transmitted and received image frames, respectively, at the location (m, n). In Eq. (2), $[I_{Tx}(m, n) - I_{Rx}(m, n)]^2$ corresponds to the squared error between the original and corrupted signals as $|y(t) - x(t)|^2$. The size of the image is W (width) $\times H$ (height). High values of SNR show that the estimation error is small and, therefore, among various image fusion methods the ones that exhibit higher SNR values can be considered to improve performance. The PSNR and the MSE are measured similarly to the SNR, which are defined as [26,27]

$$\text{PSNR (dB)} = 10 \log_{10} \frac{I_{\text{peak}}^2}{\text{MSE}}, \tag{3}$$

$$\text{MSE} = \frac{\sum_{m=1}^{W} \sum_{n=1}^{H} [I_{Tx}(m, n) - I_{RX}(m, n)]^2}{N_{\text{column}} \times N_{\text{row}}}, \tag{4}$$

where I_{peak}^2 denotes the squared peak intensity of the measured frame, and N_{column} and N_{row} are the number of columns and rows of the images, respectively. It can be seen that PSNR $\geq$ SNR. Both will be equal only when the original clean signal is constant and with the maximum amplitude. In the case of PSNR, the major focus is on the peak intensity I_{peak} of the measured frame to determine the signal bandwidth or number of bits to represent the signal. Therefore, the major issue is how the high-intensity regions of the image will be affected by the noise. This is much more content-specific than the SNR, which can be adopted in many applications, such as image compression.
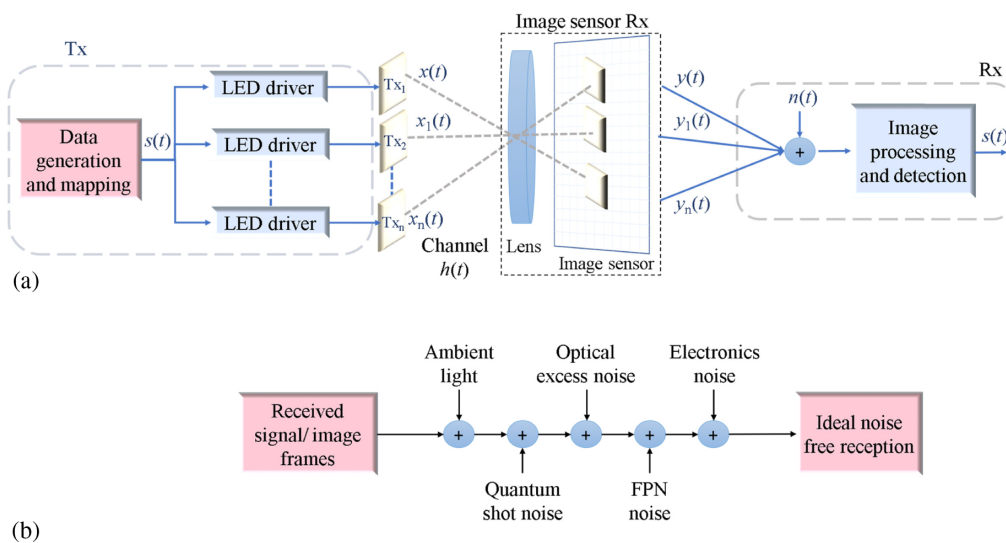

Fig. 1. (a) Schematic block diagram of MIMO–OCC link. (b) Different sources of noise in the OCC Rx end.
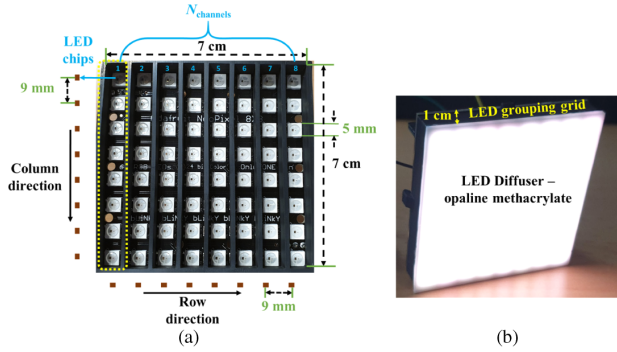
Fig. 2. Tx configuration: (a) Tx dimensions with LED grouping and (b) Tx with LED grouping grid and diffuser.

B. Developed MIMO–OCC System

A simple design of the MIMO Tx unit is adopted from our previous work in [12], as illustrated in Fig. 2. It is composed of a 64-NeoPixel array with an 8×8 small-chip LED [28], as shown in Fig. 2(a), and a 1 cm thick LED grouping grid that is placed over the Tx LED array, as shown in Fig. 2(b). The LED grid is designed to divide a 64-NeoPixel chip LED into eight different column-wise groups with eight chip LEDs per group to allow eight different data transmission channels using a single NeoPixel LED array. A 2 mm thick opaline methacrylate LED diffuser, which is commonly used, is placed over the Tx. The size of the LED array is 7.2×7.2 cm^2. The characterization of the proposed MIMO Tx unit in terms of its optical radiation pattern and output optical power–current–voltage ($L_{\text{lux}} - I - V$) curves was performed in [12]. Note, it is recommended to drive each LED with $I_{\text{LED}} = 20$ mA [12,28]. Therefore, for the LED array, the drive current $I_{\text{LED-array}}$ was set to 1.28 A to measure $L_{\text{lux}} - I - V$. It was found that the NeoPixels used either as a single LED chip or an LED-array together with the grid and diffuser depicted liner $L_{\text{lux}} - I - V$ plots, which are highly desirable in IM VLC systems [12].

Figure 3 illustrates the data mapping on the controller side for the proposed MIMO–OCC using two 64-NeoPixel Tx units and an Arduino Uno microcontroller-based driver per Tx. NeoPixels are controlled using Arduino software. First, N_{pixels} are assigned to N_{chips} per NeoPixel Tx, which are then grouped, column-wise, into 8-N_{channels}. To support rotational movements and study the angular behavior of multichannel Txs, the rotation angle within the range of $0° < \theta < 90°$ was changed at $10°$ steps, as shown in the inset (i) of Fig. 3. The data generated using the Arduino unit is mapped to the LED addresses with a frequency $f_s = (t_{\text{chip}})^{-1}$, where t_{chip} is the 1-bit time per NeoPixel

chip with the minimum value set to 2.5 ms due to a Arduino hardware limitation to ensure flicker-free transmission at a f_s of 400 Hz [12]. NRZ–OOK data bit streams with RGB (P_i, P_j, and P_k) as $P_i + P_j + P_k = 1$ and $P_i + P_j + P_k = 0$ is used for the IM of Txs for transmission over the free-space channel. Note, the same data is transmitted by all eight LEDs per N_{channel}, as shown in Fig. 4, while Txs 1 and 2 are transmitting different data signals. For example, the predefined 8-bit data in N_{channel1} shown in Fig. 4(a) is transmitted by all eight LEDs in the Tx$_1$, as shown in Fig. 2(a). Note that the data is transmitted simultaneously by all the channels in Tx$_1$ and Tx$_2$. Moreover, the N_{channel1} is the inverted version of N_{channel2} in the Tx$_1$, which is adopted for the synchronization of each LED group transmitting different packets. The anchor-based transmission needs considering when (i) transmitting long data streams via the proposed Tx design or in other techniques such as massive MIMO [6]; and (ii) for links experiencing blocking and shadowing [11].

Figure 5 shows an example of the RS-based capturing of the proposed multichannel Tx. In the RS-based capturing mode, the camera sequentially integrates all illuminated pixels at the exposure time $t_{\text{rwo-exp}}$, which is the same as scanning. The RS-based Rx reported in the literature captures a single bit for $t_{\text{rwo-exp}}$ [16]. In RS-based cameras, the readout time t_{readout} ensures that there is no overlapping of the rows of pixels and allows multiple exposures of a single captured image. In the proposed scheme, using multichannel Txs, 8 bit (1 bit per channel) of data are captured in a single row over $t_{\text{rwo-exp}}$, as shown in Fig. 5. This approach ensures flicker-free transmission at a higher R_b, in contrast to traditional RS schemes capturing only a single bit/$t_{\text{rwo-exp}}$. Note that the proposed Tx has a small surface area for capturing sufficient lights with a controller limitation defined by a f_s of 400 Hz. In flicker-free transmission, the R_b can be improved by increasing the surface area of the Tx unit (i.e., a higher number of LEDs).

The number of rows depends on the R_b and the transmission distance. The maximum number of visible bits per group in a single frame and the frame time are given as

$$N_{\text{visible}} = \lfloor t_{\text{frame}} \cdot f_s \rfloor . \tag{5}$$

$$t_{\text{frame}} \leq N_{\text{row}} \times t_{\text{row-shift}} + t_{\text{row-exp}}, \tag{6}$$

where N_{row} is the pixel rows, which is based on the camera resolution; $t_{\text{row-shift}}$ is the row shift; and t_{frame} is frame time. Note that: (i) $t_{\text{row-exp}}$ of the last row per frame is a very small value; and (ii) in the RS-based capturing mode, there is a delay in the start of each row, which results in a $t_{\text{row-shift}}$. It was shown in [12] that
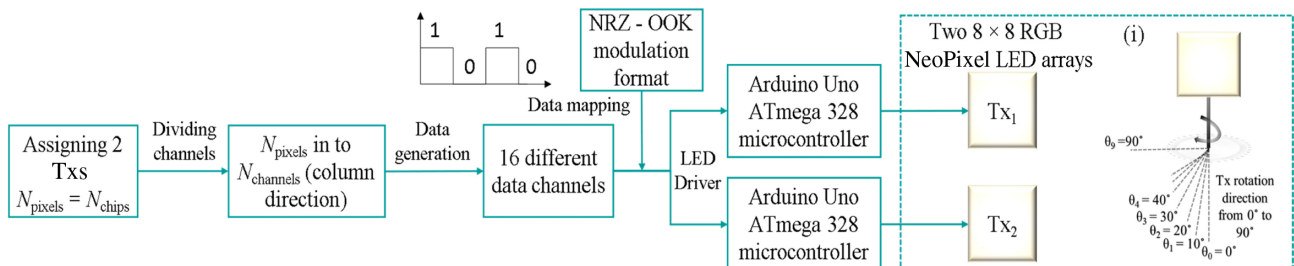

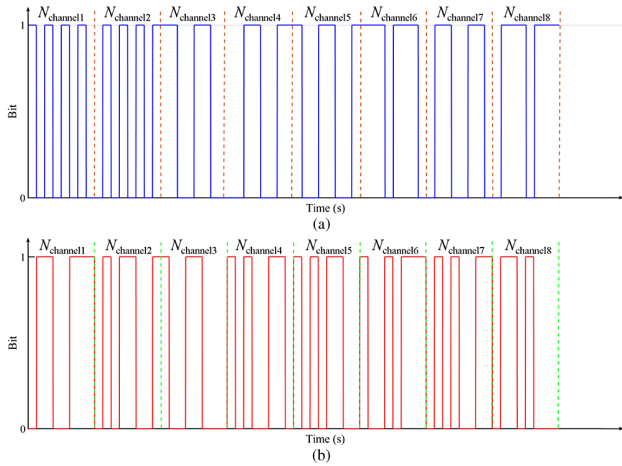**Fig. 3.** Data mapping in Arduino domain: inset i) angular orientation of Tx.

Fig. 4.   Transmitted bits through (a) Tx_1 and (b) Tx_2.

Fig. 5.   RS-based capturing of the proposed multichannel Tx.

$N_{visible}$ will change with respect to both the distance between the Tx and the Rx and the camera resolution. Based on $N_{visible}$, the data transmission rate is given as

$$R_b = N_{channels} \times f_s, \tag{7}$$

where $N_{channels}$ is the number of LED groups in the Tx unit.

C. Detection Scheme to Study the Tx Angular Rotation Influence

Figure 6 illustrates the flowchart for the detection when considering the Tx's angular rotation as $0° < \theta < 90°$ in the proposed
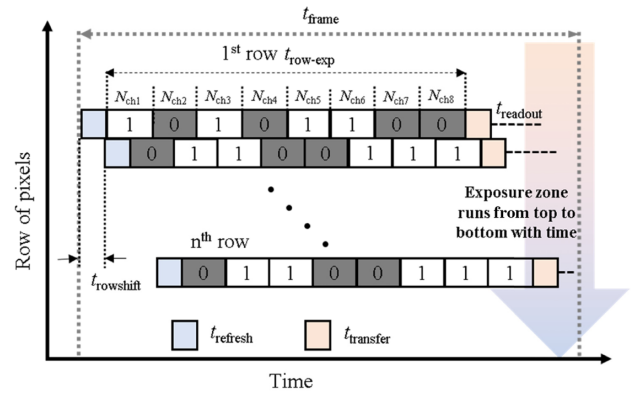
systems. At the Rx, we used a RaspiCam with a given SS, resolution, and frame rate for capturing images (i.e., recording a video stream for 5 s) of IM light sources over L of 30 to 110 cm. The overall detection process is divided into three main stages:

Stage 1: _Video recording and frame division_. The RaspiCam Rx records the data and calibration video streams that represent the captured transmitted information and the Tx's template shape, respectively. The calibration videos, which outline the intensity compensation of the data video frames, are used for equalization as the IS captures multiple light Txs as different point sources on different sections of the IS. Therefore, the image frame is divided to distinguish multiple light sources for detection. Note that a considerably smaller image containing the signal information is transmitted to reduce the processing time at the Rx.
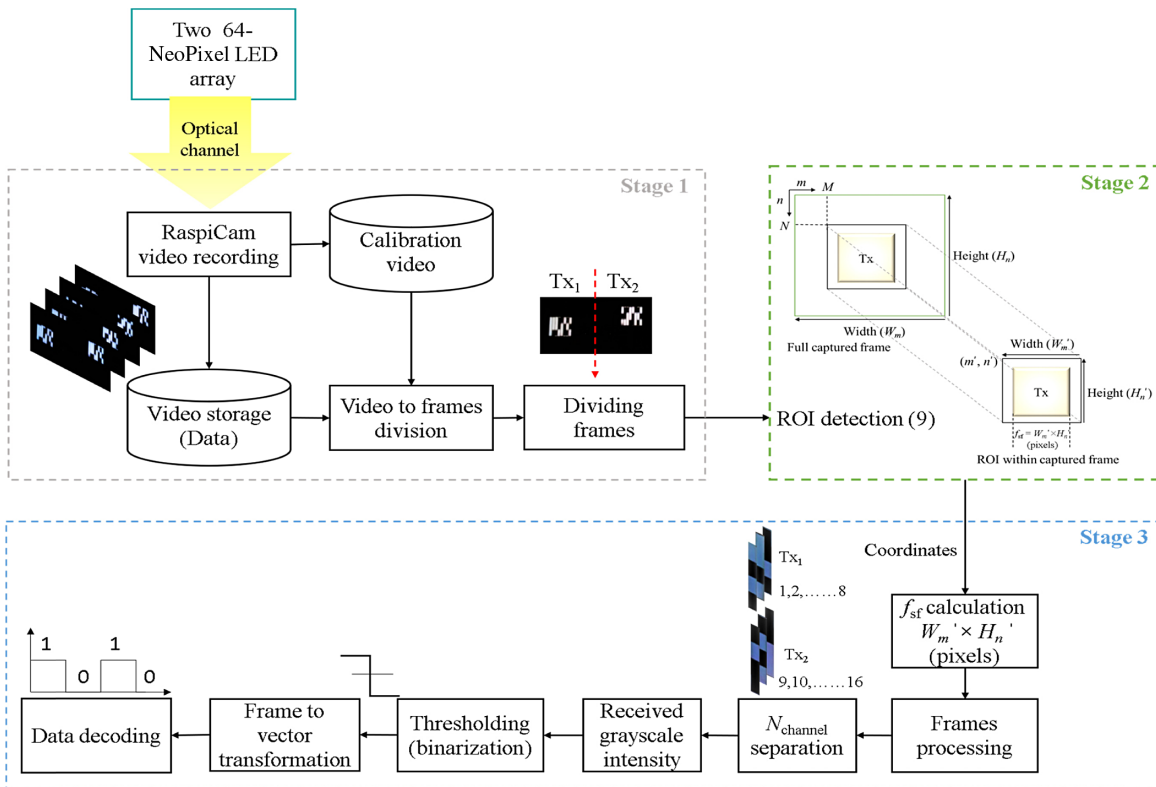

Fig. 6.   Flowchart illustrating the data detection process.

51

Stage 2: *Region of interest (ROI) detection*. Here, we perform ROI detection [29] over the divided frames, and then use the obtained coordinates, which define boundaries of the ROI, for image cropping. The ROI template used to define ROI in the full calibration capture frame. It is given as

$$\text{ROI} = (m', n', W'_m, H'_n),\qquad(8)$$

where m' and n' are top corner coordinates, and W'_m and H'_n are the width and height of the captured image frame, respectively. Here, we have adopted an image processing technique known as template matching [30] to determine the target ROI in the calibration image frame and then to find the position of the target ROI_{temp} in the data image frame, given as [30]

$$\text{ROI}_{\text{temp}} = \sum_{m=0}^{W_m} \sum_{n=0}^{H_n} \left\{ P\left(m', n'\right) - P'\left(M + m', N + n'\right) \right\}^2,\qquad(9)$$

where the coordinate of a single point in ROI is (m', n') with a pixel value $P(m', n')$, while the coordinate of the overlapping point and its pixel value are $(M + m', N + n')$ and $P'(M + m', N + n')$, respectively. The overlapping points of the data image frame and ROI image are calculated using template matching. The coordinate (M, N) is the origin of the template image on the full captured image. It is assumed that the sizes of the template and the fully captured input image are $W'_m \times H'_n$ (width × height) and $W_m \times H_n$ (width × height), respectively. The ROI_{temp} obtained from Eq. (9) is used to crop the data image frames. The values of ROI_{temp} must change dynamically because in this technique the shape of the Tx unit changes with θ and the distance between the Tx and the camera settings. This technique can be further adapted to detect multiple ROIs within a single image frame based on its template coordinate points.

Stage 3: *Frame processing and data detection*. The ROI cropped images from the previous stage are used to calculate the spatial frequency components f_{sf}, which refers to the projection of a target (i.e., the Tx LED array over a captured image in terms of pixels [30, 31]). As shown in Stage 3 of Fig. 6, in terms of pixels f_{sf} of ROI_{temp} is $W'_m \times H'_n$. Next, f_{sf} separated images are processed for N_{channel} separation followed by image processing. As outlined in Stage 3 of Fig. 6, each N_{channel} is converted from the RGB color format to the grayscale for both calibration and data frames to retrieve the intensity profile. As the intensity levels for NRZ–OOK data signals are set as $P_i + P_j + P_k = 1$ (with $I_{\text{peak}} = 255$) and $P_i + P_j + P_k = 0$, the threshold level is set based on the average of the received image intensity profile in ROI. Following thresholding, binarization of the data frames is performed to convert the frame into a vector transformation, which is applied to the remaining frames for decoding the transmitted data bit streams. Finally, the received data bit vector is then compared with the transmitted data to ascertain the success of the reception of received bits by determining the ratio of the wrongly decoded bits to the total number of transmitted bits (i.e., the number of bit errors).

3. MEASUREMENT SETUP

The measurements were performed for two different transmission setups, as illustrated in Fig. 7. As previously mentioned, this investigation focused on the angular rotation of Tx units within multichannel OCC. Both Tx units rotate with θ of 0° to 90°. A Raspberry Pi camera used as a Rx is mounted at the top of the display panel at a height h_{Rx} of 18 cm and an angle θ_c of 90°, as shown in Fig. 7. In both the setups, the radial distance r between the Tx_1 and Tx_2 is changed with respect to the transmission length L between camera and the Txs. Note, r was increased to ensure that both Tx units are captured at the same time in a single image frame.

In transmission setup1, both Tx units are placed at the same distance but different heights h_{Tx_1} (same as the camera height h_{Rx}) and h_{Tx_2} at 25 cm, as shown in Fig. 7(a). Note that the actual transmission distance between both Tx units and camera is $l = \sqrt{L^2 + (\frac{r}{2})^2}$, as shown in Fig. 7(a). For example, for L and r of 30 and 20 cm, l is ~ 32 cm. Note that the difference between L and l is rather small; therefore, for further analysis and simplicity we will only use L.

In transmission setup 2, both Tx units are placed at the same height $h_{\text{Tx}} = h_{\text{Rx}}$, but at different distances L_1 and L from the camera, as shown in Fig. 7(b), where $(L_1 - L) = 30$ cm.

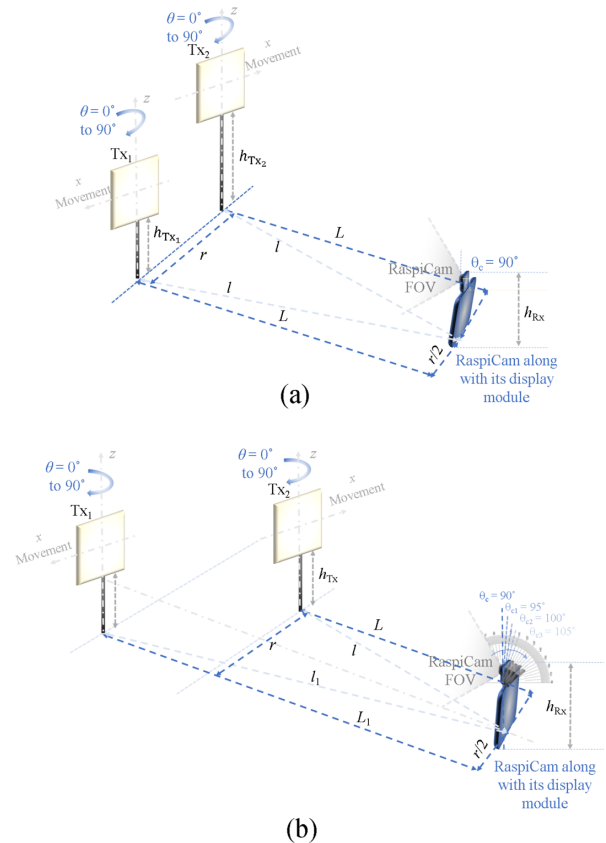The experimental setups to investigate the angular behavior of the proposed MIMO–OCC scheme are shown in Fig. 8.

(a)

(b)

Fig. 7. Transmission setups: (a) Tx units placed at different heights and (b) Tx units placed at a different distance.
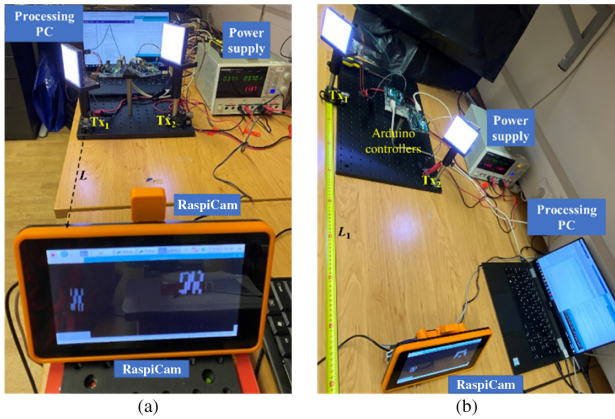
52

Fig. 8. Experiment setup: (a) Tx units placed at different heights and (b) Tx units placed at a different distance.

Table 1. Key Parameters of the Experimental Setup

Parameter	Value
RaspiCam chip size	5.09 mm (H) × 4.930 mm (W)
	Diagonal: 4.60 mm
RaspiCam resolution	1920 × 1080 pixels
Raspberry display size	7″ (diagonally)
Raspberry display resolution	800 × 400 pixels
t_{chip}	2.5 ms
f_s	400 Hz
RaspiCam frame rate	30 fps
N_{row}	1080 pixels
Tx	8 × 8 RGB NeoPixel LED array
$N_{channels}$	16 LED groups with eight groups
	each Tx and 8LED/group
$I_{LED-array}$	1.28 A (for each Tx unit)
t_{frame}	0.216 ms
SS	200, 400 and 800 μs
R_b	6.4 kbps
L	30–110 cm
L_1	60–140 cm
r	25–45 cm
Tx Rotation angle θ	0°–90°
Rx angle θ_c	90°

The Tx units are controlled using an Arduino Uno board, which is an open source microcontroller board based on ATmega328 [32]. A 64-bit long data stream (i.e., eight bits per group, as shown in Fig. 4) is generated in the Arduino software domain for each Tx unit and mapped to each LED (i.e., address) using the Arduino Uno board. The key experimental parameters are listed in Table 1. A Raspberry Pi (PiCamera V2) is the camera used, which is based on a Sony IMX219 sensor [33]. The RaspiCam is attached to the Raspberry touchscreen display to provide easy interface and control over the camera capturing modes and settings. Experiments were performed for nine transmission distances and three different values of SS (see Table 1) for θ of 0° to 90°. The NRZ–OOK signal was recorded for 5 s (a total of 150 frames).

4. EXPERIMENTAL RESULTS AND ANALYSIS

A. Tx Units Placed at the Same Distance and Different Heights

Figure 9(a)–9(c) show examples of captured image frames, f_{sf}, and the grayscale intensity profiles for the detected data per $N_{channels}$ for a range of L, θ, and SS. It can be seen that the shape of the captured Tx changes due to angular tilting, which results in the loss of data bits. To avoid this, the first and last pixel rows in each image frame are eliminated from the top and bottom of each Tx ROI. The received intensity distribution within the image frame is shown in the form of grayscale intensity profiles for the captured original images. These intensity profiles play an important role in determining the higher and lower intensities (i.e., representing 1 and 0) in the received image frames for further thresholding and demodulation [11]. The dotted yellow box in the original image frames defines the ROI, which fills only the f_{sf} of the captured Tx within the full image frame. The clear and sharp distinction between the data lines can be seen for θ up to 40°, and L and SS of 50 cm and 200 μs, respectively, as shown in Fig. 9(a). Since the lines get saturated for higher values of θ, which reduces the f_{sf} and SS, as shown in Figs. 9(b) and 9(c), it makes it challenging to separate $N_{channels}$, which then affects the data demodulation (i.e., higher number of error bits). We have therefore shown the intensity distribution in the form of a quantized intensity profile of the captured image frame for θ of 70°, L of 90 cm, and SS of 800 μs, [Fig. 9(c)]. Therefore, data detection at L up to 110 cm was performed for θ up to 80° with SS of 200 and 400 μs, and θ of 70° with SS of 800 μs.

Table 2 shows the average f_{sf} of the captured Tx image with respect to L and θ. It can be seen that the f_{sf} (reduces) and the shape (square to rectangle) of the Txs changes with L and θ. Considering the average f_{sf}, we see very little changes in L (10 cm) and θ (10°). For a L of 30–50 cm, the f_{sf} has ∼2 and 3 times more high-frequency components than for a L of 60–90 cm for a range of θ, [Figs. 9(a)–9(c)]. Therefore, it can be said that a reduced number of pixels of the Tx image leads to lower high-frequency components and, consequently, the channel can be seen as a low-pass filter with a cutoff frequency that decreases with increasing L and θ. Further analysis is performed for f_{sf} at different values of L and θ and its impact on the communications link performance in terms of successful reception and PSNR.

Figure 10(a) then illustrates the performance analysis of the angular behavior of the multichannel MIMO–OCC link in terms of the percentage success of the received bits with respect to θ for various values of L and SS. In this setup, the average time window for offline OCC data extraction (only) was about 0.98 s using the predefined data processing algorithm depicted in Fig. 6. It can be seen that, for L up to 80 cm, 100% reception success is achieved for θ of 50° for SS of 200 and 400 μs; and for θ of 30° for SS values of 800 μs, [Fig. 10(a)]. Note that, for L of 30 cm, 100% success is achieved for θ of 0° to 80° and for SS values of 200 and 400 μs. It can also be seen that the reception success reduces further with f_{sf} (i.e., less than ∼50% at θ of 0°, as shown in Table 2), and increases with SS, which results in channel saturation. As a result, it is challenging to separate the $N_{channels}$ and, therefore, the decoding of received bits, [Figs. 10(a)].
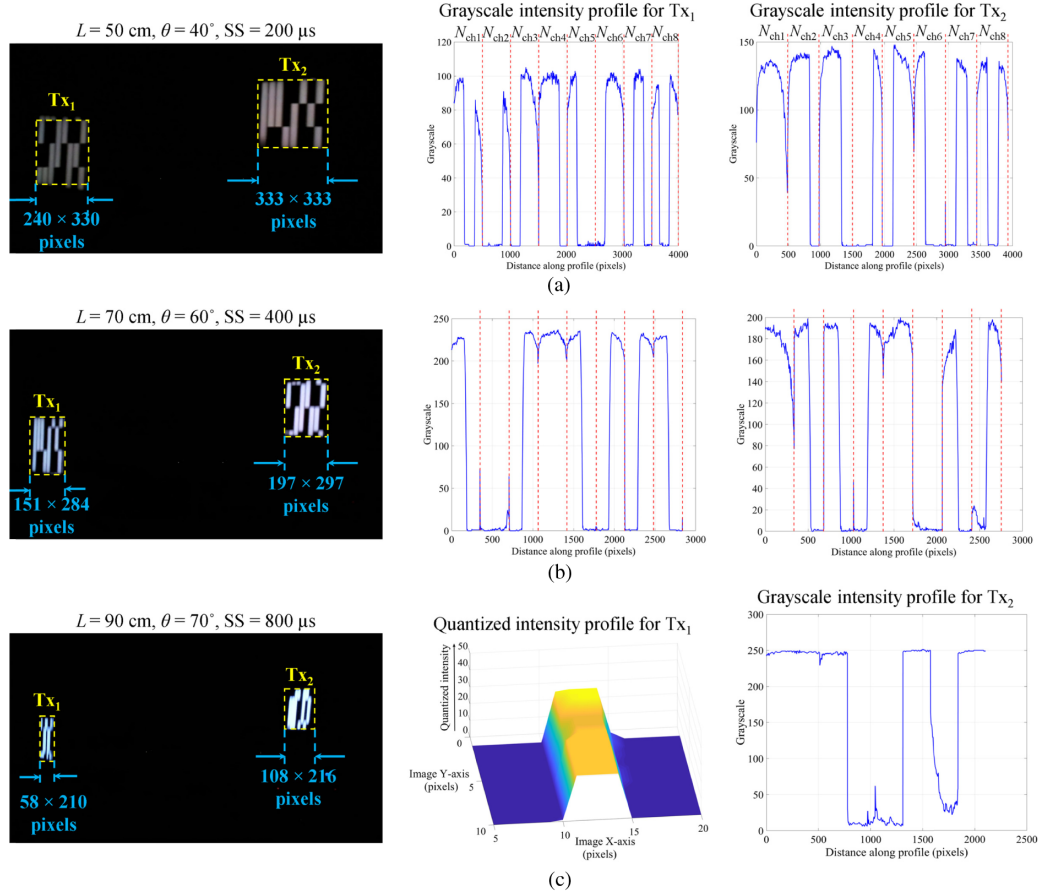
53

Fig. 9. Grayscale and quantized intensity profiles of originally captured images for data detection at: (a) L of 50 cm, θ of 40°, and SS of 200 µs, (b) L of 70 cm, θ of 60°, and SS of 400 µs, and (c) L of 90 cm, θ of 70°, and SS of 800 µs.

Table 2. Average f_{sf} in Pixels with Respect to L and θ^a

L (cm)	θ 0°–20°	θ 30°–50°	θ 60°–80°
30–50	450 × 450	210 × 310	200 × 300
	459 × 459	300 × 300	171 × 290
60–80	155 × 285	150 × 280	145 × 260
	200 × 299	195 × 294	185 × 285
90–110	78 × 230	65 × 215	55 × 200
	115 × 240	105 × 235	100 × 125

*Upper values are for the Tx$_1$ and bottom for the Tx$_2$.

As previously mentioned in Section 2, in OCC, the data is captured in the form of a 2D image; therefore, the conventional SNR measurement cannot fully reflect the quality of the link. Here, we have adopted PSNR, which is widely used as a quality metric in image processing systems. Equations (3) and (4) are used to compute the MSE between the transmitted and received images with respect to ROI$_{temp}$ [Eq. (9)] as given by

$$\text{MSE} = \frac{\sum_{m=1}^{W_m} \sum_{n=1}^{H_n} [ROI_{\text{temp}}(m, n) - I_{\text{RX}}(m, n)]^2}{W_m \times H_n}. \quad \textbf{(10)}$$

As the input image has an 8-bit unsigned integer data type with $I_{\text{peak}}^2 = 255$, the PSNR is computed by substituting

Eq. (10) and I_{peak}^2 in Eq. (3). Figure 10(b) shows the performance of the OCC link in terms of PSNR with respect to θ for different values of SS and link spans. As shown, PSNR increases with SS due to the fact that the images of captured Tx at higher SS are more saturated compared to those captured at a lower SS, as shown in Fig. 9(c). Note that the PSNR decreases with a decreasing f_{sf} [70% than at θ of 0°, as shown in Table 2 and Fig. 10(b)] with respect to θ and L. This is due to the fact that the Tx units move away from the camera field of view with increasing θ and L; therefore, a small amount of light passes through the camera lens and hence fewer photons are incident on the pixels of the image sensor and thus, there is reduced f_{sf}. With 100% reception success, the PSNR value of ~22 dB is measured for SS of 200 µs, which increases by 3 and 7 dB for SS of 400 and 800 µs, respectively, for L of 30 cm at θ of 0°.

Based on the N_{channel} and N_{visible} for each Tx unit in the image frames, the data throughput is given as

$$\text{Data throughput} = N_{\text{channel}} \times N_{\text{visible}} \times \left(\frac{\text{fps}}{2}\right). \quad \textbf{(11)}$$

Figure 11 illustrates the performance analysis of the proposed multichannel MIMO–OCC in terms of data throughput calculated with respect to θ and L. For θ of 0°, the maximum data throughput of 1.92 kb/ps is observed for a L of 30 cm, where an 8-bit data stream (4-bit/N_{channel}/Tx) is seen by the
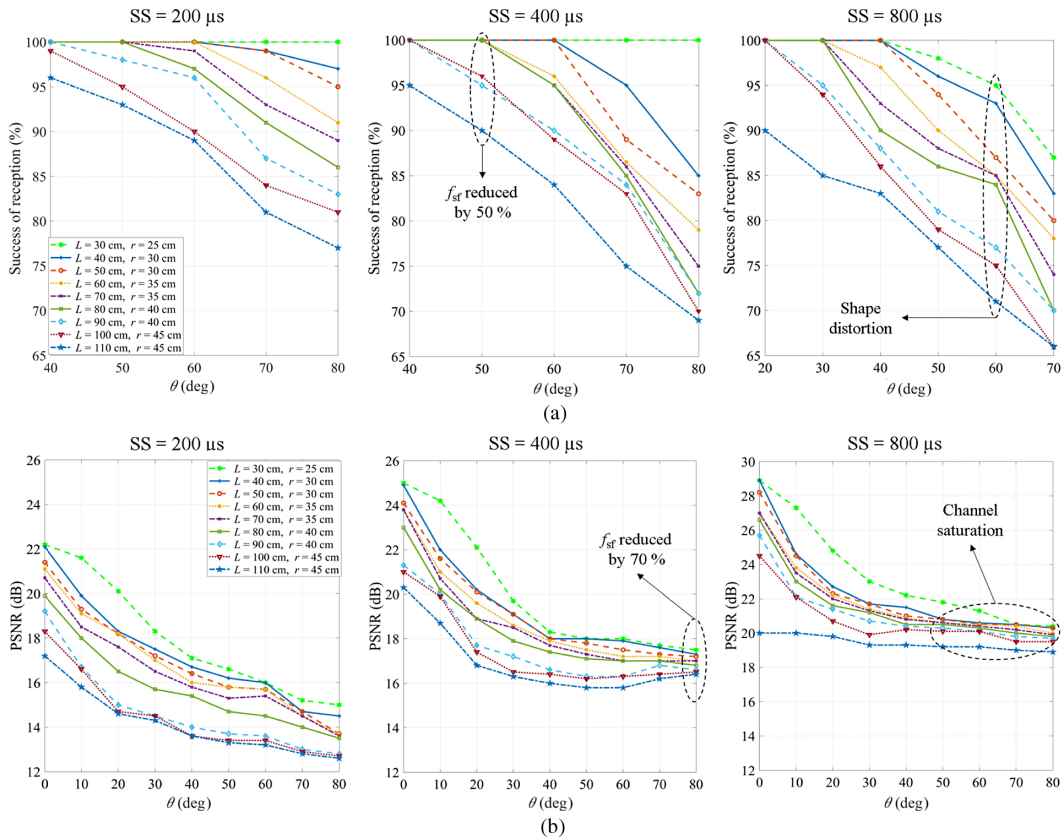
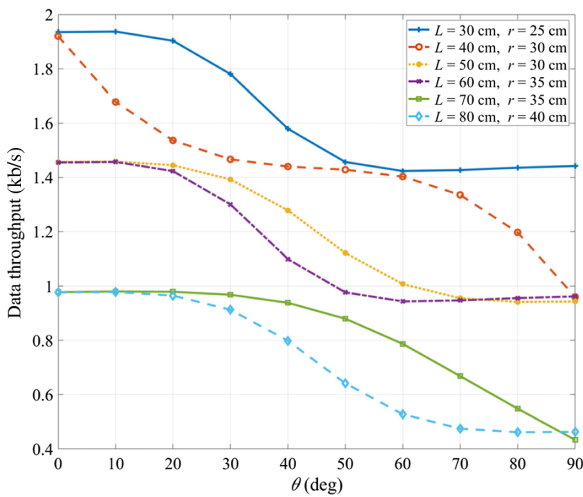**Fig. 10.** Performance analysis: (a) success of reception and (b) PSNR.

Fig. 11. Data throughput with respect to change in L and θ.

camera. The f_{sf} is decreased with increasing L and θ, thus resulting in a reduced $N_{visible}$ and data throughput. For θ of 40°, the data throughput of 1.44 kb/s is observed for a L of 50 cm, where a 6-bit data stream (3-bit/$N_{channel}$/Tx) is seen by the camera, as shown in Fig. 9(a). For a L of 90 to 110 cm, a 2-bit stream (1-bit/$N_{channel}$/Tx) is visible to the camera, as shown in Fig. 9(c), and therefore the data throughput of 480 b/s is obtained for each θ.

B. Tx Units Placed at Different Distances

Figure 12 shows the captured image frames, f_{sf}, and the grayscale intensity profiles of the detected data for each $N_{channels}$, L, θ, and SS. The clear and sharp distinction between the data lines can be seen at θ of 20° and 30°, L of 40 and 60 cm, and SS of 200 and 400 µs, respectively [Fig. 12(a)]. Note that in this setup, due to an increasing tilting angle θ, the Tx_1 at L_1 of 130 cm is not visible and the Tx_2 at L of 100 cm is too small to separate the $N_{channel}$ for demodulation, as shown in Fig. 12(c). Therefore, data detection was carried out for L up to 90 cm at θ up to 70° for all values of SS.

Table 3 shows the average f_{sf} of the captured Tx image with respect to L and θ. The f_{sf} for the Tx_2 (closer to the Rx) at a L of 30–40 cm has ~ 2 to 3 times more high-frequency components than the Tx_1 (closer to the Rx) for L of 60–70 cm with respect to θ, as shown in Figs. 9(a)–9(c). In this case, it can be said that the large reduction in the f_{sf} of the Tx image is due to r between the Txs. An increase in r and θ reduces the f_{sf}, which results in higher bit errors and a lower PSNR.

Figures 13(a) and 13(b) illustrate the performance analysis of the angular behavior of the multichannel MIMO–OCC link in terms of the percentage of the success of the received bits and PSNR. In this setup, the average time window for offline OCC data extraction (only) was about 1 s using a predefined data processing algorithm, as shown in Fig. 6. It can be seen that for L and L_1 of up to 60 and 90 cm, a 100% success is achieved for θ of 40° with SS of 200 and 400 µs and for θ of 30° with SS of 800 µs, as shown in Fig. 13(a). As previously mentioned, the
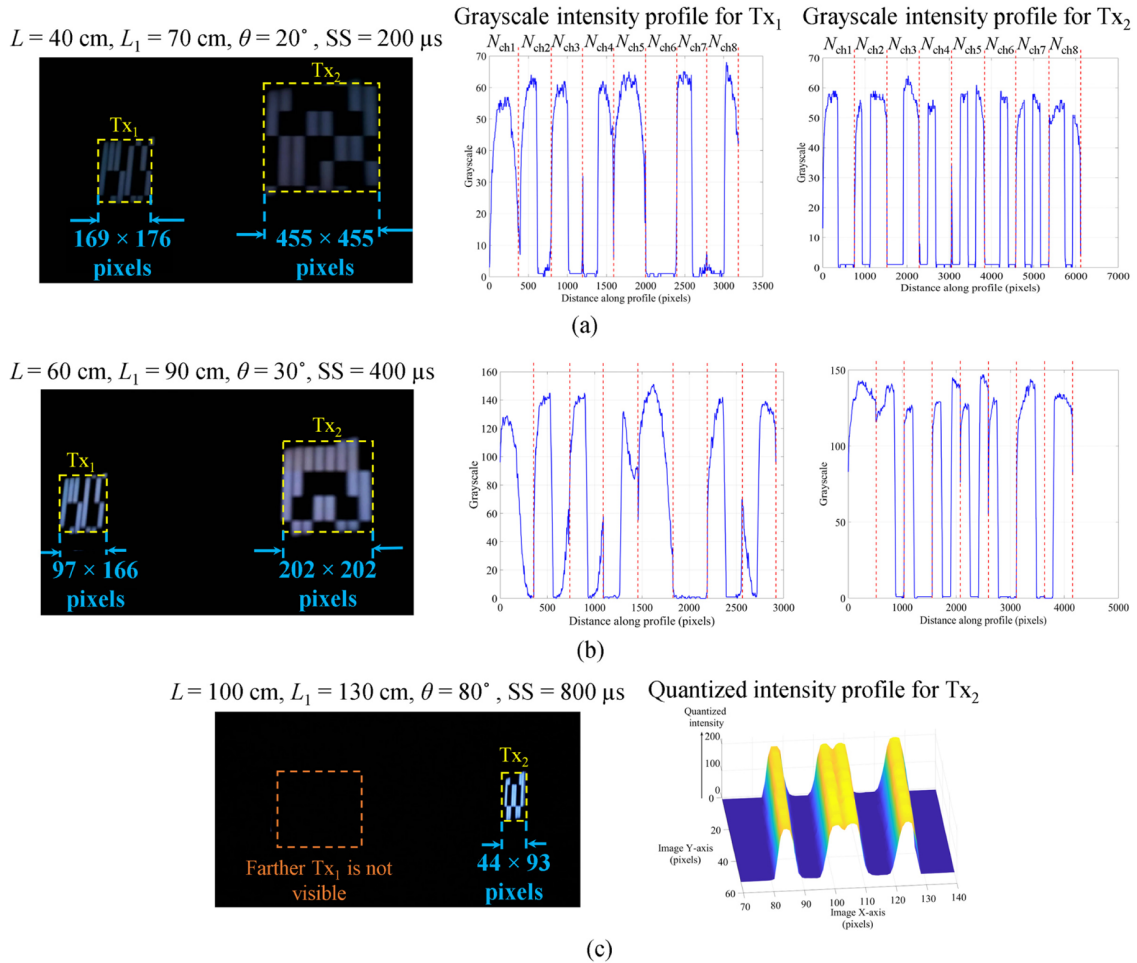
Fig. 12. Grayscale and quantized intensity profiles of originally captured images for data detection at: (a) L of 40 cm, θ of 20°, and SS of 200 μs, (b) L of 60 cm, θ of 30°, and SS of 400 μs, and (c) L of 100 cm, θ of 80°, and SS of 800 μs.

Table 3. Average f_{sf} in Pixels with Respect to Ranges of L and θ (Upper values are for the Tx$_1$ and bottom for the Tx$_2$)

L and L_1 (cm)	θ 0°–20°	θ 30°–50°	θ 60°–70°
60–70	165 × 175	160 × 210	148 × 200
30–40	450 × 451	349 × 351	170 × 289
80–90	210 × 210	190 × 200	125 × 155
50–60	100 × 170	95 × 165	80 × 150
90	100 × 160	70 × 150	56 × 175
120	80 × 155	50 × 140	40 × 100

data reception success is also affected by the f_{sf}. Note that in this setup the Tx$_1$ is placed farther than the Tx$_2$ with respect to the camera. Therefore, with an increasing L and θ, the f_{sf} becomes smaller [f_{sf} is reduced by 80% for θ increasing from 0° to 70° for all values of L, as shown in Table 3 and Fig. 13(b)]. Note that at $L = 100$ cm and $L_1 = 130$ cm, the Tx$_1$ is no longer seen by the camera, as shown in Fig. 12(c). The PSNR of ∼13 dB is measured for a SS of 200 μs, which is increased by 2 and 6 dB for a SS of 400 and 800 μs, as shown in Fig. 13(b), respectively, for L of 90 cm at θ of 70°. The maximum PSNR of 22, 25, and

29 dB are observed for a SS of 200, 400, and 800 μs, respectively, for a L of 30 cm and θ of 0°.

Figure 14 illustrates the data throughput as a function of θ for the proposed multichannel MIMO–OCC system. The data throughput decreases with the f_{sf} due to the increased link span and θ. For θ of 0°, the maximum data throughput of 1.68 kb/s is observed at L of 40 cm, where the 7-bit data stream (3-bit/$N_{channel}$ for Tx$_1$ and 4-bit for Tx$_2$) is visible to the camera. For θ of 30°, the data throughput is reduced by 480 b/s for L of 60 cm, and only a 5-bit data stream (2-bit/$N_{channel}$ for Tx$_1$ and 3-bit for Tx$_2$), as shown in Fig. 12(b), is captured by the camera.

We have shown results for both setups in terms of the success rates of received bits, PSNR, and data throughput (e.g., a 100% success rate with a PSNR of ∼ 14 and 17 dB were achieved for θ of 50°, L of up to 80 cm, and SS of 200 and 400 μs, respectively). Note that in this case, the f_{sf} was reduced by up to ∼50% compared to the f_{sf} obtained in case of Txs without the inclusion of rotation. The maximum data throughputs of 1.9 and 0.9 kb/s were achieved at θ of 0° and 50°, respectively, for a L of up to 60 cm. A higher data throughput of 1.9 kb/s is observed for the transmission setup 1 due to the Tx units being located in the same plane; in the transmission setup 2, however,
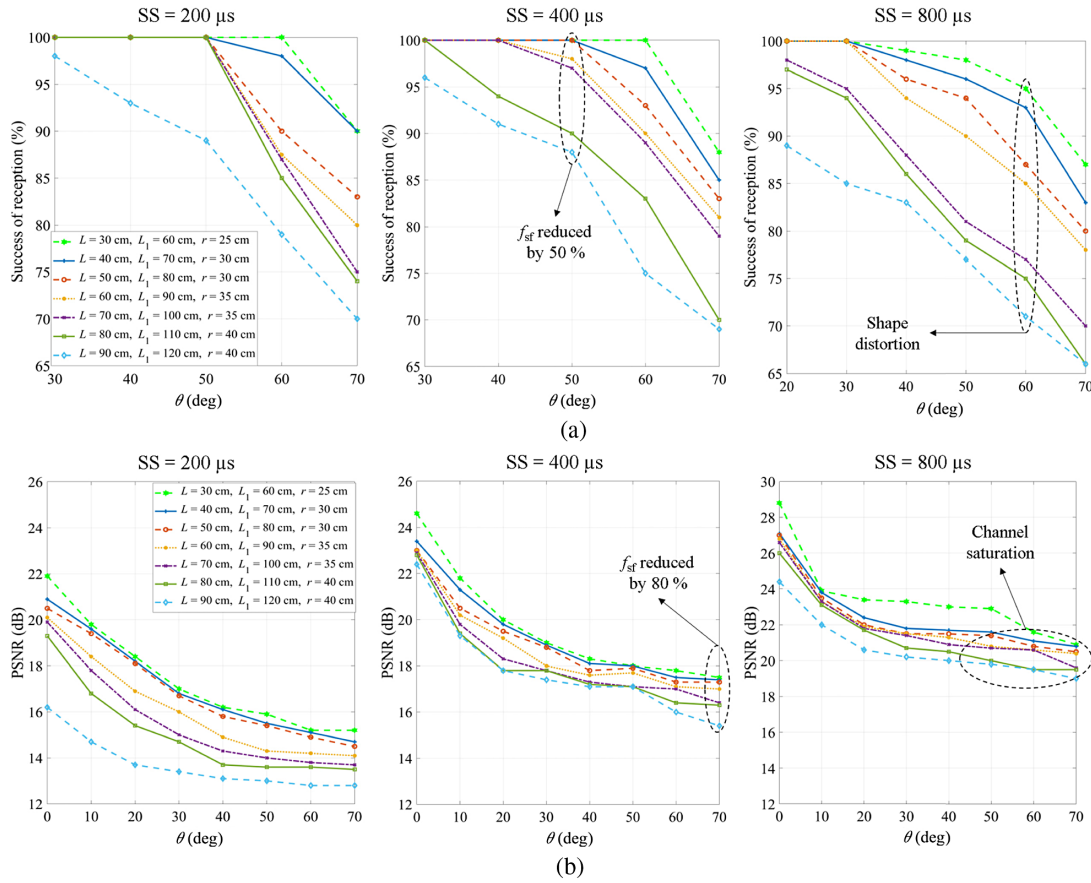
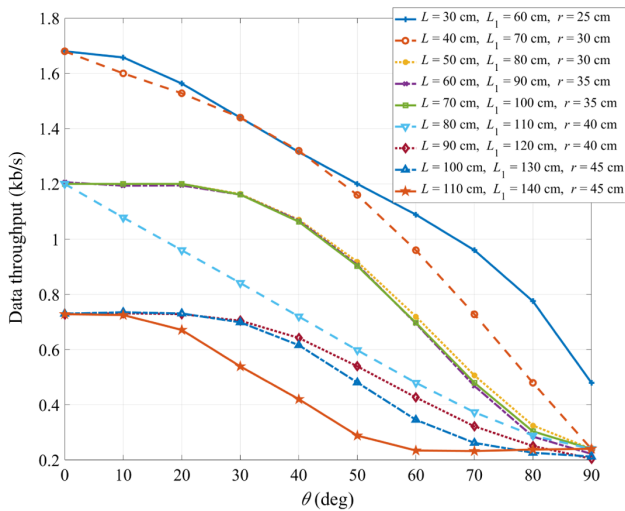**Fig. 13.** Performance analysis: (a) success of reception and (b) PSNR.

Fig. 14. Data throughput with respect to change in L and θ.

the data throughput is reduced to 1.68 kb/s as the Tx units are placed apart from each other at $(L_1 - L)$, as shown in Fig. 7(b). Therefore, the difference in the distances between the Tx units results in a decreased f_{sf}, which leads to a lower $N_{visible}$ and a reduced data throughput.

5. CONCLUSIONS

In this paper, we demonstrated f_{sf}-based angular behavior of multichannel MIMO–OCC for two different transmission setups where the Tx units are placed at different heights and distances from each other and the camera. We showed that the proposed study provided a 100% success rate in data reception at the optimum θ up to 50° for both the transmission setups at lower captured values of f_{sf}, which is projected onto the image sensor in the form of pixels. We provided a general solution based on f_{sf} to investigate the MIMO–OCC considering the angular movement of the Txs. We believe the proposed study can be adopted for longer transmission distances based on f_{sf} and employing a Tx with a larger illuminating surface area for use in indoor environments [e.g., using Txs with surface areas of 14×14 cm^2, L can be extended to 1.6 m (i.e., $2 \times L$) and placing the Tx units at r of 80 cm apart can provide an optimum angle $\theta > 50°$ for each case].

Unlike LOS and NLOS OCC links, the proposed system can be further adopted in indoor IoT-based links with multi-Txs/Rxs and mobility, which offers an improved solution when consideration of the optimum angular orientation of multiple Tx units is critical. Although the small-scale experiments were only conducted for demonstration purposes, it is envisioned that the proposed study can readily be expanded using image processing techniques such as shape restoration using neural

networks and code extraction techniques to improve the success rate of received bits.

Disclosures. The authors declare no conflicts of interest.

REFERENCES

1. M. J. Jang, "15.7 amendment-optical camera communications study group (SG 7a)," IEEE 802.15 WPAN (2020).
2. R. Boubezari, H. Le Minh, Z. Ghassemlooy, and A. Bouridane, "Smartphone camera based visible light communication," J. Lightwave Technol. **34**, 4121–4127 (2016).
3. Z. Ghassemlooy, L. N. Alves, S. Zvanovec, and M.-A. Khalighi, *Visible Light Communications: Theory and Applications* (CRC Press, 2017).
4. IEEE Standard for Local and Metropolitan Area Networks—Part 15.7: Short-range wireless optical communication using visible light, IEEE Standard 802.15.7-2011 (2011).
5. C. Jurado-Verdu, V. Matus, J. Rabadan, V. Guerra, and R. Perez-Jimenez, "Correlation-based receiver for optical camera communications," Opt. Express **27**, 19150–19155 (2019).
6. W. Huang, P. Tian, and Z. Xu, "Design and implementation of a real-time CIM-MIMO optical camera communication system," Opt. Express **24**, 24567–24579 (2016).
7. M. Uysal, C. Capsoni, Z. Ghassemlooy, A. Boucouvalas, and E. Udvary, "Optical camera communications," in *Optical Wireless Communications* (Springer, 2016), pp. 547–568.
8. "IEEE 802.15. Documents TG7r1," 2020, https://mentor.ieee.org/802.15/dcn/15/15-15-0746-01-007a-tg7r1-channel-model-document-for-high-rate-pdcommunications.pdf.
9. Panasonic news release, "Start the business of information collaboration services using the 'Hikari ID' technology," (in Japanese) https://news.panasonic.com/jp/press/data/2015/12/jn151209-3/jn151209-3.html.
10. M. Shahjalal, M. K. Hasan, M. Z. Chowdhury, and Y. M. Jang, "Smartphone camera-based optical wireless communication system: requirements and implementation challenges," Electronics **8**, 913 (2019).
11. S. R. Teli, S. Zvanovec, and Z. Ghassemlooy, "Performance evaluation of neural network assisted motion detection schemes implemented within indoor optical camera based communications," Opt. Express **27**, 24082–24092 (2019).
12. S. R. Teli, V. Matus, S. Zvanovec, R. Perez-Jimenez, S. Vitek, and Z. Ghassemlooy, "Optical camera communications for IoT–rolling-shutter based MIMO scheme with grouped LED array transmitter," Sensors **20**, 3361 (2020).
13. C.-W. Chow, C.-Y. Chen, and S.-H. Chen, "Visible light communication using mobile-phone camera with data rate higher than frame rate," Opt. Express **23**, 26080–26085 (2015).
14. V. P. Rachim and W. Chung, "Multilevel intensity-modulation for rolling shutter-based optical camera communication," IEEE Photon. Technol. Lett. **30**, 903–906 (2018).
15. W. Wang, C. Chow, C. Chen, H. Hsieh, and Y. Chen, "Beacon jointed packet reconstruction scheme for mobile-phone based visible light communications using rolling shutter," IEEE Photon. J. **9**, 1–6 (2017).
16. V. Nguyen, Y. Tang, A. Ashok, M. Gruteser, K. Dana, W. Hu, E. Wengrowski, and N. Mandayam, "High-rate flicker-free screen-camera communication with spatially adaptive embedding," in *35th Annual IEEE International Conference on Computer Communications*, San Francisco, California, USA, 2016, pp. 1–9.
17. K. L. Hsu, Y.-C. Wu, Y.-C. Chuang, C.-W. Chow, Y. Liu, X.-L. Liao, K.-H. Lin, and Y.-Y. Chen, "CMOS camera based visible light communication (VLC) using grayscale value distribution and machine learning algorithm," Opt. Express **28**, 2427–2432 (2020).
18. Y. Yang, J. Hao, and J. Luo, "CeilingTalk: Lightweight indoor broadcast through LED-camera communication," IEEE Trans. Mob. Comput. **16**, 3308–3319 (2017).
19. N. B. Hassan, Z. Ghassemlooy, S. Zvanovec, M. Biagi, A. M. Vegni, M. Zhang, and P. Luo, "Non-line-of-sight MIMO space-time division multiplexing visible light optical camera communications," J. Lightwave Technol. **37**, 2409–2417 (2019).
20. N. B. Hassan, Z. Ghassemlooy, S. Zvanovec, P. Luo, and H. Le-Minh, "Non-line-of-sight $2 \times N$ indoor optical camera communications," Appl. Opt. **57**, B144–B149 (2018).
21. W.-C. Wang, C.-W. Chow, L.-Y. Wei, Y. Liu, and C.-H. Yeh, "Long distance non-line-of-sight (NLOS) visible light signal detection based on rolling-shutter-patterning of mobile-phone camera," Opt. Express **25**, 10103–10108 (2017).
22. W. A. Cahyadi and Y. H. Chung, "Wide receiver orientation using diffuse reflection in camera-based indoor visible light communication," Opt. Commun. **431**, 19–28 (2019).
23. C.-W. Chow, Z.-Q. Li, Y.-C. Chuang, X.-L. Liao, K.-H. Lin, and Y.-Y. Chen, "Decoding CMOS rolling-shutter pattern in translational or rotational motions for VLC," IEEE Photon. J. **11**, 1–5 (2019).
24. Q. N. Pham, V. P. Rachim, J. An, and W.-Y. Chung, "Ambient light rejection using a novel average voltage tracking in visible light communication system," Appl. Sci. **7**, 670 (2017).
25. F. de Souza Campos, J. A. C. Ulson, J. W. Swart, M. J. Deen, O. Marinov, and D. Karam, "Temporal noise analysis and measurements of CMOS active pixel sensor operating in time domain," in *26th Symposium on Integrated Circuits and Systems Design (SBCCI)*, Curitiba, Brazil, 2013, pp. 1–5.
26. Q. Wang, Y. Shen, and J. Jin, "Performance evaluation of image fusion techniques," in *Image Fusion* (Academic, 2008), pp. 469–492.
27. J. Price and T. Goble, "Signals and noise," in *Telecommunications Engineer's Reference Book*, F. Mazda, ed. (Butterworth-Heinemann, 1993), pp. 1–15.
28. P. Burgess, "WS2812B: Intelligent control LED integrated light source," in Adafruit NeoPixel Uberguide, https://cdn-shop.adafruit.com/datasheets/WS2812B.pdf.
29. M. D. Thieu, T. L. Pham, T. Nguyen, and Y. M. Jang, "Optical-RoI-signaling for vehicular communications," IEEE Access **7**, 69873–69891 (2019).
30. C. Xiu and R. Wang, "Hybrid tracking based on camshift and template matching, in *29th Chinese Control and Decision Conference (CCDC)*, Chongqing, China, 2017, pp. 5753–5756.
31. *Visible Light Communication, Shlomi Arnon, ed.* (Cambridge University, 2015).
32. Atmel Corporation, "8-bit Microcontroller with 4/8/16/32K bytes in-system programmable flash," (2009), https://www.sparkfun.com/datasheets/Components/SMD/ATMega328.pdf.
33. Sony Corporation, "IMX219PQH5-C Datasheet," 2020, https://datasheetspdf.com/pdf/1404029/Sony/IMX219PQH5-C/1.

4.3 Optical camera communications link using an LED-coupled illuminating optical fiber

This chapter is a version of the published manuscript:

Connection to my Ph.D. thesis:

Motivated by a new and emerging fiber-optic lighting technology as an alternative to discrete illumination fixtures and semi-discrete LED stripes, a novel wireless communications link using an illuminating optical fiber as a Tx in OCC for the IoT is proposed and demonstrated. We demonstrate an indoor proof-of-concept system using an illuminating plastic optical fiber coupled with a light-emitting diode and a commercial camera as the Tx and the Rx, respectively. For the first time, to the best of our knowledge, we experimentally demonstrate such technology showing flicker-free wireless transmission within the off-axis camera rotation angle θ of 0–45° and the modulation frequencies of 300 and 500 Hz. This transmission setup resembles the indoor dynamic, mobility, and multicasting scenarios for transmission of low R_b information. We also show that a reception success rate of 100% is achieved for the camera exposure and gain of 200 μs and 25 dB, respectively.

Optics Letters

Optical camera communications link using an LED-coupled illuminating optical fiber

Shivani Rajendra Teli,[1,*] **Klara Eollosova,**[1] **Stanislav Zvanovec,**[1]
Zabih Ghassemlooy,[2] **and Matej Komanec**[1]

[1]*Faculty of Electrical Engineering, Czech Technical University in Prague, Prague, Czech Republic*
[2]*Optical Communication Research Group, Faculty of Engineering and Environment, Northumbria University, Newcastle, UK*
*Corresponding author: telishiv@fel.cvut.cz

In this Letter, we propose and demonstrate a novel wireless communications link using an illuminating optical fiber as a transmitter (Tx) in optical camera communications. We demonstrate an indoor proof-of-concept system using an illuminating plastic optical fiber coupled with a light-emitting diode and a commercial camera as the Tx and the receiver, respectively. For the first time, to the best of our knowledge, we experimentally demonstrate flicker-free wireless transmission within the off-axis camera rotation angle range of 0–45° and the modulation frequencies of 300 and 500 Hz. We also show that a reception success rate of 100% is achieved for the camera exposure and gain of 200 μs and 25 dB, respectively. © 2021 Optical Society of America

Optical camera communications (OCC) and visible light communications (VLC) utilizing light-emitting diodes (LEDs) as a transmitter (Tx) and photodetectors (PDs)/cameras as a receiver (Rx), respectively, offer functionalities of vision, data communications, and localization, which can be used in many Internet of things (IoT) applications [1,2]. The major advantages of using a complementary metal-oxide semiconductor (CMOS)-based camera Rx are (i) availability and advancements of smartphones and surveillance cameras in indoor environments such as shopping malls, hospitals, and offices; (ii) a higher signal-to-noise ratio due to longer exposure time t_F and larger size photosensitive area which helps to increase the transmission distance d; and (iii) the rolling shutter (RS) property of a CMOS-based camera, which integrates light in a row-by-row manner similar to a scanning function. Therefore, the RS-based camera offers data rates R_b higher than the frame rate f_R of the camera [3].

Fiber-optic lighting is emerging as an alternative to discrete illumination fixtures and semi-discrete LED stripes [4–6]. Typically, plastic optical fibers (POFs) are used for illumination [6] due to their low cost and easy light coupling using high-power light sources such as xenon or halogen lamps and LEDs [7,8]. Recently, a silica-based fiber-optic illuminator has emerged, which uses laser light sources due to their small diameters [9]. These illuminating optical fibers, which are easy to bend, can be used for illumination in a range of applications such as IoT, interior designs, shopping centers, aircrafts, fashion,

health, and safety. These applications thrive on the fiber's low cost (especially in the case of POFs), low weight, easy bending, and mechanical properties. Moreover, it can support low data rate (i.e., few bits/second to kbits/second) indoor OCC-based IoT applications [2]. In this Letter, we introduce a novel concept of OCC that uses an illuminating POF as the Tx, termed as illuminating optical fiber-based OCC (OF-OCC). The intensity modulated (IM) white LED is used to couple the light into the illuminating POF, which basically acts as a long length optical antenna for illumination, data communications, indoor localization, and sensing.

A camera-based Rx is used to capture the length d_f of the illuminating POF for extracting data information. We consider the impact of the off-axis angular orientation θ of the camera on data capturing and detection over d_f. This transmission setup resembles the indoor dynamic, mobility, and multicasting scenarios for transmission of low R_b information. The lab-scale measurements are carried out in two sections: (i) optical and electrical characterization of the LED measured directly and LED-coupled POF as a radiating Tx; and (ii) data capturing considering θ of the camera-based Rx. We analyze the quality of the captured data in terms of the success rate of received bits for a range of θ with respect to t_F and the camera gain G_v. The proposed OF-OCC scheme, to the best of our knowledge, is the first experimental-based study on an OCC link using a LED-coupled illuminating POF.

We have used a 1 m long polymethyl methacrylate (PMMA) POF with a 3.6 dB/m attenuation (measured by the cutback technique). The core and cladding diameters were 1.6 and 2 mm, respectively [see the measured real dimensions in Fig. 1(a)], a core refractive index of 1.46, and a numerical aperture of ~ 0.50. Both ends of the POF were cut and polished. Light from a cold white LED (LA CW20WP6, Light Avenue) of a size 500×500 μm^2 was directly coupled from one end of the POF using a 5D stage (3D micromovement stage Thorlabs, MAX313D/M with pitch and yaw tilt platform Thorlabs, APY002/M). The light from the other end of the POF was captured using a silica PD and power meter (Thorlabs, S121C, wavelength range of 400–1100 nm) for monitoring of LED-coupling performance.

At first, we optimize the coupling of light from the LED to the POF by monitoring the optical power level at the end of the
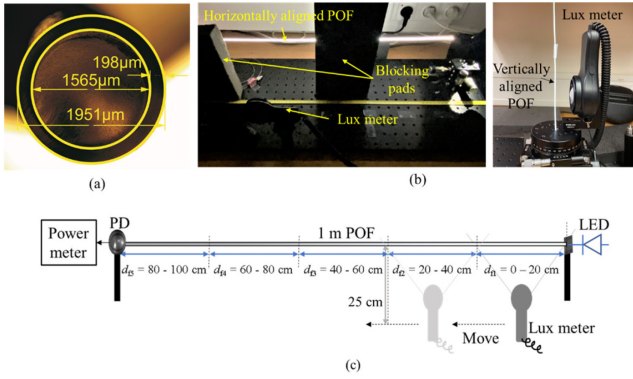
Fig. 1. (a) Microscope photograph of the used PMMA POF with measured core and cladding dimensions, including the cladding thickness, (b) experimental setup for POF characterization of L-I-V and illumination pattern, and (c) characterization over d_f.
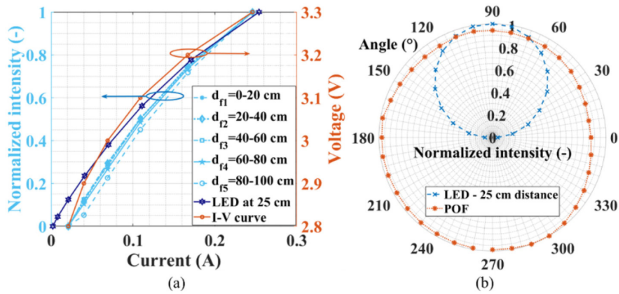

Fig. 2. POF and LED characterization: (a) L-I-V curves over d_f and (b) radiation pattern.

POF, which was about 11 dBm for the LED at its maximum current. Based on the POF attenuation, which was measured by the cutback technique to be 3.6 dB/m, and the LED total output power of 19 dBm, the coupling efficiency was estimated to be close to 40%. Figures 1(b) and 1(c) show the experimental setups for measuring (i) optical power–current–voltage (L-I-V)

characteristics using a lux meter (Voltcraft MS-200LED, $\pm 3\%$ accuracy); and (ii) the radiation profile of the POF. Next, the lux meter at 25 cm from the POF was used to measure the power profiles along the POF, which is split into segments of 20 cm long ($d_{f1} - d_{f5} = (0:20:100)$ cm) starting from the LED coupling, as illustrated in Fig. 1(c).

Figure 2(a) depicts the measured L-I-V characteristics of the illuminating POF for a range of d_f. Also shown is the L-I-V plot of the LED measured directly at a distance of 25 cm which depicts similar optical characteristics to those of commonly used LED sources in VLC systems. Note (i) the drop in the illumination level with respect to the increasing d_f; as expected; and (ii) linear L-I plots, i.e., a wide dynamic range and thus a higher signal-to-noise ratio, which is highly desirable in IM-VLC systems.

The optical radiation pattern of the POF was measured to obtain the spatial intensity distribution over 360° to illustrate radiation uniformity as depicted in Fig. 2(b). Note that the illuminating pattern represents a closed hemisphere with a slight deviation of $\sim 10\%$ from the maximum normalized intensity for angles of $+30$ to $-30°$. This small variation is due to possible fiber bending, random tensions, and contractions over the POF length. Also shown is the radiation profile for the LED measured at a distance of 25 cm, which represents a complete hemisphere (i.e., very close to a Lambertian emitter with the order of 1).

The aim of the proposed scheme is to investigate an OF-OCC system using the illuminating POF as the Tx and a camera as the Rx; see Fig. 3(a). A non-return-to-zero (NRZ) on-off-keying data format (most commonly used in OCC) generated in MATLAB and uploaded to an arbitrary waveform generator (AWG Rohde & Schwarz HMF2550 50 MHz) is used for IM of the LED (biased at I_b of 300 mA) via the bias-T (BT-A11). The IM light is coupled into the POF. During all experiments, the LED was covered by a black shield in order to capture only the signal from the illuminating POF. Table 1 shows all the key experimental parameters adopted in this Letter.

A CMOS RS-based camera positioned at the center of the POF at the radial distance d_r of 50 cm and with a total rotation
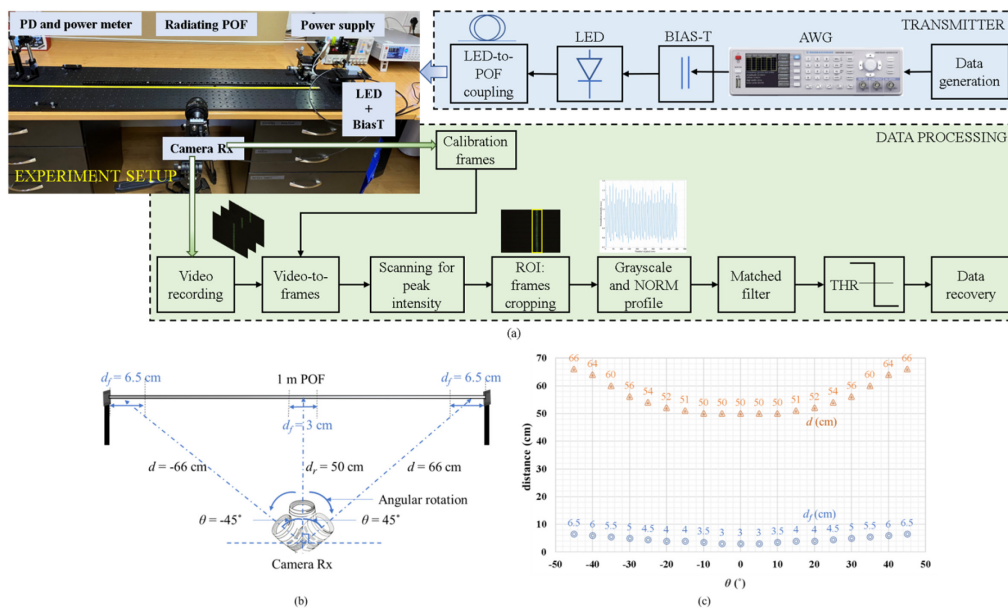

Fig. 3. OCC over POF: (a) data reception flowchart, (b) schematic of data capturing, and (c) variation of d and d_f with respect to θ.

Table 1. Key Experimental Parameters

Parameter	Value
LED bias current I_b and supply voltage	300 mA and 3.3 V
Bias-T	BT-A11
Rx	IC capture USB 2.0 camera
Resolution	648×484 pixels
f_R	25 fps
t_F	200, 400 µs
G_v	25, 20, 15 dB
d_r (radial distance)	50 cm (from center of POF)
d (center-to-ends of POF)	66 cm (center-to-ends of POF)
f_s (modulation frequency)	300, 500 Hz
θ	$-45° > 0° > 45°$
Data packet size	6 b/packet [110010]

angle θ of $\pm 45°$ [see Fig. 3(b)] captures the IM illumination. Note that the actual transmission distances d and d_f vary with θ; see Fig. 3(c). Note that all the measurements are performed in indoor ambient light conditions. The camera set to capture in RS mode sequentially integrates all illuminated pixels at the exposure time, which is the same as scanning [10,11]. In RS-based cameras, the readout time ensures that there is no overlapping of the rows of pixels, thus allowing multiple exposures of a single captured image. This feature offers simultaneous capturing of multiple incoming light states in a single frame, as each row is exposed once to the light as well as flicker-free operation [10,11]. Consider that the illuminating intensity of the POF is low and reduces further with d_f [see Fig. 2(a)]; for the camera, we used t_F of 200 and 400 µs and G_v of 15, 20, and 25 dB. The OCC data processing was performed using traditional image processing techniques. Both the recorded data and calibration video streams containing the captured signal and the POF template shape and intensity compensation, respectively, are

divided into image frames prior to frame-by-frame processing to decode the received data. Following frame division, peak intensity scanning is performed to locate the captured POF in the image frame and calculate the region-of-interest (ROI) to obtain the coordinates [see Fig. 3(a)], which define the ROI boundaries of a full captured frame [12]. Next, the ROI cropped images are converted from RGB to grayscale to retrieve the intensity profile. Finally, the transmitted data stream is regenerated using matched filtering, thresholding, and binarization of the data frames by converting them into a vector transformation.

The current proof-of-concept experiments were performed under the ambient light, where we measured the background light intensity of 150 lx (± 3 lx) from the ceiling lamps. The measurements were carried out for d, t_F, θ, and G_v; see Table 1. The data packet of 6 bits [110010] was generated and transmitted at f_s of 300 and 500 Hz using a repeat packet strategy to improve the link performance. Figure 4 shows the examples of captured image frames and their normalized and quantized intensity profiles. The intensity profiles play an important role in determining the higher and lower intensities representing 1 and 0 bits in the received image frames for further thresholding and demodulation. It can be seen that the intensity profile improves with increasing G_v, which enhances signal amplification while passing through the camera analog-to-digital converter (ADC) prior to being focused on the image sensor (IS) [3]. This is due to the fact that G_v presents the software-defined global gain of both the IS and the column amplifier block, which is given as G_v (dB) $= 20 \log_{10}[V_{ADC}/V_{pixels}]$, where V_{ADC} is the voltage value, which is sampled by the ADC, and V_{pixles} is the voltage obtained from the pixel integration of light during the exposure time. Therefore, higher G_v mitigates the influence of ambient light on the integrity of data reception; and reducing t_F. Also captured are the intensity profiles having an interferometric shape due to the ambient light, which is captured together with the light from the illuminating POF.
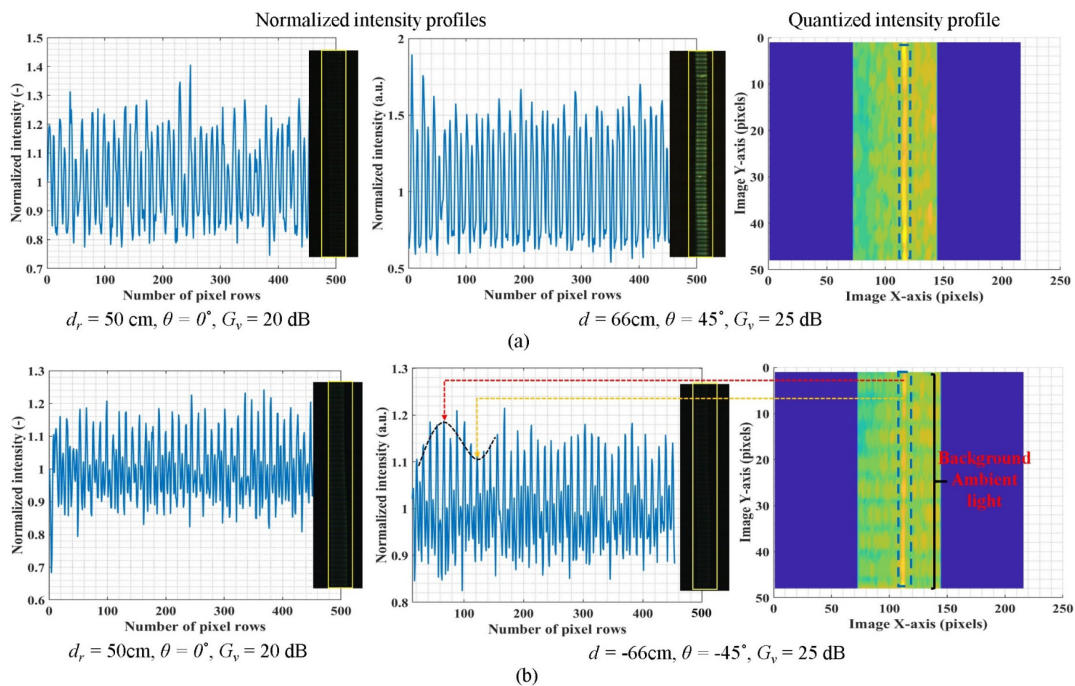

Fig. 4. Examples of captured illuminating POF at (a) $f_s = 300$ Hz and $t_F = 200$ µs, and (b) $f_s = 500$ Hz and $t_F = 400$ µs. The yellow and red arrows highlight the intensity variations due to background ambient light.
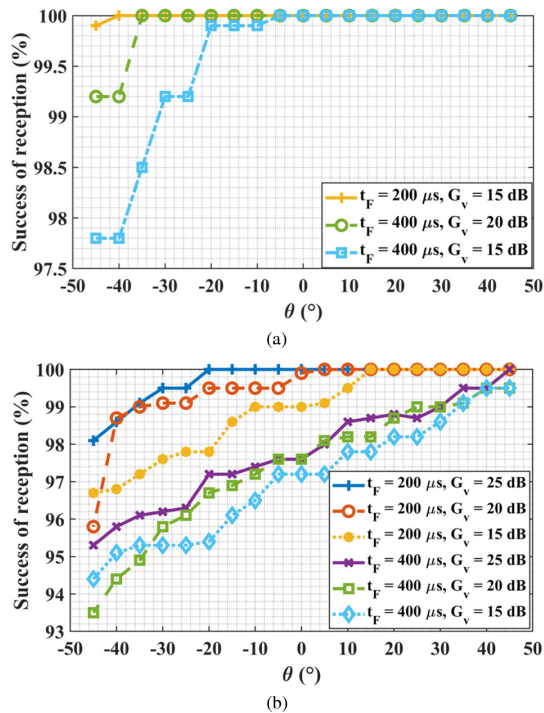
Fig. 5.   Performance of OF-OCC: the success of reception with respect to θ for f_s of (a) 300 and (b) 500 Hz.

At θ of 0° and 45°, 21–36, and 23–39, repeated data packets were captured in every image frame at f_s of 300 and 500 Hz, respectively. Considering that only a small number of bits is transmitted, the OCC link performance is analyzed in terms of the reception success, which is defined as the ratio of incorrectly decoded bits to the total number of transmitted bits. Figure 5 shows the performance of the proposed the OF-OCC link in terms of the reception success rate. It can be seen from Fig. 5(a) that, for f_s of 300 Hz (i) 100% (i.e., error-free transmission) reception success rates are achieved at θ of −40°, −35°, and −5° for t_F of 200 and 400 μs and G_v of 15 and 25 dB, respectively; and (ii) the reception success rates decrease below the θ values mentioned in (i) (i.e., near the end of the POF) with the lowest value of 97 % at t_F of 400 μs and G_v of 15 dB. For f_s of 500 Hz, the reception success rates of > 93% are achieved for $\theta > -45°$ for all values of t_F and G_v, which has increased to > 97% when closer to the LED; see Fig. 5(b). Note that the performance of the OCC link improves when the camera is closer to the LED regardless of θ and d. This is due to the increasing illumination levels as seen from the $L\text{-}I\text{-}V$ characteristics in Fig. 2(a) and the intensity profiles in Fig. 4.

In this Letter, we proposed and experimentally demonstrated a novel concept of the OCC system using an illuminating POF as the Tx and a camera as the Rx. We evaluated the proposed OF-OCC system for range of camera orientation angles and showed that, despite the small diameter of POF, flicker-free transmission with 100% reception success rates was possible. It is envisioned that the proposed study can be further expanded by increasing d and f_s and by optimizing G_v and t_F to overcome the noise effect in different environments and thereby improve the reception success rates, which was not the focus of this Letter. This first proof-of-concept result paves the way for new OF-OCC systems capable of transmitting low data rate information as part of IoT in smart environments.

Disclosures.   The authors declare no conflicts of interest.

Data Availability.   Data underlying the results presented in this paper are not publicly available at this time but may be obtained from the authors upon reasonable request.

REFERENCES

1. H. Aksu, L. Babun, M. Conti, G. Tolomei, and A. S. Uluagac, IEEE Commun. Mag. **56**(11), 138 (2018).
2. S. R. Teli, S. Zvanovec, and Z. Ghassemlooy, *IEEE International Conference on Internet of Things and Intelligence System (IOTAIS)*, Bali, Indonesia, 2018, pp. 40–45.
3. T. Le, N. Le, and Y. M. Jang, *International Conference on Information and Communication Technology Convergence (ICTC)*, Jeju, South Korea, 2015, pp. 124–128.
4. V. Guerra, C. Guerra, J. Rabadan, R. Perez-Jimenez, and B. Ortega, in *12th International Symposium on Communication Systems, Networks and Digital Signal Processing (CSNDSP)* (IEEE, 2020).
5. D. Křemenáková, J. Militký, B. Meryová, and V. Lédl, World J. Eng. **10**, 223 (2013).
6. J. Huang, D. Křemenáková, J. Militký, and G. Zhu, Autex Res. J. **15**, 13 (2015).
7. J. Yang, Z. Liu, B. Xue, Z. Liao, L. Feng, N. Zhang, J. Wang, and J. Li, IEEE Photonics J. **10**, 1 (2018).
8. Y. Wang, S. Su, G. Zhang, G. Sun, J. Zhang, J. Wang, and Y. Ren, Proc. SPIE **10847**, 108470J (2018).
9. W. S. Klubben, S. L. Logunov, E. J. Fewkes, J. Mooney, P. M. Then, P. G. Wigley, H. Schreiber, K. Matias, C. J. Wilson, and M. Ocampo, Proc. SPIE **9702**, 970218 (2016).
10. T. Kuroda, *Essential Principles of Image Sensors* (2017).
11. S. R. Teli, S. Zvanovec, R. Perez-Jimenez, and Z. Ghassemlooy, Appl. Opt. **59**, 10357 (2020).
12. A. Duque, R. Stanica, H. Rivano, and A. Desportes, Comput. Commun. **160**, 52 (2020).

63

4.4 Performance evaluation of neural network assisted motion detection schemes implemented within indoor optical camera based communications

This chapter is a version of the published manuscript:

Connection to my Ph.D. thesis:

Most optical links suffer from the data loss and delay due to the optical shadowing caused by the users in indoor environments. Therefore, we have developed a NN assisted MD system to track and detect the user motion over the mobile phone camera Rx-based OCC link. It can be used to perform a relatively basic control of present or future smart devices in IoT environments such as OCC-based smart homes where the device control via MD can aptly be facilitated. To evaluate the proposed scheme, we have carried out an experimental investigation of a static indoor downlink OCC employing a mobile phone front camera as the Rx and an 8×8 RGB LED array (the same as Tx array from the previous studies in Section 4.1 and Section 4.2). Note, the Tx array in this study is used without grouping grid and diffuser in order to analyze the performance of each RGB LED as a point source in an array using GS mode of the camera Rx. The captured motion was applied to the NN and evaluated for a number of NN assisted MD schemes. The results demonstrated that the best performance was achieved using Resilient Backpropagation NN algorithm with the fastest convergence at a minimum error MSE and processing time of 10^{-5} and 0.67 s, respectively as well as the percentage of success for MD of 100 % up to a 1.6 m OCC link.

Performance evaluation of neural network assisted motion detection schemes implemented within indoor optical camera based communications

SHIVANI RAJENDRA TELI,[1,*] STANISLAV ZVANOVEC,[1] AND ZABIH GHASSEMLOOY[2]

[1]*Dept. of Electromagnetic Field, Faculty of Electrical Engineering, Czech Technical University in Prague, Prague, 16627, Czech Republic*
[2]*Optical Communications Research Group, Faculty of Engineering and Environment, Northumbria University, Newcastle-upon-Tyne, NE1 8ST, UK*
*telishiv@fel.cvut.cz

Abstract: This paper investigates the performance of the neural network (NN) assisted motion detection (MD) over an indoor optical camera communication (OCC) link. The proposed study is based on the performance evaluation of various NN training algorithms, which provide efficient and reliable MD functionality along with vision, illumination, data communications and sensing in indoor OCC. To evaluate the proposed scheme, we have carried out an experimental investigation of a static indoor downlink OCC link employing a mobile phone front camera as the receiver and an 8×8 red, green and blue light-emitting diodes array as the transmitter. In addition to data transmission, MD is achieved using a camera to observe user's finger movement in the form of centroids via the OCC link. The captured motion is applied to the NN and is evaluated for a number of MD schemes. The results show that, resilient backpropagation based NN offers the fastest convergence with a minimum error of 10^{-5} within the processing time window of 0.67 s and a success probability of 100 % for MD compared to other algorithms. We demonstrate that, the proposed system with motion offers a bit error rate which is below the forward error correction limit of 3.8×10^{-3}, over a transmission distance of 1.17 m.

1. Introduction

The optical wireless communications (OWC) technology covering ultraviolet, infrared and visible bands is a complementary technology to the dominated radio frequency (RF) based wireless systems that could be used for addressing the bandwidth bottleneck is a possible option for Internet of things (IoT) [1, 2]. The visible spectrum band (i.e., 370-780 nm) known as visible light communications (VLC) is being considered as a possible option in 5th generation (5G) wireless networks for indoor environments. VLC utilizing the light-emitting diodes (LEDs) based lighting fixture offers four independent functionalities of data communications, illumination, localization and sensing in indoor environments [3, 4]. In addition, VLC can offer massive MIMO (multiple in multiple output) capabilities using LED and photodetector (PD) arrays for IoT applications in both indoor and outdoor environments [5]. This feature of VLC is unique compared to massive MIMO in RF-based systems, which is too complex to implement.

The wide spread use of smartphones (six billion of them) with high-spec cameras are opening up new possibilities for VLC in applications where the need for high-data rate [6, 7]. Such applications include indoor localization, sensing, intelligent transportation systems, shopping areas, etc. The camera-based VLC, also termed as optical camera communications (OCC), has been studied within the framework of OWC and considered as part of the IEEE 802.15.7rl standard [8, 9]. OCC utilizes the built-in complementary metal-oxide-semiconductor camera

in smart devices as the receiver (Rx) for capturing two-dimensional data in the form of image sequences, thus enabling multidimensional data transmission. OCC with multiple functionalities of vision, data communications, localization and motion detection (MD) [8–10] can be used in all-optical IoT (OIoT) [5] based network application including device-to-device communications, mobile atto-cells, vehicle-to-everything (V2X), smart environments (home, office, surveillance), etc. [11]. In smart environments (i.e., home and offices) OOC-based MD can be utilized to effectively control smart devices [10, 12, 13]. This is very convenient and cost-effective as users carry smartphones with inbuilt cameras, which can be used as a Rx for both OCC and MD compared with other user interface methods such as gesture control (using a single webcam) and an infrared 3D camera for PC [14, 15]. MD based schemes such as (i) Li-Tech - shape detection and 3-D monitoring using visible light sensors [16]; (ii) Li-Sense - offering data communication and fine-grained, real-time human skeleton reconstruction using VL, which utilizes the shadowing effect and 324 PDs [17]; and (iii) a number of gesture recognition schemes [14, 15] have been proposed.

In OCC, image processing is critical for retrieving the transmitted data from the captured image frames. In recent years, intelligent machine-learning techniques (i.e., neural networks (NN)) have been adopted in image recognition for identifying objects' shape in the image, transcribing speech into a text, matching classified items and predicting the relevant results from network training [18]. In NN-based feature recognition schemes, multiple hidden layers with artificial neurons are used to train the network. These artificial neurons represent the main constituent, which receives multiple input samples in order to train the NN.

In [12] first reported by the authors, the initial results of MD performance based on images and centroid data samples (i.e., both considered as the input to NN representing the motion) using the variable learning rate backpropagation algorithm for training. The results in [12] demonstrate that, NN trained with centroid data samples performs only 5000 iterations in a time window of up to 4 s while the conventional NN trained using images can perform up to 8138 iterations in a time window of up to 9 s. Even though [12] provides a promising approach for MD, such long time windows could not be applied in real-time cases. Since the time windows have been obtained using a basic backpropagation algorithm, it is necessary to further perform more detailed analyzes of the proposed scheme based on the centroid data samples and using different transfer function-based algorithms for NN in order to reduce the time window and a number of iterations. In this paper, the focus is on the experimental investigation of NN-based MD for OCC performance using a number of transfer function-based training algorithms. In doing so, we include a wide scale of training parameters including the processing time (PT), iterations carried out by NN for MD, the percentage of success for MD and mean squared error (MSE). Unlike conventional NN schemes [18], the proposed NN-based MD is trained with centroid data samples and different transfer function algorithms, thus providing more accurate detection. In this work, experimental investigations are conducted for an indoor static downlink OCC with a smartphone front camera used as the Rx. The NN training is performed using eight different transfer function-based training algorithms for MD over the transmission distance L of up to 2 m. The OCC link quality in terms of the bit error rate (BER) and peak signal-to-noise ratio performance (PSNR) with respect to L is also analyzed simultaneously. The proposed NN-based MD can be used for control of data communications in OIoT networks.

The rest of the paper is structured as follows: Section 2 provides details of the proposed NN based MD in OCC. Experiment results are discussed in Section 3. Conclusions are drawn in Section 4.

2. Proposed NN based MD in OCC

2.1. System overview

Figure 1(a) illustrates the system overview of the proposed OCC-based NN assisted MD in an indoor environment. A data packet generation output, which is in a 12.8 kbits non-return-to-zero (NRZ) on-off keying (OOK) format, is first mapped according to the addresses of 8×8 red, green and blue (RGB) Neo pixel LED array using an Arduino Uno board (an open source microcontroller board based on the ATmega328 [19]). The intensity modulated (IM) light signal is transmitted over the free space channel. On the Rx side, an Android smartphone's front camera with the frame rate of 30 frames per second (fps) and a resolution of 1920×1080 pixels is used to capture the images (i.e., a video stream) of the IM LED array. In this work, the mobile phone is assumed to be located in a static position directly beneath the LED transmitter (Tx) at a height of 20 to 200 cm.
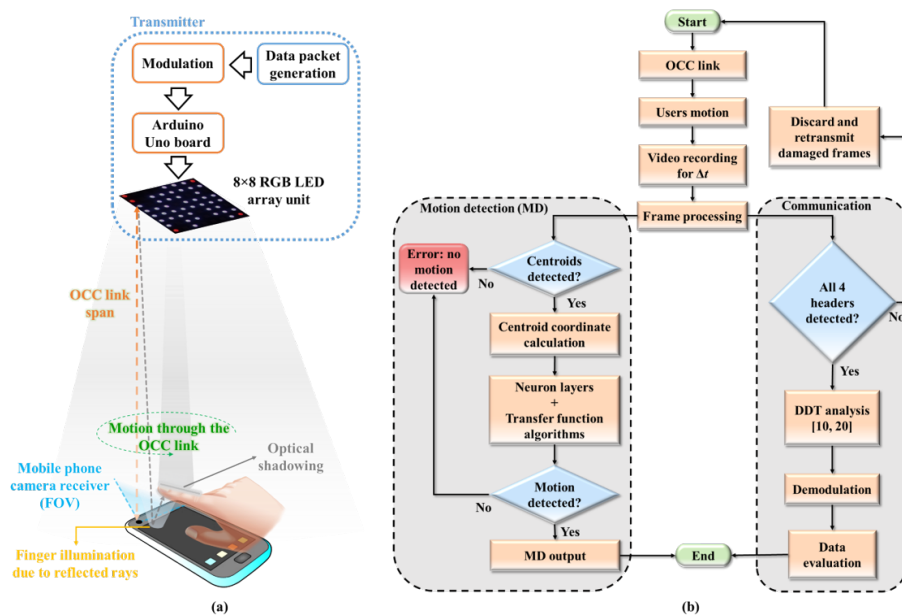
Fig. 1. System overview: (a) proposed NN assisted MD in OCC, and (b) a flowchart of MD and communication analysis.

Figure 1(b) shows the flowchart of MD and communication analysis on the Rx side. Note, motion is achieved by the user's finger moving over the camera. Both the RGB LEDs and finger movement are simultaneously captured by the camera in the form of a video stream, which is then divided into frames for post-image processing using MATLAB. Typically, the recorded video length depends on the motion duration Δt with the mean and maximum values of ~ 2.5 s and 4.5 s, respectively. For a camera, with a frame rate of 30 fps the captured frames of 75 and 135 are for Δt of 2.5 s and 4.5 s, respectively. As shown in Fig. 1(a), the user's finger hovering a few centimeters above the camera's screen will result in shadowing and reflected light rays. Note that, the illuminated finger is readily traceable by the camera using a tracking function, and its motion is expressed as centroids, which represent the center of a moving finger in the form of consecutive coordinate points [20], see Fig. 2. Note, in Fig. 2, each coordinate point represents the center of a moving finger tracked in a particular time frame. The key principle of MD is to compare the changes between the frames (a series of images) following video processing. The frame resolution is measured in terms of the pixels and inter-frame time, which is 33.3 ms (1 s/30 fps).

The motion between two consecutive frames can be simply determined as the difference between the centroid coordinates $(x_2 - x_1, y_2 - y_1)$ in $(N + 1)^{th}$ and N^{th} frame. The coordinate position of motion centroid (MC), which is obtained from the user's finger movement, is applied to a pre-trained NN system for detection and identification of user's motions. For the demonstration purpose, we consider five motion patterns, which are created from two simple natural motions in a straight, circular and curvature lines. These motions can be used to control smart devices, e.g., straight and circular motions can be used for turning ON and OFF of a device.
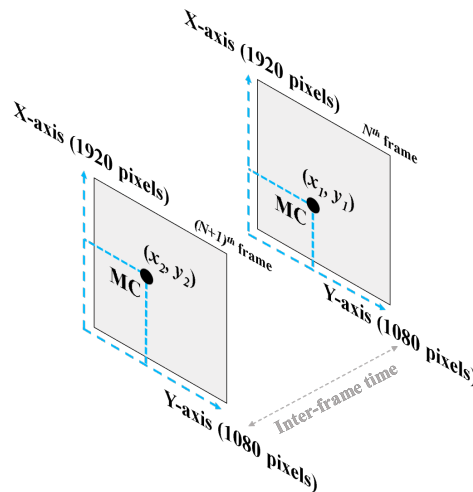
Fig. 2. Example of MC detection in two frames.

2.2. Data compensation scheme

We have adopted a transmit data compensation scheme based on the anchor LEDs (four per frame) and a synchronization LED for time synchronization, which is located in the first frame as in [12], in order to overcome blocking or shadowing due to mobility as depicted in Fig. 3(a). The data compensation scheme is based on discarding damaged frames due to the blocking of the anchor LEDs and requesting re-transmission. Note that, obstacles may fully/partially block one or more anchor LEDs, thus resulting in damaged frames, see Fig. 3(b), which will lead to increased BERs. The use of anchor LEDs (i.e., four-bit per frame in this case) results in reduced data throughput per frame, thus the trade-off between the BER and the data throughput.
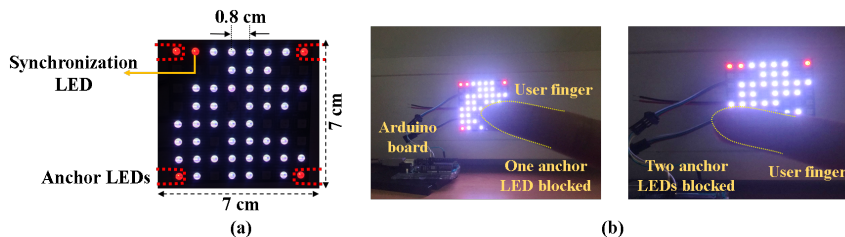

Fig. 3. (a) Transmitter configuration and (b) damaged frames due to blocking of one and two anchor LEDs.

For the proposed scheme with the transmit data compensation scheme, the data rate can be

given as:

$$R_d = N_L \times L_{\text{FR}} - N_A, \tag{1}$$

where N_L and N_A denote the number of data transmission, and anchors plus synchronization LEDs, respectively and L_{FR} is the flickering rate of LEDs (20 pulses per second in this work). For the proposed system, the maximum achievable R_d is 1.199 kbps (i.e., $64 \times 20 - 81$). Note, if the number of anchor LEDs is reduced the data throughput will slightly increase. E.g., for the anchor LEDs of 3, 2 and 1, the data rates are 1.219 kbps, 1.239 kbps and 1.259 kbps, respectively.
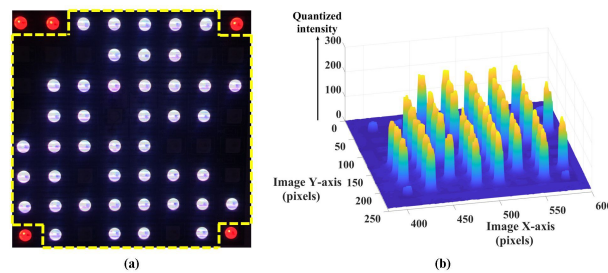
Fig. 4. (a) Identified data area excluding anchor and synchronization bits and (b) quantized intensity of the detected data.

For the proposed OCC-based scheme, we have adopted an efficient detection scheme of differential detection threshold (DDT) [10,21]. In the DDT scheme, the threshold level is defined in terms of the quantized intensity level within the range of [0-255]. Figure 4(a) represents the identified data area within the frame, while Fig. 4(b) provides the quantized intensity of the detected data. Based on DDT the initial value of threshold level was set to 181 level of quantized intensity as in [10, 21]. Note, the threshold level can be adaptively set based on the intensity levels in the image frame.

2.3.   NN-based MD for OCC

The proposed scheme can be trained using the transfer function algorithms in order to improve the MD performance by identifying only the predefined motions. Figure 5 illustrates the NN structure for MD performance evaluation within the context of OCC.
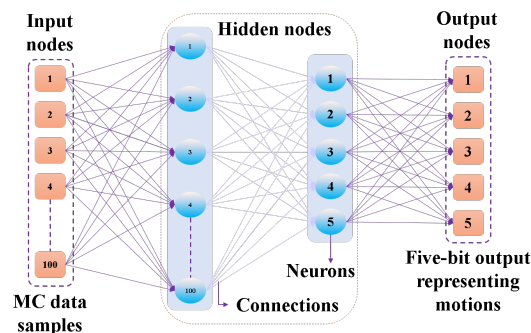

Fig. 5. NN structure for MD performance evaluation.

The input nodes are the coordinate positions of 100 centroid data samples, which represent 20 centroid data samples per predefined motions (i.e., variants of linear, circular and curvature

movements) for an OCC link span ranging from 20 cm to 200 cm. There are two hidden layers of 100 and 5 neurons, respectively. The hidden layers are used to detect and identify the user's motion, the output of which is expressed in the form of five-bit training labels representing the five predefined motions.

Note, for the training of NN, we have used eight possible transfer function-based algorithms as listed in Table 1. When selecting the most suitable training algorithm a number of factors needs considering including the number of neurons N_n in the hidden layers, PT, error measurement and the type of network used for pattern recognition, etc. [22]. In this work, we train the NN with MC and use pattern recognition to identify the classification of input signals or patterns in order to evaluate the link performance.

Table 1. **Training algorithms used for MD [21]**

Transfer function algorithm	Acronym
Levenberg-Marquardt	LM
Resilient Backpropagation	RP
Scaled Conjugate Gradient	SCG
Conjugate Gradient with Powell/Beale Restarts	CGB
Fletcher-Powell Conjugate Gradient	CGF
Polak-Ribiere Conjugate Gradient	CGP
One Step Secant	OSS
Gradient descent	GDX

The key system and NN training parameters are given in Table 2. The training parameters of training goal, iterations and time were set to the same values for all training algorithms in order to evaluate their performance under the same training environment.

Table 2. **System parameters.**

Description	Values
Capture device	Android mobile phone front camera with 1920×1080 pixels resolution and operated in the auto mode
Capture speed	30 fps
Tx	8×8 Neo pixel RGB LED array
Tx's flicker rate	20 Hz
Frame period at the Tx	50 ms
OCC link span	20 - 200 cm
NN hidden layers	two hidden layers with 100 and 5 neurons each
Epochs/training iterations	1000
Training time limit	infinite (allows NN to take sufficient time for training)

3. Results

Figures 6(a)-6(c) shows the experimental results of the detected MC representing variants of linear and circular motions as well as the curvatures. The solid grey line represents the actual considered motions while the dots represent detected MC tracked from user's finger movement over the smartphone's front camera when receiving data from the Tx. The coordinate points of these MC are used further to determine the probability of success for MD. Note, due to tracking some centroids are deviated from the actual motion path (highlighted in small blue circles) while some part of other light sources (highlighted in small red boxes) are captured within the surrounding. However, the NN training output is not affected due to these small number of deviated centroids and other light sources.

(a)

(b)

(c)
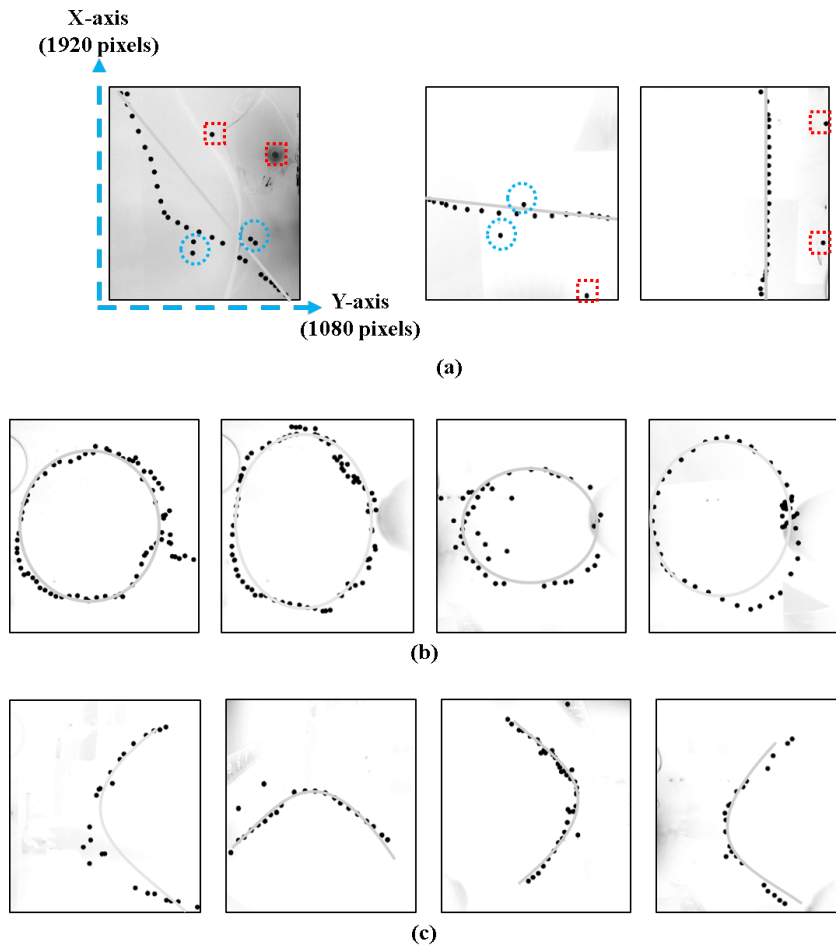
Fig. 6. Experiment results for MC representing variants of (a) linear motion, (b) circular motion, and (c) curvatures. Note, the solid grey line represents actual motion pattern while the dots represent MC.

To evaluate the system performance, we have used two criteria of MSE and the PT for all transfer function algorithms, which are obtained by averaging over 1000 training iterations for the OCC link span ranging from 20 - 200 cm, as depicted in Fig. 7(a). As mentioned in Table 2, the training time limit was set to infinite in order to examine properly all the training algorithms,

considering that some will take longer time to converge with the predicted accurate output. Note that, in a real-world application using NN with infinite networks a time complexity approach can be considered based on Markov Chain Monte Carlo method, which is compatible with large networks [23]. As shown in Fig. 7(a), the RP algorithm converges faster than others reaching the minimum MSE and PT of 5.1×10^{-5} and 0.67 s, respectively. The conjugate gradient algorithms (SCG, CGB, CGF and CGP) also perform well and can be used in networks with a large number of neuron weights due to the modest memory requirements [21]. Note, the LM algorithm offers the worst performance in terms of both the PT and MSE. This is because LM is designed for the least square problems, which are approximately linear in contrast to pattern recognition problems where the output neurons are generally saturated [21]. Both GDX and OSS algorithms converge rapidly provided the training is stopped too soon, but at the cost of inconsistent results [21]. Figure 7(b) illustrates the percentage of success for MD performed over a total of 100 experiments with respect to L for all algorithms listed in Table 1. The percentage of success for MD was determined based on the comparison of the exact input with five-bit output of NN, which represents the five predefined motions. It can be seen that RP display the best performance with the MD accuracies of 100 and 96.5 % over a link spans of 1.6 and 2 m (i.e., the maximum range in this work). The reduction in accuracy for increasing L is due to the fact that the illumination level of finger becomes lower as it moves away from the Tx. However, this does not have a significant impact on NN training and therefore, these reduced accuracy levels are still acceptable.
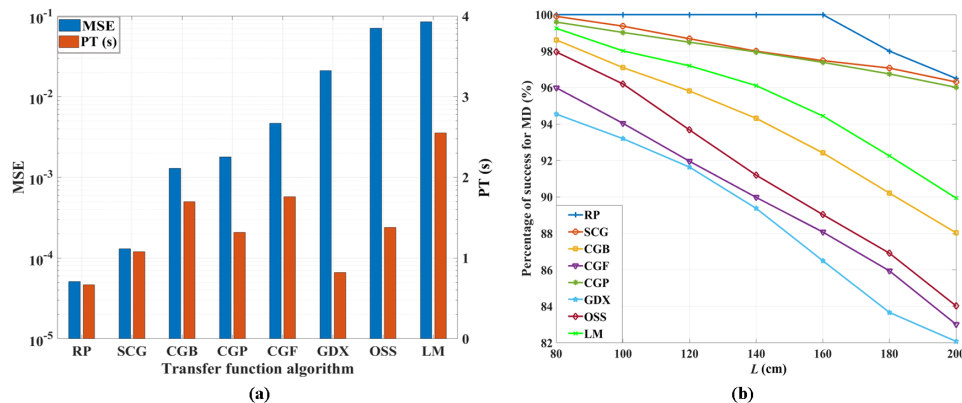

Fig. 7. MD performance: (a) the MSE and the PT, and (b) the percentage of success vs. the transmission distance L.

With RP displaying the best performance, we have further investigated it's complexity of NN in terms of MSE and PT. Note, in general, N_n in the hidden layers can be larger or smaller than the number of input nodes (i.e., data samples). Large or small N_n will result in a complex NN and a higher number of training iterations and PT, respectively. Thus, the trade-off between N_n and NN training complexity is illustrated in Table 3.

Table 3. **NN analysis.**

NN layers	Epochs/training iterations	MSE	PT (s)
100-50-5-5	4000	2.1×10^{-3}	2 s
100-25-5-5	7000	4.3×10^{-2}	4.3 s
100-10-5-5	10000	5.3×10^{-2}	5.2 s

Since the proposed scheme offers simultaneous indoor data transmission via OCC and MD, next, we evaluated the link's BER and PSNR performances. Since in OCC the data is captured in the form of a two-dimensional image, a conventional SNR measurement cannot fully reflect the quality of the link. Therefore, we have adopted PSNR, which is widely used as a quality metric in image processing systems, as given by [24]:

$$PSNR = 10\log_{10}\frac{I_{peak}^2}{Avg(I_{Tx} - I_{Rx})^2},\qquad(2)$$

where I_{peak}^2 denotes the squared peak intensity of the measured frame, I_{Tx} and I_{Rx} are the intensities of the transmitted and received frames.

Note that, user's motion will result in partial shadowing, which will ultimately affect the BER performance. Figure 8 shows the link's BER and PSNR performance against L for 12.8 kbits of data and four-bit header at a R_d of 1.199 kbps, where error-free data transmission is achieved at L up to 80 cm. Note, at the forward error correction (FEC) limit of 3.8×10^{-3} at L of 1.17 m, which is achieved because of the data compensation scheme. The transmission span of 1.17 m is a typical range in environments such as hospital wards, etc. Figure 8 depicts the BER performance as a function of PSNR for the proposed link. At a BER of 10^{-5}, well below the FEC limit of 3.8×10^{-3}, the PSNR is ~ 20 dB.
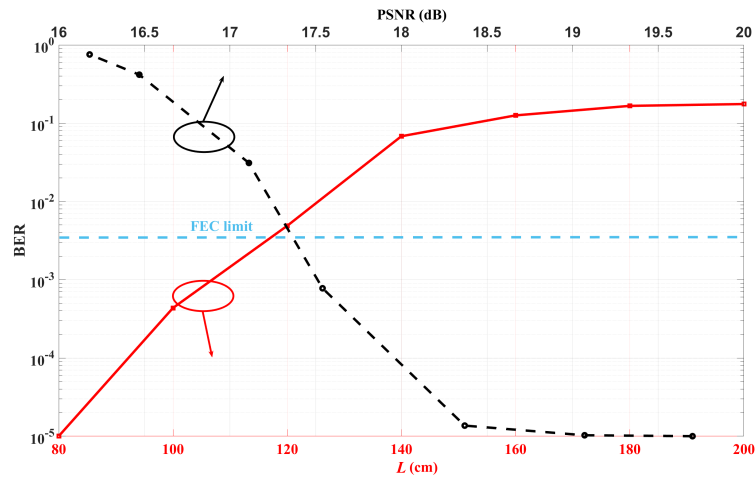

Fig. 8. OCC performance analysis: the BER performance as a function of the transmission span L, and the PSNR with respect to BER.

Finally, we compared the performance of the proposed NN assisted MD in OCC systems with MoC [10], TNMD [12], VLC-based MD [13] and LiSense [17] as shown in Table 4. In MoC, TNMD and the proposed NN assisted MD in OCC systems Android smartphone front camera has been used as Rx whereas, in VLC based MD and LiSense use PD-based Rx. Note, NN-based schemes offer improved performance compared to VLC-based systems. The highest percentage of success for MD of 96 % at L up to 200 cm is observed for the proposed scheme with the RP algorithm (with measured PSNR of 16.18 dB). The same percentage of success for MD is achieved for MoC a complex but a reliable Quadrant division based MD algorithm, but at L of 12 cm. Higher percentage of success for MD of 97 % is observed for TNMD with the basic NN algorithm at a maximum L of 125 cm. The improvement offered by the proposed NN assisted MD in OCC link, which uses a mobile phone camera as the Rx for MD and data transmission, is due to the use of RP algorithm within NN.

Table 4. **Comparison of existing MD schemes.**

	MoC [10]	TNMD [12]	VLC based MD [13]	LiSense [17]	NN assisted MD in OCC
Tx	8×8 red dot matrix LED array with 10 illumination LEDs	8×8 RGB LED array	20 RGB LEDs	5 off-the-shelf commercial LED lights	8×8 Neo pixel RGB LED array
Rx	Android smartphone front camera (1920×1080 pixels)	Android smartphone front camera (1920×1080 pixels)	9 PDs	324 PDs with 90°field of vision in a 3m× 3m area	Android smartphone front camera (1920×1080 pixels)
Detection algorithm	Quadrant division based MD algorithm	Trained neuron based MD	Pattern detection algorithm	LiSense: Sensing of light and analysing the shadow patterns	NN based detection using best training algorithm for MD
Motion distance (between detector and user)	7 - 8 cm	Up to 10 cm	Not specified	User moving in free-space between LEDs and PDs (2.65 m height)	Up to 10 cm
MD accuracy	96 % at L of 12 cm	97 % at L of 125 cm	Not specified but states high level of accuracy up to L of 60 cm	Blockage detection with respect to incident angle: 100 % at (0, 32) and 58-90 % at (43.2, 45)	96 % accuracy up to L of 200 cm
L	12 - 18 cm	25 - 200 cm	40 - 100 cm	Height of room: 265 cm	20 - 200 cm

4. Conclusion

The performance of NN assisted MD OCC link was experimentally evaluated for eight different transfer function based training algorithms with training parameters of PT, the number of iterations, the percentage of success for MD and MSE. We showed that, the best performance was achieved using the RP algorithm with the fastest convergence at a minimum error (MSE) and a PT of 10^{-5} and 0.67 s, respectively as well as the percentage of success for MD of 100 % up to a 1.6 m OCC link. For higher L, the OCC link will experience shadowing due to fingers' movement thus the need for diversity based Rx. We also demonstrated that, using the transmit data compensation scheme a high-quality data transmission with the FEC limit 3.8×10^{-3}, was achieved at 1.17 m OCC link. The reliability and efficiency of the proposed scheme were assessed

by comparing it with other existing techniques. The NN for MD analysis can be further extended to increase the link spans based on pattern recognition algorithms and using different transmitter configurations for mobility and multiuser indoor smart home environments. On the other hand, the date rate can be enhanced using a high capture speed camera with rolling shutter and a larger LED array as the Rx and the Tx, respectively in a MIMO OCC link.

Funding

References

1. P. H. Pathak, X. Feng, P. Hu, and P. Mohapatra, "Visible light communication, networking, and sensing: A survey, potential and challenges," IEEE Commun. Surv. Tutorials **17**, 2047–2077 (2015).
2. Z. Ghassemlooy, S. Zvanovec, M.-A. Khalighi, W. O. Popoola, and J. Perez, "Optical wireless communication systems," Optik **151**, 1–6 (2017).
3. S. Zvanovec, P. Chvojka, P. A. Haigh, and Z. Ghassemlooy, "Visible light communications towards 5G," Radioengineering **24**, 1–9 (2015).
4. Z. Ghassemlooy, W. Popoola, and S. Rajbhandari, *Optical wireless communications: system and channel modelling with Matlab®* (CRC press, 2019).
5. S. R. Teli, S. Zvanovec, and Z. Ghassemlooy, "Optical internet of things within 5G: Applications and challenges," in *2018 IEEE International Conference on Internet of Things and Intelligence System (IOTAIS),* (IEEE, 2018), pp. 40–45.
6. R. Boubezari, H. Le Minh, Z. Ghassemlooy, and A. Bouridane, "Smartphone camera based visible light communication," J. Light. Technol. **34**, 4121–4127 (2016).
7. T. Nguyen, A. Islam, T. Hossan, and Y. M. Jang, "Current status and performance analysis of optical camera communication technologies for 5G networks," IEEE Access **5**, 4574–4594 (2017).
8. I. Takai, S. Ito, K. Yasutomi, K. Kagawa, M. Andoh, and S. Kawahito, "LED and CMOS image sensor based optical wireless communication system for automotive applications," IEEE Photonics J. **5**, 6801418 (2013).
9. M. J. Jang, "IEEE 802.15 WPAN 15.7 amendment-optical camera communications study group (SG 7a)," (2019 [Online accessed 6 March 2019]).
10. S. Teli, W. A. Cahyadi, and Y. H. Chung, "Optical camera communication: Motion over camera," IEEE Commun. Mag. **55**, 156–162 (2017).
11. Z. Ghassemlooy, L. N. Alves, S. Zvanovec, and M.-A. Khalighi, *Visible light communications: theory and applications* (CRC Press, 2017).
12. S. R. Teli, W. A. Cahyadi, and Y. H. Chung, "Trained neurons-based motion detection in optical camera communications," Opt. Eng. **57**, 1–4 (2018).
13. A. Sewaiwar, S. V. Tiwari, and Y.-H. Chung, "Visible light communication based motion detection," Opt. Express **23**, 18769–18776 (2015).
14. N. Lalithamani, "Gesture control using single camera for PC," Procedia Comput. Sci. **78**, 146–152 (2016).
15. D. Ionescu, V. Suse, C. Gadea, B. Solomon, B. Ionescu, and S. Islam, "A new infrared 3D camera for gesture control," in *2013 IEEE International Instrumentation and Measurement Technology Conference (I2MTC),* (IEEE, 2013), pp. 629–634.
16. E. Alizadeh Jarchlo, X. Tang, H. Doroud, V. P. G. Jimenez, B. Lin, P. Casari, and Z. Ghassemlooy, "Li-Tect: 3-D monitoring and shape detection using visible light sensors," IEEE Sensors J. **19**, 940–949 (2019).
17. T. Li, C. An, Z. Tian, A. T. Campbell, and X. Zhou, "Human sensing using visible light communication," in *Proceedings of the 21st Annual International Conference on Mobile Computing and Networking,* (ACM, 2015), MobiCom '15, pp. 331–344.
18. Y. Lecun, Y. Bengio, and G. Hintin, "Deep learning," Nature **521**, 436–444 (2015).
19. Atmel datasheet, "8-Bit microcontroller with 4/8/16/32K bytes in-system programmable flash," (Atmel Corporation, 2009).
20. J. C. Nascimento, A. J. Abrantes, and J. S. Marques, "An algorithm for centroid-based tracking of moving objects," in *1999 IEEE International Conference on Acoustics, Speech, and Signal Processing. Proceedings. ICASSP99 (Cat. No.99CH36258),* vol. 6 (IEEE, 1999), pp. 3305–3308.
21. Y. H. Kim and Y. H. Chung, "Experimental outdoor visible light data communication system using differential decision threshold with optical and color filters," Opt. Eng. **54**, 1–3 (2015).
22. Mathworks, "Choose a multilayer neural network training function," https://in.mathworks.com/help/deeplearning/ug/choose-a-multilayer-neural-network-training-function.html;jsessionid=2e10b001e2c1c97fcac09f6004e6.
23. C. K. I. Williams, "Computation with infinite neural networks," Neural Comput. **10**, 1203–1216 (1998).
24. Q. Huynh-Thu and M. Ghanbari, "Scope of validity of PSNR in image/video quality assessment," Electron. Lett. **44**, 800–801 (2008).

4.5 Optical camera communication system for Internet of things based on organic light emitting diodes

This chapter is a version of the published manuscript:

Connection to my Ph.D. thesis:

High-speed OLED based short-range VLC links have already been addressed in the literature [97–99]. However, the investigation of using OLED panels for long-range optical links needs to be investigated for their use in outdoor OCC cases. Therefore, in this study we perform an experimental demonstration of OLED-based OCC system for both indoor and outdoor IoT environments. It is shown that despite the low emitted power of OLED devices, long range links can be established based on OCC. One outdoor and two indoor scenarios are tested, validating the bit error rate (BER) below 10^{-6} for indoor link spans shorter than 40 m and providing the BER of 10^{-3} for outdoor long range links up to 120 m.

Optical camera communication system for Internet of Things based on organic light emitting diodes

P. Chavez-Burbano✉, S. Vitek, S.R. Teli, V. Guerra, J. Rabadan, R. Perez-Jimenez and S. Zvanovec

The inclusion of organic light emitting diodes (OLEDs) in high-end devices, such as TVs and smart-phones, along with the insertion of cameras embedded in daily use devices, provides the opportunity to establish optical camera communication (OCC) systems based on OLED emitters for Internet of Things (IoT). This Letter presents an experimental demonstration of this OLED-based OCC system for IoT. The results suggest that despite the low emitted power of OLED devices, long range links can be established based on OCC. One outdoor and two indoor scenarios are tested, validating BER below 10^{-6} for short range and give just 3.56×10^{-3} for long range links.

Introduction: Nowadays, organic light emitting diodes (OLEDs) have been massively introduced within both the solid state lighting and the high-resolution displays markets due to their low power consumption and cost-efficient manufacturing process. Worldwide companies such as Samsung, LG, Apple, and Sony, have been integrating OLEDs in their high-end smartphones (i.e. Samsung Galaxy S7, iPhone X), high-end TVs (i.e. Sony A1, LG OLED65B7V) and flexible decorative lamps.

OLEDs have been proposed as emitters for implementing visible-light communication (VLC) systems and for future 5G systems [1]. Haigh *et al.* presented an OLED-based implementation using on–off keying (OOK) at 250 kbps with a bit error rate (BER) of 10^{-6} [2]. This system was improved by using pre-equalisation and multiple-input multiple-output (two emitters and nine receiver sections), increasing the data rate up to 1.8 Mbps [3]. In [4], a 54.9 Mbps OLED-based system was introduced. The authors used a high performance artificial neural network equaliser for classifying the input signal based on a training sequence for an RGB polymer LED. In the same way, orthogonal frequency division multiplexing has been proposed for increasing the data rate of OLED-based VLC systems. In [5], this modulation was combined with power allocation in order to achieve 10 Mbps using a 350 kHz bandwidth emitter. Chen *et al.* demonstrated a 51.6 Mbps transmission with a BER of 3.8×10^{-3} by implementing offset quadrature amplitude modulation [6]. However, these high-rate solutions were reached at extremely short distances (below 15 cm), and further experiments only achieved 1 m span limit. To the authors' knowledge, currently there is no literature addressing tests with OLED based VLC systems for medium and longer distances, outdoor cases, neither the use of cameras as receivers.

In this work, the idea of using optical camera communication (OCC) systems for IoT based on OLEDs, instead of other traditional VLC schemes already proposed for data transportation in IoT networks [7], is presented and experimentally validated. In this way, longer distances can be easily reached for systems that require relatively low data transmission rates (up to 1 kbps). Since OCC systems can be affected by the blooming effect, different exposure times were tested in this work. High exposure times affect several pixels rows due to the overlapped scanning of rolling shutter cameras, creating visible white halos around the illuminated portions and therefore image distortion between the bits' bands.

System description: The proposed OCC system is based on the utilisation of OLED devices as transmitters and a rolling-shutter camera as a receiver. There are several types of OLED emitters that can be used. Bendable panels are implemented in rooms, on clothing or embedded into decoration appliances. OLED monitors are usually implemented as advertisement devices. Finally, OLED screens are implemented as part of electronic devices such as smartphones and tablets. The signal is modulated using OOK during the experiments. Nonetheless, its under-sampled variants in frequency, amplitude or phase can be used for avoiding possible flickering. These modulations are part of the communication modes proposed for OCC by the IEEE 802.15.7m Optical Wireless Communications Task Group [8]. At the beginning of the transmission, a calibration signal (clock-like signal) is sent in order to adjust the system's thresholds. The OLED-device transmits the modulated signal by switching between the on and off states accordingly at frequency f_s.

On the receiver side, two types of cameras can be implemented: smart-device cameras such as those embedded into watches, smart-phones, tablets or glasses, and closed circuit television (CCTV) cameras such as the ones used for security and surveillance purposes. As it is shown in Fig. 1, each frame is captured by the camera at predetermined frames per second (fps) using N_y pixels of vertical resolution, and stored for its corresponding processing. To speed up the processing performance, a smaller image with only the emitter's signal information is required, so the first step is the detection of the region of interest (ROI), which can be multi-target (several simultaneous emitters). The first frame is binarised using Otsu's algorithm and dilated for finding the sources as image regions, which extrema points can be extracted. The obtained coordinates that define the boundaries of the ROI are used for the image cropping. In the multi-target case, the frame is cropped in several images, one per target. Since the first frame contains the calibration signal, the histogram information of its three channels (red, green and blue) is used for calculating the corresponding threshold values by assuring that the 50% of the data belong to each bit's level. Then, the remaining frames are binarised applying these threshold values, and the obtained B/W image (binary matrix) is projected on a 1D vector by averaging each row. Finally, this vector is decoded using (1) which calculate the corresponding number of pixels per bit (n_{bit}) in order to acquire the transmitted data. The number of consecutive ones or zeros are divided by the estimated n_{bit}. Nevertheless, since there may be sampling frequency offset, the final output takes into account the decimal part of the division, adding one bit when needed.

$$n_{bit} = \frac{N_y}{f_s} \cdot \text{fps} \qquad (1)$$
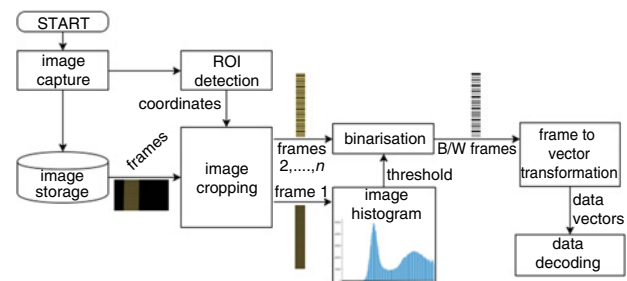

Fig. 1 *OCC data processing flowchart*

To validate the proposed system, three test cases were performed at the Faculty of Electrical Engineering building of the Czech Technical University in Prague: an indoor case up to 4 m, a corridor up to 120 m, and finally an outdoor test up to 120 m. In all cases, a 751 m bendable bar type OLED panel was used as the emitter, with an area of 187.84 mm × 37.84 mm and 85% of spatial luminous uniformity. This panel was switched by a MOSFET-based driver which implements an OOK non-return to zero modulation. An USB rolling-shutter camera with variable exposure time (from 100 μs to 30 s) was selected as the receiver. This camera has a video resolution of 720 × 540 pixels, manual white balance of 0 dB, gain of 3 dB, selectable frame rate (fps), brightness and contrast of 25/100, zero Hue, and saturation of 70. For distances up to 40 m, the camera worked with a lens of 12.5 − 75 mm and F/1.8. For longer indoor test outdoor tests, the camera was mounted on a 10/1000 macro telephoto lens with focal length of 1000 mm, geometrical relative aperture 1 : 10 and angular field-of-view (FOV) of 2.5°.

At the beginning of the transmission, a calibration sequence was sent, then the data were encapsulated within 2-bytes long packets that had specific start and end delimiters (0xA sequence). In total, 1200 frames were recorded and stored per each trial. Finally, the videos were off-line processed using MATLAB routines following the procedure described in Fig. 1.

Indoor experiment: The indoor experiment was performed within a 6 m × 6 m room. The distance between the emitter and the receiver was set to 4 m, while the switching frequency varied from 500 to 5000 Hz with steps of 500 Hz. The camera's frame rate was changed among five values: 17.5, 19.01, 25, 30, and 50 fps; while its exposure time was set to two different values: 400 and 500 μs.

Fig. 2 depicts measured BER for different switching frequencies. It can be seen that the trials of 30 and 50 fps reached the best BER results, less than 10^{-2} for 5 kHz. Taking into account the packet encoding and the fact that each 2-byte packet was repeated twice in order to ensure its detection, the achieved data rates were approximately 120

77

and 200 bps, respectively. In general, the system worked properly up to 2.5 kHz, for all the frame rates, with less than 10^{-5} BER.
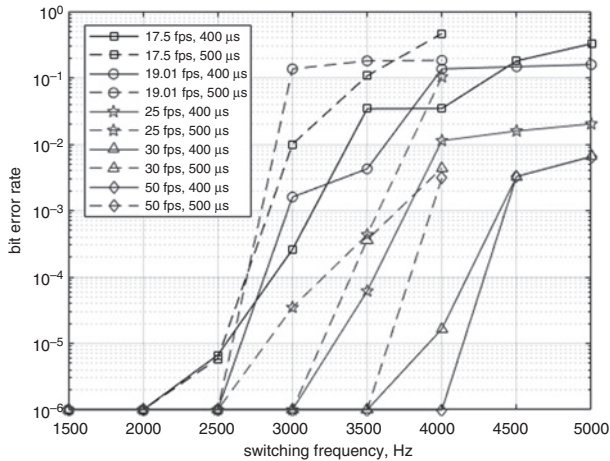

Fig. 2 *BER versus switching frequency of the 4 m-long indoor scenario*

Indoor corridor measurements: For longer indoor distances, two sets of trials were carried out in a 200 m corridor. In both experiments, the switching frequency was set to 1 kHz, the frame rate was set to 25 and 50 fps, and the exposure time was 400 μs. These values were selected using (1) and considering that the target link range was longer than in the previous experiment.

In the first case, the distance ranged from 10 to 40 m in steps of 5 m and the receiver used the 75 mm focal-length lens. The system worked as expected compared to the previous experiment, for both camera frame rates, the measured BER value remained less than $< 10^{-6}$ for all cases.

In the second case, the distance varied from 20 to 120 m in steps of 20 m. Furthermore, the camera was mounted on the telescope, and the captured images were vertically compressed 2 : 1 to simplify the location of the emitter at the beginning of the trials. As shown in Fig. 3, the BER increased from 9.68×10^{-3} at 40 m to 5.29×10^{-2} at the limit test distance (120 m), demonstrating that the OLED-based OCC system can achieve longer distances. However, the use of the telescope may introduce misalignment errors and presented some problems related to the stability of the receiver.
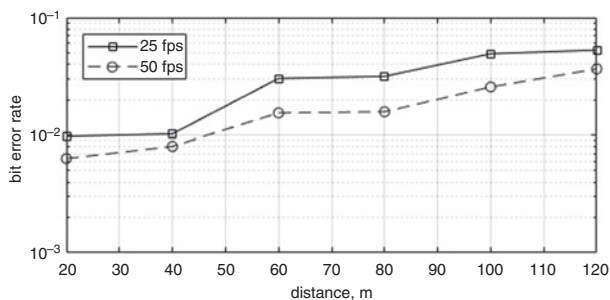

Fig. 3 *Dependence of BER on distance in the case of OCC system tested within an indoor corridor using a telescope at the receiver side*

Outdoor measurements: Finally, the experimental tests were performed on the roof of the faculty building (approximately 30 m above ground). The measurements were taken in June 2018 during a scattered cloudy afternoon with the following atmospheric conditions measured by the meteorological station placed at one side of the link: temperature of 18°C, wind speed of 9 km/h and 60% humidity. The small wind speed and mostly the reduced link range limited the possible harmful effect of turbulence. In this experiment, two link distances were tested (60 and 120 m), and the switching frequency was established to 1 kHz. The camera was mounted on the telescope with a binning of 2 : 1. In addition, the tested frame rates were 25 and 50 fps, and the exposure time was 400 μs.

In this case, as shown in Table 1, using a 50 fps frame rate for a distance of 60 m, the 1 kHz transmission achieved less than 3×10^{-5} BER, and BER of 3.56×10^{-3} was experienced in the case of 120 m link.

78

Table 1: BER measured in the case of the outdoor scenario.

Distance (m)	25 fps	50 fps
60	2.77×10^{-3}	$< 3 \times 10^{-5}$
120	6.54×10^{-3}	3.56×10^{-3}

Conclusion: Based on the results of the different tested indoor and outdoor cases, the feasibility of an OCC system for IoT based on OLED devices was demonstrated. The indoor transmissions showed that the system can be implemented with a standard USB camera of 30 fps, obtaining BERs below 1.7×10^{-5} for measurements inside a standard room (4 m) with switching frequency up to 4 kHz, and less than $< 10^{-6}$ for distances shorter than 40 m with 1 kHz.

These experiments also proved that the camera's exposure time influenced the decoding accuracy due to the blooming effect. Using smaller exposure time limited the overlapping read time between the rows, minimising the white halos. The exposure time of 400 μs allowed an easier calibration due to the better distribution of the bands' width and improved the threshold levels' calculation and the decoding process. The laboratory tests showed that for each selected camera's frame rate, the BER's measurements are better with an exposure time of 400 μs rather than 500 μs.

The results shown in Table 1, verified that an outdoor OLED-based OCC system is feasible. In the same way, the number of projected pixels from the panel in the frame in the outdoor tests assured that longer distances can be easily achieved so this system can even be applied for Smart Cities. Implementations for environmental conditions monitoring, disaster detection, or smart traffic management are viable using spatial division multiple access allowing several emitters spatially separated within the FOV of the camera.

P. Chavez-Burbano (*Facultad de Ingenieria en Electricidad y Computacion, Escuela Superior Politecnica del Litoral, Guayaquil, Guayas, Ecuador*)

✉ E-mail: paxichav@espol.edu.ec

S. Vitek, S.R. Teli and S. Zvanovec (*Faculty of Electrical Engineering, Czech Technical University in Prague, Czech Republic*)

V. Guerra, J. Rabadan and R. Perez-Jimenez (*IDeTIC, Universidad de Las Palmas de Gran Canaria, Las Palmas, Spain*)

References

1 Zvanovec, S., Chvojka, P., Haigh, P., *et al*.: 'Visible light communications towards 5G', *Radioengineering*, 2015, **24**, (1), pp. 1–9
2 Haigh, P., Ghassemlooy, Z., Rajbhandari, S., *et al*.: 'Visible light communications using organic light emitting diodes', *Commun. Mag.*, 2013, **51**, (8), pp. 148–154
3 Haigh, P., Ghassemlooy, Z., Papakonstantinou, I., *et al*.: 'A MIMO-ANN system for increasing data rates in organic visible light communications systems'. IEEE Proc. Int. Conf. on Commun., Budapest,Hungary, June 2013, pp. 5322–5327
4 Haigh, P, Bausi, F., Le Minh, H, *et al*.: 'Wavelength-multiplexed polymer LEDs: towards 55 mb/s organic visible light communications', *J. Sel. Areas Commun.*, 2015, **33**, (9), pp. 1819–1828
5 Le, S., Kanesan, T., Bausi, F., *et al*.: 'A 10 Mb/s visible light transmission system using a polymer light-emitting diode with orthogonal frequency division multiplexing', *Opt. Lett.*, 2014, **39**, (13), pp. 3876–3879
6 Chen, H., Xu, Z., Gao, Q., *et al*.: 'A 51.6 Mb/s experimental VLC system using a monochromic organic LED', *Photon. J.*, 2018, **10**, (2), pp. 1–12
7 Kim, C., and Koh, S.: 'Device management and data transport in IoT networks based on visible light communication', *Sensors*, 2018, **18**, (8), p. 2741
8 Nguyen, T., Islam, A., Yamazato, T., *et al*.: 'Technical issues on IEEE 802.15.7 m image sensor communication standardization', *Commun. Mag.*, 2018, **56**, (2), pp. 213–218

4.6   400 m rolling-shutter-based optical camera communications link

This chapter is a version of the published manuscript:

E. Eso, **S. R. Teli**, N. B. Hassan, S. Vitek, Z. Ghassemlooy, S. Zvanovec, "400 m rolling-shutter-based optical camera communications link," *Optics Letters*, vol. 45(5), pp. 1059-1062, 2020.

Connection to my Ph.D. thesis:

Motivated by the implementation of 120 m long OCC link in Section 4.5, we developed a novel technique to increase the link span of a RS-based OCC system by reducing the spatial bandwidth of the camera in the out-of-focus regions. A 400 m LOS RS-based OCC link with 100% reception success in data transmission achieving an R_b of 450 bps, which is to date the longest OCC link reported in these systems, is experimentally demonstrated. We successfully develop a detection method to extract the information out of the video frames. The proposed system relaxes the condition for a large surface area of the Tx light source. The proposed system is attractive in the distance critical applications requiring relatively low R_b as intelligent transport systems (e.g., exchange of safety and traffic messages and positioning-related information) for smart traffic management.

Optics Letters

400 m rolling-shutter-based optical camera communications link

Elizabeth Eso,[1] **Shivani Teli,**[2] **Navid Bani Hassan,**[3] **Stanislav Vitek,**[2] **Zabih Ghassemlooy,**[1,4] **and Stanislav Zvanovec**[2]

[1]*Optical Communication Research Group, Northumbria University Newcastle, UK*
[2]*Faculty of Electrical Engineering, Czech Technical University in Prague, Prague, Czech Republic*
[3]*Department of Physics, University of Strathclyde, Glasgow, UK*
[4]*QIEM, HI, Chinese Academy of Sciences, Quanzhou, China*
Corresponding author: elizabeth.eso@northumbria.ac.uk

In this Letter, we develop a novel technique, to the best of our knowledge, to increase the link span (L_s) of a rolling shutter (RS)-based optical camera communications (OCC) system by reducing the spatial bandwidth of the camera in the out-of-focus regions. We demonstrate a 400 m line-of-sight RS-based OCC link, which is to date the longest L_s reported in these systems, and develop a detection method to extract the information out of the video frames, successfully. The proposed system relaxes the condition of a large surface area for the transmitter light source. Consequently, we show that at 400 m L_s and exposure times of 100–80 μs, a data rate of 450 bps is achieved successfully. © 2020 Optical Society of America

Optical camera communications (OCC) is considered as a pragmatic form of visible light communications (VLC), which utilizes an image sensor (IS) (i.e., cameras) as the receiver (Rx) and light-emitting diodes (LEDs), laser diodes (LDs), and liquid crystal displays as the transmitter (Tx) [1,2]. In OCC, the camera captures two-dimensional data in the form of image sequences, thus enabling multidimensional data transmission over the free-space channel. OCC offers multiple functionalities of vision, data communications, and localization, which can be used in a number of applications including all-optical Internet of Things (OIoT) [3,4]. OIoT-based applications include device-to-device communications, mobile attocells, vehicle-to-everything (V2X), smart environments, etc. [2], which releases the needed radio frequency spectrum for use in areas most required. Inspired by IoT, the Internet of Vehicles (IoV) is currently of high interest within the research community [4]. Recently, the widespread use of LEDs as tail-lights, brake lights, headlights, and street and traffic lights has opened up the potential opportunities for implementation of the intelligent transportation systems (ITS) to mitigate traffic congestion and therefore improve quality of life and the economy [2]. In addition, the availability of cameras in traffic networks, security surveillance, vehicles, etc., can be effectively

exploited as an optical Rx, thus enabling the implementation of VLC-OCC links.

One of the advantages of camera-based Rxs over photodiodes is the higher signal-to-noise ratio (SNR) due to longer exposure time (T_{exp}) and larger overall photosensitive area, which results in longer link distances. OCC can be deployed in ITS for vehicle-to-vehicle, infrastructure-to-vehicle, and vehicle-to-infrastructure (V2I) communications; therefore, a long link span helps to establish a robust system [2,5]. The complementary-metal-oxide-semiconductor (CMOS)-based rolling shutter (RS) camera, which sequentially (row by row) integrates light illuminating the pixels thus operating similarly as scanning function, can be used to increase the data rate (R_b) higher than the frame rate (R_f) of the camera [6]. In Ref. [7], global-shutter (GS)-based OCC with a R_b of 15 bps over a link range of 328 m was reported for use in smart city applications with ~4% wrongly decoded received bit streams. In Ref. [8], a RS-based OCC link for outdoor application with a maximum link span of 120 m, a bit error rate (BER) of $> 10^{-2}$ (at 120 m), and an achieved maximum R_b of 200 bps at a 4 m link span was reported. Further research on long-distance OCC links (beyond 120 m) using RS is yet to be investigated, to the author's best knowledge.

In order to establish long-distance VLC, there are a number of options including large-area light sources with high-power (meeting the eye safety), multiple light sources, wide-area optical Rx (at cost of reduced bandwidth), and multiple Rxs (i.e., cameras). In Ref. [7], a large-sized Tx with a dimension of 48×48 cm² was used. However, using a large Tx is impractical; therefore, in this Letter, we propose a novel reception technique in order to increase the transmission link span of RS-based OCC by reducing the camera's spatial bandwidth in the out-of-focus areas. This helps to have a larger footprint of the light source on the IS without reducing the field of view (FoV). We also develop a detection algorithm to effectively extract the received information from captured video frames. Previous works reported on OCC have used mainly cameras in the focused mode. However, cameras can also be used in their defocused modes depending on applications, e.g., indoor non-line-of-sight (LOS) communications or V2I-VLC [9]. We have
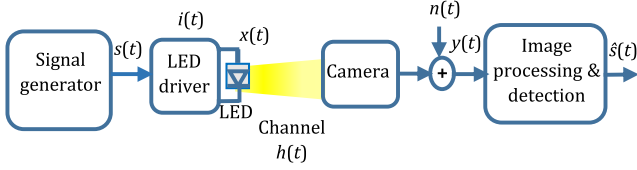
Fig. 1. Schematic block diagram of the long-distance OCC link.

Fig. 2. Example of lens, image sensor, and object configuration.

used a light source (i.e., 2.5×2.5 cm^2) that is 19 times smaller than the source that was adopted in Ref. [7]. The proposed system is attractive in distance critical applications requiring relatively low R_b as in ITS (e.g., exchange of safety and traffic messages and positioning-related information) for smart traffic management. In this work, we achieve a communication link of up to 400 m with 100% success rate in data transmission achieving a R_b of 450 bps. The demonstrated system, to the best of our knowledge, is the longest link span achieved for a RS-based OCC link.

The block diagram of the proposed system is shown in Fig. 1. At the Tx, on–off keying non-return to zero (OOK-NRZ) data $s(t)$ are used for intensity modulation of the LED [a 2.5×2.5 cm^2 size chip on board (COB)] via the LED driver. The intensity-modulated light $x(t)$ is transmitted over a free-space channel and captured at the Rx using a CMOS RS camera with a 1000 mm telephoto lens. For the LOS link, the received signal is given by [10]

$$y(t) = \eta x(t) \circledast h(t) + n(t), \tag{1}$$

where $h(t)$ is the combined impulse response of the channel and camera, η is the quantum efficiency of the IS, and $n(t)$ is the additive white Gaussian noise including the ambient light-induced shot noise and the noise in the camera (i.e, fixed pattern, thermal, photocurrent shot, and flicker noise sources) [11]. The channel DC gain for the LOS link can be obtained as [10]

$$H(0)_{\text{LOS}} = \begin{cases} \frac{A_{\text{Tx-img}}(m+1)}{2\pi d_L^2} \cos^m(\Phi) g(\theta) T_s(\theta), & 0 \le \theta \le \xi \\ 0, & \theta > \xi \end{cases}, \tag{2}$$

where $A_{\text{Tx-img}}$ is the area of the projected illuminated light source on the IS, d_L is the distance between the Tx and the camera's lens, and $T_s(\theta)$ and $g(\theta)$ are the gains of the optical filter and optical concentrator, respectively. Φ denotes the irradiance angle, ξ is the FoV semi-angle of the camera, and m represents Lambertian order of emission of the Tx. The incidence angle $\theta = \phi_{\text{tilt}} + \sin^{-1}[(H_{\text{Tx}} - H_{\text{Rx}})/d_L]$, while the Rx tilt angle and heights of the Tx and Rx are denoted as ϕ_{tilt}, H_{Tx}, and H_{Rx}, respectively.

Usually, CMOS camera sensors (adopted as the Rx in this work) use the RS readout method, such that each pixel row is exposed in a row-by-row sequential manner with a fixed time delay (row readout time T_r). Moreover, in RS-based cameras, the exposure of each row takes place before the readout and not all at once, as in the case of GS-based cameras. Consequently, each pixel row's exposure does not commence at the same time. This is an advantage in OCC systems, which can lead to increased R_b higher than the camera's R_f, but at the cost of reduced coverage distance; hence, we propose a new technique to extend this coverage distance. Note that with RS-OCC, a
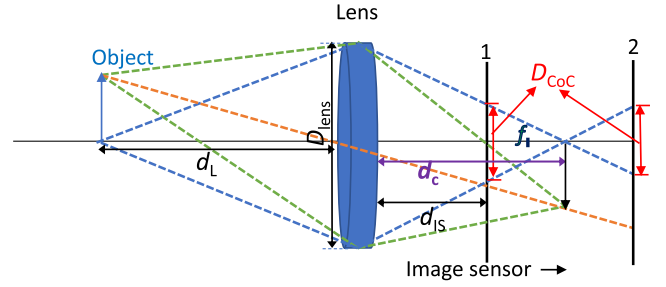
flicker-free transmission is achievable; hence, we employ this technique in this work.

Note that in OCC, the captured Tx's focused image size decreases with the increasing link span as given by the relationship $d_{\text{img}} = d_{\text{Tx}} f / d_L$, where d_{Tx} and d_{img} are the diameter of the Tx and the diameter of the projected Tx's image on the IS at the focal length f of the lens in use, respectively. This therefore constitutes a limitation for RS-based OCC links, as the received signal area on the IS of the camera, which determines the number of rows N_{rows} (i.e., the ON and OFF states of the Tx) obtainable, decreases with the increasing transmission distance. Consequently, we reduce this limitation by operating the camera in its out-of-focus (defocused) mode. Figure 2 shows a lens, object, and IS configuration. The IS could be moved from position 1 to 2 where varying sizes of the projected object's image are obtainable. Importantly, we use the defocusing feature of the camera, i.e., by altering the distance between the 1000 mm telephoto lens and the IS, to allow the Tx's image to converge beyond the focal point, whereby a larger footprint of the Tx is obtained.

Consequently, more N_{rows} are visible [detectable by the Rx (camera)], as illustrated in Fig. 3 for the defocused modes. Note that defocusing of the camera results in a disc-shaped pattern known as a circle of confusion (CoC), which is convoluted with the image as given by [12]

$$G_o(x, y) = G_i(x, y) \circledast \circledast G_{\text{CoC}}(x, y), \tag{3}$$
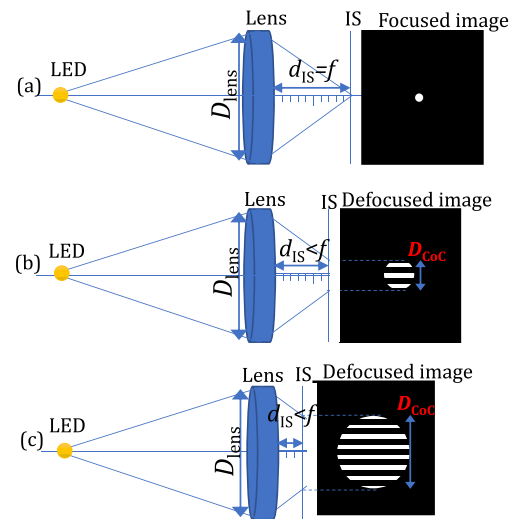

Fig. 3. Examples of width of captured Tx images on IS based on varying lens and IS configurations.

where $G_o(x, y)$ and $G_i(x, y)$ are the defocused and focused image intensity functions, respectively. $\circledast\circledast$ is the two-dimensional convolution operator, and $G_{CoC}(x, y)$ is the CoC disc function, which is the same shape as the camera's lens aperture. For a circular aperture, we have [12]

$$G_{CoC}(x, y) = U\left(\sqrt{x^2 + y^2}\right) - U\left(\sqrt{x^2 + y^2} - 0.5 D_{CoC}\right), \quad \text{(4)}$$

and the diameter of CoC, D_{CoC}, is the same as the width of the defocused image of a point source and is given as [12]

$$D_{CoC} = \frac{D_{lens}}{2 d_c} |d_c - d_{IS}|, \quad \text{(5)}$$

where $U(.)$ is the Heaviside step function, $D_{lens} = f/f_{stop}$ is the diameter of the lens aperture, f_{stop} is the focal stop number of the lens aperture, d_{IS} is the distance between the center of the lens to the IS, and d_c represents the distance between the center of the lens and the image, which can be obtained as [12]

$$d_c = \frac{d_L f}{d_L - f}. \quad \text{(6)}$$

Note that the size of CoC depends on the aperture diameter D_{lens} for collecting the light rays of d_{IS} and d_c. Consequently, to increase defocusing (i.e., D_{CoC}) in order to have the best signal area, $|d_c - d_{IS}|$ must be maximized, and lower values of f_{stop} should be used to obtain larger D_{lens}. However, the amount of achievable defocusing is limited to the camera's optics design configuration. Figure 4 illustrates the N_{rows} as a function of the transmission distances for focused and three different defocused image modes for d_{IS} of f, $0.3f$, $0.5f$, and $0.7f$, $f = 1000$ mm and $D_{lens} = f/10$, and width of rows $= 0.05$ cm. The N_{rows} increases with d_{IS}, e.g., at d_L of 20 m, the N_{rows} has increased from two for the focused image mode to 33, 52, and 71 for d_{IS} of $0.7f$, $0.5f$, and $0.3f$, respectively, thus enabling longer RS-OCC link spans. The width of one row in pixels (representing one bit or symbol for a fixed camera pixel clock) [13], $w_b = 1/(2 f_{Tx} T_r)$, where f_{Tx} denotes the Tx's switching frequency. Note that the N_{rows} increasing with the defocusing is at the cost of reduced light intensity level per pixel [i.e., lower peak SNR (PSNR)/pixel], since the received light is spread over a higher number of pixels. Interestingly, the latter can be compensated for by increasing the gain parameter of the camera (i.e., its sensitivity), the aperture size, and T_{exp} (within the
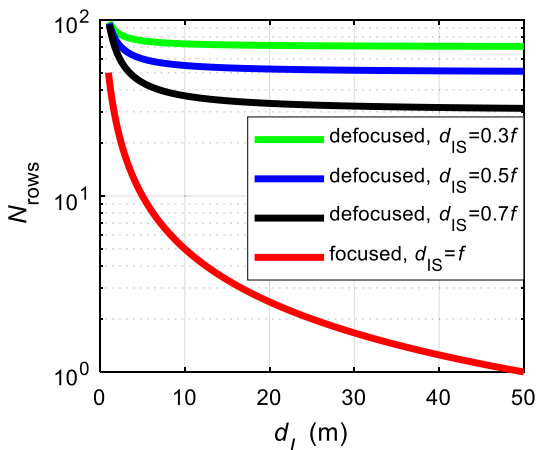
required bandwidth) so as to capture more light but only to the extent that the rows still remain distinctive and not mixed up. In addition, a robust image processing algorithm (Fig. 5) is proposed to enhance the success rate of received bits.

Consequently, at the Rx side, the output of the camera (IS) is processed off-line in MATLAB. As portrayed in the detection flowchart (Fig. 5), every video frame is converted from the red, green, and blue (RGB) color format to grayscale for both calibration and data videos after pixelation (i.e., digitizing the image to obtain the intensity/pixel value). The data videos are the captured transmitted data, whereas the captured calibration videos are the template shape of the Tx, which is used for equalization or otherwise described as the intensity compensation of the data video frames. Next, the region of interest (ROI) is selected (i.e., the footprint of the light source on the IS, which is the CoC) and then averaged over the rows to form a column vector. In order to avoid noise amplification at the start and end of the pixel rows in each frame, at least 10-pixel rows are eliminated from the top and bottom of the CoC. The received signal is then up-sampled to increase the resolution of the received signal. The correlation between the transmitted and received signal is carried out to determine the delay between them in order to extract the required received samples. A matched filter (MF) (via postprocessing in MATLAB) is applied to recover the data. The recovered data bits vector is then compared with the transmitted data to ascertain the success rate of received bits by determining the ratio of the wrongly decoded bits to the total number of transmitted bits (i.e., BER).

The system configuration and experimental setup for the long-distance OCC are shown in Fig. 6. The Tx was located on the sixth floor (height of 25 m), and the Rx was placed outdoors at a height of 1.40 m above the ground. At the start of the measurement campaign, the weather was partly cloudy/sunny while by the end it was sunny, with a temperature range of 23°C–25°C and wind speed and humidity of 2–6 mph and 51%–65%, respectively. The key experimental parameters include the LED
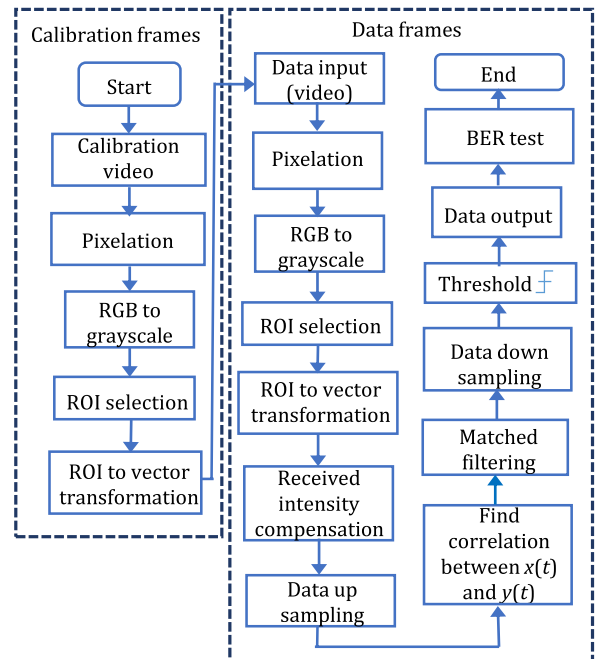

Fig. 4. N_{rows} versus d_L for a range of d_{IS}.

Fig. 5. Flowchart of detection.

drive current, FoV, and m, which are 0.33 A, 122°, and 0.96, respectively. The Tx data packet is 18 bits, the Rx's R_f is set to 25 fps for all experimental configurations considered, and the number of received data bits is $\sim$32 per frame. The Rx's video resolution, pixel size, lens aperture, and f are 648×484 (RGB32), $2.2 \times 2.2\ \mu m^2$, $f/10$, and 1000 mm, respectively. Measurements were carried out for a range of link spans L_s and $T_{\exp}$ of 150 to 400 m and 100 to 800 μs, respectively. Image frames of the transmitted data were captured with up to 100% success rate of received bits for all links considered in this work. In order to quantify the link performance for each L_s, we used the image quality metric of PSNR, which is given as [14]

$$P_{SNR} = 10 \log \frac{I_{\max}^2}{\epsilon(i)}, \qquad (7)$$

where $I_{\max}$ is the maximum possible pixel value, $I_{\max} = 2^n - 1$, $n = 8$ for a grayscale image, and $\epsilon(i)$ is the pixel luminance mean squared error, which is defined by

$$\epsilon(i) = \frac{1}{N_{rows}} \sum_{1}^{N_{rows}} (I_{Tx}(i) - I_{Rx}(i))^2. \qquad (8)$$

$I_{Tx}(i)$ and $I_{Rx}(i)$ are the difference between pixel and average pixel values for transmitted and received symbols (1 and 0), respectively, while i represents the row's index number. Figure 7 shows the PSNR versus L_s for a range of $T_{\exp}$. As illustrated, PSNR improves with $T_{\exp}$ and decreases with the increasing L_s, e.g., for $T_{\exp}$ of 800 μs, PSNR drops by 2.1 dB when increasing L_s from 200 to 400 m. The maximum values of PSNR are 3.3 and 0.2 dB for $T_{\exp}$ of 800 μs and 100 μs at L_s of 150 m, respectively.

We have developed a novel technique to increase the link span of RS-based OCC by reducing the spatial bandwidth of the camera in the out-of-focus regions. The experimental analysis of the proposed scheme demonstrates a 100% success rate of received bits for a L_s of up to 400 m using a small surface area Tx of $2.5 \times 2.5\ cm^2$. The choice of the $T_{\exp}$ played a key role in determining the value of PSNR. To the best of the authors'
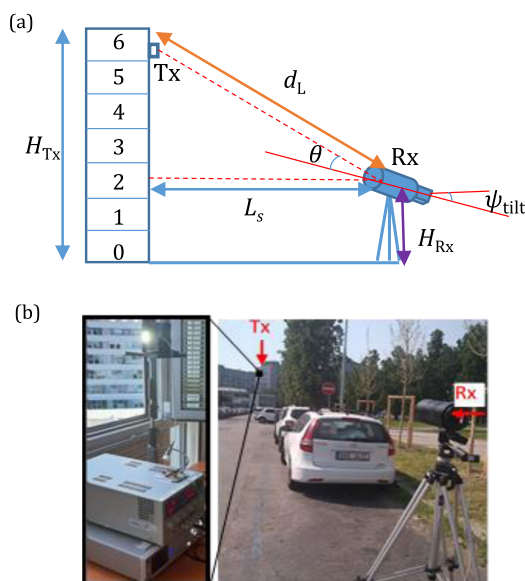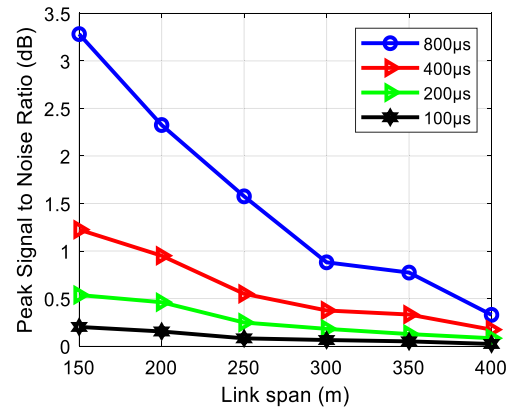

Fig. 7. PSNR versus link span for a range of camera's $T_{\exp}$.

knowledge, no works have been reported for long-distance OCC links using RS.

Disclosures. The authors declare no conflicts of interest.

REFERENCES

1. M. J. Jang, *IEEE 802.15 WPAN 15.7 Amendment Study Group* (2019).
2. Z. Ghassemlooy, L. N. Alves, S. Zvanovec, and M.-A. Khalighi, *Visible light communications: Theory and Applications* (CRC Press, 2017).
3. M. K. Hasan, M. Z. Chowdhury, M. Shahjalal, V. T. Nguyen, and Y. M. Jang, Appl. Sci. **8**, 2527 (2018).
4. S. R. Teli, S. Zvanovec, and Z. Ghassemlooy, "Optical Internet of Things within 5G: applications and challenges," in *IEEE International Conference on IoT and Intelligence Systems (IOTAIS)*, Bali, Indonesia, 1 November 2018, pp. 40–45.
5. P. Luo, M. Zhang, Z. Ghassemlooy, H. L. Minh, H. M. Tsai, X. Tang, and D. Han, IEEE Photon. Technol. Lett. **28**, 139 (2016).
6. T. Nguyen, C. H. Hong, N. T. Le, and Y. M. Jang, "High-speed asynchronous optical camera communication using LED and rolling shutter camera," in *2015 Seventh International Conference on Ubiquitous and Future Networks*, Sapporo, Japan, 7 July 2015, pp. 214–219.
7. P. Chavez-Burbano, V. Guerra, J. Rabadan, and R. Perez-Jimenez, "Optical camera communication for smart cities," in *2017 IEEE/CIC International Conference on Communications in China (ICCC Workshops)*, Qingdao, China, 22 October 2017, pp. 1–4.
8. P. Chavez-Burbano, S. Vitek, S. R. Teli, V. Guerra, J. Rabadan, R. Perez-Jimenez, and S. Zvanovec, Electron. Lett. **55**, 334 (2019).
9. E. Eso, Z. Ghassemlooy, S. Zvanovec, A. Gholami, A. Burton, N. B. Hassan, and O. I. Younus, "Experimental demonstration of vehicle to road side infrastructure visible light communications," in *2019 2nd West Asian Colloquium on Optical Wireless Communications (WACOWC)*, Tehran, Iran, 27 April 2019, pp. 85–89.
10. J. M. Kahn and J. R. Barry, Proc. IEEE **85**, 265 (1997).
11. N. B. Hassan, "Mimo visible light communications with camera-based receiver for intelligent transport systems," Ph.D. thesis (Northumbria University, 2019).
12. N. B. Hassan, Y. Huang, Z. Shou, Z. Ghassemlooy, A. Sturniolo, S. Zvanovec, P. Luo, and H. Le-Minh, "Impact of camera lens aperture and the light source size on optical camera communications," in *2018 11th International Symposium on Communication Systems, Networks and Digital Signal Processing (CSNDSP)*, Budapest, Hungary, 18 July 2018, pp. 1–5.
13. S. Verma, "Analysing the performance and stability of LED-to-camera links," Masters thesis (Delft University of Technology, 2017).
14. Q. Huynh-Thu and M. Ghanbari, Electron. Lett. **44**, 800 (2008).

Fig. 6. Proposed OCC link (a) system configuration and (b) experimental setup.

4.7   Experimentally derived feasibility of optical camera communications under turbulence and fog conditions

This chapter is a version of the published manuscript:

V. Matus, E. Eso, **S. R. Teli**, R. Perez-Jimenez, S. Zvanovec, "Experimentally derived feasibility of optical camera communications under turbulence and fog conditions," *Sensors*, vol. 20, pp. 757, 2020.

Connection to my Ph.D. thesis:

Long-range outdoor OCC links proposed in Section 4.5 and Section 4.6, utilized a small exposure to mitigate the sunlight effect and spatial bandwidth of the camera to increase the footprint of the captured image, respectively. For practical implementation of these approaches in outdoor scenarios, it is necessary to study the effect of atmospheric conditions such as heat-induced turbulence, attenuation due to fog and raindrops, etc. Therefore, in this work, we verify a performance of an experimental OCC system under environmental phenomena emulated in a laboratory chamber. The experimental based results demonstrate that the heat-induced turbulence does not affect OCC system significantly compared to OWC systems, while the attenuation caused by fog does decrease the signal quality. To mitigate this attenuation and to overcome the optical power loss and decrease the quantization noise induced by the ADC of the camera, a novel strategy of using the camera's built-in amplifier is proposed. This utilization of the CMOS camera's built-in amplifier opens a new possibility for OCC systems, extending the control strategy, and allowing to keep low exposure times and, thus, a high bandwidth, even in dense fog scenarios.

Experimentally Derived Feasibility of Optical Camera Communications under Turbulence and Fog Conditions

Vicente Matus [1,*] ![iD], **Elizabeth Eso** [2] ![iD], **Shivani Rajendra Teli** [3] ![iD], **Rafael Perez-Jimenez** [1] ![iD] and **Stanislav Zvanovec** [3] ![iD]

[1] Institute for Technological Development and Innovation in Communications, Universidad de Las Palmas de Gran Canaria, 35001 Las Palmas, Spain; rafael.perez@ulpgc.es
[2] Optical Communications Research Group, Northumbria University, Newcastle-upon-Tyne NE1 7RU, UK; elizabeth.eso@northumbria.ac.uk
[3] Department of Electromagnetic Field, Faculty of Electrical Engineering, Czech Technical University in Prague, Technicka, 16627 Prague, Czech Republic; telishiv@fel.cvut.cz (S.R.T.); xzvanove@fel.cvut.cz (S.Z.)
* Correspondence: vicente.matus@ulpgc.es

Abstract: Optical camera communications (OCC) research field has grown recently, aided by ubiquitous digital cameras; however, atmospheric conditions can restrict their feasibility in outdoor scenarios. In this work, we studied an experimental OCC system under environmental phenomena emulated in a laboratory chamber. We found that the heat-induced turbulence does not affect our system significantly, while the attenuation caused by fog does decrease the signal quality. For this reason, a novel strategy is proposed, using the camera's built-in amplifier to overcome the optical power loss and to decrease the quantization noise induced by the analog-digital converter of the camera. The signal quality has been evaluated using the Pearson's correlation coefficient with respect to a reference template signal, along with the signal-to-noise ratio that has been empirically evaluated. The amplification mechanism introduced allows our system to receive the OCC signal under heavy fog by gradually increasing the camera gain up to 16 dB, for meteorological visibility values down to 10 m, with a correlation coefficient of 0.9 with respect to clear conditions.

Keywords: optical camera communications (OCC); CMOS image sensor; rolling shutter; fog attenuation; heat-induced turbulence; meteorological visibility; refractive index structure parameter

1. Introduction

Digital cameras are ubiquitous consumer electronics and are being explored to deliver extra capabilities beyond traditional photography and video. A new optical communication technique using cameras as receivers has been studied in the IEEE 802.15 SG7a within the framework of optical wireless communications and considered as a candidate of IEEE 802.15.7r1, which is called Optical Camera Communication (OCC). OCC has been investigated as one of the Visible Light Communication (VLC) schemes [1]. OCC implemented within internet of things (IoT) environments provides multiple functionalities of vision, data communications, localization and motion detection (MD) [2,3] used in various IoT-based network applications including device-to-device communications [4], mobile atto-cells [5], vehicular communications [6–8], and smart cities, offices, and homes (SCOH) [9].

The majority of new generation smart devices have built-in Complementary Metal-Oxide-Semiconductor (CMOS) image sensors, providing the ability to capture photos and videos [10,11]. The strategy behind using a CMOS camera for OCC is that the image sensor performs an acquisition mechanism known as Rolling Shutter (RS), in which it sequentially integrates light on rows of pixels [12]

starting the scanning of each line with a delay with respect to the previous one. In other words, the timings of the line-wise scanning make the imaging sensor to capture different windows of time of the optical signal coming from a Light Emitting Diode (LED) transmitter (T_x). Then, each line of the image can hold a distinct portion of information.

The use of LEDs available in SCOH's lighting infrastructures, along with optical receivers, for making VLC systems is particularly challenging in outdoor environments. The potential applications of OCC in these scenarios are related to the creation and improvement of communication networks for the vehicular and pedestrian infrastructures [13], where a large number of LED lights and CMOS cameras can be found. The desirable distance coverage of the different services that can take advantage of OCC ranges from a few meters for hand-held receiver devices based on smartphones, and tens of meters for vehicular networks that support Intelligent Transportation Systems (ITS). The achievable link distance in OCC depends partly on the signal-to-noise ratio (SNR) at the receiver, which in turn depends on the transmitted power, the attenuation caused by the channel, the optical lens array of the camera and various sources of noise and interference. In the case of RS-based systems, the maximum link distance is also restricted by the number of lines of pixels covered by the transmitter. For this, the geometry of the transmitting surface, as well as the image forming lens array configuration, determine the image area in pixels [14]. The modulation and packet scheme may have an impact on the maximum link distance if the image frames must contain a number of visible symbols for demodulation. Depending on the case of application, the LED and camera-based transceivers can either have static or mobile positions and orientations, making mobility support essential, which relies on the effective detection of the pixels that have an SNR level suitable for demodulation.

The vehicular VLC (VVLC) are a significant application case with challenging conditions of relative position and motion between nodes. An analysis based on a comparison of VVLC with radio frequency (RF) vehicle-to-vehicle (V2V) links in terms of channel time variation was proposed in [15]. It was shown that the VVLC links have much slower channel time variation as compared to RF V2V links. On the other hand, the VVLC investigation in [16] obtained link duration for VVLC between neighboring vehicles are more than 5 s while in certain other cases the average link duration can be up to 15 s. The safety regulations in [17,18] provide the speed limits and inter-vehicle distance in different weather conditions for the estimation of the desired distance of coverage. Table 1 shows the speed limit based on the European Commission regarding mobility and transport standards, which may vary slightly from one European country to the other. The inter-vehicle distances outlined have been calculated based on the 2 s driving rule for good to bad weather conditions, according to the Government of Ireland, which recommends that a driver maintains a minimum of two seconds apart form the leading vehicle for good weather conditions, which is doubled to four seconds in bad weather.

Table 1. Inter-vehicle distances based on the weather condition based on regulations in [17,18].

	Speed Limits [km/h]		Inter-Vehicle Distance [m]	
Weather condition	Motor ways	Rural roads	Motor ways	Rural roads
Good weather	120–130	80–90	67–72	44-50
Bad weather (V_M = 50 m)	50	50	56	56

The performance of intensity-modulation and direct-detection method employed by LED-to-Photodiode (PD) VLC [9,19], is highly restricted by external light sources such as sunlight, public lighting, and signaling. Moreover, weather conditions, such as the presence of fog, or high temperatures, cause substantial optical distortions [20]. Addressing these challenges, authors in [21] derived a path-loss model for PD-to-LED VLC using Mie's theory and simulating rain and fog conditions in a vehicular VLC setting. They determined the maximum achievable distances as a function of the desired bit-error-ratio (BER) using pulse amplitude modulation (PAM). They found that, for a 32-PAM system, the maximum distance achievable for the desired BER of 10^{-6} is reduced from 72.21 m in clear weather, to 69.13 m in rainy conditions, and 52.85 m and 25.93 m in foggy conditions of different densities. The same Mie's theory is also used in [22] to evaluate a PD-based

VLC link under maritime fog conditions. Scattering and phase functions are derived, as well as the spectrum of the attenuation of optical signals for different distances. In [23], the authors experimented with a LED-to-PD VLC link of 1 m distance based on a single 1 W red LED and multiple PDs attached to a Fresnel lens under dense fog conditions in a laboratory chamber. The lens allows them to maintain a 25 dB signal-to-noise ratio (SNR) varying the optical gain it provides to compensate the attenuation due to the fog presence.

Atmospheric turbulence, and oceanic turbulence in the case of Underwater Wireless Optical Communication (UWOC), has been extensively studied. Guo et al. introduced the traditional lognormal model into a simulated VLC link for ITS [24]. The authors proved that VLC wavelengths in ITS performed worse than longer ones (e.g., 1550 nm), which is straightforward, taking into account that the turbulence measured by Rytov's variance has a dependence on the wavelength. In the case of UWOC, in which the use of visible-range wavelengths is mandatory due to the water absorption spectrum, Kolmogorov's turbulence spectrum is substituted by Nikishov's [25]. This turbulence spectrum fits better with the experimental measurements since it takes into account not only temperature but salinity variations.

Although the impact of turbulence has been characterized for classical optical detectors, its effect on OCC systems has not been adequately addressed yet. Works addressing channel characterization in outdoor OCC links [20] are still scarce compared to the amount of research on PD-based VLC. In the previous work [26], we evaluated the feasibility of a global shutter-based OCC link under fog conditions by the success rate of bits of vehicular link experimentally tested with a red brake light and a digital reflex camera. For a modulation index of 75%, the system showed high reliability under dense fog conditions up to a meteorological visibility of 20 m.

The contribution of this paper is to experimentally derive the feasibility of OCC in emulated outdoor conditions of fog and heat-induced turbulence using commercially available LEDs and cameras. This work is the first to report an experimental investigation on the effects of such conditions on an RS-based system. The experiments carried out for this work were done using a laboratory chamber, and the conditions emulated were of heat-induced turbulence and the presence of fog in the air. The refractive index structure parameter (C_n^2) [27] is used to estimate the level of turbulence and the meteorological visibility (V_M) as a measure of the level of fog. The fog experiments are especially relevant because we utilize the camera's built-in amplifier to overcome the fog attenuation and mitigate the relative contribution of the quantization noise induced by the analog-to-digital conversion stage, ensuring an improvement of the signal quality without increasing the exposure time, and, thus, keeping a high bandwidth.

This paper is structured as follows. Section 2 describes the used methodology, including the channel modeling, the model for the meteorological phenomena studied, and it presents the experimental design. Section 3 presents the experimental setup, describing the laboratory chamber and the OCC system employed. Section 4 shows the obtained results for heat-induced turbulence and fog experiments and performs an in-depth discussion. Finally, conclusions are drawn in Section 5.

2. Methodology

In this section, we describe the relevant processes involved in the CMOS camera mechanism of acquisition in RS-based OCC employed by our system and derive the analytical tools used for the evaluation of its performance in the experimental setting.

2.1. Channel Modelling

In CMOS image sensors, the red-green-blue (RGB) light from a Bayer filter impinges the subpixels. These entities are integrated by PDs and their driving circuit and are grouped by rows connected in parallel to amplifiers and analog/digital converter (ADC) units that are shared by columns. The output of these hardware blocks are image matrices that are sent to the camera digital signal processor (DSP), where data is compressed and delivered to the user as a media file. The sensor performs

RS acquisition, in which the start and end of the exposure of each row of pixels are determined by the circuit's fixed row-shift time (t_{rs}) and the software-defined exposure time (t_{exp}) [28]. The time parameters and circuitry mentioned are shown in Figure 1. Since t_{rs} is fixed, in order to increase the data rate, t_{exp} must be set as low as possible to make the sensor capture the highest diversity of states of the transmitter within each frame. The received power $P_{Rx}(t)$ at a camera coming from a Lambertian light source of order m and transmitted power $P_{Tx}(t)$ can be expressed as

$$P_{Rx}(t) = P_{Tx}(t) \cdot \frac{m+1}{2\pi} \cdot \cos^m \theta \frac{A_{lens} \cos \Psi}{d^2}, \tag{1}$$

where θ and Ψ are the emission and incident angles, respectively, A_{lens} is the area of the camera's external lens, and d is the link span. From the RS mechanism shown in Figure 1, we can express the energy E_i captured by the ith row as

$$E_i = \int_{i \cdot t_{rs}}^{i \cdot t_{rs} + t_{exp}} \frac{P_{Rx}(t)}{\sum_j^v \sum_k^h M_{j,k}} dt, \tag{2}$$

where h (columns), v (rows) are the dimensions of the image sensor, and $M_{[v \times h]}$ is the mask of pixels where the source shape is projected. From the integral limits, it can be derived that the bandwidth of the R_x system decreases with the augment of the exposure time. In other words, the longer is t_{exp}, the more lines are simultaneously exposed, and the received signal is integrated in longer and less diverse time windows. For this reason, frames in OCC have to be acquired within short periods.
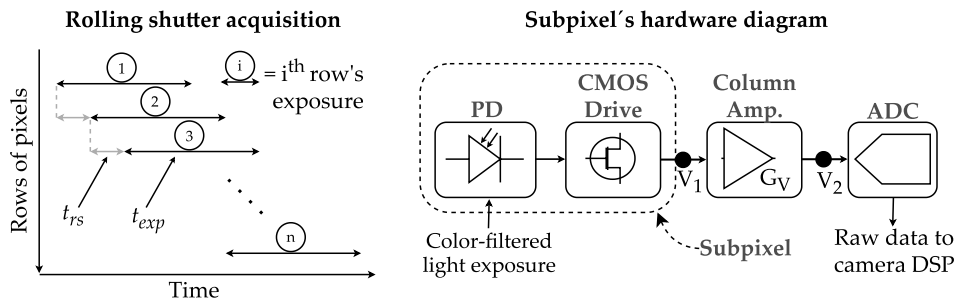

Figure 1. Typical configuration of Complementary Metal-Oxide-Semiconductor (CMOS) camera sub-pixels.

Note that low values of t_{exp}, along with the attenuation factor in outdoor channels caused by the presence of particles such as fog or by the light refraction by turbulence can result in E_i lower than the sensor's lowest threshold of detection. For overcoming this, we can take advantage of the amplifying stage in the subpixel circuitry shown in Figure 1. The voltage-ratio gain G_V of the column amplifier block behaves as

$$G_V(dB) = 20 \log_{10}(V_2 / V_1), \tag{3}$$

where V_1 is the voltage obtained from the pixel integration of light during exposure, and V_2 is the voltage value that is sampled by the ADC. In the case of the IMX219 sensor and of other CMOS sensors with the architecture shown in Figure 1, a software-defined analog gain configuration can set the value of G_V for each capture. The typical values of G_V range from 0 dB to 20.6 dB, as shown in [29].

The column gain G_V of the CMOS sensor amplifies the received signal P_{Rx} and all the noises up to the ADC. This includes the shot noise at the PD, and the thermal noises of the circuits, which can be modeled as random variables of Normal distributions with variances σ_{sh}^2, and σ_{th}^2, as:

$$\sigma_{sh}^2 = 2q_e \left(i_{pd}(x,y,c) + i_d + i_{bg} \right) B, \tag{4}$$

$$\sigma_{th}^2 = \frac{4k_B T_n B}{G_V}, \tag{5}$$

where k_B is the Boltzmann's constant, T_n is noise temperature, $B = 1/t_{rs}$ is the bandwidth, q_e is the electron charge, i_d is the dark current of the camera's pixels, and $i_{pd}(x, y, c)$ is the PD current at pixel (x, y) in the color band $c \in \{R, G, B\}$. This current is determined by the emitted spectrum of the light source, the corresponding Bayer filter, and the substrate's responsivity. Finally, i_{bg} models the contribution of the background illumination level to the shot noise. Nonetheless, since reduced exposure times are generally used, the contribution of i_{bg} can be neglected.

The signal is then sampled by the ADC, introducing quantization noise (σ_{adc}^2), that is usually modeled as a zero-mean random normal contribution whose variance depends on the resolution of the converter. This results in the SNR, which is referred at the DSP's input as:

$$SNR \approx \frac{G_V \cdot i_{pd}^2(x, y, c)}{G_V \left(\sigma_{th}^2 + \sigma_{sh}^2 \right) + \sigma_{adc}^2}. \tag{6}$$

Considering the SNR as a function of G_V, it can be observed that it has an increasing behaviour with an upper asymptote given by $i_{pd}^2(x, y, c)/(\sigma_{th}^2 + \sigma_{sh}^2)$. Especially in the cases when the signal entering the ADC is weak, e.g., as in high attenuation scenarios such as in the presence of dense fog, the relative loss due to quantization noise can be minimized by increasing the column amplification. In other words, the SNR can be optimized by the camera analog gain, unless the ADC is saturated.

Our system employs an On-off keying (OOK) modulation for each of the color bands with a fixed data input that is used as a beacon signal. For bit error ratio (BER) derivation, let us assume the system now works with a random data input of $p_0 = p_1 = 0.5$ as the probabilities of value 0 and 1, respectively. The Maximum Likelihood Estimator (MLE) threshold μ_{mle} at the detection stage of the OOK demodulation is given by

$$\mu_{mle} = (\mu_0 + \mu_1)/2, \tag{7}$$

where μ_0 and μ_1 are the expected values of the received signal for the cases of transmitted signal equal to bits 0 and 1, respectively. If the receiver's DSP applied a digital gain k_d, the resulting MLE threshold would be $\widetilde{\mu_{mle}} = k_d(\mu_0 + \mu_1)/2$. In this case, if $\mu_1 < 2^{n_{bit}}$, where n_{bit} is the bit depth, and $2^{n_{bit}}$ is the maximum digital value of the signal coming from the ADC, the BER would tend to the worst case of a coin flip (error probability equal to 0.5).

2.2. Meteorological Phenomena

The presence of fog particles and turbulence in the air are known as relevant sources of signal distortion in outdoor optical systems. These conditions can be emulated in a laboratory chamber, and well-known parameters can estimate their degree, as explained in the following derivations.

Beer's law [30] can describe the attenuation of propagating optical signals caused by fog. Generally, in optical systems, visibility V_M in km is used to characterize fog attenuation (A_f). Using the Mie's scattering model [31], A_f can be related to V_M as:

$$A_f = \frac{3.91}{V_M} \left(\frac{\lambda}{550} \right)^{-q}, \tag{8}$$

where λ denotes wavelength in nm and parameter q is the distribution size of scattering particles given by Kim's model [32], which is in the short range of visibility (<0.5 km) considered equal to zero. Thus, V_M is given by:

$$V_M = \frac{3.91}{A_f}. \tag{9}$$

The channel coefficient for fog h_f can be determined by applying Beer's law describing light scattering and absorption in a medium as:

$$h_f = e^{-A_f d}. \tag{10}$$

Consequently, the average received optical power for the LOS link at the R_x under fog is expressed as:

$$P_{Rxf}(t) = P_{Rx}(t)h_f + n(t), \tag{11}$$

where $n(t)$ denotes the addition of noises associated with σ_{th}^2 and σ_{sh}^2.

The coefficient h_f depends on the value of the product of fog-attenuation and distance ($A_f \cdot d$), which is known as the optical density of the link. This variable can have the same value for different combinations of fog level and link span, allowing to infer the influence of both variables varying only one of them.

The heat-induced turbulence of air results from variations in temperature and pressure of the atmosphere along the path of transmission. Consequently, this leads to variations of the refractive index of the air, resulting in amplitude and phase fluctuations of the propagating optical beam [33]. For describing the strength of atmospheric turbulence, the parameter most commonly used is the refractive index structure parameter (C_n^2) (in units of m$^{-2/3}$) [34,35], given by:

$$C_n^2 = \left(79 \cdot 10^{-6} \frac{P}{T^2} \right)^2 \cdot C_T^2 \tag{12}$$

where T represents temperature in Kelvin, P is pressure in millibar, C_T^2 is the temperature structure parameter which is related to the universal 2/3 power law of temperature variations [35] given by:

$$D_T = \langle (T_1 - T_2)^2 \rangle = \begin{cases} C_T^2 \cdot L_P^{2/3} & l_0 \ll L_P \ll L_0 \\ C_T^2 \cdot l_0^{-4/3} \cdot L_P^2 & 0 \ll L_P \ll l_0 \end{cases}, \tag{13}$$

where $|T_1 - T_2|$ is the temperature difference between two points separated by distance L_P, while the outer and inner scales of the small temperature variations are denoted by L_0 and l_0, respectively.

2.3. Experimental Design

For the OCC system to be tested under emulated meteorological phenomena, the following conditions were considered. The signal transmitted by the VLC lamp was chosen to be a repetitive beacon, formed by a sequence of on-off pulses of each of the RGB channels, and followed by a black (off state) pulse denoted as K, then, the beacon was arbitrarily set to the following: G-R-B-K. The K pulse allows measuring the dark intensity in the pixels that cover the lamp image, while the pure color pulses allow to estimate the inter-channel cross-talk between the LED RGB colors and the RGB subpixels of the camera, as explained in our previous work [36]. The R_x camera equipment was configured to take captures with fixed t_{exp} and different G_V sequentially. After taking reference measurements, the atmospheric conditions were emulated while the beacon transmission and capture processes were sustained. The reference and test image sequences are processed through the stages shown in Figure 2, including the extraction of relevant pixels area in the picture, the estimation and enhancing of inter-channel cross-talk, and finally, the computation correlation between the signals obtained in clear conditions and under emulated weather conditions.

The extraction of the relevant group of pixels in OCC image frames, known as Region of Interest (ROI) detection, consists of locating the projection of the source in the image. In this case, we first manually locate and extract the ROI from the reference sequence. Then, since the test group is taken with the same alignment, the ROI stays fixed. Thus, the same coordinates of it are re-utilized. The pixels containing data are then averaged by row, giving the three-channel (RGB) signal $T_{[M \times 3]}$, where N is the number of rows of the ROI. From the reference ROI, a template of one G-R-B-K beacon signal is saved as $R_{[N \times 3]}$, where M is the number of rows used by one beacon in the RS acquisition.
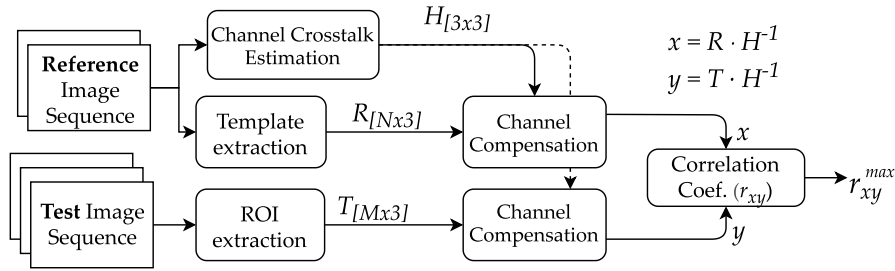
Figure 2. Flow diagram of the offline processing of data captured by cameras.

As shown in previous work [36], the inter-channel cross-talk (ICCT), which is caused by the mismatch between the LEDs and the camera's Bayer filter spectra, is estimated from clear frames and then compensated in all datasets. We separately analyze R, G, and B pulses from the beacon signal. A matrix $H_{[3\times3]}$ is obtained by averaging the contribution of each pure-LED pulse at the three RGB subpixels. In other words, a component h_{ij} from $H_{[3\times3]}$ is the average measure from the jth subpixel when the ith LED is illuminating it, where $i, j \in \{R, G, B\}$. The inverse matrix $H_{[3\times3]}^{-1}$ is used to clean all the datasets from ICCT found at this configuration. Finally, ICCT cleaned signals $x = (R \cdot H^{-1})_{[N\times3]}$ and $y = (T \cdot H^{-1})_{[M\times3]}$ are compared using the Pearson's correlation coefficient r_{xy}, which is defined as:

$$r_{xy} = \frac{\sum_{i=1}^{N}(x_i - \bar{x})(y_i - \bar{y})}{\sqrt{\sum_{i=1}^{N}(x_i - \bar{x})^2}\sqrt{\sum_{i=1}^{N}(y_i - \bar{y})^2}}, \tag{14}$$

where x_i are the reference sample points from R, of size N, y_i are N consecutive samples of T, and $\bar{x}, \bar{y}$ are the mean values. The correlation is calculated for all possible consecutive subsets $y_j, y_{j+1}, ..., y_{j+N-1}, (j + N - 1) < M$ and the maximum value r_{xy}^{max} is considered the similarity of the frame compared to the reference.

3. Experimental Setup

In this section, we describe the full setup of our experiments, which is shown in Figure 3, including the laboratory chamber used, the tools used for emulating hot and foggy weather conditions, the measurement devices used for estimating the levels of each condition, and the T_x and R_x devices that comprise the OCC link. The key experiment parameters are listed in Table 2 and the block diagram of the experimental setup is shown in Figure 4.
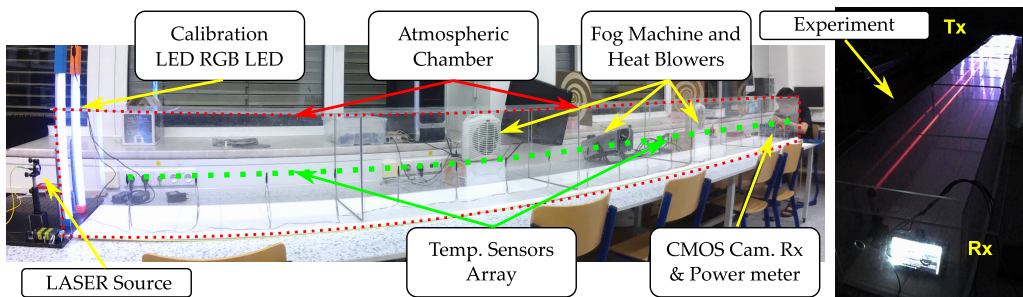

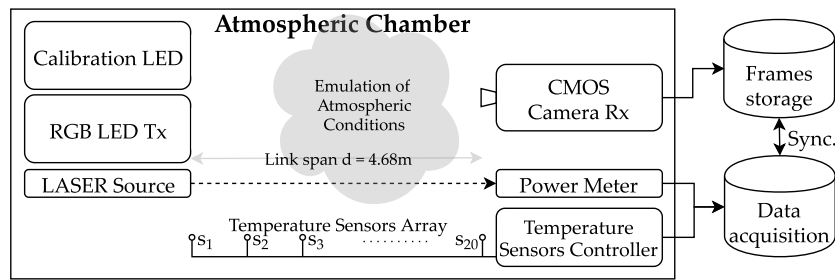**Figure 3.** Photos of the laboratory setup utilized in the experiments.

Figure 4. Block diagram of the experimental setup.

Table 2. Experiment key parameters.

Parameter	Value
	Transmitter
Device	12 V DC RGB LED strips (108×5050 SMD chips)
Front-end device	Microcontroller Atmel ATMega328p [37]
Idle power [W]	4.76
Dominant wavelengths [nm]	630 (Red), 530 (Green), 475 (Blue)
T_{chip} [s]	1/8400
	Receiver
Camera	Picamera V2 module (Sony IMX219)
Resolution	3280×2464 px
t_{exp} [µs]	60
Gain (G_V) [dB]	$0, 1, \ldots, 16$
Frame rate [fps]	30
	Laboratory chamber
Dimensions [m]	$4.910 \times 0.378 \times 0.368$
Temperature sensors	$20 \times$ Papouch Corp. TQS3-E (range: -55 to $+125^\circ C \times 0.1^\circ C$)
LASER source	Thorlabs HLS635 (635 nm) F810APC
Optical power meter	Thorlabs PM100D S120C
Heat blowers	$2 \times$ Sencor SFH7010, 2000 W
Fog machine	Antari F-80Z, 700 W

3.1. Laboratory Chamber

The atmospheric chamber set up for measurements in the facilities of the Czech Technical University in Prague [27] features two heater fans, and one Glycerine machine, that can blow hot air and fog into the chamber, respectively. For the characterization of turbulence and light scintillation in the chamber, an array of 20 temperature sensors were set up equidistantly. A laser source of 625 nm and 2 mW, and an optical power meter placed on each end of the chamber are used to measure the fog attenuation.

3.2. OCC System

The transmitter unit was built using strips of RGB LEDs connected to a microcontroller (model ATmega328p [37]) through a switching circuit based on transistors. The LED arrays were installed on aluminum rails with a white meth-acrylate diffuser. The circuitry makes the RGB channels to emit the beacon signal (idle state) repeatedly, or to send arbitrary data coming from a serial port (this feature was not used in this experiment). The chip time t_{chip} or the pulse width is set by software in the microcontroller. In the case of the experiments, this parameter was set to 1/8400 s.

The receiver was made using an Element14 Raspberry Pi board with its official camera device PiCamera V2. The firmware allows to set G_V from 1 to 16 dB and exposure time from 20 ns up to the time elapsed between frame captures, which in case of 30 fps video is approximately 33.3 ms. The fixed internal structure of the CMOS sensor (Sony IMX219) featured by the PiCamera is set to have a row-shift time $t_{rs} = 18.904$ µs [29]. The exposure time was set to $t_{exp} = 60$ µs.

Given the hardware configuration of our system in the laboratory, as shown in Figure 3, each of the image frames can contain up to 64 symbols. Since the modulation uses RGB channels, each symbol then is formed by 3 bits. The maximum throughput of this configuration at 30 fps is then 5.76 kbps.

4. Results

In this section, we show the results from the analysis of the images obtained from heat-turbulence and fog experiments carried out, as shown in Section 3. The maximum values of the correlation coefficient were computed between the ICCT-compensated reference image sequence and the images captured under different conditions, as explained in Section 2. The r_{xy}^{max} values obtained are analyzed together with the experimental parameters set: C_n^2 in the case of heat-induced turbulence, and V_M, G_V, in the case of fog.

4.1. Heat-Turbulence Experiments

The heat-turbulence experiment's reference image sequence was captured using the chamber heaters off at a stabilized laboratory temperature of 21.7 °C. Thus, the template signal extracted from these captures is the result of operating the system under a negligible level of turbulence. The remaining test image sequence was captured under the thermal influence of channel in two parts, one under a higher laboratory temperature of 32.3 °C, and a second part with the heaters of the chamber working at full power, setting another turbulence level. The C_n^2 parameter value is then calculated using the temperature sensors samples. The r_{xy}^{max} values between the frames of the test image sequence and the template are calculated. With these values, we infer the influence of this phenomenon.

The refractive index structure parameter values during the first part of the test image sequence capture ranged from $C_n^2 = 1.86 \cdot 10^{-11}$ m$^{-2/3}$ to $2.51 \cdot 10^{-11}$ m$^{-2/3}$ in high room temperature with the heaters off. In the second part, the range of turbulence increased to $4.69 \cdot 10^{-11}$ m$^{-2/3} \leq C_n^2 \leq 7.13 \cdot 10^{-11}$ m$^{-2/3}$. The obtained r_{xy}^{max} between the signals from each part of the experiment and the template are shown as histograms in Figure 5. To estimate the similarity between the r_{xy}^{max} data from the reference and from each part of the test image sequence, a Kolmogórov-Smirnov (KS) statistical test was done, which consists of a non-parametric tool that estimates if two data sets are samples from the same distribution with a confidence p-value [38]. The result is that the first part of the test image sequence has $p = 0.81$ confidence value of having the same distribution as the reference, and the second has $p = 0.83$. It can be seen an almost negligible influence of turbulence on OCC systems.
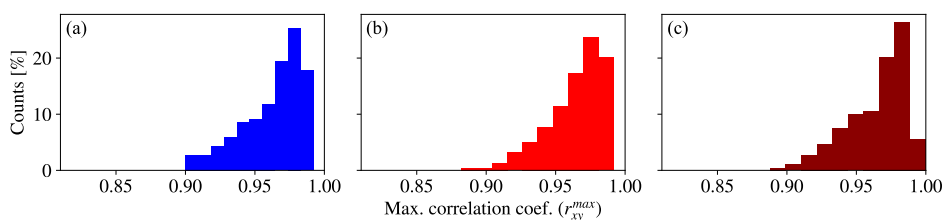

Figure 5. Distribution of maximum correlation coefficient values of image sequences taken (**a**) under a cool room temperature of 21.7 °C (no turbulence), (**b**) under a warm room temperature of 32.3 °C and with heaters off, and (**c**) with turbulence induced by the heaters.

The different ranges of turbulence analyzed presumably have the same distribution of r_{xy}^{max} values, according to the KS statistical test, and also the vast amount of them meet that $r_{xy}^{max} > 0.9$, which means that the experimental setup's behavior is considerably similar to the reference, regardless of the turbulence ranges that were induced. This robustness of the system can be attributed to the short link distance and the big field of view of the camera. Both make the refraction effects unnoticeable in the received signal of our system.

4.2. Fog Experiments

For the fog emulation experiment, the reference image sequence was taken under clear air in the laboratory chamber while the optical power meter measured the power of the laser without fog attenuation. The test image sequence was taken while the chamber was arbitrarily supplied with fog from the Antari F-80Z, while the laser power was measured in synchronicity in order to label each image with the current V_M. The value of G_V of the images was sequentially modified from 0 to 16 dB by steps of 1 dB during the test image sequence, while for the reference, it was set to zero as default.

The r_{xy}^{max} values obtained for the test images sequence varying G_V and V_M are shown as a contour plot in Figure 6. The high correlation area ($r_{xy}^{max} > 0.9$) determines three important regions (highlighted in Figure 6 by dashed circles). For the high values of visibility, the signal coming from the transmitter is not affected by the fog attenuation and is received with the highest power. Then, the increase of gain causes saturation of the ADC, affecting the correlation. In the low visibility region, the presence of dense fog attenuates the received signal and lowers the correlation. It can be seen that, in this low-visibility region, the increase of gain gives a high correlation, meaning that the camera amplifier compensates the attenuation from fog. The region in between, around 50 m visibility, shows high values of correlation regardless of the variations of gain. The three regions described are shown in Figure 7, and a non-parametric locally estimated scatterplot smoothing (LOESS) regression [39] is performed with parameter span $s = 0.5$ to show the trend of the data points. Examples of the ROI extraction from test images sequence are included to depict the effect of visibility and gain over the frames.
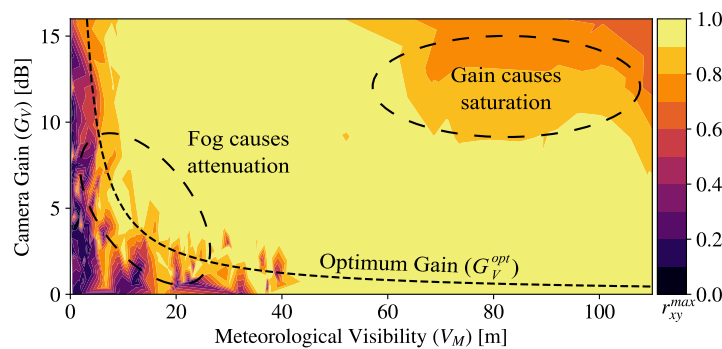

Figure 6. Maximum correlation between test and reference signals varying camera gain under emulated fog conditions of different values of meteorological visibility.
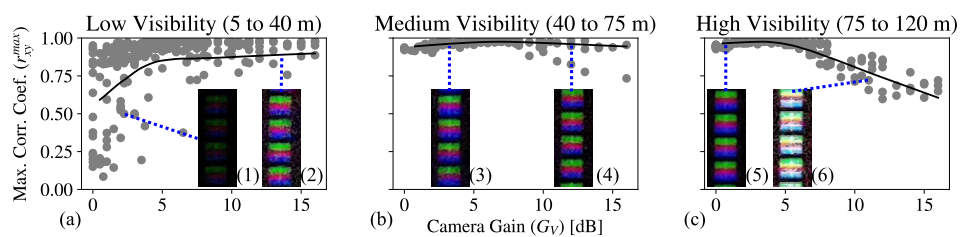

Figure 7. Maximum correlation data (gray dots) from fog-emulation experiments, separated by levels of (**a**) low, (**b**) medium, and (**c**) high visibility and their respective locally estimated scatterplot smoothing (LOESS) regression for $s = 0.5$ (black curves). The area encircled in (**a**) is the region of image frames affected by the fog attenuation and in (**b**) by gain saturation. Insets are Region of Interest (ROI) extraction examples: (1) for low visibility and low gain, (2) low visibility and high gain, (3) medium visibility and low gain, (4) medium visibility and high gain, (5) high visibility and low gain, and (6) high visibility and high gain.

From the minimum gain values in the area of $r_{xy}^{max} > 0.9$, an optimum gain curve G_V^{opt} is derived providing that there is an inverse proportionality relationship between meteorological visibility and camera gain as follows:

$$G_V^{opt}(V_M) = \frac{k_v}{V_M},\tag{15}$$

where k_v is an empirical parameter. Using curve fitting, the value $k_v = 0.0497$ dB·km was derived for our experimental setup.

In order to calculate the SNR from the empirical data obtained, we have considered that OOK modulation is used. The following approximation of the SNR has been derived (note the $1/2$ factor due to OOK):

$$SNR = \frac{1}{2} \frac{E^2 [X_{ROI}]}{V [X_{ROI}]},\tag{16}$$

where X_{ROI} comprises the samples of pixels that fall within the ROI mask $M_{[v \times h]}$ as described in Equation (2), which was determined from reference images and since the T_x and R_x are static it is the same for the whole experiment. $E[\cdot]$, and $V[\cdot]$ denote the statistical expected value and variance, respectively.

The empirical SNR definition was calculated for all the image sequences of the fog experiments. The results for the frames taken with $G_V = 11$ dB are shown in Figure 8 for the three RGB channels. This value of gain was chosen because, as shown in Figure 6, the level $G_V = 11$ dB is affected by the dense fog and also by the saturation. The SNR values in Figure 8 are plotted against optical density in logaritmic scale. They show that higher attenuation A_f values, or alternatively, longer link spans, cause a decay of the SNR. Therefore, a curve fitting was carried out assuming that the SNR decays at a rate of α dB per decade of optical density, as follows:

$$SNR(A_f d) = SNR(1) + \alpha \cdot \log(A_f d),\tag{17}$$

where SNR(1) is the estimated signal-to-noise ratio at unitary optical density.
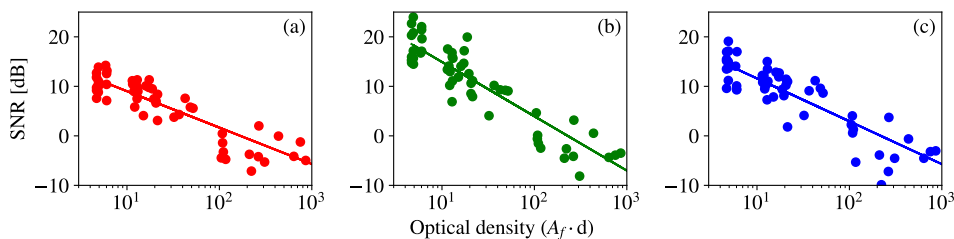

Figure 8. Empirical signal-to-noise ratio (SNR) values obtained from captures at $G_V = 11$ dB plotted against optical density values at fixed link range d and with A_f values emulated by the presence of fog. The plot in (**a**) corresponds to R channel, (**b**) to G channel, and (**c**) to B channel, and their respective fitted curves.

The SNR values obtained from the image sequences were also evaluated on their influence over r_{xy}^{max}, as shown in Figure 9. A LOESS regression also shows the trend of the scatterplots in the figure, and it can be seen that r_{xy}^{max} increases with the SNR, except for the highest SNR values in the blue channel, which are affected by saturation of the ADC. It can also be seen that SNR values higher than 5 dB make $r_{xy}^{max} > 0.9$ for most of the samples. From this, it can be concluded that r_{xy}^{max} is a valid metric for the quality of the signal in OCC, although SNR is more robust.
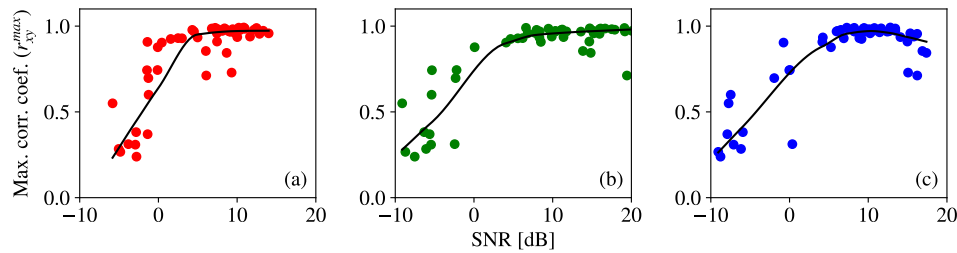
Figure 9. Values of r_{xy}^{max} from test image sequence of the fog-emulation experiment plotted against empirical SNR. The values are for frames taken with $G_V = 11$ dB. The scatter plot in (**a**) corresponds to R channel, (**b**) to G channel, and (**c**) to B channel, and the curves in black are their corresponding LOESS regression for span value $s = 0.7$.

The results obtained in this experiment show that the fog attenuation can make the power of the optical signal weaken down to the point that the noise induced by the ADC considerably affects the SNR. In other words, the conversion to digital corrupts the weak optical signal from dense fog conditions or long link spans. In these cases, the column amplifier of the camera is crucial to keep a high amplitude input at the ADC and reduce the effect of quantization.

5. Conclusions

In this paper, we presented an experimental study of the influence of two kinds of atmospheric conditions over an RS-based OCC link: the heat-induced turbulence due to random fluctuations of the refractive index of the air along the path, and the attenuation caused by the presence of fog particles in the air. The image sequences captured under the two different conditions were compared to a reference sequence of images taken under clear conditions. For this, we used the maximum value of Pearson's correlation coefficient r_{xy}^{max} to determine their similarity. We have also evaluated the signal quality by the empirical SNR obtained from the image frames and showed its relationship with r_{xy}^{max} and its dependence on the product between fog attenuation and link span, known as the optical density. The most important findings in this work are, first, that the turbulence levels emulated do not affect the signal quality considerably. For the fog experiments, we have derived an expression for the theoretical SNR as a function of the analog camera gain, showing that a CMOS camera-based OCC system can improve the SNR by using the column amplifier. In the fog experiments, the correlation r_{xy}^{max} was impaired in two different cases: for high values of V_M, when the gain is increased, the correlation drops because of the saturation of the signal, and, for low visibility, the attenuation caused by the fog impairs the similarity to the reference when the gain is low, because of the loss due to quantization noise at the ADC. It was found for the latter case that by increasing the gain of the camera, the attenuation can be compensated, allowing the OCC link to receive signal with a $r_{xy}^{max} > 0.9$ for V_M values down to 10 m. Our findings show that there is an inverse proportionality relationship between the optimum camera gain and the visibility, and that the empirical SNR decays at a rate α with the optical density. This utilization of the CMOS camera's built-in amplifier opens a new possibility for OCC systems, extending the control strategy, and allowing to keep low exposure times and, thus, a high bandwidth, even in dense fog scenarios.

Conflicts of Interest: The authors declare no conflict of interest. The funders had no role in the design of the study; in the collection, analyses, or interpretation of data; in the writing of the manuscript, or in the decision to publish the results.

References

1.　Cahyadi, W.A.; Kim, Y.H.; Chung, Y.H.; Ahn, C.J. Mobile phone camera-based indoor visible light communications with rotation compensation. *IEEE Photonics J.* **2016**, *8*, 1–8. [CrossRef]

2.　Teli, S.R.; Zvanovec, S.; Ghassemlooy, Z. Performance evaluation of neural network assisted motion detection schemes implemented within indoor optical camera based communications. *Opt. Express* **2019**, *27*, 24082–24092. [CrossRef] [PubMed]

3.　Chavez-Burbano, P.; Vitek, S.; Teli, S.; Guerra, V.; Rabadan, J.; Perez-Jimenez, R.; Zvanovec, S. Optical camera communication system for Internet of Things based on organic light emitting diodes. *Electron. Lett.* **2019**, *55*, 334–336. [CrossRef]

4.　Tiwari, S.V.; Sewaiwar, A.; Chung, Y.H. Optical bidirectional beacon based visible light communications. *Opt. Express* **2015**, *23*, 26551–26564. [CrossRef] [PubMed]

5.　Pergoloni, S.; Biagi, M.; Colonnese, S.; Cusani, R.; Scarano, G. Coverage optimization of 5G atto-cells for visible light communications access. In Proceedings of the 2015 IEEE International Workshop on Measurements & Networking (M&N), Coimbra, Portugal, 12–13 October 2015; pp. 1–5.

6.　Boban, M.; Kousaridas, A.; Manolakis, K.; Eichinger, J.; Xu, W. Connected roads of the future: Use cases, requirements, and design considerations for vehicle-to-everything communications. *IEEE Veh. Technol. Mag.* **2018**, *13*, 110–123. [CrossRef]

7.　Yamazato, T.; Takai, I.; Okada, H.; Fujii, T.; Yendo, T.; Arai, S.; Andoh, M.; Harada, T.; Yasutomi, K.; Kagawa, K.; et al. Image-sensor-based visible light communication for automotive applications. *IEEE Commun. Mag.* **2014**, *52*, 88–97. [CrossRef]

8.　Takai, I.; Ito, S.; Yasutomi, K.; Kagawa, K.; Andoh, M.; Kawahito, S. LED and CMOS image sensor based optical wireless communication system for automotive applications. *IEEE Photonics J.* **2013**, *5*, 6801418. [CrossRef]

9.　Ghassemlooy, Z.; Alves, L.N.; Zvanovec, S.; Khalighi, M.A. *Visible Light Communications: Theory and Applications*; CRC Press: Borarton, FL, USA, 2017.

10.　Boubezari, R.; Le Minh, H.; Ghassemlooy, Z.; Bouridane, A. Smartphone camera based visible light communication. *J. Lightwave Technol.* **2016**, *34*, 4121–4127. [CrossRef]

11.　Nguyen, T.; Islam, A.; Hossan, T.; Jang, Y.M. Current status and performance analysis of optical camera communication technologies for 5G networks. *IEEE Access* **2017**, *5*, 4574–4594. [CrossRef]

12.　Nguyen, T.; Hong, C.H.; Le, N.T.; Jang, Y.M. High-speed asynchronous Optical Camera Communication using LED and rolling shutter camera. In Proceedings of the 2015 Seventh International Conference on Ubiquitous and Future Networks, Sapporo, Japan, 7–10 July 2015; pp. 214–219.

13.　Chavez-Burbano, P.; Guerra, V.; Rabadan, J.; Perez-Jimenez, R. Optical camera communication for smart cities. In Proceedings of the 2017 IEEE/CIC International Conference on Communications in China (ICCC Workshops), Qingdao, China, 22–24 October 2017; pp. 1–4. [CrossRef]

14.　Chavez-Burbano, P.; Guerra, V.; Rabadan, J.; Rodriguez-Esparragon, D.; Perez-Jimenez, R. Experimental characterization of close-emitter interference in an optical camera communication system. *Sensors* **2017**, *17*, 1561. [CrossRef] [PubMed]

15.　Cui, Z.; Wang, C.; Tsai, H.M. Characterizing channel fading in vehicular visible light communications with video data. In Proceedings of the 2014 IEEE Vehicular Networking Conference (VNC), Paderborn, Germany, 3–5 December 2014; pp. 226–229.

16.　Wu, L.C.; Tsai, H.M. Modeling vehicle-to-vehicle visible light communication link duration with empirical data. In Proceedings of the 2013 IEEE Globecom Workshops (GC Wkshps), Atlanta, GA, USA, 9–13 December 2013; pp. 1103–1109.

17. Mobility and Transport (European Comission). Current Speed Limit Policies. Available online: https://ec.europa.eu/transport/road_safety/specialist/knowledge/speed/speed_limits/current_speed_limit_policies_en (accessed on 28 January 2020).

18. Road Safety Authority (Government of Ireland). The Two-Second Rule. Available online: http://www.rotr.ie/rules-for-driving/speed-limits/speed-limits_2-second-rule.html (accessed on 28 January 2020).

19. Kim, Y.h.; Chung, Y.h. Experimental outdoor visible light data communication system using differential decision threshold with optical and color filters. *Opt. Eng.* **2015**, *54*, 040501. [CrossRef]

20. Islam, A.; Hossan, M.T.; Jang, Y.M. Convolutional neural networkscheme–based optical camera communication system for intelligent Internet of vehicles. *Int. J. Distrib. Sens. Netw.* **2018**, *14*, 1550147718770153. [CrossRef]

21. Elamassie, M.; Karbalayghareh, M.; Miramirkhani, F.; Kizilirmak, R.C.; Uysal, M. Effect of fog and rain on the performance of vehicular visible light communications. In Proceedings of the 2018 IEEE 87th Vehicular Technology Conference (VTC Spring), Porto, Portugal, 3–6 June 2018; pp. 1–6.

22. Tian, X.; Miao, Z.; Han, X.; Lu, F. Sea Fog Attenuation Analysis of White-LED Light Sources for Maritime VLC. In Proceedings of the 2019 IEEE International Conference on Computational Electromagnetics (ICCEM), Shanghai, China, 20–22 March 2019; pp. 1–3. [CrossRef]

23. Kim, Y.H.; Cahyadi, W.A.; Chung, Y.H. Experimental demonstration of VLC-based vehicle-to-vehicle communications under fog conditions. *IEEE Photonics J.* **2015**, *7*, 1–9. [CrossRef]

24. Guo, L.-d.; Cheng, M.-j.; Guo, L.-x. Visible light propagation characteristics under turbulent atmosphere and its impact on communication performance of traffic system. In Proceedings of the 14th National Conference on Laser Technology and Optoelectronics (LTO 2019), Shanghai, China, 17 May 2019; p. 1117047. [CrossRef]

25. Nikishov, V.V.; Nikishov, V.I. Spectrum of Turbulent Fluctuations of the Sea-Water Refraction Index. *Int. J. Fluid Mech. Res.* **2000**, *27*, 82–98. [CrossRef]

26. Eso, E.; Burton, A.; Hassan, N.B.; Abadi, M.M.; Ghassemlooy, Z.; Zvanovec, S. Experimental Investigation of the Effects of Fog on Optical Camera-based VLC for a Vehicular Environment. In Proceedings of the 2019 15th International Conference on Telecommunications (ConTEL), Graz, Austria, 3–5 July 2019; pp. 1–5.

27. Bohata, J.; Zvanovec, S.; Korinek, T.; Abadi, M.M.; Ghassemlooy, Z. Characterization of dual-polarization LTE radio over a free-space optical turbulence channel. *Appl. Opt.* **2015**, *54*, 7082–7087. [CrossRef] [PubMed]

28. Kuroda, T. *Essential Principles of Image Sensors*; CRC Press: Borarton, FL, USA, 2017.

29. IMX219PQH5-C Datasheet. Available online: https://datasheetspdf.com/pdf/1404029/Sony/IMX219PQH5-C/1 (accessed on 28 January 2020)

30. Weichel, H. *Laser Beam Propagation in the Atmosphere*; SPIE Press: Bellingham, WA, USA, 1990; Volume 3.

31. Henniger, H.; Wilfert, O. An Introduction to Free-space Optical Communications. *Radioengineering* **2010**, *19*, 203–212.

32. Kim, I.I.; McArthur, B.; Korevaar, E.J. Comparison of laser beam propagation at 785 nm and 1550 nm in fog and haze for optical wireless communications. In Proceedings of the Optical Wireless Communications III. International Society for Optics and Photonics, Boston, MA, USA, 6 February 2001; pp. 26–37.

33. Ghassemlooy, Z.; Popoola, W.; Rajbhandari, S. *Optical Wireless Communications: System and Channel Modelling with Matlab*; CRC Press: Borarton, FL, USA, 2019.

34. Nor, N.A.M.; Fabiyi, E.; Abadi, M.M.; Tang, X.; Ghassemlooy, Z.; Burton, A. Investigation of moderate-to-strong turbulence effects on free space optics—A laboratory demonstration. In Proceedings of the 2015 13th International Conference on Telecommunications (ConTEL), Graz, Austria, 13–15 July 2015; pp. 1–5.

35. Andrews, L.C.; Phillips, R.L. *Laser Beam Propagation Through Random Media*; SPIE Press: Bellingham, WA, USA, 2005; Volume 152.

36. Jurado-Verdu, C.; Matus, V.; Rabadan, J.; Guerra, V.; Perez-Jimenez, R. Correlation-based receiver for optical camera communications. *Opt. Express* **2019**, *27*, 19150–19155. [CrossRef] [PubMed]

37. Atmel Corporation. *ATmega328p, 8-bit AVR Microcontroller with 32K Bytes In-System Programmable Flash, Datasheet*; Atmel Corporation: San Jose, CA, USA, 2015.

38. Massey, F.J., Jr. The Kolmogorov-Smirnov Test for Goodness of Fit. *J. Am. Stat. Assoc.* **1951**, *46*, 68–78. [CrossRef]

39. Cleveland, W.S.; Devlin, S.J. Locally weighted regression: an approach to regression analysis by local fitting. *J. Am. Stat. Assoc.* **1988**, *83*, 596–610. [CrossRef]

4.8 A SIMO hybrid visible light communication system for optical IoT

This chapter is a early access version of the accepted manuscript for publication in Journal:

S. R. Teli, P. Chvojka, S. Vitek, S. Zvanovec, R. Perez-Jimenez, Z. Ghassemlooy "A SIMO hybrid visible light communication system for optical IoT," *IEEE Internet of Things Journal*, 2021, *Accepted for publication* (early access version).

Connection to my Ph.D. thesis:

Unlike the hybrid wired and wireless schemes proposed in [100, 101], the VLC system with hybrid PD- and camera-based Rxs can be used in short-range indoor OIoT. Low R_b (R_{b-Low}) applications, as previously mentioned, can be supported by OCC links, while high R_b (R_{b-High}) applications such as online streaming, downloading big data, internet surfing, etc., can be supported by PD-VLC links hence offering good degrees of mobility and applications in the OIoT environments while using a single Tx. Therefore, integrating both VLC-PD and OCC (IS-based VLC) links simultaneously can provide a versatile OIoT environment, where users can have a choice based on the device to switch between high- and low-speed VLC. However, there are still challenges in the integration of both technologies within the single hybrid system, such as:

- lower and limited frame rate in contrast to high-speed PDs

- incompatibility in R_b between VLC with PDs and IS, i.e., $R_{b-High} >> R_{b-Low}$

- the use of LEDs with different modulation bandwidth in PD- and IS-based VLC links, which can result in interference and noise in other's Rxs

- the increase in the overall implementation cost due to use of multiple LEDs.

As a solution to these challenges, in this work, we propose a SIMO hybrid VLC system utilizing a single LED-based Tx, and PD- and IS-based Rxs for high- and low-speed data transmission simultaneously, respectively. We propose a new hybrid modulation format that can be used for both high- and low-speed VLC links, and develop an experimental test-bed for verification. We present results for evaluating the link performance in terms of the BER and the reception success by considering the impact of the low-speed IS-based VLC on the PD-based VLC and vice versa.

A SIMO Hybrid Visible Light Communication System for Optical IoT

Shivani Rajendra Teli, Petr Chvojka, Stanislav Vitek, Stanislav Zvanovec (Senior Member, IEEE), Rafael Perez-Jimenez, and Zabih Ghassemlooy (Senior Member, IEEE)

Abstract—**Visible light communications (VLC) is an emerging technology utilizing light emitting diodes and photodetectors (PDs) and cameras (i.e., image sensors (ISs)) as the transmitter and receivers (Rx), respectively for simultaneous data communications, illumination, localization and sensing in indoor optical Internet of Things. We propose, a single-input multiple-output (SIMO) hybrid VLC system using PD- and IS-based Rxs for simultaneous high- and low-speed (i.e., $R_{b\text{-High}}$ and $R_{b\text{-Low}}$) data transmission. In addition, we propose amplitude overlapping A_{OL} in the modulation format to increase the R_b and reduce the attenuation due to high-pass filter effect of the bias-T. We experimentally evaluate the performance of the proposed scheme considering the inter-link impacts. Results show that, at A_{OL} of 0 - 0.2, (*i*) the measured bit error rate for the PD-based VLC is below the forward error correction limit of 3.8×10^{-3} for $R_{b\text{-Low}}$ of 2.5 and 5 kb/s at $R_{b\text{-High}}$ of 35 and 60 Mb/s, respectively; and (*ii*) for the IS-based VLC link with the camera gain of 4 dB and $R_{b\text{-High}}$ of up to 70 Mb/s, the reception success rates are > 96 and 90 % at $R_{b\text{-Low}}$ of 2.5 and 5kb/s, respectively.**

Index Terms— **Internet of Things (IoT), single-input multiple output (SIMO), light emitting diodes (LEDs), visible light communications (VLC), photodiode (PD), optical camera communications (OCC), camera, image processing.**

I. INTRODUCTION

RECENT developments in Internet of Things (IoT) stems largely from interconnections and communications between a number of users and a plethora of different devices, collectively referred to as the smart devices connected to the wireless cellular networks [1]. This wireless-based IoT assists in developing and implementing the smart indoor environments (i.e., homes, offices, hospitals and industries), which enable interactions between smart devices and humans, as part of the fifth and sixth generation wireless networks. The major requirements in IoT-based communications system designs are [2]: (*i*) human value - smart applications, substantial benefits, quality of life and better utilization of resources; (*ii*) data value - secured links and fast processing; (*iii*) connectivity - protocol developments; and (*iv*) efficiency and availability. Note that, it is challenging to fulfil the aforementioned requirements by only relying on the costly and frequency spectrum congested radio frequency (RF) technologies. Alternatively, in many applications, where RF cannot be deployed due security

reasons, insufficient spectrum, etc., the optical wireless communications (OWC) technology covering ultraviolet, infrared, and visible bands can be adopted in IoT as part of the 5G wireless networks [3]. OWC utilizing the visible light spectrum (i.e., ~370-780, nm), known as visible light communications (VLC) with a useable bandwidth B of ~ 400 THz, which is 10,000 times wider than RF [4, 5], uses light-emitting diodes (LEDs) luminaries and photodetectors (PDs) to simultaneously provide data communications, illumination, localization, and sensing in mostly indoor environments [4]. VLC systems with data rates R_b within the range of 100 Mb/s to 15.7 Gb/s using polarization division multiplexing [6] and orthogonal frequency division multiplexing (OFDM) with adaptive bit loading technique [7 – 9], respectively have been reported in the literature.

Utilizing LED-based lighting infrastructures offer benefits such as lower power consumption, longer life expectancy, lower flicker factor, lower heat generation, and fast switching, where the latter is highly desirable in high-speed applications [4, 5]. To this end, extensive works have been reported by extending the point-to-point VLC links defined in IEEE 802.15.7 standard [10] also termed as light-fidelity (LiFi). LiFi utilizing off-the-shelf LEDs was proposed as an enabler for the IoT in indoor environments [11] with three main features such as precise positioning, power delivery since energy can be harvested from light, and inherent security [11]. In [12], the LiFi-enabled bidirectional IoT communications system with visible and infrared lights used in the downlink and uplink, respectively was investigated. In the proposed bidirectional LiFi-IoT system, a non-orthogonal multiple access scheme with the quality-of-service guaranteed optimal power allocation strategy was adopted to maximize the energy efficiency of both down- and up-link [12]. Therefore, the realization of all optical IoT (OIoT) using the VLC/OCC technology with multiuser bidirectional transmission [13], multiple access [14], and handover [15] features has been made possible [16].

Hybrid OWC schemes using fiber links to transmit high-speed signals from the base station/optical line terminal to the indoor access network/optical network unit, and VLC-PD links in an indoor access network have been proposed in the literature. In [17], M-ary amplitude shift keying (MASK)

quadrature amplitude modulation (QAM)-OFDM using a 2 GHz direct-modulated-laser (DML) with net data rates up to 4.18 and 3.80 Gb/s for fast Fourier transform sizes of 128 and 64 was reported. In [17], a lower frequency MASK signal modulates the power of each OFDM symbol, where the total power of an OFDM symbol denotes the MASK signal. The positive half and the full modulation depths were used to represent the low bit 0 and high bit 1, respectively. In [18], OFDM-based passive optical network was proposed for the hybrid wired and wireless optical access network. In the adaptive envelope modulation, multiple consecutive unipolar (CE) OFDM symbols are grouped together via symbols grouping and the power of each constant envelope CE-OFDM symbol group is determined by the M-ary pulse amplitude modulation (M-PAM) encoded wireless input data via power allocation. For indoor OWC, a DC bias is first added to the M-PAM signal prior to intensity modulation of the LED. Following indoor free-space transmission, at the receiver the light focused on the PD via a lens. The regenerated electrical M-PAM signal is A/D converted and demodulated to generate the transmitted data stream.

On the other hand, VLC systems employing a IS-based receiver (Rx) better known as optical camera communications (OCC) (defined within IEEE 802.15.7 SG 7 [19]) have been gaining attention in the research community and industry because of the availability of smart devices integrated with high-speed and high-quality cameras [20]. Note, the CMOS-based cameras can capture images or record video streams using the global shutter (GS)- and rolling shutter (RS)-based capturing modes at different resolutions. The RS-based cameras can simultaneously capture multiple LEDs (i.e., in ON and OFF states) in a single frame, as rows of the image pixels are exposed to the light one at a time [21], thus achieving flicker-free transmission with increased R_b. However, R_b is rather low mainly limited mainly by the camera frame-rate f_R. For human, f_R is 16 fps, as this is the threshold to which the mind no longer perceives sequences as flashing images. For films, typically f_R is used in the range of 24 to 48 fps, a value slightly above the perceptual limit, while in advanced smartphones with slow motion capabilities, f_R could be as high as 120 fps with high-definition formats such as 1280×720 pixels. For sport action and professional high-speed cameras f_R are 240 and > 1000 fps, respectively.

Unlike the hybrid wired and wireless schemes proposed in [17, 18], the VLC system with hybrid PD- and camera-based Rxs can be used in short-range indoor OIoT applications for positioning, localization, navigation [22, 23], device-to-device communications (where higher R_b is not the main requirement), mobile transactions, motion-based device control [24], small identification information, communications through advertisements [25], etc., which offer good degrees of mobility in the OIoT environments [24, 26]. A number of VLC systems for use in IoT have been reported including (i) DIMLOC - dimmable LEDs in smart buildings using a smartphone camera-based Rx [22]; (ii) integrated VLC and VLC positioning networks [27]; (iii) Foglight - spatial encoding using a projector-based on the gray-coded binary images [23]; and (iv)

LiFi4IoT - that provides three individual motes such as (a) retroreflector using downlink OCC and a liquid crystal shutter on top of a retroreflector, which enables the use of light backscattering as an uplink; (b) PD+LED operating in the sleep mode to harvest the energy from the ambient light for powering the IoT mote and for the up- and down-link; and (c) hybrid RF/LiFi where the LiFi downlink and RF uplink are established [11]. Therefore, integrating both VLC-PD and OCC (IS-based VLC) links simultaneously can provide a versatile OIoT environment, where users can have a choice based on the device to switch between high- and low-speed VLC with PDs- and ISs-based Rx, respectively as shown in Fig. 1.

However, there are still challenges in the integration of VLC technology with hybrid PD- and camera-based Rxs in the OIoT environments, such as (i) lower and limited f_R in contrast to high-speed PDs; (ii) incompatibility in R_b between VLC with PDs and IS, i.e., $R_{b\text{-High}} >> R_{b\text{-Low}}$; (iii) the use of LEDs with different modulation bandwidth B_{LED} in PD- and IS-based VLC links, which can result in interference and noise in other's Rxs; and (v) the increase in the overall implementation cost due to use of multiple LEDs. As a solution to these challenges, in this work, we propose a single-input multiple-output (SIMO) hybrid VLC system utilizing a single LED-based Tx, and PD- and IS-based Rxs for high- and low-speed data transmission simultaneously, respectively, see Fig. 1. Note, the high-speed PD-based VLC is mainly utilized for downloading big data, internet surfing, and online streaming, while the low-speed IS-based VLC is employed for transmission of short messages, identification, promotion information, control signals, and indoor localization information. It is envisaged that, the proposed scheme can provide versatile indoor services that allow users to receive data regardless of the devices used. For this reason, we propose a hybrid modulation format that can be used for both high- and low-speed VLC links, and have developed an experimental test-bed for verification. We present results for evaluating the link performance in terms of the bit error rate (BER) and the reception success by considering the impact of the low-speed IS-based VLC on the PD-based VLC and vice versa.
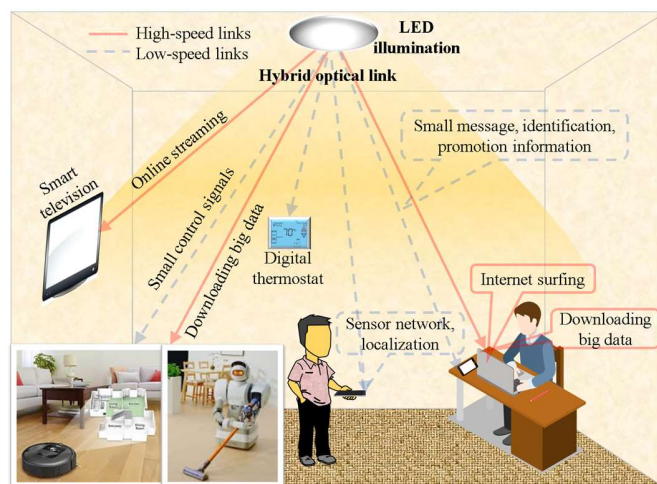

Fig. 1. SIMO hybrid VLC scheme: Concept of simultaneous high- and low-speed data transmission for versatile OIoT based indoor environment.

The remaining sections are organized as follows: Section II

gives a brief outlook and limitations of previous related works; Section III provides an overview of the proposed OIoT: SIMO hybrid VLC scheme; Section IV presents experiment results and discussion; Section V summarizes the performance and results of the proposed scheme and Section VI concludes the article along with future outlook.

II. Related works

A. Fuzzy logic-based network selection in hybrid OCC/LiFi: A switching mechanism was used to select OCC or LiFi link (not both) based on the network selection factor obtained using the fuzzy logic [28]. Even though the major focus was on the network selection, the main points of modulation/demodulation, data processing, and BER performance for both links needs further investigation. The work was further extended using the fuzzy logic and round-robin scheduling for assigning an appropriate network to the users in a hybrid OCC/LiFi system [29]. However, similar to the scheme in [28], the paper lacked details on simultaneous data transmission and processing.

B. VLC-OCC hybrid wireless systems: A 15-Wt LED lamp is used for simultaneous data transmission at high- and low-speed in VLC and OCC link, respectively [30]. Note, to utilize the dimming functionality of LED, Manchester coding and variable pulse position modulation were used for OCC and VLC, respectively, where the later was transmitted only during 'high' duration of OCC (i.e., the ON state). However, the bandwidth efficiency of the system was low since only the ON state of the signal in the VLC link was utilized.

C. Hybrid OCC/LiFi with multilevel LED: Similar to [17, 18], a unipolar multilevel LED-based hybrid encoding scheme was proposed in [31]. In OCC and LiFi, the data were transmitted using different power levels of the LED (i.e., intensity shift keying (ISK)) and multilevel OOK, respectively. In ISK, the 'high' and 'low' levels (i.e., bits '1' and '0') were modulated at power levels of 39, 35.0, and 36.7 dBm, respectively. However, to detect a small difference of ~1 dB between high and low levels, a highly sensitive IS-based Rx with a highly precise and complex data processing is required. Moreover, changing the power levels corresponding to the varying amplitude depths of the ON and OFF bits, which affects signal detection and processing, will need further investigation.

The limitation of bandwidth efficiency and the effect of multilevel LED transmission based on varying amplitude depths of the ON and OFF signal levels in hybrid signal detection as well as the comprehensive analysis of data processing lacked in [28-31] are addressed in the proposed SIMO hybrid VLC scheme for OIoT.

III. Optical IoT: SIMO Hybrid VLC scheme

As previously mentioned, unlike conventional PD-based VLCs with R_b of 100 Mb/s up to 15.7 Gb/s [6 − 9], the camera-based Rx in OCC has a limited R_b of few kb/s due to low capture speed of the camera i.e., ranging typically from 30 to 60 fps [32]. As outlined above, there are several challenges that need addressing prior to full utilization of hybrid VLC using a single LED Tx for both PD- and IS-based VLC. The major advantage of this scheme is that, being able to use either links depending

on the needs in indoor OIoT environments with reduced complexity. To demonstrate the SIMO hybrid VLC concept, we propose a bipolar modulation format that facilitates both low- and high-speed transmissions using a single LED, which is outlined below. This is followed by a detailed overview of the proposed SIMO hybrid VLC scheme.

A. The Proposed Modulation Format

Figure 2 shows the time waveforms of the proposed modulation format adopted in SIMO hybrid VLC, where the signal with $R_{b\text{-High}}$ (i.e., with the bit duration $T_{b\text{-High}}$ shown in blue) is superimposed on the signal with $R_{b\text{-Low}}$ (i.e., $T_{b\text{-Low}}$ in orange). The data and the superimposed $s(t)$ signals are in the non-return-to-zero on-off keying (NRZ-OOK) and bipolar formats, respectively. Note that, $T_{b\text{-Low}} = iT_{b\text{-High}}$, where $i \geq 2$, , i.e., $R_{b\text{-High}} = i \cdot R_{b\text{-Low}}$. Since $R_{b\text{-Low}}$ is the lower bound, then the LED is intensity modulated at the modulation frequency, which is given as:

$$f_{s-\text{Low}} = R_{b-\text{Low}} \times N_{\text{Low}}, \tag{1}$$

where N_{Low} is the number of samples of $R_{b\text{-Low}}$, which is given in terms of the number of samples of high-speed link N_{High} as:

$$N_{\text{Low}} = \frac{R_{b-\text{High}} \times N_{\text{High}}}{R_{b-\text{Low}}} = \frac{f_{s-\text{High}}}{R_{b-\text{Low}}}. \tag{2}$$

From (2) and (1), we have:

$$f_{s-\text{High}} = R_{b-\text{Low}} \times N_{\text{Low}} = f_{s-\text{Low}}. \tag{3}$$

Therefore, the generated signal $s(t)$ will contain two different data rates modulated with $f_{s\text{-Low}}$. Note, (3) is valid for two different data rates (i.e., $R_{b\text{-High}} \neq R_{b\text{-Low}}$), which is defined as:

$$s(t) = Signal(f_{s-\text{Low}})_{T_{b-\text{Low}}} \tag{4}$$
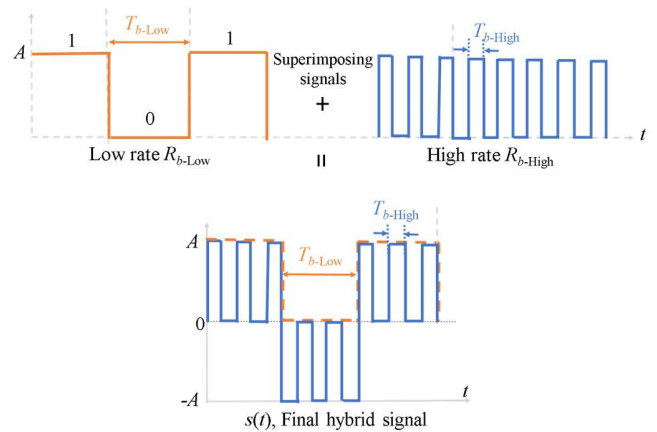$$+ Signal(f_{s-\text{High}})_{T_{b-\text{High}}}.$$

Fig. 2. Proposed modulation format for simultaneous transmission of high- and low-speed VLC-PD and OCC links, respectively.

To increase signal levels (i.e., A-depth) and therefore improve the BER performance as well as maintain the high quality of low-speed link, we provide a solution based on A overlap A_{OL}, see Fig. 3. As it will be shown in the experimental demonstration, this approach mitigates the frequency dependency of the high-pass filter (HPF) effect due to the use

of bias-T in intensity modulation the LED with $s(t)$. Figure 3(a) shows $s(t)$ for A_{OL} of 0, i.e., no overlap between $+A$ and $-A$ levels. Figures 3(b) and (c) depict $s(t)$ with the overlapping regions. Note, higher A_{OL} leads to improved link performance for the high-speed VLC link at the cost of deteriorating performance deterioration the low-speed VLC (i.e., OCC) link. Thus, the need for optimization of signal overlapping. Note, more details on this will be given in the experimental part. The values for A_{High} and A_{Low} for high- and low-speed VLC links are given as:

$$A_{High} = A + \frac{A_{OL}}{2}, A_{Low} = A - \frac{A_{OL}}{2}, \tag{5}$$

where $A_{OL}/2$ is due to the increase of A_{OL} for both positive and negative signal levels.
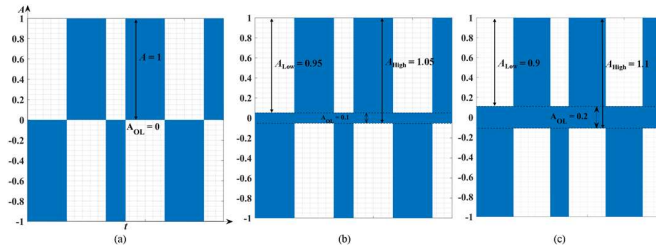

Fig. 3. Solution in terms of A_{OL} to reduce the effect of attenuation from HPF of bias-T on data recovery for A_{OL} of : (a) 0, (b) 0.1, and (c) 0.2.

B. SIMO hybrid VLC scheme: Experiment setup

Figure 4 illustrates the block diagram of the proposed SIMO hybrid VLC scheme intended for used in OIoT. On the Tx side, a high-speed NRZ-OOK data stream with $5 < R_{b\text{-}High} < 70$ Mb/s and a step of size 5 Mb/s is superimposed onto a 10-bit long low-speed data (i.e., [0011011001]) with $1 < R_{b\text{-}Low} < 10$ kb/s to produce $s(t)$. $s(t)$ generated in MATLAB, is uploaded to the arbitrary waveform generator (AWG-Teledyne test tools T3AWG3252 with a sampling frequency of 1 GS/s) the output of which is used for intensity modulation of the LED via the bias-T (BT-A11). We have used a commercially available red LED with a peak wavelength λ_r of 630 nm (Vishay VLMS1500-GS08) with its power-current-voltage characteristics described in [6]. The LED was biased at a bias current I_b of 90 mA with

the transmit output power P_t of ~3.3 mW [6]. Table I shows the key parameters adopted in this work. The intensity modulated light signal is transmitted over a 1 m long free space channel via an optical lens, see the experimental setup in Fig. 4.

TABLE I
KEY EXPERIMENTAL PARAMETERS

Parameter	Value
Red LED	**Vishay VLMS1500-GS08**
• Bias current of the LED, I_b	90 mA
• Transmit optical power P_t	~3.3 mW
Bias-T	**BT-A11**
• Frequency range	300 Hz – 10 GHz
PD	**PDA10A2**
• Wavelength	200 – 1100 nm
• B	150 MHz
• Peak responsivity	0.44 A/W @ 730 nm
• Active area	0.8 mm^2
Optical lens (on Tx and Rx side)	**Thorlabs ACL25416U**
• Focal length f_c	16 mm
Camera Rx	**IC capture 2.4 imaging source**
• Resolution	648×484 pixels
• f_R	25 fps
• Exposure time	100 μs
• G_v	4 – 8 dB
$R_{b\text{-}High}$	**5 – 70 Mb/s**
• Data length	6×10^6 bits
$R_{b\text{-}Low}$	**1 – 10 kb/s**
• Data length	10 bits superimposed over $R_{b\text{-}High}$
Transmission distance d	**1 m**

On the Rx side, we have used two types of detections: (*i*) a CMOS RS-based IC capture camera with a pixel size 2.2×2.2 μm^2; and (*ii*) a PD-based Rx (Thorlabs PDA10A2) connected to a real-time oscilloscope (Keysight MSDS104A with 20 GSa/s sampling rate) for detecting the low- and high-speed signals, respectively. Following optical to electrical conversions, the regenerated signal at the output of IS-based Rx (OCC link) is given by:
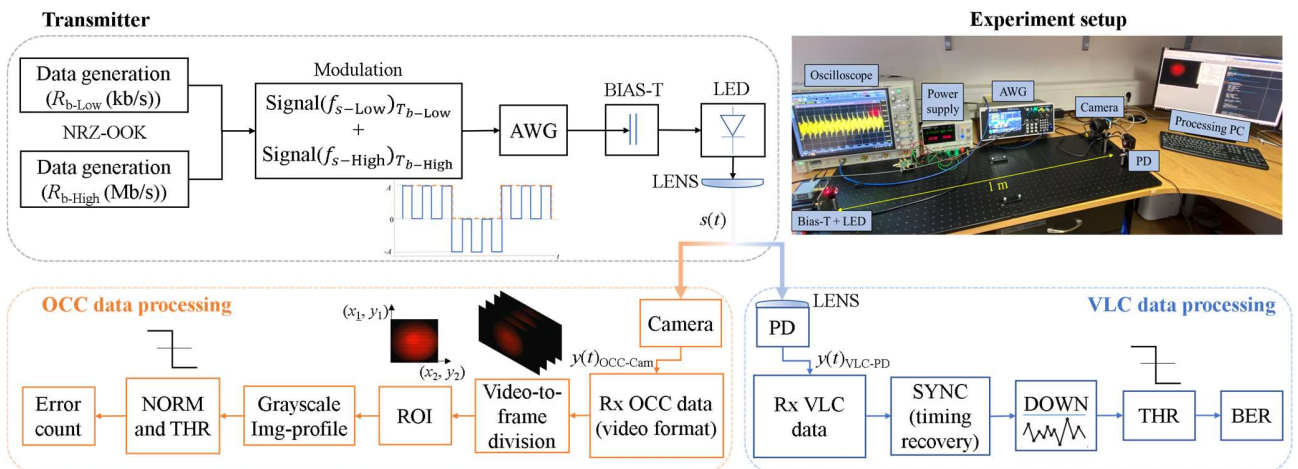

Fig. 4. Block diagram of the proposed OIoT: SIMO Hybrid VLC scheme including experiment setup inset. Note that, 'NORM', 'ROI', 'DOWN', 'THR' and 'BER' blocks refer to normalization, region-of-interest, down-sampling, thresholding and bit error rate, respectively.

$$y(t)_{\mathbf{OCC-Cam}} = \eta G_v s(t) \otimes h_{\mathrm{OCC}}(t) + n_{\mathrm{OCC}}(t), \qquad (6)$$

where $h_{\mathrm{OCC}}(t)$ is the combined impulse response of the channel and the camera, η is the quantum efficiency of the camera, $\otimes$ is the time domain convolution, $n_{\mathrm{OCC}}(t)$ is the additive white Gaussian noise, which includes the ambient light induced shot noise and the noise in the camera such as fixed pattern, photocurrent shot, and flicker noise sources [24, 33], and G_v presents the software defined global gain of the IS and the column amplifier block, which is given as [33, 34]:

$$G_v(\mathrm{dB}) = 20\log_{10}\frac{V_{\mathrm{ADC}}}{V_{\mathrm{pixels}}}, \qquad (7)$$

where V_{ADC} is the voltage value, which is sampled by the analog-to-digital converter (ADC), and V_{pixles} is the voltage obtained from the pixel integration of light during the exposure time. In the RS-based capturing mode, (*i*) the camera sequentially integrates all illuminated pixels at the exposure time $t_{\mathrm{row\text{-}exp}}$, which is the same as scanning [34, 35]; and (*ii*) the readout time $t_{\mathrm{read\text{-}out}}$ ensures that there is no overlapping of the rows of pixels, thus allowing multiple exposures of a single captured image. Note, $t_{\mathrm{read\text{-}out}}$ protects rows of pixels from overlapping. In a single captured image, the RS scheme allows multiple exposures, which enables multiple incoming light states to be captured simultaneously within a single frame as each row is exposed once to the light. Using the RS effect of a CMOS camera is advantageous in ensuring flicker-free data transmission with increased $R_{b\text{-Low}}$ [35, 36]. In RS-based camera, the bit duration is given as:

$$T_{b-\mathrm{Low}} = t_{\mathrm{row-exp}} \times N_{\mathrm{row}}, \qquad (8)$$

where N_{row} is the pixel rows, which is based on the camera resolution.

The IS-based Rx was set to capture a video stream at f_R, resolution, interframe time and exposure time of 25 fps, 648×484 (red-green-blue (RGB)32) pixels, ~5 ms and 100 μs, respectively. Note, a low-speed signal is captured by changing G_v with the range of 4-8 dB. The output of the camera is captured using the IC capture 2.4 software for further offline data processing in MATLAB based on traditional image processing techniques, see Fig. 4. As shown in Fig. 4, the captured signal in the form of a video stream is divided into image frames for further frame-by-frame processing to decode the received data. Next, in camera-based VLC the transmission distance d between the LED and the camera needs considering, since as this distance increases, the size of region-of-interest (ROI) in the picture reduces, thus reducing the number of received messages per frame. ROI is defined as [37]:

$$\mathrm{ROI} = \min\left(1, \frac{l_{\mathrm{LED}} \cdot f_c}{d \cdot l_{\mathrm{IS}}}\right), \qquad (9)$$

where l_{LED} and l_{IS} are the sizes of the LED and IS, respectively. By performing the ROI the coordinates, which define boundaries of the ROI in a full captured frame, are obtained as given by:

$$\mathrm{ROI} = \mathrm{Img}\{(x_1, y_1); (x_2, y_2)\}, \qquad (10)$$

where (x_1, y_1) and (x_2, y_2) are the top-left and bottom-right coordinates, respectively of the captured LED in the image frames, see Fig. 4. The ROI cropped image is then converted from RGB to the grayscale to retrieve the intensity profiles, which are normalized for thresholding and binarization of data frames and converting them to a vector transformation for decoding the data bit streams. Finally, the received data bit vector is compared with the transmitted data stream to ascertain the success of reception of received bits by determining the ratio of the wrongly decoded bits to the total number of transmitted bits (i.e., the number of bit errors). Note, the link performance can be improved by adopting the repeat packet strategy, where each packet is transmitted multiple times.

As for the high-speed VLC link, the regenerated signal at the output of PD is given as:

$$y(t)_{\mathrm{VLC-PD}} = \Re G_{\mathrm{PD}} s(t) \otimes h_{\mathrm{VLC}}(t) + n_{\mathrm{VLC}}(t), \qquad (11)$$

where $\Re$ is PD's responsivity, G_{PD} is PD's gain, $h_{\mathrm{VLC}}(t)$ is the combined transfer function of the channel and PD, and $n_{\mathrm{VLC}}(t)$ is the additive white Gaussian noise dominated by the background induced lights. The output of the optical Rx is applied to the synchronization module to determine the time delay between transmitted and received signals, followed by down-sampling and thresholding to recover the data, see Fig. 4. The received data bit stream is compared with the transmitted bits to determine the BER performance.

IV. EXPERIMENT RESULTS AND DISCUSSION

As the main aim of the proposed scheme is to provide simultaneous data transmission at low- and high-speed, therefore it is necessary to study the inter-link impact on the system performance. This will be done in two stages.

1) The analysis of the attenuation effect on the PD-based VLC link due to the bias-T at $R_{b\text{-Low}}$. A solution based on adjusting the A level of the hybrid signal and increasing $R_{b\text{-Low}}$ is proposed to improve the BER performance.

2) The effect of $R_{b\text{-High}}$ on low-speed signal is analyzed with respect to A_{OL}, $R_{b\text{-Low}}$, and G_v.

A. The effect of $R_{b\text{-Low}}$ on the VLC-PD Link

We measured the frequency response of the bias-T using a spectrum analyzer (Rohde & Schwarz FSW) to study its frequency dependent attenuation due to $R_{b\text{-Low}}$ on the high-speed link. The bias-T acts as an HPF, which attenuates the low frequency range, see Fig. 5. The insets in Fig. 5 illustrate the highly attenuated received high-speed signals for $1 < R_{b\text{-Low}} < 10$ kb/s. Thus, leading to the reduced A_{High} depth and hence increased BER. Note, at higher frequencies the effect of bias-T is negligible, see the 1 MHz signal in insets in Fig. 5. Therefore, to improve the BER performance, a solution based on $A_{\mathrm{OL}} > 0$ was proposed in Section III, see Figs. 3(b) and (c).
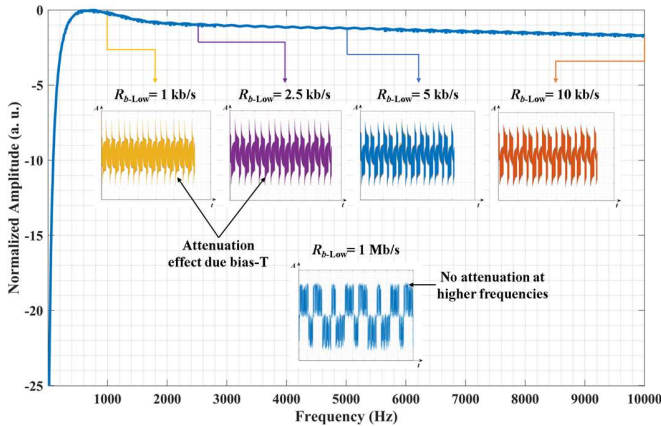
Fig. 5. The frequency response of bias-T and its attenuation effect on the received high-speed signal due to the low-speed signal. Insets show the received high-speed signal with and without attenuation effects with respect to varying $R_{b\text{-Low}}$.

For reference, we first measured the frequency response of the LED using spectrum analyzer (Rohde & SchwarzFSW) with a 3-dB bandwidth of < 50 MHz, see Fig. 6 [6], which is used as a Tx in the VLC link. For the high-speed link with the reference signal, we adopted a well-known strategy of zero-padded guard intervals as headers [6, 38] to obtain the real-valued signal. In this case, we achieved error-free transmission for $5 < R_{b\text{-High}} < 70$ Mb/s with a step of size 5 Mb/s by transmitting 6×10^6 bits. Examples of captured eye diagrams at the Rx are illustrated in Fig. 7, where the two-level OOK signal show a wide eye-opening, i.e., error-free transmission. Note, the eye-opening reduces with increasing $R_{b\text{-High}}$, which corresponds to the LEDs' frequency response (3 dB $B_{\text{LED}} < 50$ MHz) as shown in Fig. 6 [6].
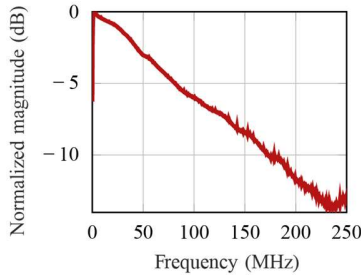

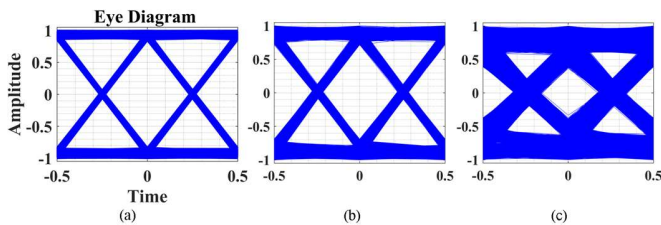Fig. 6. Measured frequency response of the LED showing the 3-dB bandwidth slightly below 50 MHz.

Fig. 7. The eye diagram of the received error free independent high-speed VLC link at $R_{b\text{-High}}$ for : (a) 5 Mb/s, (b) 30 Mb/s, and (c) 70 Mb/s.

For high-speed link, every transmitted VLC data packets were saved and compared with the regenerated data patterns by separating the high and low bit of the low-speed signal with respect to 10-bit data sequence [0011011001]. To analyze the performance of high-speed PD-based VLC link with respect to

low-speed OCC link in the proposed hybrid scheme, we have considered three main parameters: (i) $5 < R_{b\text{-High}} < 70$ Mb/s with a step of size 5 Mb/s; (ii) $1 < R_{b\text{-Low}} < 10$ (1, 2.5, 5, 10) kb/s; and (iii) $0 < A_{\text{OL}} < 0.2$ with a step of size 0.1. Figure 8(a) depicts the BER as a function of $R_{b\text{-High}}$ for the VLC-PD link and received hybrid signal for range of A_{OL} and $R_{b\text{-Low}}$. It can be seen from Fig. 8(b) that, the A depth of the received signal increases with A_{OL}, which leads to the improved performance of VLC-PD. This corresponds to Eq. (5). As shown in Fig. 8(a), for $R_{b\text{-High}}$ of up to 70 Mb/s; the BER plots are below the forward error correction (FEC) limit of 3.8×10^{-3} for $R_{b\text{-Low}}$ of 10 kb/s and $0 < A_{\text{OL}} < 0.2$. At the FEC BER limit for $R_{b\text{-Low}}$ of 5 kb/s, $R_{b\text{-High}}$ values are reduced by 7, 10, and 12 Mbps for A_{OL} of 0.2, 0.1 and 0, respectively. We observe more reduction in $R_{b\text{-High}}$ by about 33 and 51 Mbps for $R_{b\text{-Low}}$ of 2.5 and 1 kb/s, respectively.
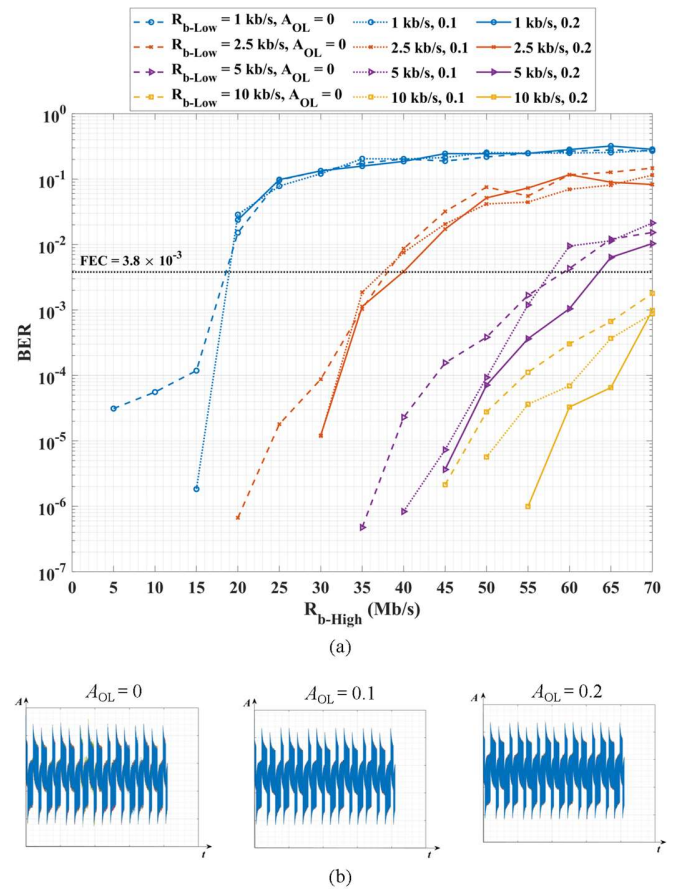

(a)

(b)

Fig. 8. Performance analysis: (a) BER versus the $R_{b\text{-High}}$ for VLC-PD link; and (b) received hybrid signal for a range of $R_{b\text{-Low}}$ and A_{OL}.

To further improve the BER performance of VLC-PD, we carried out further measurement for $0.3 < A_{\text{OL}} < 0.5$ with a step of size 0.1, see Fig. 9(a). Note, according to Eq. (5), A_{Low} decreases with the increasing A_{OL}. On the other hand, further increase in A_{OL} significantly increases the A depth of the received signal, see Fig. 9(b). It can be seen that, the FEC limits are met at around $R_{b\text{-High}}$ of 41 Mbps for $R_{b\text{-Low}}$ of 2.5 kb/s and A_{OL} of 0.3-0.5. In Fig. 9(a), the curves at $R_{b\text{-Low}}$ of 2.5 kbps and A_{OL} of 0.4 and 0.5 depict BER well below the forward error correction (FEC) limit until $R_{b\text{-High}}$ of 43 Mbps and degrades further with the increasing $R_{b\text{-High}}$. The reason for this is the 3-

dB frequency response of the LED, which is about 50 MHz, see Fig. 6 [6]. However, for lower values of $R_{b\text{-Low}}$ the BER plots are well above the FEC limits.
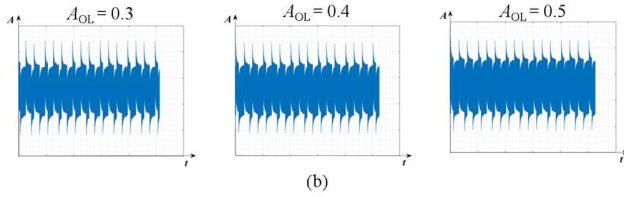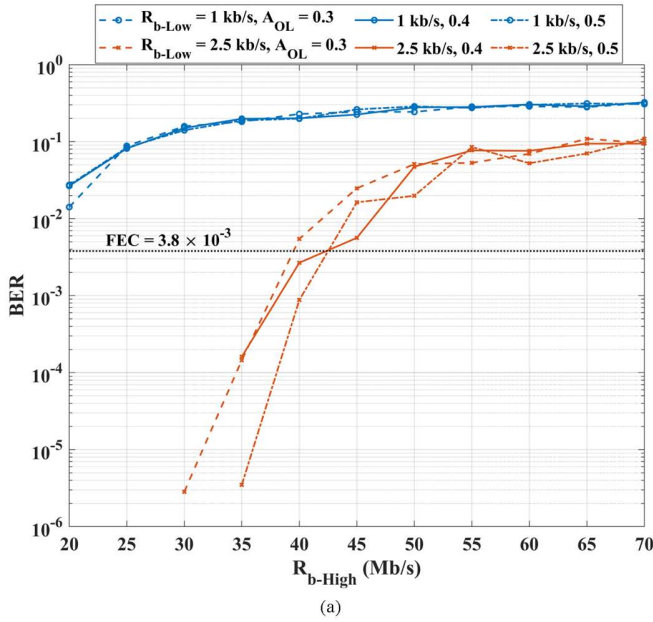

Fig. 9. Performance analysis: (a) BER performance as a function of $R_{b\text{-High}}$ for the VLC-PD link; and (b) received hybrid signal for $R_{b\text{-Low}}$ of 1 and 2.5 kbps and A_{OL} of 0.3, 0.4, and 0.5.

B. The effect of $R_{b\text{-High}}$ on Low-speed OCC (IS-based VLC) link

Increasing A_{OL} improves the performance of the PD-based VLC link at the cost of reduced A_{Low} levels, see Eq. (5). This results in reduced intensity levels between 'high' and 'low' of the low-speed signal in the received image frame. Therefore, it is essential to analyze the performance of OCC link considering the high-speed VLC, A_{OL}, and G_v.

Like VLC-PD, first, we considered only the OCC link for $1 < R_{b\text{-Low}} < 10$ (i.e., 1, 2.5, 5, 10) kb/s and captured a 4 s video stream (i.e., 25 fps) of the intensity modulated LED. In every image frame, 4, 10, 20, and 22 repeated data packets of 10-bit long [0011011001] were captured at $R_{b\text{-Low}}$ of 1, 2.5, 5 and 10 kb/s, respectively. Considering that, a smaller number of bits were transmitted the OCC link performance is analyzed in terms of the reception success, which is defined as the ratio of incorrectly decoded bits to the total number of transmitted bits. We have achieved 100 , 97, and 75 % reception success rates for $R_{b\text{-Low}}$ of 1 and 2.5, 5, and 10 kb/s, respectively.

The performance of OCC link in the hybrid scheme is studied for $R_{b\text{-High}}$, $R_{b\text{-Low}}$, A_{OL}, and $4 < G_v < 8$ dB, see Fig. 10. It can be seen that, the intensity levels of the received low-speed signal are marginally affected for higher values of A_{OL}, which corresponds to the reduced A_{Low} as shown in Fig. 3 and Eq. (5),

see Fig. 10(a). Figure 10(b) illustrates the normalized intensity profiles for A_{OL} of 0 and 0.2 as well as the threshold levels based on the mean of the high and low normalized intensities. Note, the threshold level can be adaptively set based on the intensity levels in the image frame.
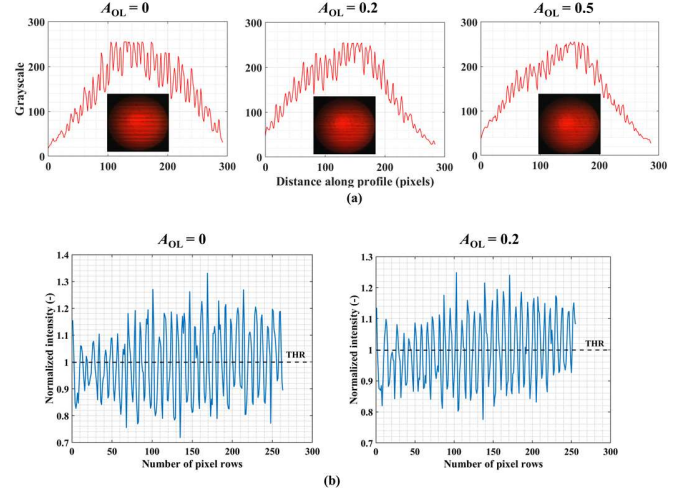

Fig. 10. Effect of A_{OL} on the low-speed OCC link at $R_{b\text{-Low}}$ = 2.5 kb/s and G_v = 8 dB for: (a) grayscale, and (b) normalized intensity profiles.

Figure 11 demonstrates the gray scale levels of low-speed OCC with $R_{b\text{-Low}}$ and G_v of 5 kb/s and 4 dB, respectively for $R_{b\text{-High}}$ of 10 and 70 Mb/s. It shows higher levels of amplitude fluctuation at $R_{b\text{-High}}$ of 10 Mb/s compared with $R_{b\text{-High}}$ of 70 Mb/s. This is because of the higher number of bits being superimposed per bit of $R_{b\text{-Low}}$ for $R_{b\text{-High}}$ of 70 Mb/s compared with $R_{b\text{-High}}$ of 10 Mb/s, see blue waveforms in Figs. 11(a) and (b).
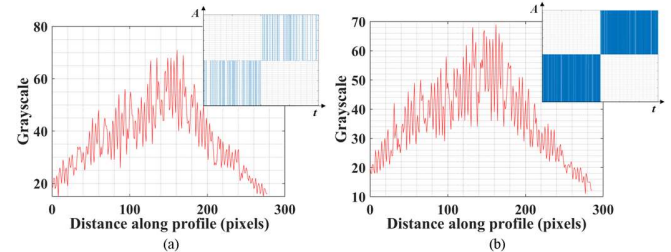

Fig. 11. Effect of high-speed VLC on OCC link at $R_{b\text{-Low}}$ = 5 kb/s and G_v = 4 dB for $R_{b\text{-High}}$ of: (a)10 Mb/s, and (b) 70 Mb/s. Note, blue waveform in insets represents the transmitted signal at respective $R_{b\text{-Low}}$ and $R_{b\text{-High}}$.

Next, we have investigated the performance of OCC link in terms of the reception success for $R_{b\text{-Low}}$ of 1 and 2.5 kb/s. The 100 % (error-free transmission) reception success is achieved at $R_{b\text{-Low}}$ of 1kb/s for $0 < A_{OL} < 0.2$ and G_v of 4-8 dB. Therefore, for further analysis as in the VLC-PD link, we considered higher values of A_{OL} (i.e., $0.3 < A_{OL} < 0.5$) for $R_{b\text{-Low}}$ of 1 and 2.5 kb/s, see Figs. 12(a) and (b) (note, error-free plots, i.e., 100 % reception success plots are not shown in Fig. 12(a)). It can be seen that, at G_v of 4 dB the reception success rates are above 95 and 94 % for 1 and 2.5 kb/s, respectively. From Fig. 12, the performance of OCC links degrades with increase in G_v and A_{OL} (this corresponds to Figs. 9 and 3 and Eqs. (5) and (7)). In our recent works [33], we investigated how higher values of G_v ensured reception of the low-speed signal, see Eq. (7), even
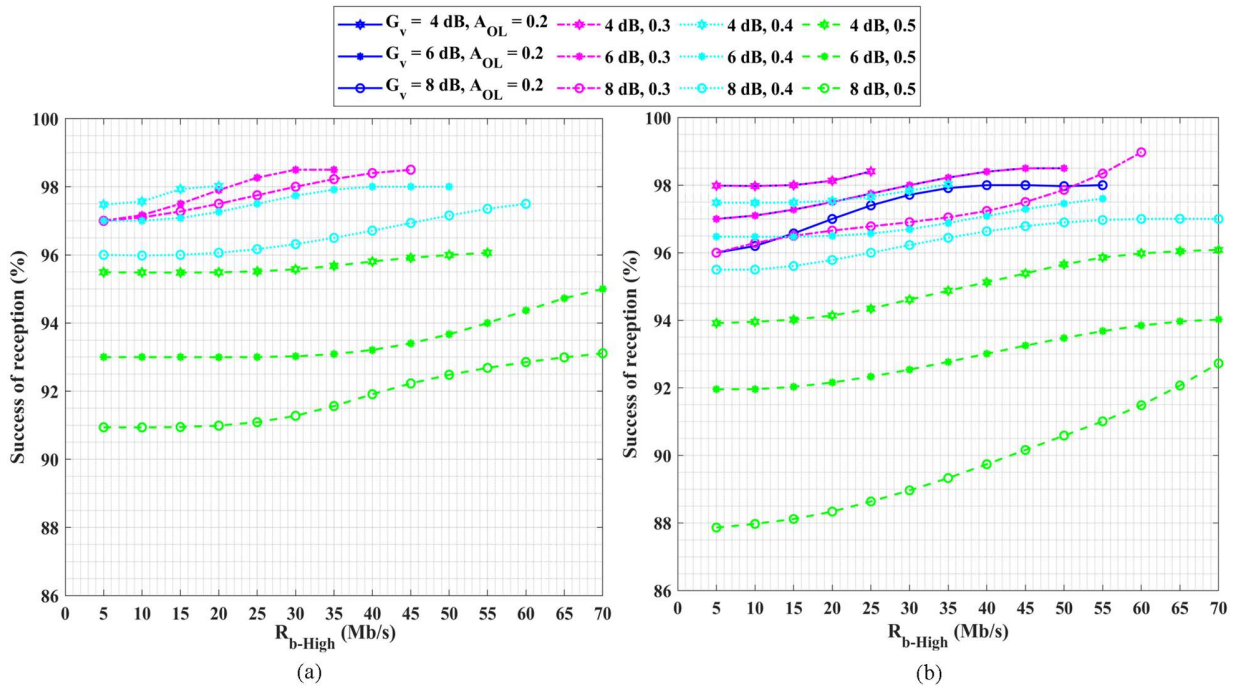
Fig. 12. Performance of OCC link in the proposed hybrid scheme: the success of reception performance as a function of $R_{b\text{-High}}$, G_v and A_{OL} for $R_{b\text{-Low}}$ of: (a) 1 kb/s, and (b) 2.5 kb/s.

in outdoor envirnments under turbulence and fog conditions. This is because increasing G_v improves signal amplification passing through the camera ADC and to be focused on the IS, which results in intensity saturation within the captured image frames. Therefore, in this work we carry out analysis for the OCC link by changing G_v that can be further beneficial in multi-Tx-based hybrid schemes. For the system with a line-of-sight propagation path with much reduced level of ambient light at the Rx (i.e., ~4 lux (±0.2 lux)), increasing G_v results in saturation of the focused LED light in the captured image frame. Thus leading to reduced A levels of the received 1 and 0 bits on the RS captured frame. However, it can be seen from Fig. 12 that, an reception success > 91 and 88 % are achieved even for higher values of G_v of 8 dB and A_{OL} of 0.5 for $R_{b\text{-Low}}$ of 1 and 2.5 kb/s, respectively.

Figure 13 depicts the reception success versus $R_{b\text{-High}}$ of the OCC link for $R_{b\text{-Low}}$ of 5 kb/s for range of G_v and A_{OL}. It can be seen that, the lowest and highest reception success rates are within the band of 88-92% and 92.5-94% within the $4 < G_v < 8$ dB and $0 < A_{\text{OL}} < 0.2$, respectively for $R_{b\text{-High}}$ of 5-70 Mb/s. Considering that f_R of the IS-based Rx is limited, increasing $R_{b\text{-Low}}$ degrades the performance of OCC link. If $T_{b\text{-Low}}$ exceeds $t_{\text{read-out}}$ of the camera, it leads to more transition frames, increased overlap between the captured data rows and higher aliasing, thus, degrading the performance of the link. For example, at $R_{b\text{-Low}}$ of 10 kb/s, the measured reception success rate is dropped to $65 – 70$ % for G_v of 4 dB, A_{OL} of 0, and for $5 < R_{b\text{-High}} < 70$ Mb/s.
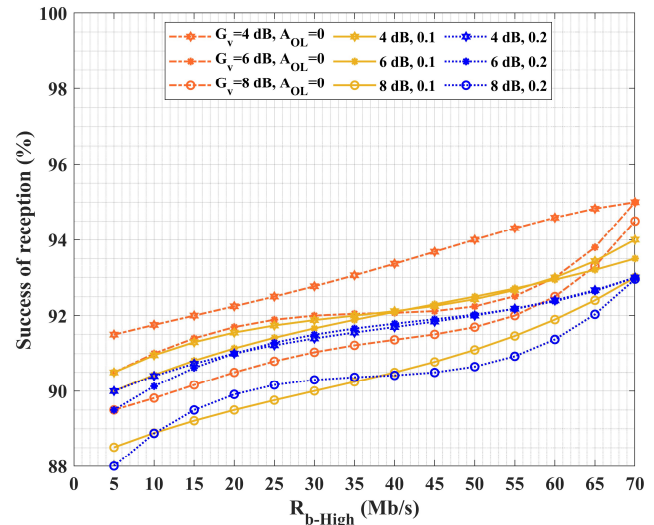

Fig. 13. The reception success rate for the OCC link in the proposed hybrid scheme: the success of reception at $R_{b\text{-Low}} = 5$ kb/s.

V. SUMMARY OF RESULTS

We summarized the performance of the proposed SIMO hybrid VLC scheme based on the results obtained as follow:
1) A solution to overcome the attenuation effect from the bias-T used to drive the LED in terms of A_{OL} was provided. The effect of A_{OL} on both high- and low-speed PD- and IS-based VLC links, respectively was analyzed as:
   (i) A_{OL} helps to improve the BER performance of PD-based VLC link by increasing the A depth of the hybrid signal. For example, at $0 < A_{\text{OL}} < 0.2$ BER below the FEC limit of $3.8×10^{-3}$ is measured for $R_{b\text{-Low}}$ of 2.5, and 5 kb/s at reduced $R_{b\text{-High}}$ of 10 and 35 Mb/s, respectively. While, at $0.3 < A_{\text{OL}} < 0.5$ the BER FEC

limits are met at $R_{b\text{-High}}$ of 41 Mbps for $R_{b\text{-Low}}$ of 2.5 kb/s.

(ii) For the IS-based VLC link (i.e., OCC), increasing A_{OL} reduces the total A_{Low} level, thus reducing the difference between 'high' and 'low' intensity levels of the captured data in the image frame. However, to improve the OCC performance even for higher A_{OL}, a solution is proposed to use the minimum G_v to limit the incoming light and avoid the saturation effect on the received low-speed signal in the image frame. For example, at G_v of 4 dB, $0 < A_{\text{OL}} < 0.2$ and $5 < R_{b\text{-High}} < 70$ Mb/s, the reception success of > 96 and 90 % are measured at $R_{b\text{-Low}}$ of 2.5 and 5 kb/s, respectively.

(iii) We also analyzed the performance of the OCC link at higher G_v for implementation of the future multi-Tx/light source-based hybrid scheme to overcome the noise effect. It was shown that, for $5 < R_{b\text{-High}} < 70$ Mb/s the reception success of > 88 % is measured at G_v of 8 dB for $R_{b\text{-Low}}$ of 2.5 kb/s ($0 < A_{\text{OL}} < 0.5$) and 5 ($0 < A_{\text{OL}} < 0.2$) kb/s.

Therefore, it is necessary to balance the performance of both high- and low-speed PD- and IS-based VLC links in the proposed hybrid scheme by providing the optimized solution to improve individual performances regardless of the bias-T attenuation and A_{OL} effects on the VLC and OCC links, respectively.

2) From the summary of results presented based on the performance analysis, $0 < A_{\text{OL}} < 0.2$, $R_{b\text{-Low}}$ of 2.5 and 5kb/s, $5 < R_{b\text{-High}} < 60$ Mb/s, and G_v of 4 dB can be considered as the parameters with optimum values derived from the experimental demonstration of the proposed SIMO hybrid VLC scheme for OIoT environments. These values can help further implementation of the proposed scheme in real and extended OIoT environments.

3) Based on the summary of results, we have proposed a solution for the limitations within hybrid VLC-OCC schemes [28-31] described in Section II Related works.

(i) We have proposed a hybrid modulation scheme for transmission of high- and low-speed data simultaneously using a single LED source which was not investigated in [28, 29].

(ii) The bandwidth of the hybrid VLC/OCC scheme in [30] was limited thus the data rates of 1.67 kbps ($R_{b\text{-Low}}$) and 100 kbps ($R_{b\text{-High}}$) were reported for the OCC and VLC links, respectively. This issue was addressed using a red chip LED Tx, with the option of adding green and blue LEDs to produce a white light for illumination and data communications using a red chip LED and the proposed hybrid modulation format. Based on this, we have achieved $R_{b\text{-Low}}$ of 2.5 and 5kb/s and $5 < R_{b\text{-High}} < 60$ Mb/s.

(iii) As in [31], changing the power levels corresponding to the varying amplitude depths of the data bit stream affects the signal detection process, which is not investigated. In the proposed SIMO hybrid VLC scheme, we have provided detailed data processing for high- and low-speed signals captured using PD- and IS-based Rxs along with A_{OL} solution to improve the

BER performance of PD-based VLC link by increasing the A depth of the hybrid signal, and using the optimal G_v of 4 dB to improve the performance of IS-based VLC link.

VI. CONCLUSIONS AND FUTURE OUTLOOK

This paper demonstrated experimental implementation of OIoT: the SIMO hybrid VLC scheme in indoor static environment. A single red LED-based Tx with a bias-T was used for simultaneous transmission of high- and low-speed signals. For this reason, we proposed a hybrid modulation scheme with $R_{b\text{-High}}$ and $R_{b\text{-Low}}$ of up to 60 Mb/s and 5 kb/s for high-speed VLC and low-speed OCC links, respectively. The results demonstrated that, increasing $R_{b\text{-High}}$ and $R_{b\text{-Low}}$ improved the OCC and VLC performance, respectively. As part of the modulation format, we introduced the concept of the A_{OL} to increase the transmission rate, and reduce the bias-T induced attenuation. We addressed the problems of bandwidth efficiency, the effect of multilevel LED transmission due to A_{OL} and provided a comprehensive analysis of data processing for the PD- and IS-based VLC links. It is envisioned that; the proposed SIMO hybrid VLC scheme can provide versatile OIoT-based indoor services that can allow users to receive data regardless of their devices.

Within the hybrid transmission environment, high-speed VLC links can be used for large amount of data downloading, internet surfing, and online streaming, while the low-speed links can be used to transmit short messages, identification and promotion information, control signals, and indoor localization within OIoT environments. As a part of potential future development of the proposed scheme in practical scenarios, green and blue colors can be added to the red LED to produce a white light for illumination while still offering data communications via the red chip LED. In this way, the proposed scheme can overcome the problem of bandwidth efficiency. Equalization techniques [39, 40] and different modulation formats such as OFDM [41] can be implemented to improve the reception success rate and the BER performance for low-speed and high-speed VLC links, respectively. The scheme can also be tested for various transmission ranges between the LED and camera- and PD-based Rxs along with different angular orientations to support mobility in OIoT environments.

REFERENCES

[1] H. Aksu, L. Babun, M. Conti, G. Tolomei and A. S. Uluagac, "Advertising in the IoT Era: Vision and Challenges," *IEEE Communications Magazine*, vol. 56, no. 11, pp. 138-144, 2018.

[2] N. Wang, P. Wang, A. Alipour-Fanid, L. Jiao and K. Zeng, "Physical-Layer Security of 5G Wireless Networks for IoT: Challenges and Opportunities," *IEEE Internet of Things Journal*, vol. 6, no. 5, pp. 8169-8181, Oct. 2019.

[3] IEEE Standard for Local and Metropolitan Area Networks_Part 15.7: Short-Range Wireless Optical Communication Using Visible Ligh, IEEE Standard 802.15.7, Dec. 2018. [Online]. Available: http://standards.ieee.org/_ndstds/standard/802.15.7-2011.html

[4] Z. Ghassemlooy, S. Zvanovec, Moh. A. Khalighi, W. O. Popoola, J. Perez, "Optical wireless communication systems", *Optik*, vol. 151, pp. 1-6, 2017.

[5] P. H. Pathak, X. Feng, P. Hu, and P. Mohapatra, "Visible light communication, networking, and sensing: A survey, potential and challenges,"

IEEE Commun. Surveys Tuts., vol. 17, no. 4, pp. 2047-2077, 4th Quart., 2015.Z. Ghassemlooy, L.N. Alves, S. Zvanovec, and M.A. Khalighi, eds. *Visible Light Communications: Theory and Applications*, CRC Press, 2017.

[6]   P. Chvojka, *et al*., "Visible light communications: increasing data rates with polarization division multiplexing," *Opt. Lett.* Vol. 45, pp. 2977-2980, 2020.

[7]   I.-C. Lu, C.-H. Yeh, D.-Z. Hsu, and C.-W. Chow, "Utilization of 1-GHz VCSEL for 11.1-Gbps OFDM VLC wireless communication," *IEEE Photonics Journal*, vol. 8, no. 3, Jun. 2016.

[8]   M. S. Islim et al., "Towards 10 Gb/s orthogonal frequency division multiplexing-based visible light communication using a GaN violet micro-LED," *Photon. Res*., vol. 5, no. 2, pp. A35-A43, 2017.

[9]   R. Bian, I. Tavakkolnia and H. Haas, "15.73 Gb/s Visible Light Communication With Off-the-Shelf LEDs," *Journal of Lightwave Technology*, vol. 37, no. 10, pp. 2418-2424, 15 May15, 2019.

[10] S. Rajagopal, R. D. Roberts, and S. K. Lim, "IEEE 802.15.7 visible light communication: modulation schemes and dimming support," *IEEE Communications Magazine*, vol. 50, no. 3, pp. 72–82, 2012.

[11] I. Demirkol, D. Camps-Mur, J. Paradells, M. Combalia, W. Popoola and H. Haas, "Powering the Internet of Things through Light Communication," *IEEE Communications Magazine*, vol. 57, no. 6, pp. 107-113, 2019.

[12] C. Chen, S. Fu, X. Jian, M. Liu, X. Deng and Z. Ding, "NOMA for Energy-Efficient LiFi-Enabled Bidirectional IoT Communication," *IEEE Transactions on Communications*, vol. 69, no. 3, pp. 1693-1706, 2021.

[13] Y. Chen, S. Li and H. Liu, "Dynamic Frequency Reuse Based on Improved Tabu Search in Multi-User Visible Light Communication Networks," *IEEE Access*, vol. 7, pp. 35173-35183, 2019.

[14] Y. Hou, S. Xiao, H. Zheng and W. Hu, "Multiple access scheme based on block encoding time division multiplexing in an indoor positioning system using visible light," *IEEE/OSA Journal of Optical Communications and Networking*, vol. 7, no. 5, pp. 489-495, May 2015.

[15] J. Sanusi, S. Idris, A. M. Aibinu, S. Adeshina and A. N. Obadiah, "Handover in Hybrid LiFi and WiFi Networks," *2019 15th International Conference on Electronics, Computer and Computation (ICECCO)*, Abuja, Nigeria, 2019, pp. 1-6.

[16] S. R. Teli, S. Zvanovec and Z. Ghassemlooy, "Optical Internet of Things within 5G: Applications and Challenges," *2018 IEEE International Conference on Internet of Things and Intelligence System (IOTAIS)*, Bali, pp. 40-45, 2018.

[17] J. Y. Sung, C. W. Chow, C. H. Yeh, and Y. C. Wang, "Service integrated access network using highly spectral-efficient MASK-MQAM-OFDM coding," *Opt. Express*, vol. 21, pp. 6555-6560, 2013.

[18] C. Chen, W. D. Zhong, D. Wu, "Integration of variable-rate OWC with OFDM-PON for hybrid optical access based on adaptive envelope modulation," *Optics Communications*, vol. 381, pp. 10-17, 2016.

[19] M. J. Jang, "IEEE 802.15 WPAN 15.7 amendment-optical camera communications study group (SG 7a)," (2021 [Online accessed 9 February 2021]).

[20] S. Teli, W. A. Cahyadi and Y. H. Chung, "Optical Camera Communication: Motion over Camera," *IEEE Communications Magazine*, vol. 55, no. 8, pp. 156-162, Aug. 2017.

[21] T. Le, N. Le and Y. M. Jang, "Performance of rolling shutter and global shutter camera in optical camera communications," *2015 International Conference on Information and Communication Technology Convergence (ICTC)*, Jeju, 2015, pp. 124-128.

[22] X. Liu, X. Wei and L. Guo, "DIMLOC: Enabling High-Precision Visible Light Localization Under Dimmable LEDs in Smart Buildings," *IEEE Internet of Things Journal*, vol. 6, no. 2, pp. 3912-3924, April 2019.

[23] S. Ma, Q. Liu and P. C. -. Sheu, "Foglight: Visible Light-Enabled Indoor Localization System for Low-Power IoT Devices," *IEEE Internet of Things Journal*, vol. 5, no. 1, pp. 175-185, Feb. 2018.

[24] S. R. Teli, S. Zvanovec, R. Perez-Jimenez and Z. Ghassemlooy, "Spatial frequency-based angular behavior of a short-range flicker-free MIMO-OCC link," *Applied Optics*, vol. 59, no. 33, pp. 10357-10368, 2020.

[25] R. Boubezari, H. Le Minh, Z. Ghassemlooy and A. Bouridane, "Smartphone Camera Based Visible Light Communication,"*Journal of Lightwave Technology*, vol. 34, no. 17, pp. 4121-4127, 1 Sept.1, 2016.

[26] S. Mangold, "Research team demonstrates LEDs that use visible light to talk to each other and internet," [Online] Available: https://phys.org/news/2015-09-team-visible-internet.html#jCp

[27] H. Yang, W. Zhong, C. Chen, A. Alphones and P. Du, "QoS-Driven Optimized Design-Based Integrated Visible Light Communication and

[28] Positioning for Indoor IoT Networks," *IEEE Internet of Things Journal*, vol. 7, no. 1, pp. 269-283, Jan. 2020.

[28] M. K. Hasan, M. Shahjalal, M. Z. Chowdhury, M. T. Hossan, and Y. M. Jang, "Fuzzy logic based network selection in hybrid OCC/Li-Fi communication system," *in Proc. 10th Int. Conf. Ubiquitous Future Netw. (ICUFN)*, Prague, Czech Republic, Jul. 2018, pp. 95–99.

[29] M. K. Hasan, M. Z. Chowdhury, M. Shahjalal, and Y. M. Jang, "Fuzzy based network assignment and link-switching analysis in hybrid OCC/LiFi system," *Wireless Commun. Mobile Comput*., vol. 2018, Nov. 2018, Art. no. 2870518.

[30] D. T. Nguyen, S. Park, Y. Chae and Y. Park, "VLC/OCC Hybrid Optical Wireless Systems for Versatile Indoor Applications," *IEEE Access*, vol. 7, pp. 22371-22376, 2019.

[31] M. K. Hasan, N. T. Le, M. Shahjalal, M. Z. Chowdhury and Y. M. Jang, "Simultaneous Data Transmission Using Multilevel LED in Hybrid OCC/LiFi System: Concept and Demonstration," *IEEE Communications Letters*, vol. 23, no. 12, pp. 2296-2300, Dec. 2019.

[32] S. R. Teli, S. Zvanovec and Z. Ghassemlooy, "The first tests of smartphone camera exposure effect on optical camera communication links," *2019 15th International Conference on Telecommunications (ConTEL)*, Graz, Austria, pp. 1-6, 2019.

[33] V. Matus, E. Eso, S. R. Teli, R. Perez-Jimenez and S. Zvanovec, "Experimentally derived feasibility of optical camera communications under turbulence and fog conditions," *SENSORS*, vol. 20, pp.1-15, 2020.

[34] T. Kuroda, "Essential principles of image sensors," *CRC press*, 2017.

[35] C.-W. Chow, C.-Y. Chen, and S.-H. Chen, "Visible light communication using mobile-phone camera with data rate higher than frame rate," *Opt. Express*, vol. 23, pp. 26080–26085, 2015.

[36] V. P. Rachim and W. Chung, "Multilevel intensity-modulation for rolling shutter-based optical camera communication," *IEEE Photonics Technology Letters*, vol. 30, pp. 903–906, 2018.

[37] A. Duque, R. Stanica, H. Rivano, A. Desportes, "Analytical and simulation tools for optical camera communications," *Computer Communications*, vol. 160, pp. 52-62, 2020.

[38] W. Ozan, R. Grammenos and I. Darwazeh, "Zero Padding or Cyclic Prefix: Evaluation for Non-Orthogonal Signals," *IEEE Communications Letters*, vol. 24, no. 3, pp. 690-694, 2020.

[39] O. I. Younus et al., "Data Rate Enhancement in Optical Camera Communications Using an Artificial Neural Network Equaliser," *IEEE Access*, vol. 8, pp. 42656-42665, 2020.

[40] X. Li, Z. Ghassemlooy, S. Zvanovec, R. Perez-Jimenez and P. A. Haigh, "Should Analogue Pre-Equalisers be Avoided in VLC Systems?" *IEEE Photonics Journal*, vol. 12, no. 2, pp. 1-14, April 2020.

[41] T. Nguyen, M. D. Thieu and Y. M. Jang, "2D-OFDM for Optical Camera Communication: Principle and Implementation," *IEEE Access*, vol. 7, pp. 29405-29424, 2019.

Shivani Rajendra Teli is a Ph.D. scholar in the Faculty of Electrical Engineering, Czech Technical University (CTU) in Prague. She is currently working as an Early Stage Researcher within visible light-based interoperability and networking (ViSIoN) which is a project under European Union's Horizon H2020 Marie Skłodowska-Curie Innovative Training Network (MSCA ITN). She received her M. Sc. degree from Department of Information and Communications Engineering, Pukyong National University, Busan, Korea and Bachelor's degree from Savitribai Phule Pune University, Maharashtra, India, in 2018 and 2015, respectively. Her research interests are wireless communication systems, visible light communications and optical camera communications for Internet of things.

Petr Chvojka received his M.Sc. and Ph.D. degrees from the Faculty of Electrical Engineering, Czech Technical University (CTU) in Prague, in 2013 and 2018, respectively. He worked as a research fellow at the Department of Electromagnetic Field, CTU in Prague focusing on optical systems design and modelling, including inorganic and organic devices and digital signal processing techniques for visible light communications as a member of the Wireless and Fiber Optics Group. He worked at CTU in Prague until 2020 when he joined the ComAp company developing solutions for power generation and engine control.

Palmas de Gran Canaria, Spain. He is a full professor at the ULPGC, where he leads the IDeTIC Research Institute. His current research interests are in the field of Optical Camera Communications (OCC), optical indoor channel characterization and the design of robust visible light communications (VLC) systems for indoor communications, especially applied for sensor interconnection and positioning. He is also pursuing a new PhD in Telecommunications History at Universidad de La Laguna. He has been awarded with the Gran Canaria Science Prize (2007), the Vodaphone Foundation Research Award (2010) and the RSEAPGC Honor Medal (2017).

Stanislav Vítek graduated at the Czech Technical University in Prague in 2002 and received Ph.D. degree from the Czech Technical University in Prague in 2008. Recently he is an assistant professor with Dept. of Radioelectronics at the Faculty of Electrical Engineering at the Czech Technical University in Prague. Member of numerous international teams focused to networks of robotic telescopes. His main research interests are signal and image processing, embedded systems, machine learning and database systems.

Prof. Zabih Ghassemlooy Fellow, SOA; Fellow, IET; Senior Member, IEEE, Member of ACM, CEng, BSc (Hons.) in EE Engineering, Manchester Metropolitan Univ., (1981), MSc (1984) and PhD (1987) from Manchester Univ., UK. 1987-88 as a Post-Doctoral Research Fellow at City Univ., UK. 1988-2004 joined Sheffield Hallam University, UK, and 2004-14 joined Faculty of Eng. & Env., Northumbria University, UK as an Associate Dean Research, and currently is the Head of Optical Communications Research Group. He is a Research Fellow (2016-) and a Distinguished Professor (2015-) at the Chinese Academy of Science. He was the Vice-Chair of EU Cost Action IC1101 (2011-16) and is Vice- Chair of the EU COST Action CA19111 NEWFOCUS (European Network on Future Generation Optical Wireless Communication Technologies, 2020-2024). He has published over 950 papers (more than 370 journals and 8 books), 100 keynote/invited talks, supervised 10 Research Fellows and 65 PhD students. His research interests are in the areas of optical wireless communications, free space optics, visible light communications, hybrid RF and optical wireless communications. He is the Chief Editor of the British Journal of Applied Science and Technology and the International Journal of Optics and Applications, Associate Editor of a number of international journals, and Co-guest Editor of a number of special issues OWC. He is the Vice-Cahir of OSA Technical Group of Optics in Digital Systems (2018-). He is the Chair of the IEEE Student Branch at Northumbria University, Newcastle (2019-). From 2004-06 he was the IEEE UK/IR Communications Chapter Secretary, the Vice-Chairman (2006-2008), the Chairman (2008-2011), and Chairman of the IET Northumbria Network (Oct 2011-2015).

Prof. Stanislav Zvanovec received his M.Sc. and Ph.D. degrees from the Faculty of Electrical Engineering, Czech Technical University (CTU) in Prague in 2002 and 2006, respectively. To date, he works as a full professor and deputy head of the Department of Electromagnetic Field and chairperson of PhD branch at CTU. His current research interests include Free Space Optical and fiber optical systems, Visible Light Communications, OLED, RF over optics and electromagnetic wave propagation issues for millimeter wave band. He is the author of two books (and co-author of the recent book Visible Light Communications: Theory and Applications), several book chapters and more than 250 journal and conference papers.

Prof. Rafael Perez-Jimenez (Madrid, 1965) received his MS degree in 1991 from Universidad Politécnica de Madrid, Spain, and his Ph.D. degree (Hons) in 1995 from Universidad de Las

5 | Conclusion

This thesis provided analyses, design and implementation of OCC systems for IoT applications. The state-of-the-art was presented with an emphasis on the advantages and limitations of OCC technology and its utilization for IoT-based applications.

The core of the thesis is divided into three main parts. The first part introduces the new developed technologies based on MIMO and radiating fiber Tx's for OCC-based IoT links. As reported in [J1], despite the small area of display, flicker-free transmission is established using multiple channels within a single Tx unit with perfect inter-LED synchronization. The scheme was mainly proposed for use in short-range and low R_b MIMO-OCC systems for IoT applications (display-based communication links or display-to-camera communications). In [J2] we used the Tx design proposed in [J1] for experimental analysis of various angular orientations of multiple Tx units to offer a valid solution irrespective of the availability of LOS and NLOS paths. Moreover, in [J3] we proposed and experimentally verified a novel and unique optical wireless communications link using an illuminating optical fiber as a Tx in OCC for IoT motivated from a new and emerging fiber-optic lighting technology as an alternative to discrete illumination fixtures and semi-discrete LED stripes.

The second part was focused on the methodology of design and analysis of OCC based applications for indoor and outdoor IoT environments. Based on publication [J4], we have shown that optical shadowing represents an extremely challenging topic in OCC systems. For the suppression of this effect, to address optical shadowing and control of smart devices within indoor OCC based IoT, the methodology of NN assisted MD functionality was proposed. The results show that the proposed NN assisted MD in OCC system provides better results in terms of higher MD accuracy (100%), less processing time (0.67 s) and long transmission spans (1.6 m) as compared to already existing MD schemes. Furthermore, in [J5], we investigated the OCC system for IoT based on OLEDs for long-range indoor and outdoor IoT-based applications. It was shown that despite the low emitted power of OLED devices, long range indoor and outdoor links can be established. In next step, we extended the measurement campaign to increase the transmission link spans further for outdoor applications such as intelligent transport systems (e.g., exchange of safety and traffic messages and positioning-related information) for smart traffic management. In [J6], we developed a novel technique of reducing the spatial bandwidth of the camera in the out-

of-focus regions to achieve communication of up to 400 m. For practical implementation of outdoor links, it was necessary to study the effect of atmospheric conditions such as heat-induced turbulence, attenuation due to fog and raindrops, etc. Therefore, in [J7], we studied an experimental OCC system under environmental phenomena emulated in a laboratory chamber. The experimental based results demonstrated that the heat-induced turbulence does not affect OCC system significantly, while the attenuation caused by fog can be mitigated by a proposed novel strategy of using the camera's built-in amplifier to overcome the optical power loss and to decrease the quantization noise induced by the ADC of the camera. This utilization of the CMOS camera's built-in amplifier opens a new possibility for OCC systems, extending the control strategy, and allowing to keep low exposure times and, thus, a high bandwidth,even in dense fog scenarios.

Finally, we proposed in [J8] the methodology to integrate both VLC-PD and OCC (IS-based VLC) links simultaneously to provide a versatile OIoT environment, where users can have a choice based on the device to switch between high- and low-speed VLC with PDs- and ISs-based Rx. For this reason, we proposed as well a hybrid modulation format that was used for both high- and low-speed VLC links, and experimentally verified the whole hybrid VLC-OCC scheme.

The results attained in this thesis have, as well, opened a number of directions for future research, as can be seen from the number of citations. Despite the fact that the proposed OCC technologies and methodologies for indoor and outdoor IoT environments offer significant improvement in system performance and link reliability, there are still many challenges in this area for which the author suggests future works as follows:

- The MIMO-OCC scheme can be enhanced further using large size commercially available display Tx and multi-channel based modulation schemes in order to enhance link span and R_b, respectively. The NN assisted MD based on pattern recognition algorithms can be developed in an Python or Android based application for smart phone and implemented over MIMO-OCC links to provide real-time device control within smart environments. The fiber optic lighting-based OCC scheme can be tested for different types of commercially available plastic optical fibers and improve coupling efficiency to enhance the emission and hence the link spans.

- The long range outdoor links can be implemented within smart city projects by utilizing the already available lighting infrastructure such as street and traffic lights and surveillance cameras. Within this, efficient ROI detection and positioning algorithms can be developed in order to establish communication links between moving vehicles and the infrastructure.

- As a part of potential future development of the hybrid VLC scheme in practical scenarios, the proposed scheme can overcome the problem of bandwidth efficiency using multiple wavelengths. Equalization techniques and different modulation

formats such as OFDM can be implemented to improve the reception success rate and the BER performance for low- and high-speed VLC links, respectively.

References

[1] F. Boccardi, R. W. Heath, A. Lozano, T. L. Marzetta, and P. Popovski, "Five disruptive technology directions for 5G," *IEEE Communications Magazine*, vol. 52, no. 2, pp. 74–80, 2014.

[2] "Everything you need to know about 5G," 2021. [Online]. Available: http://spectrum.ieee.org/video/telecom/wireless/everything-you-need-to-know-about-5g

[3] N. Wang, P. Wang, A. Alipour-Fanid, L. Jiao, and K. Zeng, "Physical-layer security of 5G wireless networks for IoT: Challenges and opportunities," *IEEE Internet of Things Journal*, vol. 6, no. 5, pp. 8169–8181, 2019.

[4] "Transformative 5G standards near completion," 2021. [Online]. Available: https://www.forbes.com/sites/jasonbloomberg/2017/06/14/transformative-5g-standards-near-completion/#4ea8524a25c4

[5] J. Ding, M. Nemati, C. Ranaweera, and J. Choi, "IoT connectivity technologies and applications: A survey," *arXiv preprint arXiv:2002.12646*, 2020.

[6] P. S. Nagendra Reddy, K. T. Kumar Reddy, P. A. Kumar Reddy, G. N. Kodanda Ramaiah, and S. N. Kishor, "An IoT based home automation using android application," in *2016 International Conference on Signal Processing, Communication, Power and Embedded System (SCOPES)*, 2016, pp. 285–290.

[7] N. A. Othman and I. Aydin, "A new IoT combined body detection of people by using computer vision for security application," in *2017 9th International Conference on Computational Intelligence and Communication Networks (CICN)*, 2017, pp. 108–112.

[8] R. Patel, V. K. Dabhi, and H. B. Prajapati, "A survey on IoT based road traffic surveillance and accident detection system (A smart way to handle traffic and concerned problems)," in *2017 Innovations in Power and Advanced Computing Technologies (i-PACT)*, 2017, pp. 1–7.

[9] H. Aksu, L. Babun, M. Conti, G. Tolomei, and A. S. Uluagac, "Advertising in the IoT era: Vision and challenges," *IEEE Communications Magazine*, vol. 56, no. 11, pp. 138–144, 2018.

[10] M. Uysal, Z. C. Capsoni, Ghassemlooy, A. Boucouvalas, and R. E. Udvary, *Optical wireless communications - An emerging technology*. Springer, 2016.

[11] Z. Ghassemlooy, L. N. Alves, S. Zvanovec, and M.-A. Khalighi, *Visible light communications: Theory and applications*. CRC press, 2017.

[12] Z. Ghassemlooy, S. Zvanovec, M.-A. Khalighi, W. O. Popoola, and J. Perez, "Optical wireless communication systems," *Optik*, vol. 151, pp. 1 – 6, 2017.

[13] P. H. Pathak, X. Feng, P. Hu, and P. Mohapatra, "Visible light communication, networking, and sensing: A survey, potential and challenges," *IEEE Communications Surveys & Tutorials*, vol. 17, no. 4, pp. 2047–2077, 2015.

[14] T. Komine and M. Nakagawa, "Fundamental analysis for visible-light communication system

using LED lights," *IEEE Transactions on Consumer Electronics*, vol. 50, no. 1, pp. 100–107, 2004.

[15] T. Koonen, "Indoor optical wireless systems: Technology, trends, and applications," *Journal of Lightwave Technology*, vol. 36, no. 8, pp. 1459–1467, 2017.

[16] T. Nguyen, A. Islam, T. Hossan, and Y. M. Jang, "Current status and performance analysis of optical camera communication technologies for 5G networks," *IEEE Access*, vol. 5, pp. 4574–4594, 2017.

[17] S. Zvanovec, P. Chvojka, P. A. Haigh, and Z. Ghassemlooy, "Visible light communications towards 5G," *Radioengineering*, vol. 24, no. 1, pp. 1–9, 2015.

[18] P. Haigh, "Using equalizers to increase data rates in organic photonic devices for visible light communications systems," Ph.D. dissertation, University of Northumbria, 2014.

[19] I. Demirkol, D. Camps-Mur, J. Paradells, M. Combalia, W. Popoola, and H. Haas, "Powering the internet of things through light communication," *IEEE Communications Magazine*, vol. 57, no. 6, pp. 107–113, 2019.

[20] C. Chen, S. Fu, X. Jian, M. Liu, X. Deng, and Z. Ding, "NOMA for energy-efficient LiFi-enabled bidirectional IoT communication," *IEEE Transactions on Communications*, vol. 69, no. 3, pp. 1693–1706, 2021.

[21] N. Chaudhary, O. I. Younus, L. N. Alves, Z. Ghassemlooy, S. Zvanovec, and H. Le-Minh, "An indoor visible light positioning system using tilted LEDs with high accuracy," *Sensors*, vol. 21, no. 3, p. 920, 2021.

[22] R. Boubezari, H. Le Minh, Z. Ghassemlooy, and A. Bouridane, "Smartphone camera based visible light communication," *Journal of Lightwave Technology*, vol. 34, no. 17, pp. 4121–4127, 2016.

[23] S. Teli, W. A. Cahyadi, and Y. H. Chung, "Optical camera communication: Motion over camera," *IEEE Communications Magazine*, vol. 55, no. 8, pp. 156–162, 2017.

[24] W. A. Cahyadi, Y. H. Kim, Y. H. Chung, and C.-J. Ahn, "Mobile phone camera-based indoor visible light communications with rotation compensation," *IEEE Photonics Journal*, vol. 8, no. 2, pp. 1–8, 2016.

[25] K.-L. Hsu, Y.-C. Wu, Y.-C. Chuang, C.-W. Chow, Y. Liu, X.-L. Liao, K.-H. Lin, and Y.-Y. Chen, "Cmos camera based visible light communication (vlc) using grayscale value distribution and machine learning algorithm," *Optics Express*, vol. 28, no. 2, pp. 2427–2432, 2020.

[26] W. Liu and Z. Xu, "Some practical constraints and solutions for optical camera communication," *Philosophical Transactions of the Royal Society A*, vol. 378, no. 2169, p. 20190191, 2020.

[27] M. Jang, "IEEE 802.15 WPAN 15.7 amendment-optical camera communications study group (SG 7a)," 2021. [Online]. Available: https://www.ieee802.org/15/pub/SG7a.html

[28] N.-T. Le and Y. M. Jang, "Performance evaluation of MIMO optical camera communications based rolling shutter image sensor," in *2016 Eighth International Conference on Ubiquitous and Future Networks (ICUFN)*.   IEEE, 2016, pp. 140–144.

[29] N. M. Tuan, T. V. Phuong, T.-H. Do, and N. T. V. Khanh, "An highly realistic optical camera communication simulation framework for internet of things applications," in *2021 21st ACIS International Winter Conference on Software Engineering, Artificial Intelligence, Networking*

and Parallel/Distributed Computing (SNPD-Winter).   IEEE, 2021, pp. 240–242.

[30]   K. Kadam and M. R. Dhage, "Visible light communication for IoT," in *2016 2nd International Conference on Applied and Theoretical Computing and Communication Technology (iCATccT)*.   IEEE, 2016, pp. 275–278.

[31]   Z. Wang, Q. Wang, W. Huang, and Z. Xu, *Visible light communications: Modulation and signal processing*.   John Wiley & Sons, 2017.

[32]   C.-W. Chow, C. Yeh, Y. Liu, and Y. Liu, "Improved modulation speed of LED visible light communication system integrated to main electricity network," *Electronics Letters*, vol. 47, no. 15, pp. 867–868, 2011.

[33]   M. Kavehrad, "Sustainable energy-efficient wireless applications using light," *IEEE Communications Magazine*, vol. 48, no. 12, pp. 66–73, 2010.

[34]   A. M. Vegni and T. D. Little, "Handover in VLC systems with cooperating mobile devices," in *2012 International Conference on Computing, Networking and Communications (ICNC)*. IEEE, 2012, pp. 126–130.

[35]   P. IEEE 802, "PHY and MAC standard for short-range wireless optical communication using visible light," 2010.

[36]   B. Lin, X. Tang, Z. Ghassemlooy, C. Lin, and Y. Li, "Experimental demonstration of an indoor VLC positioning system based on OFDMA," *IEEE Photonics Journal*, vol. 9, no. 2, pp. 1–9, 2017.

[37]   A. T. Hussein, M. T. Alresheedi, and J. M. Elmirghani, "Fast and efficient adaptation techniques for visible light communication systems," *IEEE/OSA Journal of Optical Communications and Networking*, vol. 8, no. 6, pp. 382–397, 2016.

[38]   "Augmented reality for iOS," 2021. [Online]. Available: https://www.apple.com/uk/ios/augmented-reality/

[39]   K. E. Laver, B. Lange, S. George, J. E. Deutsch, G. Saposnik, and M. Crotty, "Virtual reality for stroke rehabilitation," *Cochrane Database of Systematic Reviews*, no. 11, 2017.

[40]   H. Yang, W.-D. Zhong, C. Chen, A. Alphones, and P. Du, "QoS-driven optimized design-based integrated visible light communication and positioning for indoor IoT networks," *IEEE Internet of Things Journal*, vol. 7, no. 1, pp. 269–283, 2019.

[41]   P. Zhang, Q. Wang, Y. Yang, Y. Wang, Y. Sun, W. Xu, J. Luo, and L. Chen, "Enhancing the performance of optical camera communication via accumulative sampling," *Optics Express*, vol. 29, no. 12, pp. 19 015–19 023, 2021.

[42]   "Photron fastcam SA-Z." [Online]. Available: https://photron.com/fastcam-sa-z/

[43]   H. Nguyen, V. Nguyen, C. Nguyen, V. Bui, and Y. Jang, "Design and implementation of 2D MIMO-based optical camera communication using a light-emitting diode array for long-range monitoring system," *Sensors*, vol. 21, no. 9, p. 3023, 2021.

[44]   W. Huang, P. Tian, and Z. Xu, "Design and implementation of a real-time CIM-MIMO optical camera communication system," *Optics Express*, vol. 24, no. 21, pp. 24 567–24 579, 2016.

[45]   P. Luo, M. Zhang, Z. Ghassemlooy, H. Le Minh, H.-M. Tsai, X. Tang, L. C. Png, and D. Han, "Experimental demonstration of RGB LED-based optical camera communications," *IEEE Photonics Journal*, vol. 7, no. 5, pp. 1–12, 2015.

[46]   N. B. Hassan, Z. Ghassemlooy, S. Zvanovec, M. Biagi, A. M. Vegni, M. Zhang, and P. Luo,

"Non-line-of-sight MIMO space-time division multiplexing visible light optical camera communications," *Journal of Lightwave Technology*, vol. 37, no. 10, pp. 2409–2417, 2019.

[47]   M. Shahjalal, M. Hasan, M. Z. Chowdhury, Y. M. Jang *et al.*, "Smartphone camera-based optical wireless communication system: Requirements and implementation challenges," *Electronics*, vol. 8, no. 8, p. 913, 2019.

[48]   A. Duque, R. Stanica, H. Rivano, and A. Desportes, "Analytical and simulation tools for optical camera communications," *Computer Communications*, vol. 160, pp. 52–62, 2020.

[49]   Y. LeCun, Y. Bengio, and G. Hinton, "Deep learning," *Nature*, vol. 521, no. 7553, pp. 436–444, 2015.

[50]   O. I. Younus, N. B. Hassan, Z. Ghassemlooy, P. A. Haigh, S. Zvanovec, L. N. Alves, and H. Le Minh, "Data rate enhancement in optical camera communications using an artificial neural network equaliser," *IEEE Access*, vol. 8, pp. 42 656–42 665, 2020.

[51]   K. Yu, J. He, and Z. Huang, "Decoding scheme based on CNN for mobile optical camera communication," *Applied Optics*, vol. 59, no. 23, pp. 7109–7113, 2020.

[52]   S. R. Teli, W. A. Cahyadi, and Y. H. Chung, "Trained neurons-based motion detection in optical camera communications," *Optical Engineering*, vol. 57, no. 4, p. 040501, 2018.

[53]   T. Fujihashi, T. Koike-Akino, P. V. Orlik, and T. Watanabe, "High-throughput visual MIMO systems for screen-camera communications," *IEEE Transactions on Mobile Computing*, vol. 20, no. 6, pp. 2200–2211, 2020.

[54]   Philips, "Adafruit neopixel uberguide, WS2812B datasheet," 2021. [Online]. Available: https://cdn-learn.adafruit.com/downloads/pdf/adafruit-neopixel-uberguide.pdf

[55]   M. Tanaka, "Give me four: Residual interpolation for image demosaicing and upsampling." [Online]. Available: http://www.ok.sc.e.titech.ac.jp/~mtanaka/research.html

[56]   X. Li, B. Gunturk, and L. Zhang, "Image demosaicing: A systematic survey," in *Visual communications and image processing 2008*, vol. 6822.   International Society for Optics and Photonics, 2008, p. 68221J.

[57]   S. Arnon, *Visible light communication*.   Cambridge University Press, 2015.

[58]   F. Cao, X. Gong, C. He, and T. Ngai, "Removing the effect of blooming from potential energy measurement by employing total internal reflection microscopy integrated with video microscopy," *Journal of Colloid and Interface Science*, vol. 503, pp. 142–149, 2017.

[59]   N. Mansurov, "Understanding ISO, shutter speed and aperture-a beginner's guide," *Photographylife, September*, vol. 23, 2018.

[60]   C.-W. Chow, Z.-Q. Li, Y.-C. Chuang, X.-L. Liao, K.-H. Lin, and Y.-Y. Chen, "Decoding CMOS rolling-shutter pattern in translational or rotational motions for VLC," *IEEE Photonics Journal*, vol. 11, no. 2, pp. 1–5, 2019.

[61]   I. Takai, S. Ito, K. Yasutomi, K. Kagawa, M. Andoh, and S. Kawahito, "LED and CMOS image sensor based optical wireless communication system for automotive applications," *IEEE Photonics Journal*, vol. 5, no. 5, pp. 6 801 418–6 801 418, 2013.

[62]   T. Yamazato, I. Takai, H. Okada, T. Fujii, T. Yendo, S. Arai, M. Andoh, T. Harada, K. Yasutomi, K. Kagawa *et al.*, "Image-sensor-based visible light communication for automotive applications," *IEEE Communications Magazine*, vol. 52, no. 7, pp. 88–97, 2014.

[63]   C. Danakis, M. Afgani, G. Povey, I. Underwood, and H. Haas, "Using a CMOS camera sensor

for visible light communication," in *2012 IEEE Globecom Workshops*. IEEE, 2012, pp. 1244–1248.

[64] B. W. Kim, J.-H. Yoo, and S.-Y. Jung, "Design of streaming data transmission using rolling shutter camera-based optical camera communications," *Electronics*, vol. 9, no. 10, p. 1561, 2020.

[65] V. P. Rachim and W.-Y. Chung, "Multilevel intensity-modulation for rolling shutter-based optical camera communication," *IEEE Photonics Technology Letters*, vol. 30, no. 10, pp. 903–906, 2018.

[66] W.-C. Wang, C.-W. Chow, C.-W. Chen, H.-C. Hsieh, and Y.-T. Chen, "Beacon jointed packet reconstruction scheme for mobile-phone based visible light communications using rolling shutter," *IEEE Photonics Journal*, vol. 9, no. 6, pp. 1–6, 2017.

[67] V. Nguyen, Y. Tang, A. Ashok, M. Gruteser, K. Dana, W. Hu, E. Wengrowski, and N. Mandayam, "High-rate flicker-free screen-camera communication with spatially adaptive embedding," in *IEEE INFOCOM 2016-The 35th Annual IEEE International Conference on Computer Communications*. IEEE, 2016, pp. 1–9.

[68] Y. Yang, J. Hao, and J. Luo, "Ceilingtalk: Lightweight indoor broadcast through LED-camera communication," *IEEE Transactions on Mobile Computing*, vol. 16, no. 12, pp. 3308–3319, 2017.

[69] N. B. Hassan, Z. Ghassemlooy, S. Zvanovec, P. Luo, and H. Le-Minh, "Non-line-of-sight 2× N indoor optical camera communications," *Applied Optics*, vol. 57, no. 7, pp. B144–B149, 2018.

[70] W.-C. Wang, C.-W. Chow, L.-Y. Wei, Y. Liu, and C.-H. Yeh, "Long distance non-line-of-sight (NLOS) visible light signal detection based on rolling-shutter-patterning of mobile-phone camera," *Optics Express*, vol. 25, no. 9, pp. 10 103–10 108, 2017.

[71] I. S. Association *et al.*, "IEEE standard for local and metropolitan area networks-part 15.7: short-range wireless optical communication using visible light," *IEEE: Piscataway, NZ, USA*, pp. 1–309, 2011.

[72] W. A. Cahyadi and Y. H. Chung, "Wide receiver orientation using diffuse reflection in camera-based indoor visible light communication," *Optics Communications*, vol. 431, pp. 19–28, 2019.

[73] N. B. Hassan, Y. Huang, Z. Shou, Z. Ghassemlooy, A. Sturniolo, S. Zvanovec, P. Luo, and H. Le-Minh, "Impact of camera lens aperture and the light source size on optical camera communications," in *2018 11th International Symposium on Communication Systems, Networks & Digital Signal Processing (CSNDSP)*. IEEE, 2018, pp. 1–5.

[74] Q. N. Pham, V. P. Rachim, J. An, and W.-Y. Chung, "Ambient light rejection using a novel average voltage tracking in visible light communication system," *Applied Sciences*, vol. 7, no. 7, p. 670, 2017.

[75] F. de Souza Campos, J. A. C. Ulson, J. W. Swart, M. J. Deen, O. Marinov, and D. Karam, "Temporal noise analysis and measurements of CMOS active pixel sensor operating in time domain," in *2013 26th Symposium on Integrated Circuits and Systems Design (SBCCI)*. IEEE, 2013, pp. 1–5.

[76] T. Kuroda, *Essential principles of image sensors*. CRC press, 2017.

[77] J. Perez-Ramirez and D. K. Borah, "A single-input multiple-output optical system for mobile

communication: Modeling and validation," *IEEE Photonics Technology Letters*, vol. 26, no. 4, pp. 368–371, 2013.

[78] Q. Wang, Y. Shen, and J. Jin, "Performance evaluation of image fusion techniques," *Image Fusion: Algorithms and Applications*, vol. 19, pp. 469–492, 2008.

[79] J. Cha, V. Mariappan *et al.*, "PHY/MAC for variable transparent amplitude-shape-color (VTASC) modulation," *IEEE P802. 15 Working Group for Wireless Personal Area Networks (WPANs)*, 2016.

[80] T. Yamazato, "V2X communications with an image sensor," *Journal of Communications and Information Networks*, vol. 2, no. 4, pp. 65–74, 2017.

[81] K. Ebihara, K. Kamakura, and T. Yamazato, "Spatially-modulated space-time coding in visible light communications using 2× 2 LED array," in *2014 IEEE Asia Pacific Conference on Circuits and Systems (APCCAS)*. IEEE, 2014, pp. 320–323.

[82] T. Nagura, T. Yamazato, M. Katayama, T. Yendo, T. Fujii, and H. Okada, "Improved decoding methods of visible light communication system for ITS using LED array and high-speed camera," in *2010 IEEE 71st Vehicular Technology Conference*. IEEE, 2010, pp. 1–5.

[83] M. Kowalczyk, "Two-channel MIMO-OCC transmission system on a smartphone," in *Photonics Applications in Astronomy, Communications, Industry, and High Energy Physics Experiments 2017*, vol. 10445. International Society for Optics and Photonics, 2017, p. 104450H.

[84] W. Du, J. C. Liando, and M. Li, "Softlight: Adaptive visible light communication over screen-camera links," in *IEEE INFOCOM 2016-The 35th Annual IEEE International Conference on Computer Communications*. IEEE, 2016, pp. 1–9.

[85] S.-H. Chen and C.-W. Chow, "Hierarchical scheme for detecting the rotating MIMO transmission of the in-door RGB-LED visible light wireless communications using mobile-phone camera," *Optics Communications*, vol. 335, pp. 189–193, 2015.

[86] C.-W. Chow, C.-Y. Chen, and S.-H. Chen, "Enhancement of signal performance in LED visible light communications using mobile phone camera," *IEEE Photonics Journal*, vol. 7, no. 5, pp. 1–7, 2015.

[87] K. Liang, C.-W. Chow, and Y. Liu, "RGB visible light communication using mobile-phone camera and multi-input multi-output," *Optics Express*, vol. 24, no. 9, pp. 9383–9388, 2016.

[88] P. Ji, H.-M. Tsai, C. Wang, and F. Liu, "Vehicular visible light communications with LED taillight and rolling shutter camera," in *2014 IEEE 79th Vehicular Technology Conference (VTC Spring)*. IEEE, 2014, pp. 1–6.

[89] T. Nguyen, A. Islam, and Y. M. Jang, "Region-of-interest signaling vehicular system using optical camera communications," *IEEE Photonics Journal*, vol. 9, no. 1, pp. 1–20, 2016.

[90] M. D. Thieu, T. L. Pham, T. Nguyen, and Y. M. Jang, "Optical-ROI-signaling for vehicular communications," *IEEE Access*, vol. 7, pp. 69 873–69 891, 2019.

[91] S. Teli and Y.-H. Chung, "Selective capture based high-speed optical vehicular signaling system," *Signal Processing: Image Communication*, vol. 68, pp. 241–248, 2018.

[92] I. Takai, T. Harada, M. Andoh, K. Yasutomi, K. Kagawa, and S. Kawahito, "Optical vehicle-to-vehicle communication system using LED transmitter and camera receiver," *IEEE Photonics Journal*, vol. 6, no. 5, pp. 1–14, 2014.

[93] Y. Goto, I. Takai, T. Yamazato, H. Okada, T. Fujii, S. Kawahito, S. Arai, T. Yendo, and K. Kamakura, "A new automotive VLC system using optical communication image sensor," *IEEE Photonics Journal*, vol. 8, no. 3, pp. 1–17, 2016.

[94] M. K. Hasan, N. T. Le, M. Shahjalal, M. Z. Chowdhury, and Y. M. Jang, "Simultaneous data transmission using multilevel LED in hybrid OCC/LiFi system: concept and demonstration," *IEEE Communications Letters*, vol. 23, no. 12, pp. 2296–2300, 2019.

[95] D. T. Nguyen, S. Park, Y. Chae, and Y. Park, "VLC/OCC hybrid optical wireless systems for versatile indoor applications," *IEEE Access*, vol. 7, pp. 22 371–22 376, 2019.

[96] M. Hasan, M. Z. Chowdhury, M. Shahjalal, V. T. Nguyen, Y. M. Jang *et al.*, "Performance analysis and improvement of optical camera communication," *Applied Sciences*, vol. 8, no. 12, p. 2527, 2018.

[97] P. A. Haigh, Z. Ghassemlooy, S. Rajbhandari, and I. Papakonstantinou, "Visible light communications using organic light emitting diodes," *IEEE Communications Magazine*, vol. 51, no. 8, pp. 148–154, 2013.

[98] P. A. Haigh, Z. Ghassemlooy, I. Papakonstantinou, F. Tedde, S. F. Tedde, O. Hayden, and S. Rajbhandari, "A MIMO-ANN system for increasing data rates in organic visible light communications systems," in *2013 IEEE International Conference on Communications (ICC)*. IEEE, 2013, pp. 5322–5327.

[99] P. A. Haigh, F. Bausi, H. Le Minh, I. Papakonstantinou, W. O. Popoola, A. Burton, and F. Cacialli, "Wavelength-multiplexed polymer LEDs: Towards 55 Mb/s organic visible light communications," *IEEE Journal on Selected Areas in Communications*, vol. 33, no. 9, pp. 1819–1828, 2015.

[100] J.-Y. Sung, C.-W. Chow, C.-H. Yeh, and Y.-C. Wang, "Service integrated access network using highly spectral-efficient MASK-MQAM-OFDM coding," *Optics Express*, vol. 21, no. 5, pp. 6555–6560, 2013.

[101] C. Chen, W.-D. Zhong, and D. Wu, "Integration of variable-rate OWC with OFDM-PON for hybrid optical access based on adaptive envelope modulation," *Optics Communications*, vol. 381, pp. 10–17, 2016.

Author's Publications

List of Author's Publications Related to the Doctoral Thesis

All authors contributed equally unless otherwise stated.

Papers in Peer-Reviewed Journals with Impact Factor:

[J1] **S. R. Teli**, V. Matus, S. Zvánovec, R. Perez-Jimenez, S. Vitek, and Z. Ghassemlooy, "Optical camera communications for IoT–rolling-shutter based MIMO scheme with grouped LED array transmitter," Sensors, vol. 20, pp. 3361, 2020.

[J2] **S. R. Teli**, S. Zvánovec, R. Perez-Jimenez, and Z. Ghassemlooy, "Spatial frequency based angular behavior of a short-range flicker-free MIMO-OCC links," Applied Optics, vol. 59, pp. 10357-10368, 2020.

[J3] **S. R. Teli**, K. Eollosova, S. Zvanovec, Z. Ghassemlooy, and M. Komanec, "Optical camera communications link using an LED-coupled illuminating optical fiber," Optics Letters, vol. 46, pp. 2622-2625, 2021.

[J4] **S. R. Teli**, S. Zvanovec, and Z. Ghassemlooy, "Performance evaluation of neural network assisted motion detection schemes implemented within indoor optical camera based communications," Optics Express, vol. 27(17), pp. 24082-24092, 2019.

[J5] P. Chavez-Burbano, S. Vitek, **S. R. Teli**, V. Guerra, J. Rabadan, R. Perez-Jimenez, and S. Zvanovec, "Optical camera communication system for Internet of Things based on organic light emitting diodes," Electronics Letters, vol. 55(6), pp. 334-336, 2019.

[J6] E. Eso, **S. R. Teli**, N. B. Hassan, S. Vitek, Z. Ghassemlooy, and S. Zvanovec, "400 m rolling-shutter-based optical camera communications link," Optics Letters, vol. 45(5), pp. 1059-1062, 2020.

[J7] V. Matus, E. Eso, **S. R. Teli**, R. Perez-Jimenez, and S. Zvanovec, "Experimentally derived feasibility of optical camera communications under turbulence and fog conditions," Sensors, vol. 20, pp. 757, 2020.

[J8] **S. R. Teli**, P. Chvojka, S. Vitek, S. Zvanovec, R. Perez-Jimenez, and Z. Ghassemlooy "A SIMO hybrid visible light communication system for optical IoT," IEEE Internet of Things, 2021, Accepted for publication.

Papers and Abstracts in Conference Proceedings Listed in the Web of Knowledge:

[C1] **S. R. Teli**, S. Zvánovec, Z. Ghassemlooy, "Experimental characterization of fiber optic lighting - optical camera communications," In: IEEE International Symposium on Personal, Indoor and Mobile Radio Communications, 2021, Accepted.

[C2] **S. R. Teli**, S. Zvánovec, Z. Ghassemlooy, "Flicker-free multi-channel transmitter orientation in camera based optical wireless communications," In: 14th Pacific Rim Conference on Lasers and Electro-Optics, IEEE/OSA, pp. 1-3, 2020.

[C3] **S. R. Teli**, V. Matus, S. Zvanovec, R. Perez-Jimenez, S. Vitek, and Z. Ghassemlooy, "The first study of MIMO scheme within rolling-shutter based optical camera communications," In: 2020 12th International Symposium on Communication Systems, Networks and Digital Signal Processing (CSNDSP), IEEE, pp. 1-5, 2020.

[C4] V. Matus, V. Guerra, C. Jurado-Verdu, **S. R. Teli**, S. Zvanovec, J. Rabadan, and R. Perez-Jimenez, "Experimental evaluation of an analog gain optimization algorithm in optical camera communications," 2020 12th International Symposium on Communication Systems, Networks and Digital Signal Processing (CSNDSP), IEEE, pp. 1-5, 2020.

[C5] **S. R. Teli**, S. Zvanovec, and Z. Ghassemlooy, "The first tests of smartphone camera exposure effect on optical camera communication links," In: 2019 15th International Conference on Telecommunications (ConTEL) IEEE, pp. 1-6.

[C6] **S. R. Teli**, S. Zvanovec and Z. Ghassemlooy, "Experimental investigation of neuron based motion detection in internet of things using optical camera communications," 2019 26th International Conference on Telecommunications (ICT), IEEE, Hanoi, Vietnam, 2019, pp. 202-205.

[C7] **S. R. Teli**, S. Zvanovec and Z. Ghassemlooy, "Optical internet of things within 5G: applications and challenges," 2018 IEEE International Conference on Internet of Things and Intelligence System (IOTAIS), IEEE, Bali, 2018, pp. 40-45.

Citations in Web of Knowledge and Scopus (except self-citations):

Journal Paper [J1]:

[J1,Cit1] H. Nguyen, V. Nguyen, C. Nguyen, V. Bui, and Y. Jang, "Design and implementation of 2D MIMO-based optical camera communication using a light-emitting diode array for long-range monitoring system," Sensors, vol. 21(9), pp. 3023, 2021.

[J1,Cit2] A. Mederos-Barrera, C. Jurado-Verdu, V. Guerra, J. Rabadan, and R. Perez-Jimenez, "Design and experimental characterization of a discovery and tracking system for optical camera communications," Sensors, vol. 21(9), pp. 2925, 2021.

[J1,Cit3] F. Ahmed, O. Ali, M. Alam, and Y. Jang, "Interference cancellation and proper thresholding using deep learning method in optical camera communication," 3rd International Conference on Artificial Intelligence in Information and Communication, ICAIIC 2021, pp. 471, 2021.

[J1,Cit4] B. W. Kim, J. Yoo, and S. Jung, "Design of streaming data transmission using rolling shutter camera-based optical camera communications", Electronics (Switzerland), vol. 9, no. 10, pp. 1-9, 2020.

[J1,Cit5] M. F. Ahmed, M. Shahjalal, M. O. Ali and Y. Min Jang, "Neural network-based LED detection in vehicular system for high data rate in OCC," 2020 International Conference on Information and Communication Technology Convergence (ICTC), pp. 662-665, 2020.

Journal Paper [J2]:

[J2,Cit1] C. Jurado-Verdu, V. Guerra, V. Matus, C. Almeida, and J. Rabadan, "Optical camera communication as an enabling technology for microalgae cultivation," Sensors, vol. 21, no. 5, pp. 1-26, 2021.

Journal Paper [J4]:

[J3,Cit1] P. Zhang, Q. Wang, Y. Yang, Y. Wang, Y. Sun, W. Xu, J. Luo, and L. Chen, "Enhancing the performance of optical camera communication via accumulative sampling," Optics Express, vol. 29, no. 12, pp. 19015-19023, 2021.

[J3,Cit2] M. F. Ahmed, M. K. Hasan, M. Shahjalal, M. M. Alam, and Y. M. Jang, "Experimental demonstration of continuous sensor data monitoring using neural network-based optical camera communications," IEEE Photonics Journal, vol. 12, no. 5, 2020.

[J3,Cit3] J. He, Z. Huang, and K. Yu, "High-accuracy scheme based on a look-up table for motion detection in an optical camera communication system," Optics Express, vol. 28, no. 7, pp. 10270-10279, 2020.

[J3,Cit4] J. Zhang, X. Zhao, Y. Wu, P. Cao, X. Wang, F. Shi, and Y. Niu, "Analysis and modeling of football team's collaboration mode and performance evaluation using network science and BP neural network", Mathematical Problems in Engineering, 2020.

Journal Paper [J5]:

[J5,Cit1] N. M. Tuan, T. V. Phuong, T. Do, and N. T. Vu Khanh, "An highly realistic optical camera communication simulation framework for Internet of Things applications," Proceedings - 2021 21st ACIS International Semi-Virtual Winter Conference on Software Engineering, Artificial Intelligence, Networking and Parallel/Distributed Computing, SNPD-Winter 2021, pp. 240, 2021.

[J5,Cit2] M. Z. Chowdhury, M. Shahjalal, M. K. Hasan, and Y. M. Jang, "The role of optical wireless communication technologies in 5G/6G and IoT solutions: Prospects, directions, and challenges," Applied Sciences, vol. 9, no. 20, 2019.

Journal Paper [J6]:

[J6,Cit1] B. W. Kim, J. Yoo, and S. Jung, "Design of streaming data transmission using rolling shutter camera-based optical camera communications," Electronics, vol. 9, no. 10, pp. 1-9, 2020.

[J6,Cit2] F. Seguel, C. Azurdia-Meza, N. Krommenacker, P. Charpentier, V. Bombardier, and C. Carreno, "Miner video tracking and identification using optical camera communications in a wireless multimedia sensor network," 2020 12th International Symposium on Communication Systems, Networks and Digital Signal Processing, CSNDSP 2020.

Journal Paper [J7]:

[J7,Cit1] R. Miclea, V. Ungureanu, F. Sandru, and I. Silea, "Visibility enhancement and fog detection: Solutions presented in recent scientific papers with potential for application to mobile systems," Sensors, vol. 21, no. 10, 2021.

[J7,Cit2] H. A. Kadhum, M. A. A. Ali, and H. M. Mikhlif, "Investigation of modulated signal transmission in optical fiber irradiated by gamma photons," Nonlinear Optics Quantum Optics, vol. 53, no. 3-4, pp. 311-322, 2021.

[J7,Cit3] H. M. Mikhlif, M. A. A. Ali, and Z. A. Saleh, "Underwater wireless optical communication: A case study of chlorophyll effect," Journal of Optical Communications, 2021.

Conference Paper [C5]:

[C5,Cit1] L. H. Pham, D. N. Tran, J. Y. Byun, C. H. Rhie, and J. W. Jeon, "A smartphone-based laser measuring system for gap and flush assessment in car body," IEEE Transactions on Industrial Electronics, vol. 68, no. 7, pp. 6297-6307, 2021.

Conference Paper [C6]:

[C6,Cit1] Q. Chen, T. Zong, H. Wen, K. Geng, R. Deng, Q. Xu, K. Luo, and M. Chen, "YCbCr color pre-enhancement based MISO-4CSK-OCC system," Journal of Optoelectronics Laser, vol. 31, no. 5, pp. 468-474, 2020.

Conference Paper [C7]:

[C7,Cit1] C. Chen, S. Fu, X. Jian, M. Liu, X. Deng, and Z. Ding, "NOMA for energy-efficient LiFi-enabled bidirectional IoT communication," IEEE Transactions on Communications, vol. 69, no. 3, pp. 1693-1706, 2021.

[C7,Cit2] S. Grigoryeva, A. Alimkhanova, and A. Baklanov, "Organization of an automated heat modes control system through LED lighting," 2020 International Multi-Conference on Industrial Engineering and Modern Technologies, FarEastCon 2020.

[C7,Cit3] M. Galal, W. P. Ng, R. Binns, and A. A. E. Aziz, "Experimental characterization of RGB LED transceiver in low-complexity LED-to-LED link," Sensors (Switzerland), vol. 20, no. 20, pp. 1-12, 2020.

[C7,Cit4] K. Yu, J. He, and Z. Huang, "Decoding scheme based on CNN for mobile optical camera communication," Applied Optics, vol. 59, no. 23, pp. 7109-7113, 2020.

[C7,Cit5] M. Petkovic, D. Vukobratovic, A. Munari, and F. Clazzer, "Relay-aided slotted aloha for optical wireless communications," 2020 12th International Symposium on Communication Systems, Networks and Digital Signal Processing, CSNDSP 2020.

[C7,Cit6] K. Janeczek, A. Araźna, W. Stęplewski, and T. Serzysko, "Traceability of printed circuit board assemblies using embedded electronic components," IET Microwaves, Antennas and Propagation, vol. 14, no. 8, pp. 785-790, 2020.

[C7,Cit7] E. A. Grigoryev, A. E. Baklanov, S. V. Grigoryeva, A. Z. Alimkhanova, and V. M. Sayun, "A new approach to physical encoding in VLC data transmission technology," International Conference of Young Specialists on Micro/Nanotechnologies and Electron Devices, EDM, pp. 221, 2020.

[C7,Cit8] D. Vukobratovic, and F. J. Escribano, "Adaptive multi-receiver coded slotted ALOHA for indoor optical wireless communications," IEEE Communications Letters, vol. 24, no. 6, pp. 1308-1312, 2020.

[C7,Cit9] J. He, Z. Huang, and K. Yu, "High-accuracy scheme based on a look-up table for motion detection in an optical camera communication system," Optics Express, vol. 28, no. 7, pp. 10270-10279, 2020.

[C7,Cit10] W. Li, F. Wang, Y. Pan, L. Zhang, and J. Liu, "Computing cost optimization for multi-BS in MEC by offloading," Mobile Networks and Applications, 2020.

[C7,Cit11] J. Ding, M. Nemati, C. Ranaweera, and J. Choi, "IoT connectivity technologies and applications: A survey," IEEE Access, vol. 8, pp. 67646-67673,2020.

SHIVANI RAJENDRA TELI

 02.05.1994   ✉ telishiv@fel.cvut.cz   📍 Prague, Czech Republic   ⚲ Female

 ResearchGate   Google Scholar   LinkedIn

EDUCATION

📅 **05.2018-PRESENT**

POSTGRADUATE STUDY IN RADIOELECTRONICS, CZECH TECHNICAL UNIVERSITY IN PRAGUE

<u>Dissertation thesis:</u> Design and implementation of optical camera-based communication systems for internet-of-things applications

📅 **02.2016-02.2018**

MASTER'S DEGREE IN INFORMATION AND COMMUNICATION ENGINEERING, PUKYONG NATIONAL UNIVERSITY, BUSAN, SOUTH KOREA

<u>Dissertation thesis:</u> Efficient Short-Range Optical Camera Communication with Motion and selective Capture

📅 **02.2011-02.2015**

BACHELOR'S DEGREE IN ELECTRONICS AND TELECOMMUNICATION, INDIRA COLLEGE OF ENGINEERING AND MANAGEMENT, INDIA

<u>Dissertation thesis:</u> Patient monitoring using telemetry system

ACADEMIC EXPERIENCES

📅 **02.05.2018 – PRESENT**

EARLY STAGE RESEARCHER #6 (ESR #6), CZECH TECHNICAL UNIVERSITY IN PRAGUE

Wireless and fiber optics team

<u>Project:</u> VisIoN - Visible light based Interoperability and Networking: European Union's Horizon 2020 research and innovation programme under the Marie Skłodowska-Curie grant agreement no 764461

📅 **02.02.2016 – 02.02.2018**

RESEARCHER, PUKYONG NATIONAL UNIVERSITY

Mobile Transmission System Lab

<u>Projects:</u> Research and development project funded by Brain Busan 21 of 2016

Research project funded by Korean National Research Foundation from Ministry of Education

EXTRA-CURRICULAR

📅 **2015 – PRESENT**

- VisIoN training school, workshops and industrial visits based on VLC networking
- 3 Month secondment in IDeTIC, Universidad de Las Palmas de Gran Canaria, Spain
- Training in Embedded Systems & Robotics- Nutan Infotronics Pvt. Ltd.
- Bharat Sanchar Nigam Limited Telecommunications: A-level course
- Workshop in mobile making- Nutan Infotronics Pvt. Ltd.
- Technologies: MATLAB, Arduino (MEGA, NUNO, etc.) and Python (intermediate level)
- Typesetting: LaTeX, Microsoft Office
- Language: Marathi (Native), Hindi (National), English (Fluent)